Simulations and components for novel fast wave microwave amplifiers and sources

Kathleen Matheson

SUPA and the Department of Physics

University of Strathclyde

Thesis submitted for the degree of Ph.D.

July 2014

This thesis is the result of the author's original research. It has been composed by the author and has not been previously submitted for examination which has led to the award of a degree.

The copyright of this thesis belongs to the author under the terms of the United Kingdom Copyright Acts as qualified by University of Strathclyde Regulation 3.50. Due acknowledgement must always be made of the use of any material contained in, or derived from, this thesis.

Abstract

A three dimensional parameterised model of an X-band 2nd harmonic gyro-travelling wave amplifier (gyro-TWA) with a helically corrugated interaction region has been created and optimised in the Particle-in-Cell code MAGIC-3D, to achieve an output power and saturated efficiency of ~1.0MW and ~27% respectively at 9.4GHz. This numerical model has been benchmarked to an experiment [Bratman, 2000] which demonstrated an output power and saturated efficiency of ~1.1MW and ~29% respectively at 9.4GHz, for similar input parameters. The numerical model has been coded in the Cartesian co-ordinate system which offers greater numerical stability over previous models, and has been shown to accurately and consistently reproduce results comparable to the experimental measurements. The good agreement between the simulation data and the experimental measurements naturally present the numerical model as a suitable benchmark tool to investigate potential efficiency and bandwidth enhancement of the amplifier, achieved through parameter profiling of the microwave circuit. The model predicts that a helical down taper of length 14cm to an output mean radius (r_0) and corrugation amplitude (l) of ~11.3mm and ~1.8mm respectively i.e. ~80% of the original helical waveguide's r_0 and l values, positioned 4cm before the end of the original uniform helical interaction region of the amplifier, could increase both the saturated efficiency of the amplifier by ~2.5% at 10.0GHz, from ~28.6% to ~31.1% and its bandwidth by 800MHz, from 1.8GHz to 2.6GHz.

In addition, an X-band Marie-type mode converter has been simulated and fabricated which effectively converts from the fundamental mode in rectangular waveguide to the cylindrical TE_{01} mode with minimal reflections, over an optimised 2.0GHz

bandwidth. This converter has been used to test a Penning cathode mesh with the experimental measurements confirming that the mesh transmitted an RF signal in the TE_{01} mode without reflection or mode conversion.

Acknowledgements

Contents

Chapter three: Numerical and experimental methods

Chapter four: PiC simulations of a helically corrugated interaction waveguide gyro-TWA

Chapter five: PiC simulations of a parameter profiled helically
corrugated interaction waveguide gyro-TWA

Chapter six: Marie-type converter

Chapter seven: Conclusions and future work

Publications

Chapter one: Introduction

1.1: Background

World demands significantly impact upon and can help fuel scientific research. An example of this in the field of microwave generation arose during the first and second world wars where major advancements in communications and radar were made. Here higher power and higher frequency operation were sought to overcome the congestion of lower frequency bands and to facilitate the imaging of smaller objects. Today there is a desire to operate at even higher powers and at ever increasing frequencies for applications such as plasma heating and current drive [Casey, 1990 and Thumm, 2005], plasma diagnostics [Dumbrajs, 1997 and Jain, 2010], ceramic sintering [Link, 1999 and Bykov, 2004], particle acceleration [Kolomensky, 1973 and Chu, 1985], atmospheric sensing [Manheimer, 1992 and Wang, 2000], imaging [Nguyen, 2001 and Blank, 2002] communications [Kumar, 2011] and medical advancements [Tatsukawa, 2002 and Siegel, 2004]. Many low power application demands are satisfied by solid state devices but when high powers at centimetre to sub-millimetre wavelengths are required vacuum electronic devices tend to dominate [Kartikeyan, 2004].

Vacuum electronic devices are typically classified as either slow- or fast-wave. In a slow-wave device the design of the RF structure is such to reduce the phase velocity, v_{ph}, of the wave to that of the imposed electron beam, resulting in a beam-wave interaction i.e. $v_{ph} <$ the speed of light, c. In these devices the distance between the electrons and the structural walls of the device must be less than a wavelength, with

1

the slow-waves localised near to the walls. Since slow-wave devices are dependent on the RF structure it is difficult to create a high power and high frequency device as the structure period is typically akin to the wavelength of the radiation [Sprangle, 1977]. Conventional microwave tube sources are examples of slow-wave devices and include the travelling wave tube [Gilmour Jr., 1994], the klystron [Korolyov, 2004] and the magnetron [Palevsky, 1979 and Daimon, 2007]. In a fast-wave device however, no attempt is made to slow the phase velocity of the electromagnetic wave and thus $v_{ph} > c$. Such devices are less constrained by the dimensions of the RF structure allowing for the use of relatively simple structures, typically smooth over-moded waveguides. By exploiting non-resonant interaction structures, fast-wave devices can operate at much higher frequencies and with greater power handling capabilities than slow-wave devices. Examples of fast-wave devices include cyclotron resonance masers (CRMs) [Goldenberg, 1996], peniotrons [Ishihara, 1996] and free electron lasers [Roberson, 1989].

In 1958, the astrophysicist R. Q. Twiss [Twiss, 1958] recognised a gain mechanism for free-electron gyro-radiation, later to be studied concurrently, but independently, in 1959 by A. V. Gaponov [Gaponov, 1959a, Gaponov, 1959b and Hirshfield, 1977] from a classical approach and by J. Schneider [Schneider, 1959] from a quantum mechanical approach. Also in this year the mechanism was experimentally verified by R. H Pantell [Pantell, 1959 and Chu, 2004]. In this cyclotron resonance maser (CRM) mechanism or instability, it is the relativistic mass dependence of the electrons that produces electron phase bunching. This azimuthal phase bunching dominates when the v_{ph} of the electromagnetic wave exceeds c and is generated in fast-wave structures. The first successful device to utilise this instability and undergo major development was the gyrotron, with this device having some similarities to an earlier experimental device detailed in [Bott, 1965].

1.2: Beam-wave interactions in a CRM

The generation of coherent radiation in a CRM device requires, in addition to the CRM instability's azimuthal bunching mechanism (which forms variations in electron density equivalent to the wavelength of the imposed electromagnetic wave), the fulfilment of a resonance condition between said imposed wave and the periodic motion of the electrons. This generation of coherent radiation is a stimulated process whereby electron bunching results from extended interaction with the electromagnetic wave. The resonance condition between the beam and the wave is of the form

$$\omega = s\omega_c + k_z v_z \qquad \qquad \textit{Equation 1.2.1}$$

where ω is the angular frequency of the imposed electromagnetic wave, s is an integer harmonic, ω_c is the electron cyclotron frequency, k_z is the axial wavenumber and v_z the drift velocity of the beam electrons. The electron cyclotron frequency is relativistic and can be written as

$$\omega_c = \frac{eB}{\gamma m_0} \qquad \qquad \textit{Equation 1.2.2}$$

where e is the charge on the electron, B is the magnitude of the confining magnetic field, γ is the Lorentz factor and m_0 is the rest mass of the electron. The Lorentz factor is given in terms of the particle velocity as

$$\gamma = \frac{1}{\sqrt{1 - \dfrac{v^2}{c^2}}} \qquad \qquad \textit{Equation 1.2.3}$$

where v is the total velocity of the electrons. Similarly γ may be expressed in terms of the kinetic energy as a fraction of the rest energy as

$$\gamma = 1 + \frac{eV}{m_0 c^2} \qquad \qquad \textit{Equation 1.2.4}$$

where V represents a voltage.

The operational frequency and bandwidth of a CRM device can be determined from a dispersion of ω-k_z diagram which show both the electron beam, *equation 1.2.1,* (described by a straight line) and waveguide mode, *equation 1.2.5,* (described by a hyperbolic) dispersions.

$$\omega^2 = c^2(k_z^2 + k_c^2)$$
Equation 1.2.5

Here k_c is the cut-off perpendicular wavenumber, with k_c successively larger the higher the order of mode. For coupling between the electron beam and either the forwards or backwards propagating electromagnetic wave, the electron beam line and the waveguide mode must intersect at some value of k_z. Depending on the parameters, intersection may be at a crossing point or at a grazing incidence occurring at either positive or negative k_z values. As a result, a unique dispersion diagram exists for each CRM device.

1.3: Examples of CRMs

1.3.1: The gyrotron

Gyrotron [Flyagin, 1977 and Nusinovich, 2004], gyro-monotron and gyrotron oscillator are terms nowadays often interchangeably used to refer to broadly the same fast-wave oscillator, designed to emit coherent radiation at close to ω_c or one of its integer harmonics. Such devices can deliver hundreds of kilowatts of output power at millimetre and sub-millimetre wavelengths in either long pulse or continuous wave operation.

In a conventional gyrotron [Flyagin, 1988] a magnetron injection gun produces an annular electron beam. These emitted electrons acquire both axial and orbital velocity components and propagate towards the resonant cavity of the device, traversing

through a gradually increasing guide magnetic field (here the transverse (orbital) momentum of the electrons increases due to adiabatic magnetic compression of the electron beam). The externally applied axial magnetic field sustains the cyclotron motion of the electrons which track helical paths around the lines of magnetic flux, with the strength of the field such that ω_c or an integer harmonic of this is approximately matched to the frequency of the cavity eigenmode (leading to limited frequency tune-ability by the magnetic field). In the cavity region where the magnetic field is uniform, transverse components of the electric field interact with the beam electrons and the orbital kinetic energy of the electrons is converted to RF radiation. The spent electron beam then exits the cavity and experiences a region of decreasing magnetic field which no longer sustains confinement of the beam. These spent electrons then settle on the collector with the RF radiation extracted through an output window.

For the gyrotron which operates close to cut-off, the Doppler shifted $k_z v_z$ component in the beam-wave resonance condition is negligible, *equation 1.2.1*, (since k_z for such devices is close to zero), *figure 1.3.1*.
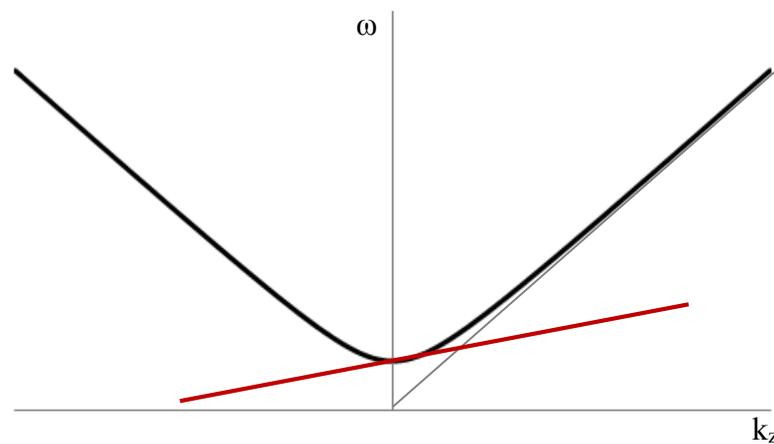
Figure 1.3.1: Generic dispersion diagram for a gyrotron.

However by operating close to cut-off, gyrotrons have a higher tolerance to velocity spread in the beam electrons since the Doppler term does not broaden the resonance. Here the guide wavelength is long and the RF fields, over the entire cavity length, are basically in phase.

1.3.2: The gyro-travelling wave tube (gyro-TWT)

For over 40 years, gyrotrons have received extensive development and are nowadays widely in use successfully and reliably delivering high powers at high frequencies in both long-pulse and continuous wave operation. However with attention largely on the gyrotron, the research and development of alternative efficient, high power and high frequency fast-wave devices has taken much longer. The realisation of a device utilising the CRM instability in an amplifier configuration presented new difficulties. The inherent narrow bandwidth and low start up current for the absolute instability of the gyrotron made it difficult to create an amplifier in this regime of operation. However, by operating with a reduced pitch factor α

$$\alpha = \frac{v_\perp}{v_z}$$
Equation 1.3.2.1

(here $v_\perp$ represents perpendicular velocity) whilst retaining grazing resonance, it was shown that these effects could be considerably mitigated and that the Doppler frequency upshift term, *equation 1.2.1,* would become more significant [Lin, 1985]. These realisations led to the development of the gyro-travelling wave tube (gyro-TWT).

Gyro-TWTs make use of a non-resonant structure to generate a travelling wave interaction in which a mildly relativistic electron beam interacts with a waveguide mode. In such devices amplification of the input electromagnetic wave occurs as it propagates with the electron beam. Conventional gyro-TWTs, with smooth bore interaction regions, have larger k_z values than that of the gyrotron and typically operate

at grazing incidence, *figure 1.3.2*, allowing for large frequency bandwidth and high tune-ability over which the group velocity, v_g, of the wave matches the beam drift velocity.
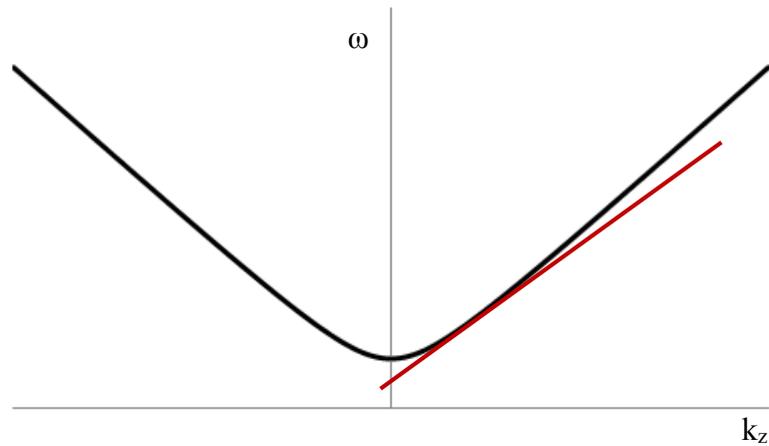
Figure 1.3.2: *Generic dispersion diagram for a gyro-TWT.*

Gyro-TWTs which make use of smooth bore interaction regions can be susceptible to spurious self-oscillations. Furthermore, degradation in beam quality owing to velocity spread of the beam electrons occurs when operating far from cut-off affecting overall electronic efficiency. Thus low k_z gyro-TWTs have limited bandwidth and are unstable to oscillations whilst large k_z devices have increased bandwidth but are sensitive to beam velocity spread. Owing to these constraints, it is difficult to make an efficient smooth-bore interaction waveguide gyro-TWT. However methods to lessen these effects and improve the performance of these amplifiers include tapering of the confining magnetic field, the interaction waveguide or both [Park, 1994].

1.3.3: The gyro-travelling wave amplifier with a helically corrugated interaction waveguide (gyro-TWA)

A novel approach to altering the dispersion characteristics of a device is to introduce a perturbation into the interaction region. As stated, with gyro-TWTs susceptible to parasitic self-oscillation and velocity spread in the electron beam it is desirable to create a regime where both these effects can be mitigated. A method to obtain such dispersion is to introduce a helical corrugation along the inner wall surface of the interaction waveguide. In this type of waveguide, a near cut-off upper order mode couples to a far from cut-off travelling spatial harmonic lower order mode, to produce an eigenwave with a near constant and finite v_g in a region of near infinite v_{ph}. This modified wave dispersion, *figure 1.3.3,* can then be matched to the electron beam's dispersion over an increased bandwidth in a region of small k_z values [Cooke, 1998, Denisov, 1998a and Zhu, 2012].
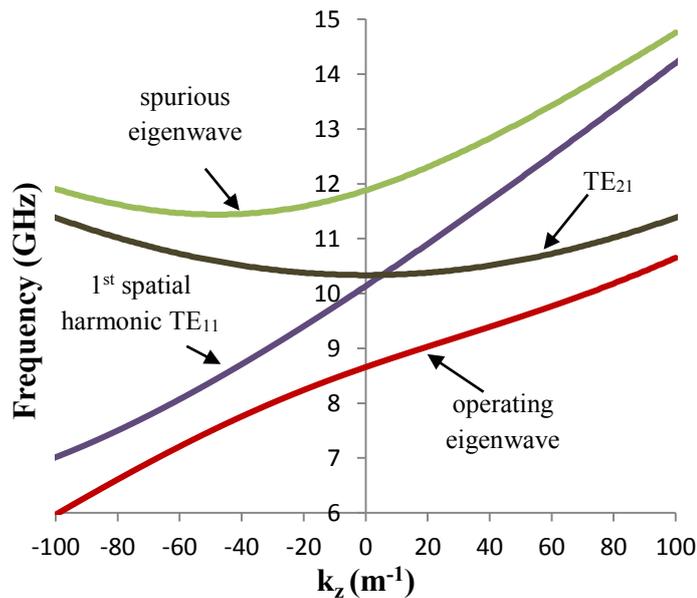
Figure 1.3.3: *Dispersion diagram for a 3-fold helically corrugated waveguide.*

Gyro-travelling wave amplifiers (gyro-TWAs) which utilise this configuration have been known to achieve in excess of 1.0MW with electronic efficiencies of ~29% in the 2nd cyclotron harmonic at X-band [Bratman, 2000].

1.3.4: The cyclotron autoresonance maser (CARM)

The cyclotron autoresonance maser (CARM) [Bratman, 1995, Bratman, 2001, Cooke, 1996 and Speirs, 2004] has the potential to be an efficient source of coherent and broadband radiation at millimetre and sub-millimetre wavelengths. In these devices, a moderately relativistic electron beam excites a travelling electromagnetic wave, propagating along the same axis as the applied confining magnetic field, with v_{ph} close to c. In this operating regime, little to no change in the resonant v_{ph} occurs despite the electron energy changing as a result of the resonant interaction. This is because the decrease in γ and subsequent increase in ω_c is compensated for by a decrease in the v_z component of the Doppler frequency upshift term, due to the orthogonal magnetic flux density of the electromagnetic wave, $B_\perp$. This decrease ensures that the particle's phase with respect to the local E-field remains constant (maintaining the interaction at the same frequency), *figure 1.3.4*. This phenomenon is known as autoresonance. Thus the predominant strength of the CARM over other CRM devices lies in its regime of operation since the large k_z value and resulting large Doppler frequency upshift of the device culminates in the magnetic field requirements for a given frequency of operation being greatly reduced without the need to operate at a harmonic. This advantage however, is at the expense of electronic efficiency which is significantly impaired due to large Doppler broadening of the resonance, from even very slight velocity spread in the electrons. Ideal operation of a CARM amplifier is at initial grazing incidence to achieve a broadband frequency tuneable device.
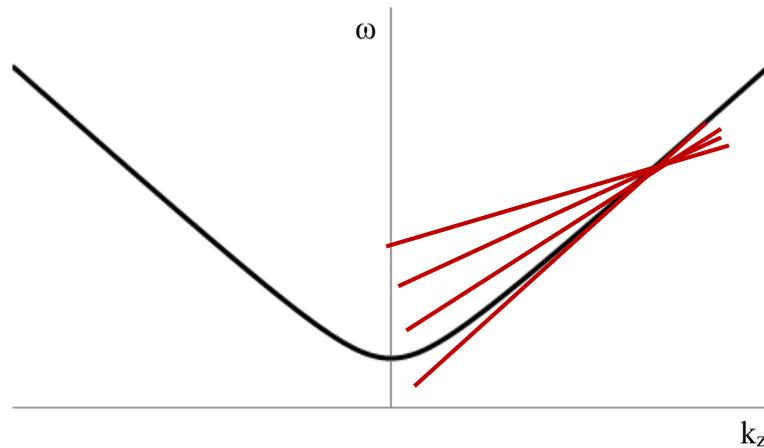
Figure 1.3.4: Generic dispersion diagram for a CARM showing autoresonance.

The primary advantage of utilising an autoresonant device is that once beam electrons become azimuthally phase bunched (a result of the CRM instability) a large amount of beam energy can be extracted, in principal, without loss of synchronism. As with both the gyro-TWT and the gyro-TWA, the CARM amplifier operates on a single pass with a convective instability, with oscillator configurations usually featuring cavities designed to provide 'external' feedback.

1.3.5: The gyro-backwards wave oscillator (gyro-BWO)

In a gyro-backwards wave oscillator (gyro-BWO) [Nusinovich, 1996 and Chen, 2000], the electron beam interacts with a backwards propagating electromagnetic wave, such that the beam velocity and the wave v_g are in opposing directions. In these devices the beam-wave intersection occurs in the negative k_z range on a dispersion diagram, *figure 1.3.5*.
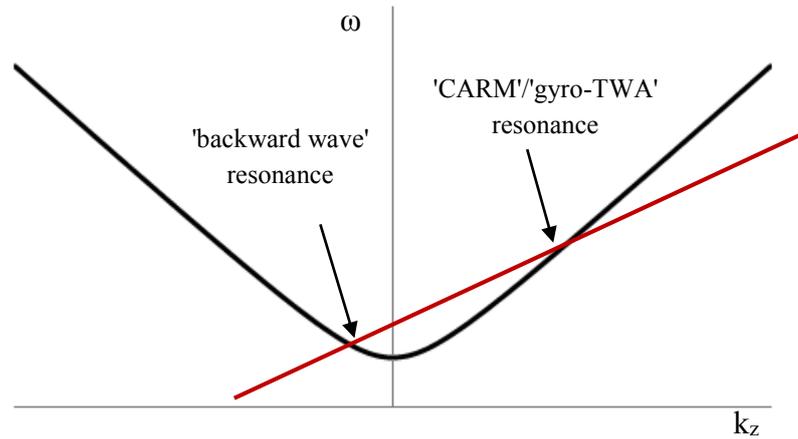
Figure 1.3.5: *Generic dispersion diagram for a gyro-BWO.*

An internal closed feedback loop between the electron beam and the electromagnetic wave results in initial build up and sustainment of oscillations (an absolute instability), whilst the use of a non-resonant circuit makes these devices readily frequency tuneable through adjustment of either the magnetic field strength or (to a limited extent) the voltage.

1.4: Previous research at the University of Strathclyde

Oversized cylindrical waveguides with a helical corrugation of the inner surface have been used in experiments undertaken at the University of Strathclyde since the late 1990's. The first experiment, in collaboration with the Institute of Applied Physics in Russia, utilised this novel waveguide as the interaction region of an X-band gyro-TWA [Denisov, 1998a, Cross, 2007 and Whyte, 2012]. The application of a 3-fold helically corrugated waveguide as the interaction region of a device has similarly been realised in an oscillator type configuration at the University of Strathclyde, specifically in both X- and W-band gyro-BWOs [He, 2005, Donaldson, 2010, Donaldson, 2013, He, 2013 and McElhinney, 2013]. This shift from the more conventional smooth cylindrical waveguide interaction region to that of a helically corrugated waveguide has allowed,

without compromise to output power or electronic efficiency, for a wider frequency tuning bandwidth and enhanced stability against spurious oscillations [He, 2006].

Helically corrugated waveguides, both 3- and 5-fold, have also been successfully used in X-band pulse compression experiments [Bratman, 2010, Burt, 2004, Mishakin, 2011, Samsonov, 2004 and Zhang, 2012] undertaken at the University of Strathclyde and in collaboration with the Institute of Applied Physics. Here a high power, short duration pulse is generated through compression of a low power, long duration pulse [Danilov, 2000]. Initial experiments were observed to achieve a compression factor of 10.9 [Burt, 2005] with a non-optimised frequency swept kilowatt pulse, with further optimised frequency swept kilowatt pulse experiments exceeding this, achieving a compression factor of 25 [McStravick, 2010] and peak powers of ~150kW. Both these results were obtained using a 3-fold helically corrugated waveguide as the dispersive medium, however a more recent advance to a 5-fold helical corrugation of the waveguide's inner surface has allowed for greater power handling capabilities, potentially up to 1GW of input power.

1.5: Research pursued

In modern microwave amplifier design, the ability to accurately and reproducibly model the non-linear electrodynamics of the system is highly desirable. For gyro-TWAs with helically corrugated interaction regions this has previously been undertaken by solving a set of 1D non-linear equations which describe the coupled beam-wave system. Multidimensional simulations have been undertaken but hitherto using predominantly cylindrical polar co-ordinates. Such co-ordinate systems have difficulties dealing with the mesh elements in the core of the system, especially for relativistic devices (even mildly relativistic devices), resulting in certain numerical problems whilst simultaneously limiting the practical resolution of the corrugated structure. Here, a Cartesian co-ordinate multidimensional simulation has been

developed in the Particle-in-Cell (PiC) code MAGIC-3D, of an X-band 2nd harmonic gyro-TWA with a helically corrugated waveguide, offering both enhanced numerical stability (even given relativistic beams) and better resolution of the geometry of the system. This simulated amplifier has parameters broadly based on those of an experiment detailed in [Bratman, 2000], allowing the simulations to be bench tested against the experimental measurements. The close comparison between the performance of the simulated amplifier to that demonstrated experimentally, and the consistency with which the simulations reproduced these results, provides assurance that the simulations were a good and physically sound representation of the experimental behaviour. This enabled the simulations to be used as a benchmarked tool to investigate potential performance enhancement of this type of amplifier (both efficiency and bandwidth) through parameter profiling of the interaction region. These parameter profiled simulations incorporated a helical down taper towards the output of the interaction region of the device and investigated the impact on the performance of the amplifier to changes in both the length and rate of the taper. The results predicted that incorporating a relatively short and rapid helical down taper into the interaction region of the gyro-TWA had the potential to increase both the saturated efficiency and bandwidth of the amplifier.

Supplementary to this investigation was the design and fabrication of an X-band Marie-type mode converter which demonstrated effective conversion from the rectangular TE_{10} mode to the cylindrical TE_{01} mode. This converter would be used as the test component for a radiation transparent plasma confinement mesh i.e. a cathode mesh designed for a laboratory experiment concerned with reproduction of auroral radiation mechanisms, with 'cold' test measurements suggesting that the cathode mesh performed as required for the experiment it was designed for.

Chapter two: Theory

2.1: Overview

Presented in this chapter are the fundamental physical processes underpinning the work contained within this thesis.

2.2: Maxwell's equations

Time varying electric and magnetic fields are described through Maxwell's equations, *equations 2.2.1-2.2.4*, wherein a modification of Ampère's law allowed the prediction of electromagnetic waves propagating at the speed of light. Below are the differential forms of this set of equations recognised as Gauss' law, Gauss' law of magnetic fields, Faraday's law of induction and Ampère-Maxwell's law respectively. All electric and magnetic fields satisfy each equation.

$$\nabla . \boldsymbol{D} = \rho_f \qquad \qquad \textit{Equation 2.2.1}$$

$$\nabla . \boldsymbol{B} = 0 \qquad \qquad \textit{Equation 2.2.2}$$

$$\nabla \times \boldsymbol{E} = \frac{-\partial \boldsymbol{B}}{\partial t} \qquad \qquad \textit{Equation 2.2.3}$$

$$\nabla \times \boldsymbol{H} = \boldsymbol{j} + \frac{\partial \boldsymbol{D}}{\partial t} \qquad \qquad \textit{Equation 2.2.4}$$

In this set of four equations D represents the electric flux density, ρ_f the free charge density, B the magnetic flux density, E the electric field strength, H the magnetic field strength and j the free current density.

Constitutive relations, *equation 2.2.5* and *equation 2.2.6*, allow manipulation of Maxwell's equations and relate B to H and D to E

$$B = \mu H \qquad \qquad \text{\textit{Equation 2.2.5}}$$

$$D = \varepsilon E \qquad \qquad \text{\textit{Equation 2.2.6}}$$

Here $\mu = \mu_0 \mu_r$ and $\varepsilon = \varepsilon_0 \varepsilon_r$ with μ_0 and ε_0 the permeability and permittivity of free space respectively and μ_r and ε_r the relative permeability and permittivity of a specific medium respectively.

The differential forms of Gauss's law and Gauss's law of magnetic fields can be expressed in integral form by applying the divergence theorem

$$\oint_s D.ds = \int_V \rho dV \qquad \qquad \text{\textit{Equation 2.2.7}}$$

$$\oint_s B.ds = 0 \qquad \qquad \text{\textit{Equation 2.2.8}}$$

with the conversion from the differential form of both Faraday's law of induction and Ampère-Maxwell's law to their integral forms requiring Stokes' theorem

$$\oint_C E.dl = -\frac{\partial}{\partial t}\int_s B.ds \qquad \qquad \text{\textit{Equation 2.2.9}}$$

$$\oint_C H.dl = \frac{\partial}{\partial t}\oint_s D.ds + \oint_s j.ds \qquad \qquad \text{\textit{Equation 2.2.10}}$$

2.3: Electromagnetic waves in waveguide

2.3.1: Boundary conditions

From the integral form of Maxwell's equations, *equations 2.2.7-2.2.10,* unique solutions to both the normal and tangential field components at the boundary between two different media can be deduced. Throughout this thesis the bounding media used was that of hollow metallic waveguide which is assumed to be a perfect conductor i.e. lossless with the fields inside the conductor vanishing. At the boundary surface of a perfect conductor both the tangential component of **E** and the normal component of **B** are continuous such that E_{tang} = 0 and B_{norm} = 0. Due to the presence of surface currents, J_s, and associated surface charge density, ρ_s, at the surface of the conductor H_{tang} = J_s and D_{norm} = ρ_s [Pozar, 2004].

An electromagnetic wave propagating in free space follows the dispersion relation

$$\omega = ck = \frac{k}{\sqrt{\mu_0 \varepsilon_0}}$$

Equation 2.3.1.1

However, in a bounded medium limits on the wavelength of radiation that can propagate exist and the dispersion relation takes the form of *equation 1.2.5.* For the gyro-devices detailed in this research the transverse cross-section of the waveguide determines k_c. This is related to the propagation factor k_z,

$$k_z = \sqrt{(k^2 - k_c^2)}$$

Equation 2.3.1.2

such that an electromagnetic wave can propagate in the waveguide when $k > k_c$ and k_z is real. When $k < k_c$ then k_z is imaginary and the electromagnetic wave evanescently decays along the waveguide. When $k = k_c$ the wave is cut-off in the waveguide.

The infinite number of varying transverse electromagnetic field distributions which can propagate in a waveguide are expressed as modes and can be differentiated by type. If there is no electric field component in the direction of propagation then a mode is said to be transverse electric (TE). Analogously if no magnetic field component is in the direction of propagation then the mode is defined as transverse magnetic (TM). A mode is transverse electromagnetic (TEM) if it has neither an electric nor a magnetic field component in the direction of propagation. Owing to boundary conditions this latter type of mode is unsupported in single conductor waveguide and will not be mentioned further. Where multiple modes propagate, the waveguide is said to be over-moded with degenerate modes having the same cut-off frequency as each other. In most waveguides, there exists a frequency band where only the fundamental mode can propagate, preferential for numerous applications as it eradicates mode competition/conversion, since the fundamental mode has the lowest cut-off frequency. Operating in this mode also minimises complexity in terms of coupling energy into the waveguide and out of it, since in over-moded waveguides propagating modes have different propagation phase constants [Collin, 1992].

2.3.2: General solutions for TE and TM waves

If it is assumed that a medium is a homogenous, isotropic, linear and source free region then Faraday's law of induction and Ampère -Maxwell's law can be expressed in the form

$$\nabla \times \boldsymbol{E} = -i\omega\mu\boldsymbol{H}$$ *Equation 2.3.2.1*

$$\nabla \times \boldsymbol{H} = i\omega\varepsilon\boldsymbol{E}$$ *Equation 2.3.2.2*

From these equations, together with the constitutive relations and appropriate vector identities, the Helmholtz (wave) equation for $\boldsymbol{E}$ and $\boldsymbol{H}$ can be determined

$$\nabla^2 \begin{bmatrix} \boldsymbol{E} \\ \boldsymbol{H} \end{bmatrix} + \omega^2\mu\varepsilon \begin{bmatrix} \boldsymbol{E} \\ \boldsymbol{H} \end{bmatrix} = 0$$ *Equation 2.3.2.3*

and since $k^2 = \omega^2 \mu\varepsilon$, the Helmholtz equation can be rewritten as

$$\nabla^2 \begin{bmatrix} E \\ H \end{bmatrix} + k^2 \begin{bmatrix} E \\ H \end{bmatrix} = 0 \qquad \text{\textit{Equation 2.3.2.4}}$$

The general solutions to these wave equations are of the form

$$\begin{bmatrix} E(x,y,z) \\ H(x,y,z) \end{bmatrix} = \left[\begin{bmatrix} E_{trans} \\ H_{trans} \end{bmatrix}(x,y) + \hat{z} \begin{bmatrix} E_z \\ H_z \end{bmatrix}(x,y) \right] e^{-ik_z z} \qquad \text{\textit{Equation 2.3.2.5}}$$

Here, E_{trans} and H_{trans} denote transverse components and E_z and H_z axial components of the electric and magnetic field respectively. These general solutions assume that the electric and magnetic fields are time harmonic with an $e^{i\omega t}$ dependence and that the electromagnetic wave propagates along the positive z direction.

Individual field components for the electric and magnetic fields can be derived from Faraday's and Ampère-Maxwell's laws

$$\frac{\partial E_z}{\partial y} + ik_z E_y = -i\omega\mu H_x \qquad \text{\textit{Equation 2.3.2.6}}$$

$$-ik_z E_x - \frac{\partial E_z}{\partial x} = -i\omega\mu H_y \qquad \text{\textit{Equation 2.3.2.7}}$$

$$\frac{\partial E_y}{\partial x} - \frac{\partial E_x}{\partial y} = -i\omega\mu H_z \qquad \text{\textit{Equation 2.3.2.8}}$$

$$\frac{\partial H_z}{\partial y} + ik_z H_y = i\omega\varepsilon E_x \qquad \text{\textit{Equation 2.3.2.9}}$$

$$-ik_z H_x - \frac{\partial H_z}{\partial x} = i\omega\varepsilon E_y \qquad \text{\textit{Equation 2.3.2.10}}$$

$$\frac{\partial H_y}{\partial x} - \frac{\partial H_x}{\partial y} = i\omega\varepsilon E_z \qquad \text{\textit{Equation 2.3.2.11}}$$

Solving these equations in terms of the axial electric and magnetic field components i.e. E_z and H_z results in the transverse field components

$$E_x = \frac{-i}{k_c^2} \left(k_z \frac{\partial E_z}{\partial x} + \omega\mu \frac{\partial H_z}{\partial y} \right) \qquad \text{\textit{Equation 2.3.2.12}}$$

$$E_y = \frac{i}{k_c^2} \left(-k_z \frac{\partial E_z}{\partial y} + \omega\mu \frac{\partial H_z}{\partial x} \right) \qquad \text{\textit{Equation 2.3.2.13}}$$

$$H_x = \frac{i}{k_c^2}\left(\omega\varepsilon\frac{\partial E_z}{\partial y} - k_z\frac{\partial H_z}{\partial x}\right)$$

$$H_y = \frac{-i}{k_c^2}\left(\omega\varepsilon\frac{\partial E_z}{\partial x} + k_z\frac{\partial H_z}{\partial y}\right)$$

2.3.3: Rectangular waveguide

In rectangular waveguide the electromagnetic waves propagate through multiple reflections of the inner surface of the waveguide, *figure 2.3.3.1.*
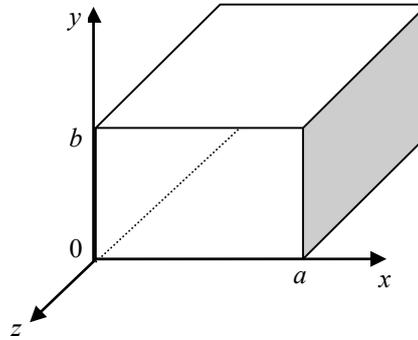
Figure 2.3.3.1: Rectangular waveguide geometry.

In such waveguides only TE$_{m,n}$ and TM$_{m,n}$ modes are supported. Here the indices *m* and *n* are used to further distinguish between modes such that they denote the number of half wave variations in the field over the major (*a*) and minor (*b*) transverse dimensions of the waveguide. Since in both transverse electric and transverse magnetic modes, $E_z = 0$ and $H_z = 0$ respectively, the Helmholtz equation can be reduced to a two-dimensional differential equation which can be solved through the method of separation of variables. From this reduced equation the transverse variation axial electric or magnetic field components for rectangular cross-sectional waveguides can be determined by exploiting boundary conditions. For TE modes this yields H_z as

$$H_z(x,y,z) = A_{mn}\cos\frac{m\pi x}{a}\cos\frac{n\pi y}{b}e^{-ik_z z}$$

where A_{mn} is an arbitrary amplitude constant. The transverse field components for TE$_{m,n}$ modes can therefore be obtained by applying the appropriate boundary conditions to the general forms of the transverse field components, *equations 2.3.2.12 – 2.3.2.15* together with the solution of H_z to yield

$$E_x = \frac{i\omega\mu n\pi}{k_c^2 b} A_{mn} \cos\frac{m\pi x}{a} \sin\frac{n\pi y}{b} e^{-ik_z z}$$ *Equation 2.3.3.2*

$$E_y = \frac{-i\omega\mu m\pi}{k_c^2 a} A_{mn} \sin\frac{m\pi x}{a} \cos\frac{n\pi y}{b} e^{-ik_z z}$$ *Equation 2.3.3.3*

$$H_x = \frac{ik_z m\pi}{k_c^2 a} A_{mn} \sin\frac{m\pi x}{a} \cos\frac{n\pi y}{b} e^{-ik_z z}$$ *Equation 2.3.3.4*

$$H_y = \frac{ik_z n\pi}{k_c^2 b} A_{mn} \cos\frac{m\pi x}{a} \sin\frac{n\pi y}{b} e^{-ik_z z}$$ *Equation 2.3.3.5*

Analogously the transverse field components for TM$_{m,n}$ modes can be determined from the appropriate reduced differential equation alongside the boundary conditions for such modes. The solution of E_z is of the form

$$E_z(x,y,z) = B_{mn} \sin\frac{m\pi x}{a} \sin\frac{n\pi y}{b} e^{-ik_z z}$$ *Equation 2.3.3.6*

where B_{mn} is an arbitrary amplitude constant. The transverse field components are therefore given as

$$E_x = \frac{-ik_z m\pi}{a k_c^2} B_{mn} \cos\frac{m\pi x}{a} \sin\frac{n\pi y}{b} e^{-ik_z z}$$ *Equation 2.3.3.7*

$$E_y = \frac{-ik_z n\pi}{b k_c^2} B_{mn} \sin\frac{m\pi x}{a} \cos\frac{n\pi y}{b} e^{-ik_z z}$$ *Equation 2.3.3.8*

$$H_x = \frac{i\omega\varepsilon n\pi}{b k_c^2} B_{mn} \sin\frac{m\pi x}{a} \cos\frac{n\pi y}{b} e^{-ik_z z}$$ *Equation 2.3.3.9*

$$H_y = \frac{-i\omega\varepsilon m\pi}{a k_c^2} B_{mn} \cos\frac{m\pi x}{a} \sin\frac{n\pi y}{b} e^{-ik_z z}$$ *Equation 2.3.3.10*

For both TE and TM modes the propagation constant k_z, *equation 2.3.1.2*, can be rewritten as

$$k_z = \sqrt{k^2 - k_c^2} = \sqrt{k^2 - \left(k_x^2 + k_y^2\right)}$$

$$= \sqrt{k^2 - \left(\frac{m\pi}{a}\right)^2 - \left(\frac{n\pi}{b}\right)^2}$$

with the cut-off frequency, f_c, expressed as

$$f_c = \frac{c}{2\pi}k_c = \frac{c}{2\pi}\left[\sqrt{\left(\frac{m\pi}{a}\right)^2 + \left(\frac{n\pi}{b}\right)^2}\right]$$

2.3.4: Cylindrical waveguide

In many aspects the underpinning theory of cylindrical waveguide, *figure 2.3.4.1,* is akin to that of rectangular waveguide, with modifications arising from the cylindrical basis set required to most efficiently define the boundaries. Again only $TE_{n,m}$ and $TM_{n,m}$ modes are supported however here the indices *n* and *m* denote the number of full wave and half wave variations of the field along azimuthal and radial paths in the waveguide respectively.
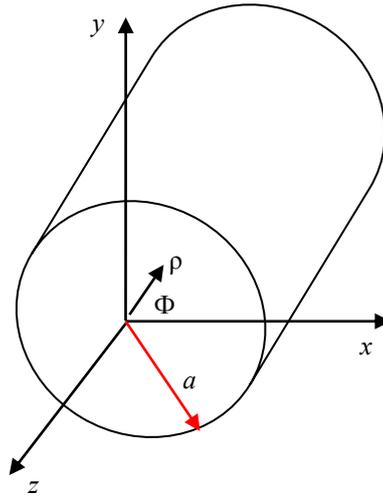
Figure 2.3.4.1: Cylindrical waveguide geometry.

The wave equation can be defined in cylindrical polar coordinates as

$$\left(\frac{\partial^2}{\partial\rho^2} + \frac{1}{\rho}\frac{\partial}{\partial\rho} + \frac{1}{\rho^2}\frac{\partial^2}{\partial\phi^2} + k_c^2\right)\begin{bmatrix} H_z(\rho,\phi) \\ E_z(\rho,\phi) \end{bmatrix} = 0$$

Equation 2.3.4.1

As for rectangular waveguide, this wave equation can be solved through the method of separation of variables to yield the general solution for H_z and E_z for TE and TM modes respectively such that

$$\begin{bmatrix} H_z(\rho,\phi) \\ E_z(\rho,\phi) \end{bmatrix} = (A\sin(n\phi) + B\cos(n\phi))J_n(k_c\rho)$$

Equation 2.3.4.2

where *A* and *B* are constants and J_n is a Bessel function of the first kind. Applying appropriate boundary conditions determines the cut-off wavenumber, k_c. For TE and TM modes it can be shown

$$k_c = \frac{\rho'_{nm}}{a} \text{ (TE modes)}, \quad k_c = \frac{\rho_{nm}}{a} \text{ (TM modes)}$$

Equation 2.3.4.3

where *a* is the waveguide radius, ρ_{nm} is the mth root of the nth Bessel function of the first kind and ρ'_{nm} is the mth root of the differential of the nth Bessel function of the first kind.

For TE modes, the transverse field components in cylindrical waveguide can be expressed as

$$E_\rho = \frac{-i\omega\mu n}{k_c^2 \rho}(A\cos n\phi - B\sin n\phi)J_n(k_c\rho)e^{-ik_z z} \qquad \text{Equation 2.3.4.4}$$

$$E_\phi = \frac{i\omega\mu}{k_c}(A\sin n\phi + B\cos n\phi)J_n'(k_c\rho)e^{-ik_z z} \qquad \text{Equation 2.3.4.5}$$

$$H_\rho = \frac{-ik_z}{k_c}(A\sin n\phi + B\cos n\phi)J_n'(k_c\rho)e^{-ik_z z} \qquad \text{Equation 2.3.4.6}$$

$$H_\phi = \frac{-ik_z n}{k_c^2 \rho}(A\cos n\phi - B\sin n\phi)J_n(k_c\rho)e^{-ik_z z} \qquad \text{Equation 2.3.4.7}$$

and similarly for TM modes it can be shown

$$E_\rho = \frac{-ik_z}{k_c}(A\sin n\phi + B\cos n\phi)J'_n(k_c\rho)e^{-ik_z z} \qquad \text{Equation 2.3.4.8}$$

$$E_\phi = \frac{-ik_z n}{k_c^2 \rho}(A\cos n\phi - B\sin n\phi)J_n(k_c\rho)e^{-ik_z z} \qquad \text{Equation 2.3.4.9}$$

$$H_\rho = \frac{i\omega\varepsilon n}{k_c^2 \rho}(A\cos n\phi - B\sin n\phi)J_n(k_c\rho)e^{-ik_z z} \qquad \text{Equation 2.3.4.10}$$

$$H_\phi = \frac{-i\omega\varepsilon}{k_c}(A\sin n\phi + B\cos n\phi)J_n'(k_c\rho)e^{-ik_z z} \qquad \text{Equation 2.3.4.11}$$

The cut-off frequency can be expressed as

$$f_c = \frac{ck_c}{2\pi} \qquad \text{Equation 2.3.4.12}$$

with the equation for k_c appropriately substituted depending on the desired mode.

2.3.5: Skin depth

Skin depth is a measure of the penetration depth of electromagnetic radiation into a conductor such as the walls of a hollow metallic waveguide. It is a function of frequency, *equation 2.3.5.1,* and as such decreases as frequency increases, with field amplitudes in conductors decaying by 1/e after a distance of one skin depth.

$$\delta_s = \sqrt{\frac{2}{\omega\mu\sigma}}$$

Here δ_s represents the skin depth and σ the conductivity.

2.3.6: Helically corrugated waveguide

The helical inner surface profile of a cylindrical waveguide, *figure 2.3.6.1*, in cylindrical co-ordinates (r,φ,z), can be represented as

$$r(\varphi,z) = r_0 + lcos(\overline{m}\varphi + \overline{k}_z z)$$

where r_0 denotes the mean radius of the helix, l the corrugation amplitude, $\overline{m}$ the number of azimuthal variations of the corrugation, φ the angle around the waveguide axis and $\overline{k}_z$ the number of axial variations of the corrugation defined as $\frac{2\pi}{d}$, where d represents the corrugation periodicity.
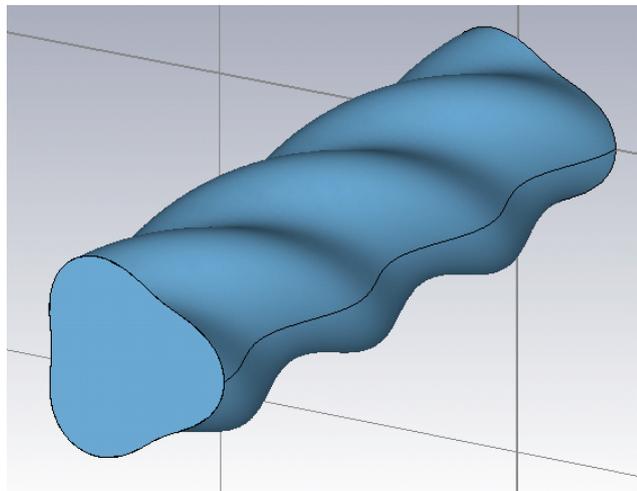
Figure 2.3.6.1: Inner 3-fold helical waveguide geometry, taken from CST Microwave Studio.

For non-zero values of both $\overline{m}$ and $\overline{k}_z$ this analytical function represents a helical corrugation with either clockwise or anti-clockwise rotation dependent upon the sign of $\overline{m}$. For the case where $\overline{m} = 0$, the analytical function represents a 1D Bragg

reflector and results in the formation of reflection zones, known as band gaps, in the dispersion characteristics of the structure.

A helical inner surface corrugation in a waveguide is an example of a non-uniform waveguide, with electromagnetic fields represented as a superposition of forwards and backwards propagating waves of different modes and their spatial harmonics [Katsenelenbaum, 1998]. However, provided the corrugation amplitude of the helical waveguide is sufficiently small, distributed coupling between two counter-rotating modes will occur. For such small non-zero corrugation amplitudes, resonant coupling of the two modes will result when the axial wavenumbers and azimuthal indices of the two modes satisfy the Bragg resonance conditions, *equation 2.3.6.2* and *equation 2.3.6.3*

$$k_{zA} - k_{zB} = \bar{k}_z \qquad\qquad \text{Equation 2.3.6.2}$$

$$m_A - m_B = \bar{m} \qquad\qquad \text{Equation 2.3.6.3}$$

Here, k_{zA}, k_{zB} denote the axial wavenumbers and m_A, m_B the azimuthal indices associated with mode A and mode B respectively [Denisov, 1998a].

The two partial rotating waves coupled in the 3-fold helically corrugated waveguide used throughout this thesis are a co-rotating (with respect to the helix) near cut-off TE_{21} wave (wave A) with small axial wavenumber

$$\bar{E} = \bar{E}_A(r)\big(a_+ e^{-ik_{zA}z} + a_- e^{ik_{zA}z}\big)e^{i(\omega t - m_A \varphi)} \qquad\qquad \text{Equation 2.3.6.4}$$

and a counter-rotating first spatial harmonic travelling far from cut-off TE_{11} wave (wave B) with large axial wavenumber

$$\bar{E} = \bar{E}_B(r)b e^{-ik_{zB1}z}e^{i(\omega t + m_B \varphi)} \qquad\qquad \text{Equation 2.3.6.5}$$

Here $k_{zB1} = k_{zB} - \bar{k}_z$ and signifies the first spatial harmonic.

The axial and azimuthal periodicity of the helical waveguide serves to scatter the waves, perturbing the counter-propagating wave to generate the spatial harmonics of

the wave at set intervals given as $k_z = k_z^0 + \frac{2n\pi}{d}$, where k_z^0 is the axial wavenumber in the smooth cylindrical waveguide. This expression comes from Floquet theorem in which waves in a periodic structure can be expanded as an infinite superposition of Floquet spatial harmonics, with all spatial harmonics simultaneously present to ensure the total field satisfies the boundary conditions [Collin, 1992].

The method of perturbation can be used to calculate the dispersion characteristics of the helically corrugated waveguide provided the corrugation amplitude, l, is small in comparison to the wavelength, λ, with this method shown to provide good agreement to 'cold' experiments. From this assumption the unperturbed dispersion equations are

$$k^2 - k_0^2 - k_{zA}^2 = 0 \qquad\qquad \textit{Equation 2.3.6.6}$$

$$k^2 - k_{0B}^2 - \left(k_{zB1} + \bar{k}_z\right)^2 = 0 \qquad\qquad \textit{Equation 2.3.6.7}$$

Here k_0 and k_{0B} denote wavenumbers which correspond to the cut-off frequencies of modes A and B respectively.

A set of two coupled wave linear differential equations of the first and second order describe the field amplitudes of the partial waves $a_\pm$ and b as functions of axial position z.

$$\frac{d^2 f}{dz^2} + 2k_0\delta f = 2\sigma k_0 b \qquad\qquad \textit{Equation 2.3.6.8}$$

$$ik_{z0}\frac{db}{dz} - \left(k_0\delta - k_{z0}\Delta_g\right)b = -\sigma k_0 f \qquad\qquad \textit{Equation 2.3.6.9}$$

Here $f = a_+(z) + a_-(z)$, with σ representing the coupling coefficient between the waves, δ a frequency mismatch, Δ_g a geometrical mismatch associated with the helical structure and k_{z0} the propagation constant for mode B at the cut-off frequency of mode A. If it is assumed both f and b vary as $f e^{-ik_z z}$ and $b e^{-ik_z z}$ respectively then the eigenwave solutions for the above set of coupled wave linear differential equations can be determined, with the dispersion equation of the form

$$(k_z^2 - 2\delta)\left(k_z + \Delta_g - \frac{\delta}{k_{z0}}\right) = \frac{2\sigma^2}{k_{z0}} \qquad \text{\textit{Equation 2.3.6.10}}$$

Here k_z is a wavevector with k_z, δ, Δ_g, σ and k_{z0} normalised to k_0. This function represents the cubic approximation of the perturbation theory. There are two allowed solutions of this dispersion equation. One solution is an upper operating eigenwave and the second a lower operating eigenwave (see *figure 1.3.3*), with the electron beam matched to the lower operating eigenwave solution. The beam (axis encircling and at the second cyclotron harmonic) resonantly interacts with the TE_{21} component of the operating eigenwave and scatters on the helically corrugated inner surface of the waveguide into the forwards propagating TE_{11} mode. To operate with higher order modes it is clear from the Bragg resonance conditions, *equation 2.3.6.2* and *equation 2.3.6.3*, that the number of azimuthal variations of the helix, $\bar{m}$, must increase in order to satisfy this criterion. As a result, an increased number of modes will satisfy resonance conditions and contribute to the dispersion characteristics of the structure. Thus the larger the value of $\bar{m}$, the increased complexity of the dispersion characteristics with more modes coupled together. The primary incentive however is in the increased power handling capabilities of the structure.

2.3.7: Coupling coefficient

The coupling coefficient between two TE modes in a helically corrugated waveguide is given as [Cooke, 1998],

$$\sigma = \frac{l}{2k_0^2 r_0^3} \frac{\mu_A'^2 \mu_B'^2 - m_A m_B r_0^2 (k_{0B}^2 + \bar{k}_z k_{zB})}{\sqrt{(\mu_A'^2 - m_A^2)}\sqrt{(\mu_B'^2 - m_B^2)}} \qquad \text{\textit{Equation 2.3.7.1}}$$

Here μ_A' and μ_B' denote the mth root of the J_n' Bessel function of the first kind ($\mu_{m.n}'$) for mode A and B respectively. This coupling coefficient represents a modification of a previously derived coupling coefficient for travelling waves [Denisov, 1982] to avoid singularities when $k_z = 0$, since in the 3-fold helical waveguide the upper mode (mode A) is close to cut-off.

2.4: Linear and nonlinear theory of the gyro-TWA

2.4.1: 1D averaged nonlinear equations

A set of four coupled nonlinear equations [Denisov, 1998a], *equations 2.4.1.1-2.4.1.4*, describe the evolution of the key dynamic parameters within the gyro-TWA system [Zhu, 2012]. The first equation, *equation 2.4.1.1*, describes how the energy of individual electrons comprising the population is driven by the amplitude of the electric field with the second, *equation 2.4.1.2*, describing how the electric field drives the electron phase. The third equation, *equation 2.4.1.3*, describes how the averaged electron energy couples to the electric field whilst the fourth equation, *equation 2.4.1.4*, describes the coupling between the partial waves of the operating eigenwave. These equations assume that the dispersion curves associated with the quadrupole field (*f*) and the dipole field (*b*) can be approximated to a parabola and a straight line respectively.

$$\frac{d\gamma}{d\zeta} = \frac{\beta_\perp}{\beta_\parallel} J_s'(\hat{r}_H) J_{m_A-s}(\hat{r}_g) Re(fe^{-i\theta}) \qquad \text{\textit{Equation 2.4.1.1}}$$

$$\frac{d\theta}{d\zeta} + \frac{k - \dfrac{sk_{H0}}{\gamma}}{\beta_\parallel} = \frac{J_s(\hat{r}_H) J_{m_A-s}(\hat{r}_g)}{\beta_\perp \beta_\parallel \gamma} \left[\frac{s^2}{\hat{r}_H} - \hat{r}_H\right] Im(fe^{-i\theta}) \qquad \text{\textit{Equation 2.4.1.2}}$$

$$\frac{d^2 f}{d\zeta^2} + 2\delta f = 2\sigma b + i\frac{8\hat{I} J_{m_A-s}(\hat{r}_g)}{N_A} \frac{1}{2\pi} \int_0^{2\pi} \frac{\beta_\perp}{\beta_\parallel} J_s'(\hat{r}_H) e^{i\theta} d\theta_0 \qquad \text{\textit{Equation 2.4.1.3}}$$

$$\frac{db}{d\zeta} + i\left(\frac{\delta}{h_0} - \Delta_g\right) b = i\frac{\sigma}{h_0} f \qquad \text{\textit{Equation 2.4.1.4}}$$

Here $\beta_\perp$ represents the normalised transverse velocity, $\beta_\parallel$ the normalised axial velocity, k the normalised free space wavenumber, σ the normalised coupling coefficient, δ the normalised frequency mismatch, Δ_g the normalised geometrical mismatch, $\hat{r}_g = k_0 r_g$ and represents the normalised electron guiding centre, $\zeta = k_0 z$ and represents a normalised axial displacement dimension, $J_{m_A-s}(\hat{r}_g)$ is the Bessel function of the first kind of order 'm_A-s' evaluated at $\hat{r}_g$, $J_s'(\hat{r}_H)$ represents the

differential of the Bessel function of the first kind of order 's' evaluated at $\hat{r}_H$, the normalised Larmor radius given as

$$\hat{r}_H = \frac{\beta_\perp \gamma}{k_{H0}}$$

where

$$k_{H0} = \frac{eB}{mck_0}$$

$$\hat{I} = \frac{eI}{4\pi\varepsilon_0 mc^3}$$

and

$$N_A = J_{m_A}^2(v)(v^2 - m_A^2)$$

where

$$v = k_0 r_0$$

such that N_A represents the dimensionless norm of the TE$_{21}$ mode [Denisov, 1998a].

By solving this set of coupled equations simultaneously, it is possible to predict the evolution of an individual electron's energy and phase and the electric field amplitude in ζ.

2.4.2: 1D linear theory

From the set of reduced coupled nonlinear equations, *equations 2.4.1.1-2.4.1.4*, a set of linear, averaged equations can be obtained. These equations describe the small signal wave excitation by the electron beam and assume that the normalised amplitudes of the perturbations of electron energies and phases together with the amplitudes of both the first spatial harmonic TE$_{11}$ mode (mode B) and the TE$_{21}$ mode (mode A) are

small. From this set of equations it is possible to find a coupled dispersion relationship for the beam and the electromagnetic wave. This dispersion relationship can then be used to calculate the small signal gain of an amplifier over a range of frequencies. The gain calculated by this method is often an overestimate of that which can be achieved in reality since it ignores all saturation effects. However it is useful to predict an amplifier's stability to oscillation and likely gain bandwidth [Chu, 1988].

The 'hot' dispersion equation of the gyro-TWA is given as

$$
\left[(k_z^2 - 2\delta) \left(k_z + \Delta_g - \frac{\delta}{k_{z0}} \right) - \frac{2\sigma^2}{k_{z0}} \right] \left[k_z - \frac{(\delta - \Delta_H)}{\beta_{\parallel 0}} \right]^2 \qquad \textit{Equation 2.4.2.1}
$$

$$
= C^3 \left(k_z + \Delta_g - \frac{\delta}{k_{z0}} \right)
$$

$$
\left(1 + \frac{2s\beta_{\parallel 0}}{\beta_{\perp 0}^2} \left[k_z - \frac{(\delta - \Delta_H)}{\beta_{\parallel 0}} \right] \right)
$$

Here

$$
\Delta_H = \frac{(s\omega_{H0} - \omega_0)}{\omega_0}
$$

and represents the magnetic field mismatch,

$$
C = \left(\frac{4\hat{I}\rho^2}{\gamma_0 N_A \beta_{\parallel 0}} \right)^{\frac{1}{3}} \qquad \textit{Equation 2.4.2.2}
$$

and represents the Pierce parameter which controls the coupling of the operating and spurious eigenwaves to the electron beam, with

$$
\rho = \frac{\beta_{\perp 0}}{\beta_{\parallel 0}} J_s'(s\beta_{\perp 0}) J_{m_A - s}(\hat{r}_g)
$$

The solutions to this 'hot' dispersion equation, *equation 2.4.2.1*, can be used to predict the linear gain and temporal growth rate of the instability driving the amplifier. This can be achieved by specifying a frequency range and solving the dispersion relationship for the wavevector, k_z. As can be seen, the equation is fifth order in k_z,

with five corresponding roots, where solutions may be either real or complex conjugate pairs. Three of the five roots correspond to the cubic approximation to the dispersion of the corrugated waveguide, *equation 2.3.6.10*, with one corresponding to the operating eigenwave with relatively low dispersion and the other pair corresponding to the spurious upper eigenwave. The fourth and fifth roots correspond to the fast and slow cyclotron modes of the beam. Real solutions to these roots imply a beam or an electromagnetic mode that is propagating, possibly with quite complex dispersion, but with stable amplitude. Imaginary conjugate pairs (e.g. as happens below the cut-off of the upper eigenwave) correspond to the evanescent decay of a cut-off signal. Where the beam comes close to the operating eigenwave, a splitting appears in the dispersions for the fast and slow cyclotron modes, and additional distortion appears in the wave dispersion relationship. If they become close enough the solutions cease to be completely separate, with the fast cyclotron mode coupling with the electromagnetic wave to yield a range of frequencies over which two of the roots become a complex conjugate pair. The interpretation of the complex roots is that they correspond to waves which are both propagating and changing amplitude, one of which, typically the electromagnetic wave in an amplifier, grows in energy whilst the other, e.g. the fast cyclotron oscillations in the beam, reduces in energy. It is interesting to note that it is possible to find a condition where no solution can be found for a real frequency, in this case the frequency is also necessarily complex. Where both the frequency and the wavevector are complex, an absolute instability is encountered which will grow itself from noise to saturation. This typically happens if the wave group velocity is low (or backwards) in the vicinity of the resonance.

2.5: Beam-wave instabilities and trapping regimes

2.5.1: The cyclotron resonance maser (CRM) instability

The gyro-TWA with a helical corrugation along the inner wall surface is an example of a fast-wave amplifier which utilises the CRM instability. The cyclotron emission resulting from this CRM instability can be understood through consideration of the orbital dynamics of electrons in a region of uniform magnetic field. Here gyrating beam electrons interact with an electromagnetic wave in an externally applied axial magnetic field, leading to azimuthal electron phase bunching. Initially the electrons are uniformly distributed along a helical trajectory orbiting around a centre position at the Larmor radius, where they co-rotate clockwise with the transverse electric field prior to interaction with the RF field, see *figure 2.5.1.1(A)*.
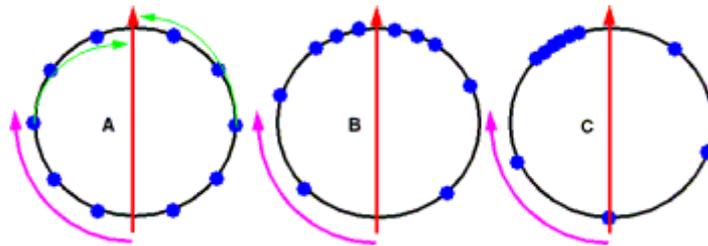
Figure 2.5.1.1: *Azimuthal electron phase bunch formation associated with the CRM instability.*

As time evolves the electrons interact with the components of the electromagnetic wave transverse to their drift motion (TE mode) causing those electrons ahead of the electric field (*RHS figure 2.5.1.1(A)*) to be accelerated, gain energy, decrease in gyro-frequency and retard in phase. Conversely, electrons which lag the field are decelerated, lose energy, increase in gyro-frequency and advance in phase, (*LHS figure 2.5.1.1(A)*). The net effect is that the electron bunch forms at the position of field maxima, *figure 2.5.1.1(B)*. No energy exchange has occurred at this point as the system is in equilibrium with electrons gaining and losing energy at much the same rate. In order for energy exchange between the beam electrons and the wave to occur,

the electron bunch must form in decelerating phase and hence the cyclotron frequency must be negatively detuned with respect to the resonant frequency of the wave, with this detuning typically on the order of ~2% to ~3%. The CRM instability is a relativistic effect as the cyclotron frequency of the electrons is energy dependent.

2.5.2: Saturation of the CRM instability

Two mechanisms lead to saturation of the CRM instability, namely depletion of the free energy of the electrons found in their rotational energy and phase trapping of the electron bunch within the wave. In the CRM instability the phase slippage occurring between the electrons and the field causes the net kinetic energy of the electron bunch to decrease. Energy conservation implies that the amplitude of the wave must increase to compensate for this effect. The maximum conversion efficiency of kinetic to field energy in both the case of depletion of the free energy of the electrons and for phase trapping of the electron bunch within the wave is estimated in *equation 2.5.2.1* and *equation 2.5.2.2* respectively.

$$\eta = \frac{\left(\gamma_{0\perp} - \gamma_{\perp,crit}\right)}{\gamma_{0\perp} - 1}$$

<div align="right">*Equation 2.5.2.1*</div>

$$\eta = \frac{2\left(\frac{\Delta\omega}{\omega}\right)\gamma_{0\perp}}{(\gamma_{0\perp} - 1)}$$

<div align="right">*Equation 2.5.2.2*</div>

Here $\gamma_{0\perp}$ represents the perpendicular relativistic factor of the electrons, $\gamma_{\perp,crit}$ the critical perpendicular relativistic factor and $\Delta\omega$ the frequency shift of the excited wave with respect to ω_c. The initial beam parameters determine which mechanism dominates in the saturation of the CRM instability. If $\gamma_{0\perp}$ is slightly greater than or approximately equal to $\gamma_{\perp,crit}$ then the rotational free energy of the electrons depletes before phase trapping can occur. When $\gamma_{0\perp} \gg \gamma_{\perp,crit}$ then the opposite occurs and the electron bunch phase traps before all the rotational free energy of the electrons has depleted. Here the electron bunch is formed and lags the wave phase but ultimately loses sufficient energy that it advances to lead the wave phase. The electron bunch takes back energy from the wave and the wave amplitude decreases. Over an extended

interaction the electrons oscillate between accelerating and decelerating phase, whilst the bunch slowly disintegrates causing oscillation in the output signal [Sprangle, 1977].

2.5.3: Weibel instability

A competing mechanism to the CRM instability is the Weibel instability [Chu, 1978], a non-relativistic instability that dominates when v_{ph} is less than the speed of light. The Weibel instability is associated with the axial phase movement of beam electrons in the same direction as wave propagation, perpendicular to the electron cyclotron orbits. The axial movement of the electrons is a consequence of the Lorentz force, arising from the transverse component of the RF magnetic field.
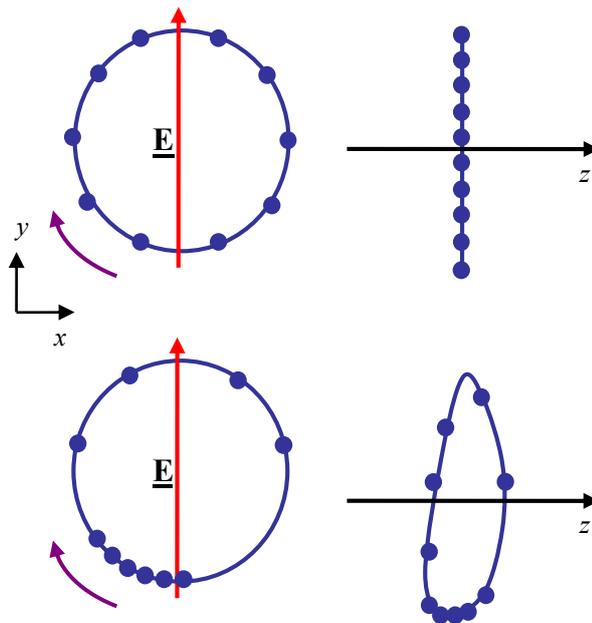
Figure 2.5.3.1: *Axial electron movement associated with the Weibel instability.*

In the Weibel instability, electrons that have a phase lag to the electric field move in the negative z direction and as a result move behind the field in phase. Conversely, those electrons that lead the field move in the positive z direction and hence travel

further ahead of the field. Thus the Lorentz force produces a variation in v_z and hence axial position with respect to the wave, with the 'effective' electron phase bunching forming at the opposite phase position of the electric field to that of the CRM instability. The result of the Weibel mechanism, imagining the beam being formed of a sequence of rings, is that the electron rings tend to tilt towards each other. For the electron phase bunch to transition into the correct phase for energy extraction i.e. a net transfer of energy from the beam electrons to the wave, the static magnetic field must be detuned.

2.5.4: CARM instability/autoresonance

As mentioned the CRM instability dominates when $v_{ph} > c$ and the Weibel instability dominates when $v_{ph} < c$. When v_{ph} approximately equals c each instability serves to complement the other and the interaction is in autoresonance. For this criterion, despite minimal phase change, the energy of the electrons is still varying. Thus after phase bunching of the beam electrons has occurred energy can be extracted from the beam without compromising synchronism [Granatstein, 1987]. It has been shown mathematically [Chu, 1978] the conditions required to achieve autoresonance

$$\frac{d\Omega_D}{dt} = \frac{-ek_z^2}{m\gamma\omega}\left[1 - \frac{\omega^2}{k_z^2c^2}\right]\overline{v}_\perp.\overline{E}_\perp \qquad \textit{Equation 2.5.4.1}$$

Here, in the term $\left[1 - \frac{\omega^2}{k_z^2c^2}\right]$ the LHS is a result of the Lorentz force and thus associated with the axial movement of electrons from the Weibel instability whilst the RHS results due to the change of the relativistic factor γ as the electrons either gain or lose energy to the field, associated with the CRM instability. In practice, the azimuthal phase bunching of the CRM instability and the axial phase movement of the Weibel instability are always competing against each other and are simultaneously present [Chu, 1978], working in opposite senses serving to cancel each other out. This implies that one mechanism must dominate otherwise in an equilibrium state between the two

bunching mechanisms no emission would occur. Invariably for fast-wave devices this dominant mechanism is the CRM instability [Chu, 2004].

2.5.5: Resonant trapping

Beam-wave coupling in cyclotron resonance masers typically involves either 'conventional' inertial electron bunching or the trapping and subsequent adiabatic deceleration of beam electrons [Sprangle, 1979, Kroll, 1980 and Sprangle, 1980], with the latter mechanism providing extended synchronism between the beam electrons and the electromagnetic wave during the energy extraction process. By firstly trapping and then decelerating the electrons it is possible to enhance device efficiency [Savilov, 1998]. In this resonant trapping regime, the potential well formed by the electromagnetic wave, also known as a separatrix, initially traps those electrons which are in close resonance with the electromagnetic wave, *figure 2.5.5.1*.
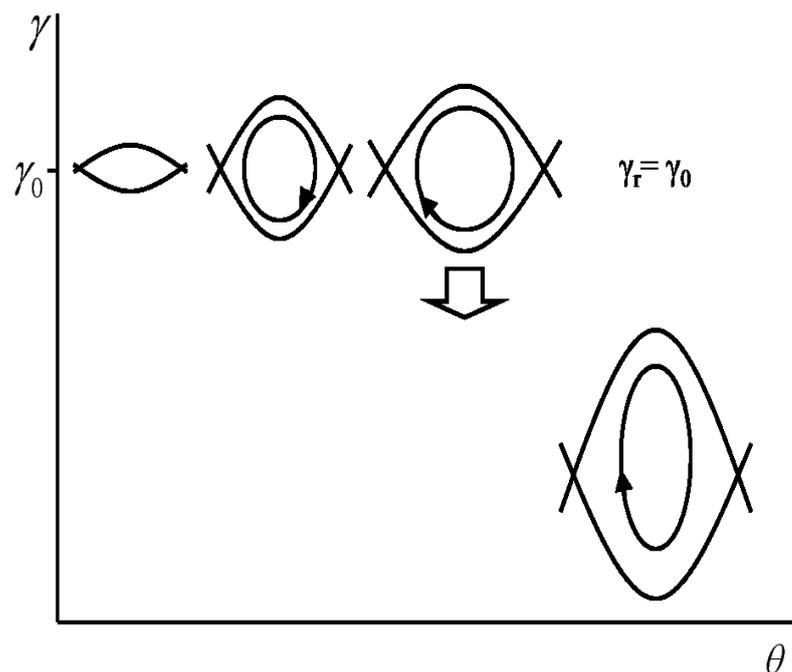
Figure 2.5.5.1: Motion of separatrix with beam-wave resonance.

The trapped electrons undertake oscillations inside the separatrix with an energy centre corresponding to exact beam-wave synchronism. These electrons in the separatrix are in constrained phase orbits and will initially lose energy and hence are decelerated. Conservation of energy dictates that the amplitude of the separatrix must increase to compensate for this decrease in electron energy. Subsequent growth of the potential well traps more electrons and further expands the separatrix. When the electrons have reached their lowest energy level they will start to advance into a position of accelerating phase. In accelerating phase the electrons absorb energy from the wave resulting in a decrease in the amplitude of the separatrix with electrons escaping from their closed orbits, moving into a regime of unconstrained phase orbits. Introducing parameter profiling in the interaction region, at a position before the electrons move into accelerating phase, can decelerate the trapped electrons to hold them in decelerating phase where they reinforce the electric field. This gradual profiling of the system parameters causes a decrease in the resonant energy at exact beam-wave synchronism, and so decreases the energy of the particles trapped in the separatrix whilst maintaining the interaction at the same frequency. However to achieve this, fulfilment of a beam-wave resonance condition from the onset of the device's interaction region is a necessity. A consequence of this is that sensitivity to velocity spread in the beam electrons remains problematic, particularly significant for devices operating with a large Doppler frequency up-conversion [Bandurkin, 2004].

2.5.6: Non-resonant trapping

For cyclotron resonance maser amplifiers with profiled interaction regions a method of beam-wave coupling utilising a 'non-resonant' trapping regime [Bandurkin, 2004] was proposed. In contrast to the trapping and adiabatic deceleration of beam electrons, this non-resonant trapping regime [Savilov, 2002] requires fulfilment of the beam-wave resonance condition at some arbitrary location in the interaction region of the device, *figure 2.5.6.1*. This non-resonant trapping regime has the potential to not only enhance device efficiency but to reduce a device's sensitivity to velocity spread in the

beam electrons [Savilov, 2001], thus it may be favourable for devices operating with a large Doppler frequency up-conversion, such as the CARM [Savilov, 1998].
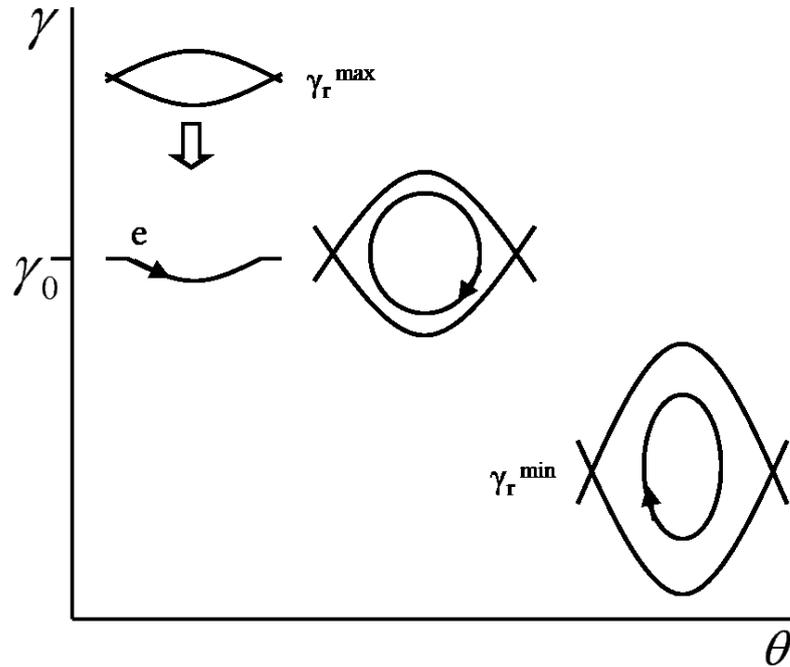
Figure 2.5.6.1: Separatrix motion with electron-wave resonance.

In this non-resonant trapping regime, the electromagnetic wave is initially far from resonance with the beam. As the electromagnetic wave is brought into close resonance with the electron beam, through parameter profiling, electrons become trapped by the wave and the separatrix expands. By the middle of the device's interaction region the beam-wave resonance condition has been satisfied with the separatrix at the initial energy of the electrons i.e. $\gamma = \gamma_r$. In this regime, as co-ordinate position increases the RF signal increases and the separatrix expands corresponding to increasing energy, thus trapping the electrons. Also the resonant energy, $\gamma_r(z)$, has decreased with increased axial co-ordinate position as a result of system profiling whereby towards the output section of the interaction region this γ_r decrease is akin to that of the 'traditional' resonant trapping regime. In terms of velocity spread of the beam electrons this non-resonant trapping regime results in fulfilment of the beam-wave resonance condition at differing locations in the interaction region for differing sections of the electron beam, culminating in a spreading of the trapping process. In

theory it is possible to achieve broadband frequency tuning for a device utilising this regime. A disadvantage of this regime however, is that a much higher drive power is required to start the interaction as a rapid increase in RF amplitude and consequently separatrix size in the region of close resonance is needed [Bandurkin, 2004]. If the parameter profiling required to implement such a regime occurs in the interaction waveguide of the device rather than through profiling of the confining magnetic field, then there is an increased potential for coupling into undesirable modes at the input, since the input radius of the system will be increased.

2.5.7: Waveguide parameter profiling

As has been discussed *(chapter 1),* the intersection of an electron beam and electromagnetic waveguide mode on a dispersion diagram indicates the frequency and bandwidth over which coupling between the two will occur. In time the interaction between the electron beam and the electromagnetic wave evolves and the beam electrons lose kinetic energy. From both the resonance condition, *equation 1.2.1* and the equation of the electron cyclotron frequency, ω_c, *equation 1.2.2*, it is clear that a decrease in kinetic energy of the beam electrons will result in an increase in ω_c, causing the beam line to shift up in frequency to a point where beam-wave synchronism is lost. One technique to maintain the resonance in cylindrical waveguide is to reduce the output aperture of the device, *figure 2.5.7.1,* resulting in an increase to the cut-off frequency, *equation 2.3.4.12*. By suitably profiling the waveguide, it is possible to track the electron beam line to maintain the resonance and improve the performance of the device, providing it is operating with a large bandwidth, typically rather far above cut-off. Near cut-off this method however does not maintain the resonance at the same frequency, with this possible only through changing the magnetic field strength. This is due to the strong dispersion when close to cut-off.
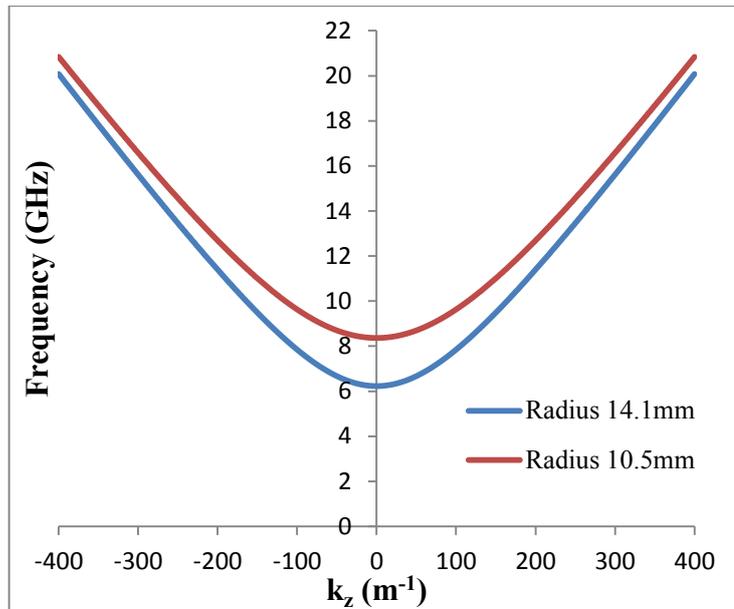
Figure 2.5.7.1: Cylindrical waveguide dispersion of the TE$_{11}$ mode for two waveguide radii.

However owing to the unique dispersion of the gyro-TWA with a helically corrugated interaction waveguide, in principle, it is possible to maintain synchronism at the same frequency through profiling the microwave circuit as the electron beam drifts up in frequency, *figure 2.5.7.2*. This can be realised by operating with a different k_z. One should anticipate a drop in the total gain in the linear limit as the output end may not be in effective resonance if the amplifier is not close to saturation.
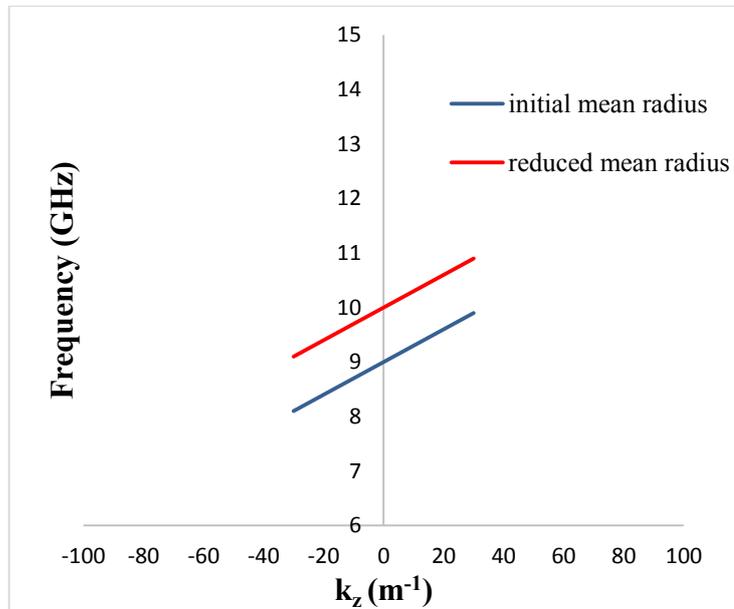
Figure 2.5.7.2: Idealised dispersion of the operating eigenwave in a helically corrugated waveguide of different mean radii.

It has therefore been anticipated that this technique could be implemented towards the output of the interaction waveguide of the X-band 2nd harmonic gyro-TWA to improve the efficiency of the amplifier. Such parameter profiling (resonant trapping of the beam electrons) would potentially enable the continuation of the beam-wave interaction resonance for the entire interaction space of the amplifier, through modification of the dispersion characteristics of the device. Moreover the inclusion of such a taper should also serve to increase the cut-off frequency of the upper mode coupled by the corrugation i.e. the TE_{21} mode (mode A) and allow for higher frequency operation. Thus an ideally configured taper has the potential to increase both the efficiency and bandwidth of the amplifier.

Chapter three: Numerical and experimental methods

3.1: Overview

The results presented within this thesis were obtained from both numerical simulations and laboratory 'cold' tests. Presented here are the numerical and experimental methods which underpin this work.

3.2: Finite difference time domain (FDTD)

Particle-in-Cell (PiC) codes can be used to simulate electromagnetic problems, solving the complete set of time-dependant Maxwell's equations, the Lorentz force equation and relativistic particle motion equations concurrently with appropriate boundary conditions imposed. An example of a PiC code used extensively throughout this work was MAGIC-3D, a finite difference time domain (FDTD) code which utilises the Yee algorithm to numerically solve electromagnetic problems [Yee, 1966, Choi, 1986, Taflove, 1975 and Taflove, 1988]. The Yee algorithm solves in space and time for both the magnetic and electric field using Maxwell's coupled curl equations. Initially two orthogonal grids are generated, creating a spatial domain of parallelepipeds of size Δx, Δy and Δz and a temporal domain with time step Δt. To ensure numerical stability

the temporal domain and the spatial domain are explicitly related. Maxwell's equations are then solved through time stepping of the electric and magnetic fields [Taflove, 1998]. To achieve this, a one half division grid offset of the magnetic field with respect to the grid of the electric field is implemented with this offset occurring in each domain. The FDTD method approximates both temporal and spatial derivatives of Maxwell's equations through substitution with finite differences, discretising in both time and space to iteratively step the electric and magnetic fields, advancing the fields such that the unknown future fields are predicted from the known past fields and particle trajectories (the leapfrog method). Updated at each time step are the six vector electromagnetic field components associated with each grid cell and the positions and velocities of each particle in the simulation.

The Yee algorithm incorporates edge elements (used to define a vector value along edges between nodes) of one field type (electric or magnetic) with centre point evaluation of the other. The Yee unit cell, *figure 3.2.1*, forms the computational grid with the magnetic field vector components known at points situated at half cell offsets between the electric field nodes in each dimension and vice versa.
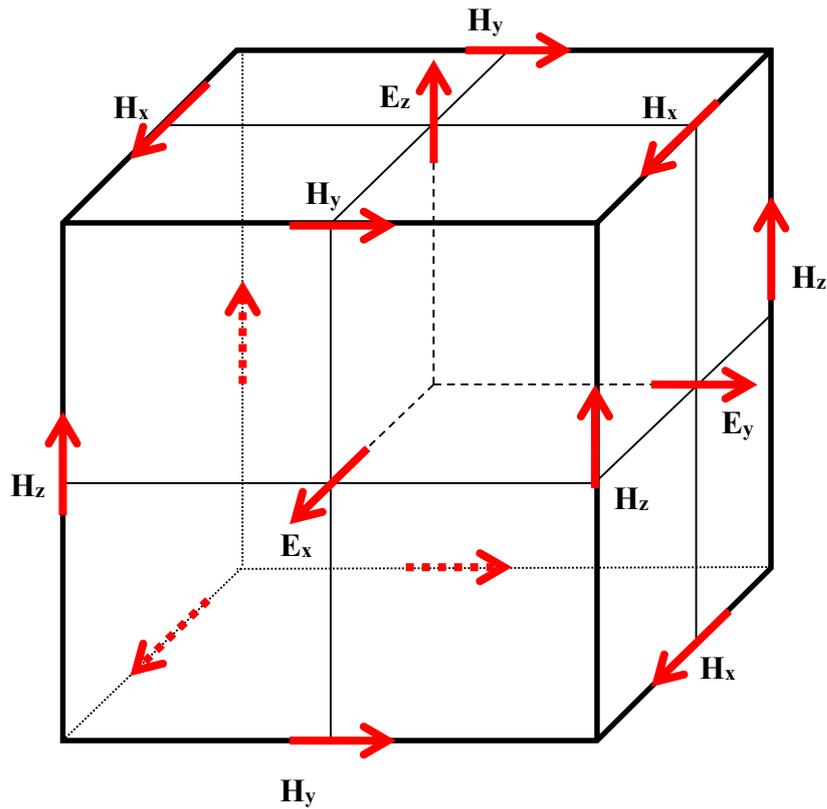
Figure 3.2.1: The Yee cell.

Hence the Yee cell is constructed such that all electric field components are centred on and surrounded by four 'circulating' magnetic field components. Conversely all magnetic field components are centred on and surrounded by four 'circulating' electric field components i.e. the centre point evaluation method [Taflove, 1995]. Calculations are interleaved in both domains with only adjoining cell interactions being considered when the fields are advanced.

FDTD codes can be computationally intensive as the entire system to be simulated must have a continuous structured grid, with the grid resolution sufficiently high to resolve both the smallest geometrical entity comprising the system and the smallest wavelength with enough sampling points. A typical constraint on this grid resolution, to produce accurate results, is that the mesh cell dimensions should be one tenth (or

less) of the wavelength calculated for the highest frequency of interest. From this grid cell resolution the maximum time step can be calculated [Sullivan, 2000]. Electromagnetic waves propagating in free space cannot exceed the speed of light, *c*, and as such this provides a physical limit to give a relationship between the spatial and temporal domains. This limit is referred to as the Courant stability criterion, *equation 3.2.1,* where the maximum time step is selected to be smaller than the smallest possible transit time for a particle across a unit cell.

$$\Delta t \leq \frac{1}{c\sqrt{\left(\frac{1}{\Delta x^2} + \frac{1}{\Delta y^2} + \frac{1}{\Delta z^2}\right)}} \qquad \text{\textit{Equation 3.2.1}}$$

This condition ensures the stability of a system and means that energy cannot propagate beyond one spatial grid cell in one time step [Taflove, 1975 and Edelvik, 2004].

3.3: Finite integration technique (FIT)

A widely used numerical solver for electromagnetic problems in both the time and frequency domain is the finite integration technique (FIT), with CST Microwave Studio an example of a modelling code which utilises this method. Both the transient and eigenmode solver of this modelling suite were used in this work, notably for the modelling of an X-band Marie-type mode converter *(chapter 6)* and to determine both the dispersion characteristics of sections of uniform helical waveguide and sections of tapered helical waveguide as a function of frequency *(chapter 4* and *chapter 5).* The transient solver of CST Microwave Studio is based on the FIT together with the perfect boundary approximation (PBA) and solves electromagnetic problems in the time domain, evaluating the transmission and reflection response of a component over a broad frequency band whilst calculating field structures in a single run. Alternatively the eigenmode solver can be used when it is necessary to determine the resonant frequencies and field structures of allowed modes within a closed component.

The FIT was first proposed in 1977 by Weiland [Clemens, 2001] and is based on the full set of Maxwell's equations in integral form discretised on a two grid system, known as the primary and dual grid, *figure 3.3.1(a)*. In the FIT, magnetic and electric grid voltages and grid fluxes are assigned to spatial objects of the grid, defined as integrals of the magnetic and electric field vectors associated with the grid, *figure 3.3.1(b)*[Schuhmann, 2001].
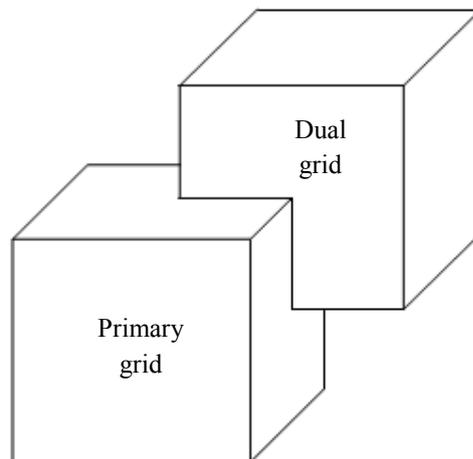
Figure 3.3.1(a): Illustration of the primary and dual grid cells used in the FIT [Weiland, 1996].
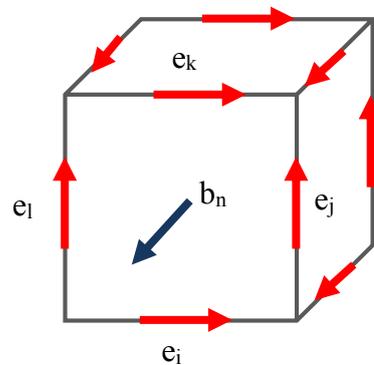
Figure 3.3.1(b): Allocation of voltages along edges and fluxes through surfaces in the FIT.

Electric grid voltages and magnetic grid fluxes are allocated to the primary grid on the edges and faces respectively. Assigned to the dual grid on the edges and faces are the magnetic grid voltages and electric grid fluxes [Munteanu, 2007]. For an individual cell surface Maxwell's equations are defined and the discretised fields summarised in

a topological matrix. The full set of these algebraic matrix equations, which retain conservation of charge and energy, are known as Maxwell's Grid Equations (MGEs). MGEs precisely represent Maxwell's equations on the grid since in this method discretisation is based entirely on the mathematical properties of the integral [Weiland, 2008]. The inclusion of matrices however, which describe material properties, allow electromagnetic problems to be solved but introduce numerical approximations. FIT is not restricted to a Cartesian coordinate gird and can be applied to non-orthogonal and irregular grids, a prime advantage over the FDTD method [Poděbrad, 2003]. However on a Cartesian coordinate grid system the FIT and FDTD methods are effectively equivalent [Weiland, 2008].

3.4: Code benchmarking

The computational results presented in this thesis have either been benchmarked against other modelling codes or to experimentally obtained measurements for similar parameter sets. The good correlation between each method provides assurance that the computational results are a good representation of the specified problem. For example, the fully optimised gyro-TWA MAGIC-3D simulation results presented in *chapter 4* have been shown to consistently reproduce results comparable to the measurements from a laboratory experiment for similar parameters, with dispersion calculations of the operating eigenwave in the 3-fold helically corrugated waveguide obtained from two different modelling codes (MAGIC-3D and CST Microwave Studio) also showing strong correlation. The good agreement between these simulation results and the experimentally obtained measurements present the computational model as a suitable foundation on which to investigate potential performance enhancement of the amplifier *(chapter 5)*.

In addition to the gyro-TWA research, an X-band Marie-type converter was modelled and fabricated *(chapter 6)*. A slight variation in one section of the inner geometry of

the converter from simulation to fabrication was required owing to limitations of the wire erosion technique used to fabricate the component. However this variation did not significantly impact on the performance of the converter, with experimental measurements found to agree favourably with simulation results from CST Microwave Studio. This presented the Marie-type converter as a suitable test device for a radiation transparent plasma confinement component *(chapter 6)*.

3.5: Network analysis

Scattering or S-parameters are used to characterise circuits at microwave frequencies where it becomes difficult to directly measure voltages and currents. Utilisation of a scattering matrix for an integer number of ports provides a complete description of a linear system where the phase angles and amplitudes of output waves on a port are related to those incident on the port and all other ports in the network [Pozar, 2004]. The transmission and reflection measurements of a signal from all ports of a device can thus be represented in a matrix.

A simple two port device, such as the Marie-type mode converter *(chapter 6)* has four S-parameters, namely S_{11}, S_{22}, S_{21} and S_{12}, which represent the forward and reverse reflection and transmission coefficients respectively. Each is a phasor quantity containing a magnitude and phase angle defined as a function of frequency, and represents a path gain which may be used to predict the output signals from a linear device as a result of its input signals. For the Marie-type converter discussed in *chapter 6,* the most critical S-parameters optimised for were the forward transmission (S_{21}) and reflection (S_{11}) coefficients, where the reflection coefficient was required to be suppressed with the vast majority of power coupled into the primary forward transmission mode.

Two types of network analyser were used to test the performance of the Marie-type converter, namely a Vector Network Analyser (VNA) and a Scalar Network Analyser (SNA). A VNA is designed to obtain both magnitude and phase measurements of a device under test (DUT) with calibration of the analyser essential to remove systematic errors (such as losses in the cables). Standard two port calibration techniques include the offset-short-load-thru and the line-reflect-line technique with known calibration standards used. For two port measurements a twelve-term error calibration is used, which determines six forward and six reverse terms associated with a stimulus at port 1 and port 2 respectively. These terms are all mathematically removed from the measured data of the DUT. Here a VNA, specifically the Anritsu 37397A model, was used to measure the forward reflection coefficient of the Marie-type converter.

A SNA cannot measure phase and thus measures only the magnitude response of a DUT. This type of analyser was used to measure the radiation pattern of the Marie-type converter in the far field (Fraunhofer) region. In this region, the radiation pattern is independent of distance and the waves behave as plane waves with power density dropping off as $\frac{1}{r^2}$. To ensure measurements are taken in the far field, the receiving antenna should be displaced a minimum set distance from the output of the DUT, given as the Fraunhofer distance [Balanis, 1982], *equation 3.5.1*. In order to be in the far field region, $r_f \gg L$ and $r_f \gg \lambda$.

$$r_f = \frac{2L^2}{\lambda}$$
Equation 3.5.1

Here r_f denotes the observer distance and L the maximum dimension of the launching antenna. Intermediate ranges below this distance include the radiating near field (Fresnel) and the reactive near field regions.

Far field measurements were undertaken to determine the mode of the output radiation from the Marie-type converter. For TE$_{n,m}$ modes radiating from cylindrical waveguide, the electric field components E_θ (radial polarisation) and E_φ (azimuthal polarisation) can be analytically obtained [Silver, 1949] from *equation 3.5.2* and *equation 3.5.3*

$$E_\theta = j^{n+1} \frac{n\omega\mu}{2R} \left[1 + \frac{\beta}{k}\cos\theta + \Gamma\left(1 - \frac{\beta}{k}\cos\theta\right)\right] \qquad \textit{Equation 3.5.2}$$

$$J_n(k_c a)\frac{J_n(ka\sin\theta)}{\sin\theta}\sin n\phi e^{-jkR}$$

$$E_\phi = j^{n+1}\frac{ka\omega\mu}{2R}\left[\frac{\beta}{k} + \cos\theta - \Gamma\left(\frac{\beta}{k} - \cos\theta\right)\right] \qquad \textit{Equation 3.5.3}$$

$$\frac{J_n(k_c a)J_n'(ka\sin\theta)}{1 - \left(\frac{k\sin\theta}{k_c}\right)^2}\cos n\phi e^{-jkR}$$

Here E_θ, E_ϕ represent the azimuthal and radial electric field components, n the azimuthal index of the mode under consideration, ω the angular frequency of the radiation, β the axial wavenumber, k the free-space wavenumber, k_c the cut-off wavenumber, a the radius of the waveguide, R the distance between the aperture output and the receiving antenna with Γ a reflection coefficient.

To obtain the far field measurements in the laboratory a receiving antenna was positioned a set distance, ~0.83m, from the output aperture of the Marie-type converter. A precision detector (model Hewlett Packard 85025A) was connected to the receiving horn through a waveguide to coaxial adapter with the other (video) end of the detector connected to a calibrated SNA (model Hewlett Packard 8757D). An RF signal of ~7dBm (corresponding to a power of ~5mW) was transmitted from a synthesised sweeper (model Hewlett Packard 83752B) which was connected to the input of the Marie-type converter, *figure 3.5.1*.
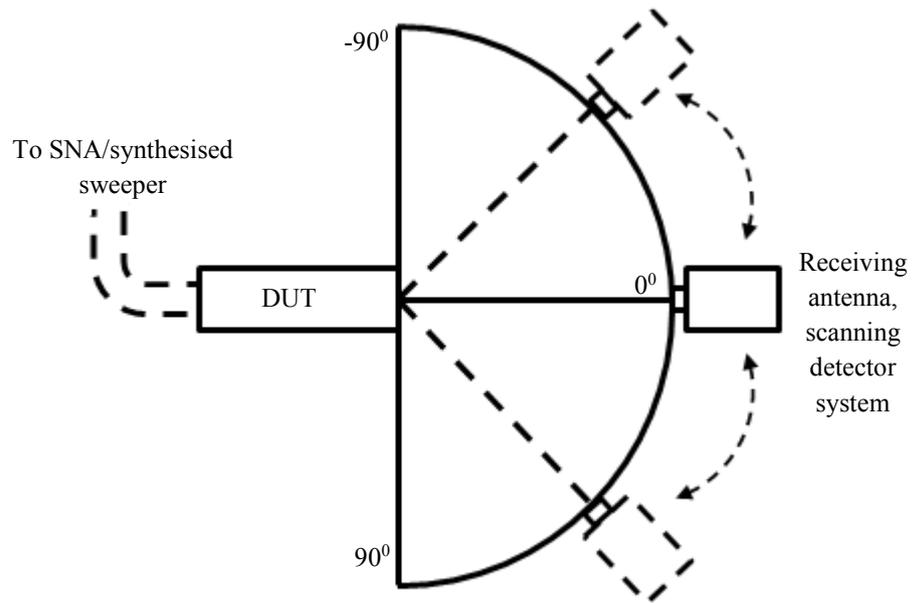
Figure 3.5.1: Scanning apparatus set up. Here the DUT was the Marie-type converter.

The receiving antenna was swept in angle from -55^0 to 55^0 in incremental positions separated by either 1^0 or 5^0 to measure the field intensity at each position. The receiving antenna was then rotated 180^0, *figure 3.5.2,* with the antenna again incrementally swept from -55^0 to 55^0, to determine the mode of the output radiation from the Marie-type converter *(chapter 6).* In essence each of these configurations measured radiation polarised normal to the scanning plane and parallel to the scanning plane.
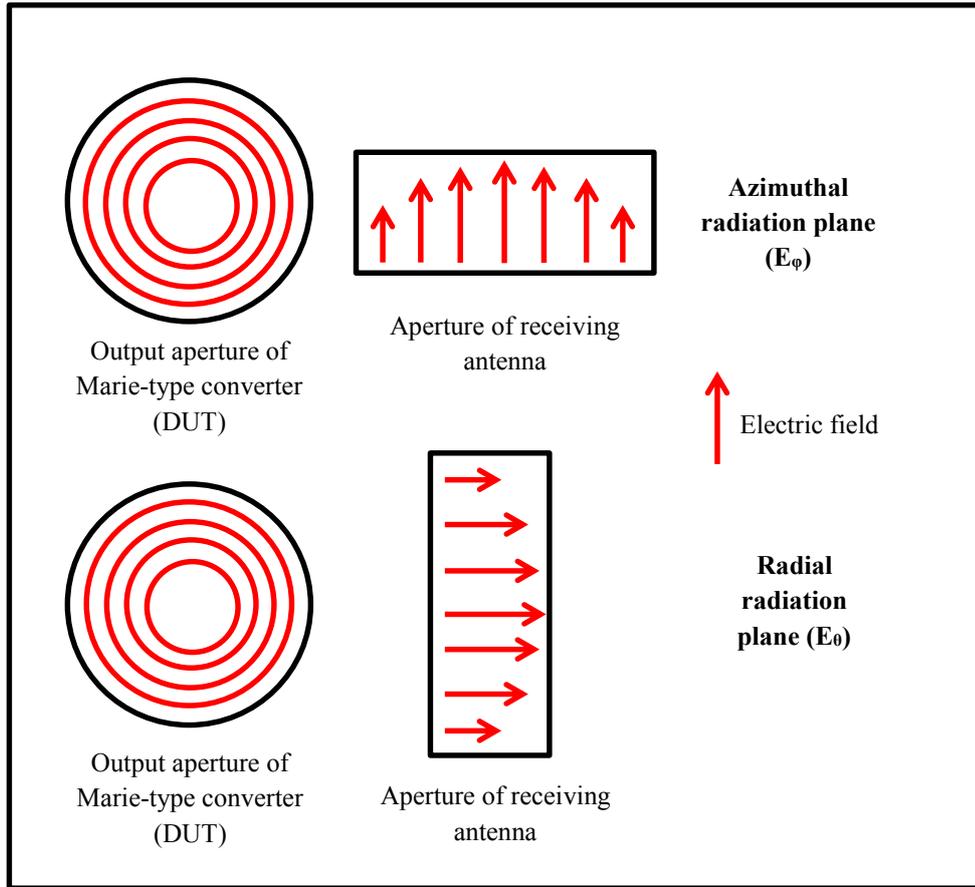
Figure 3.5.2: Orientation of the receiving antenna with respect to the output aperture of the Marie-type converter.

The Marie-type converter's polarisation (essentially defined by the polarisation of the input rectangular waveguide) was also orientated at 0^0, 45^0 and 90^0, *figure 3.5.3,* with the receiving antenna swept from -55^0 to 55^0 in both the azimuthal and radial radiation plane to substantiate the purity of the output mode.
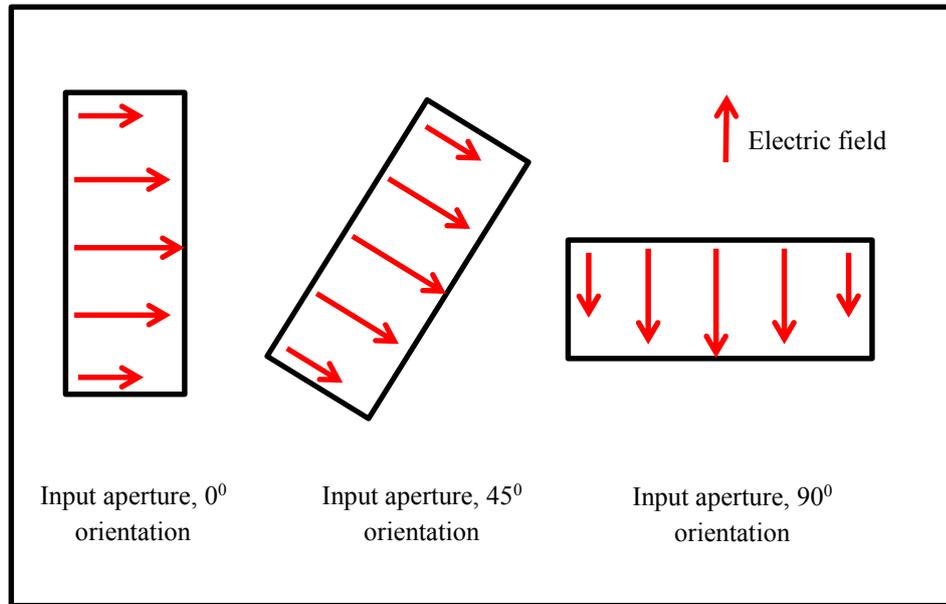
It was defined that 0^0 orientation of the Marie-type converter corresponded to the major axis of the input rectangular waveguide being normal to the plane containing the axis of the converter and the far field detector. From this reference point, 45^0 orientation was taken to be a 45^0 clockwise repositioning of the input rectangular waveguide with respect to the 0^0 orientation of the converter. Similarly for 90^0 orientation it was assumed that the major axis of the input rectangular waveguide was in the measurement plane, *figure 3.5.3*. These three orientations were sufficient to provide a detailed analysis of the pattern of output radiation from the converter, owing to the relative symmetry within the device's structure, since rotations at 180^0 and 270^0 with respect to 0^0 would mirror those of 0^0 and 90^0. This results from the device having a *y-z* plane of symmetry. As the expected output mode from the Marie-type converter was the cylindrical TE_{01} mode and since this mode is symmetric, the orientation of the Marie-type converter should have no bearing on the far field patterns. Therefore this method measures the purity of the output mode and allows an estimate of S_{21} to be inferred from S_{11}.

3.6: Technique applied to MAGIC dispersion calculations

It has been shown [Denisov, 1998a, Denisov, 1998b and Bratman, 2000] that the method of perturbation, when used to calculate the dispersive characteristics of a cylindrical waveguide with a helical corrugation along the inner wall surface, is in good agreement with 'cold' experiments provided the corrugation amplitude, *l*, of the waveguide perturbation is small in comparison to the wavelength. The gyro-TWA simulations as detailed in *chapter 4* had parameters broadly similar to those of an experiment detailed in [Bratman, 2000], for which the dispersion characteristics had been inferred from 'cold' experiments and shown to agree favourably with perturbation theory. It thus follows that dispersion characteristics obtained from modelling codes such as MAGIC-3D and CST Microwave Studio (for a comparable parameter set) should similarly match well to those determined from perturbation theory.

A linearly polarised wave can be represented as the superposition of two circularly polarised waves of opposing senses (left- and right-circularly).   These wave components may propagate with different phase constants such that the total electric field propagating along the *z*-axis of a system a distance d_z with an $e^{-ik_{z-}d_z}$ and $e^{-ik_{z+}d_z}$ dependence may be expressed as

$$\bar{E} = \frac{E_0}{2}(\hat{x} + i\hat{y})e^{-ik_{z-}d_z} + \frac{E_0}{2}(\hat{x} - i\hat{y})e^{-ik_{z+}d_z} \qquad \text{\textit{Equation 3.6.1}}$$

The above can be separated into $\hat{x}$ and $\hat{y}$ components and rewritten as

$$\bar{E} = \frac{E_0}{2}\hat{x}\left(e^{-ik_{z-}d_z} + e^{-ik_{z+}d_z}\right) \qquad \text{\textit{Equation 3.6.2}}$$

$$+ i\frac{E_0}{2}\hat{y}\left(e^{-ik_{z-}d_z} - e^{-ik_{z+}d_z}\right)$$

Simplification and rearrangement yields

$$\bar{E} = E_0 e^{-i(k_{z-}+k_{z+})\frac{d_z}{2}} \left[\hat{x} \cos(k_{z+} - k_{z-})\frac{d_z}{2} \right.$$

$$\left. - \hat{y} \sin(k_{z+} - k_{z-})\frac{d_z}{2} \right]$$

such that the resultant electric field remains linearly polarised with the polarisation rotating as it propagates along *z*, *figure 3.6.1*.
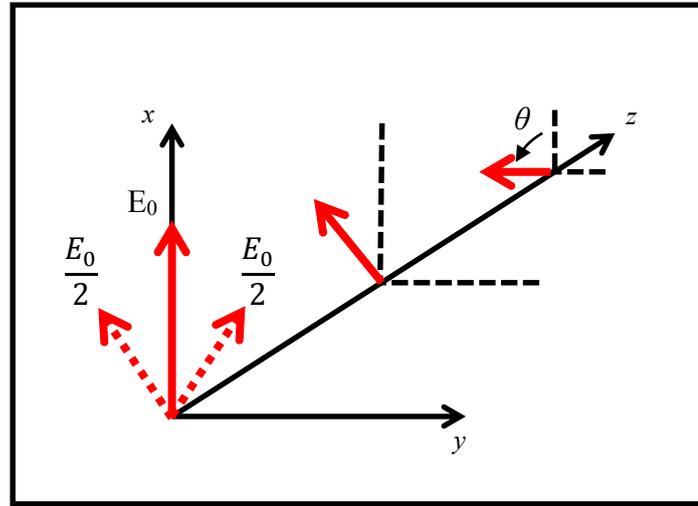
Figure 3.6.1: Illustration of linearly polarised wave rotation.

For a given point along *z*, the new plane of polarisation (with respect to the *x*-axis) makes the angle

$$\theta = \tan^{-1}\left(\frac{E_y}{E_x}\right) = -(k_{z+} - k_{z-})\frac{d_z}{2}$$

This effect is known as Faraday rotation and is nonreciprocal such that a wave reflected back to the source would continue to rotate in the same sense and thus be subjected to a 2θ rotation with respect to the *x*-axis upon arrival back at the source [Collin, 1992].

Faraday rotation can be used to calculate the dispersion characteristics of the operating eigenwave of a helically corrugated waveguide since the dispersion characteristics in such waveguides strongly depend on wave polarisation [Denisov, 1998a]. The circularly polarised component of the TE$_{11}$ wave which co-rotates with respect to the

helix will be uncoupled and virtually unperturbed as it propagates through the helical structure having dispersion closely matched to that of a TE_{11} wave in smooth bore cylindrical waveguide. Conversely the component of the circularly polarised TE_{11} wave which counter-rotates with respect to the helix will be coupled to a mode similar to that of the TE_{21} mode in smooth bore cylindrical waveguide, resulting in the operating eigenwave of the amplifier. These left- and right-handed circularly polarised wave components will propagate with different phase constants with the linearly polarised TE_{11} output radiation in the cylindrical waveguide experiencing a substantial and frequency sensitive rotation, *figure 3.6.1,* with respect to the initially injected linearly polarised TE_{11} wave. From this angle of rotation, *equation 3.6.4,* the dispersion characteristics of the operating eigenwave can be determined.

Gyro-TWAs with helically corrugated interaction waveguides significantly benefit from being sensitive to the orientation of the circularly polarised wave, since the wave can make more passes through the system before it is back in the correct polarisation to 'see' both the perturbed waveguide and electron beam and hence experience further gain. This strengthens the stability of the amplifier against convective feedback oscillation since the repeat round trips significantly reduce the cavity effective diffractive Q.

Chapter four: PiC simulations of a helically corrugated interaction waveguide gyro-TWA

4.1: Overview

To create a parameterised 3D model of any gyro device which can accurately and reliably model the non-linear dynamics of a system is highly desirable. The reproduction of the results experimentally however, truly validates the numerical results and provides a high level of confidence in the model. To date the modelling of the non-linear dynamics of gyro-TWAs with helically corrugated waveguides has focused on solving a set of 1D non-linear equations which describe the coupled beam-wave system, with multidimensional modelling hitherto predominantly undertaken in cylindrical co-ordinates. Whilst these simulations have served to give insight into the internal electrodynamics of the system, numerical stability issues limit their use as a design tool. Presented in this chapter are multidimensional simulations of an X-band 2nd harmonic gyro-TWA with a helically corrugated waveguide modelled in Cartesian co-ordinates and the iterative optimisation process which led to them. These simulations have been observed to consistently reproduce experimental measurements and offer enhanced numerical stability over multidimensional cylindrical co-ordinate models.

4.2: An experimental X-band 2nd harmonic gyro-TWA

4.2.1: Details of the gyro-TWA laboratory experiment

The simulated gyro-TWA was based on the parameters of an experimental X-band 2nd harmonic gyro-TWA with a helically corrugated waveguide built and tested at the University of Strathclyde (Scotland) and in collaboration with the Institute of Applied Physics (Russia), detailed in [Bratman, 2000]. This device was the second gyro-TWA to utilise a helically corrugated interaction waveguide and achieved an output power of ~1.1MW at 9.4GHz, corresponding to a saturated efficiency of ~29%. The linear and saturated gains of the amplifier were estimated to be up to ~47dB and ~37dB respectively with the amplifier having a measured saturated bandwidth of 2.0GHz from 8.4GHz to 10.4GHz. The device utilised a 185kV, 20A rectilinear electron beam generated by a Pierce-type electron gun with a cold velvet cathode emitting surface. A kicker positioned downstream of the cathode imparted transverse velocity to the electrons to generate an axis encircling beam with a pitch factor, α, estimated to be 1.2.

The interaction region of the device comprised of a copper cylindrical waveguide, 60cm in length, with a 3-fold helical corrugation along the inner wall surface. This helical waveguide had a mean radius, r_0, of 14.1mm, corrugation amplitude, l, of 2.2mm and axial periodicity, d, of 37.5mm. The helical waveguide coupled two partial rotating waves, a near cut-off TE_{21} wave which co-rotated with the structure and a far from cut-off first spatial harmonic TE_{11} wave which counter rotated with respect to the helix. Two 12cm long converters were positioned at either end of the helical waveguide and were designed to smoothly convert from the input cylindrical waveguide to the helical waveguide and back again. These converters provided a progressive impedance match to convert radiation in the operating eigenmode to the cylindrical waveguides which bracketed both the 12cm long cylindrical to helical

converters and the 60cm long helical waveguide. Distributed losses were positioned over a short length (~5cm) in the centre of the interaction waveguide, acting as a form of sever. Due to the coupling of the electromagnetic wave to the electron beam in the forward interaction direction, these losses had very limited effect on the strength of the forward wave but did however strongly attenuate (in this instance ~10dB) any purely electromagnetic reflected waves returning from the output to the input. This minimised the possibly of oscillations by helping to suppress feedback signals.

An electromagnetic wave was launched into the cylindrical waveguide/beam drift tube through a rectangular side wall aperture (the input coupler), with standard waveguide 16 dimensions (WG16), located downstream of the Pierce-type electron gun but before the main tube body. A linearly polarised fundamental TE_{10} wave was generated in the rectangular aperture by a conventional broadband helix TWT driven by a synthesised solid state oscillator. Upon propagation into the cylindrical waveguide/beam drift tube, the radiation signal was converted to the fundamental TE_{11} mode. At this point the wave was linearly polarised until propagation through a 'quarter wave plate' elliptical deformation in the cylindrical waveguide imparted the desired circular polarisation.

4.2.2: Experimental measurements of the gyro-TWA

The experimental results taken from [Bratman, 2000] for output power and gain as a function of input power and the measured saturated gain as a function of frequency are shown in *figures 4.2.2.1* and *4.2.2.2* respectively. Also shown is the calculated saturated efficiency of the amplifier as a function of frequency, *figure 4.2.2.3*. The response to the RF drive power was measured for a frequency of 9.2GHz however maximum output power was measured at 9.4GHz and therefore the initial simulations were refined at this latter frequency.
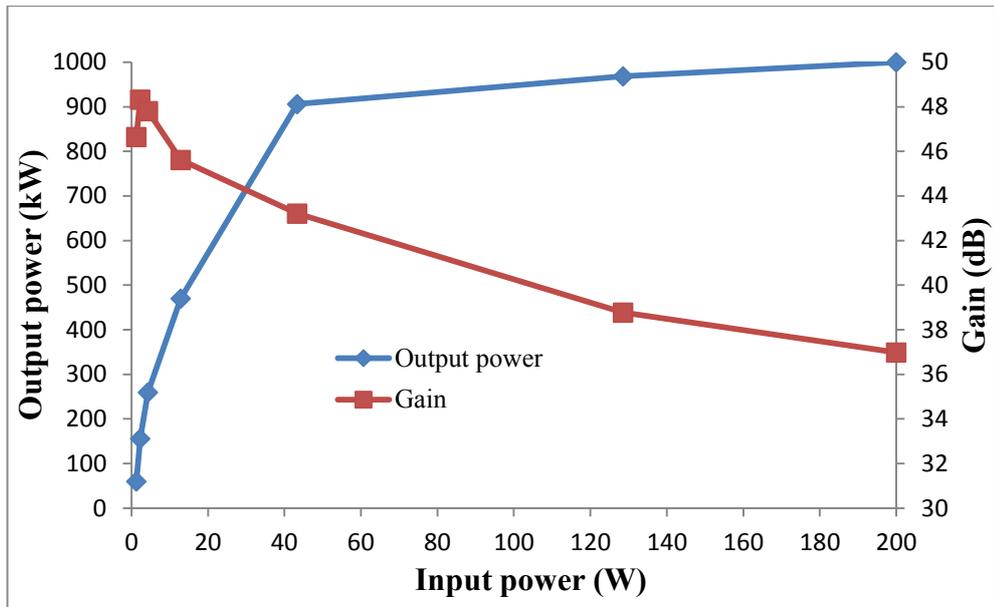
Figure 4.2.2.1: *Measured output power and gain for given input powers of the experimental X-band 2nd harmonic gyro-TWA at 9.2GHz [Bratman, 2000].*
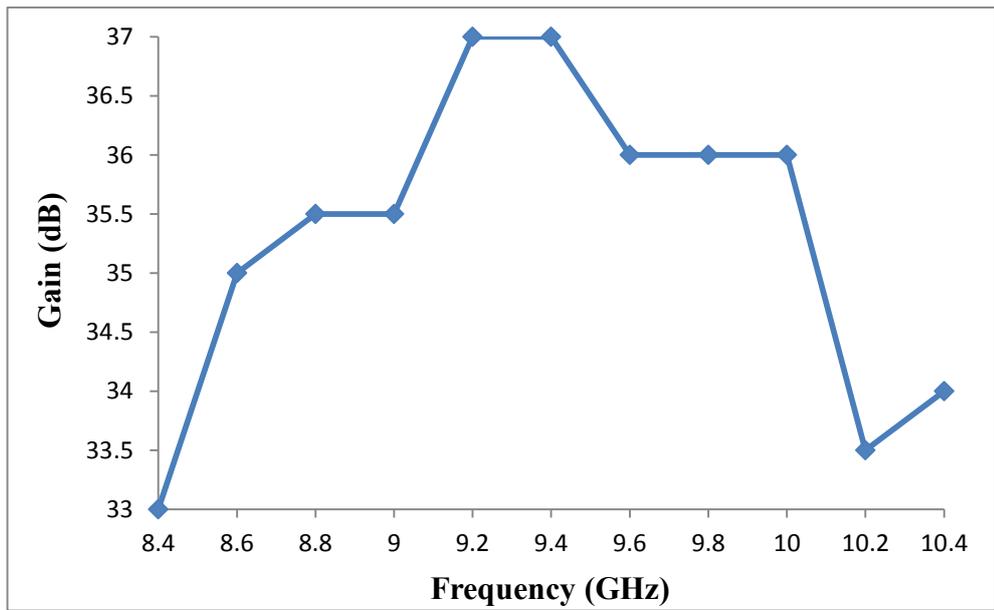
Figure 4.2.2.2: *Measured saturated gain as a function of frequency for the experimental X-band 2nd harmonic gyro-TWA [Bratman, 2000].*
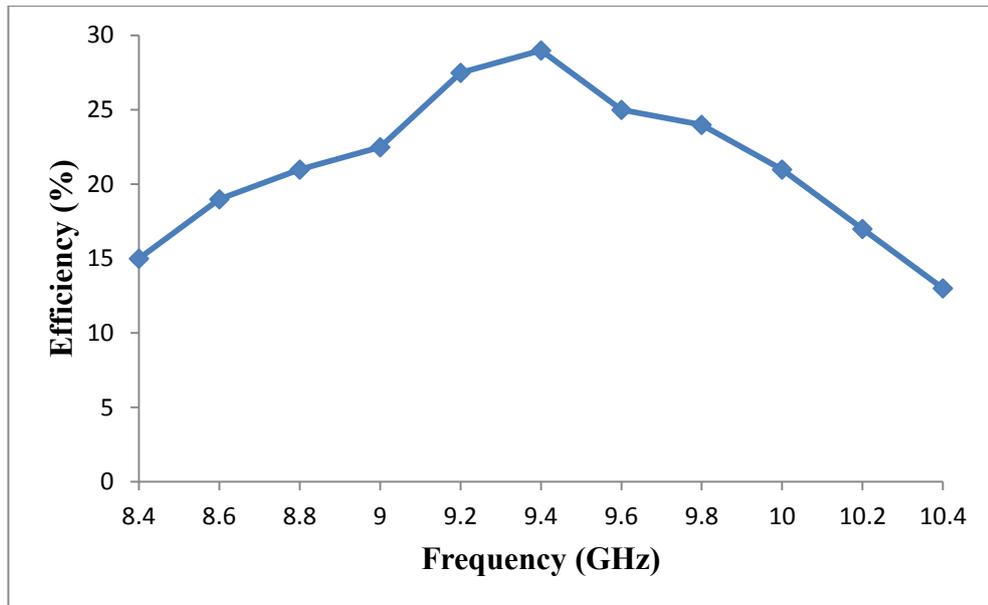
Figure 4.2.2.3: Measured saturated efficiency as a function of frequency for the experimental X-band 2nd harmonic gyro-TWA [Bratman, 2000].

These results indicate a variation of around -3dB in saturated output power over the frequency band of interest with the power dropping to around half the maximum value at the band edges (indicating a -3dB saturated power bandwidth from 8.4GHz to 10.4GHz). The optimum saturated efficiency of ~29% was measured for a frequency of 9.4GHz however the amplifier also performed favourably at 9.2GHz realising a saturated efficiency of ~27.5%. Below this frequency it was observed that the efficiency of the amplifier fell steadily measuring ~15% at 8.4GHz. This trend was also evidenced for frequencies above 9.4GHz where the efficiency steadily declined measuring ~13% at 10.4GHz.

4.3: A simulated X-band 2nd harmonic gyro-TWA

4.3.1: Details of the gyro-TWA simulations

The parameters detailed in [Bratman, 2000] were used as the starting point for 3D simulations of an X-band 2nd harmonic gyro-TWA with a helically corrugated interaction waveguide. These parameters were used to generate initial simulations in the PiC programming code MAGIC-3D with the amplifier geometry shown in *figure 4.3.1.1.*
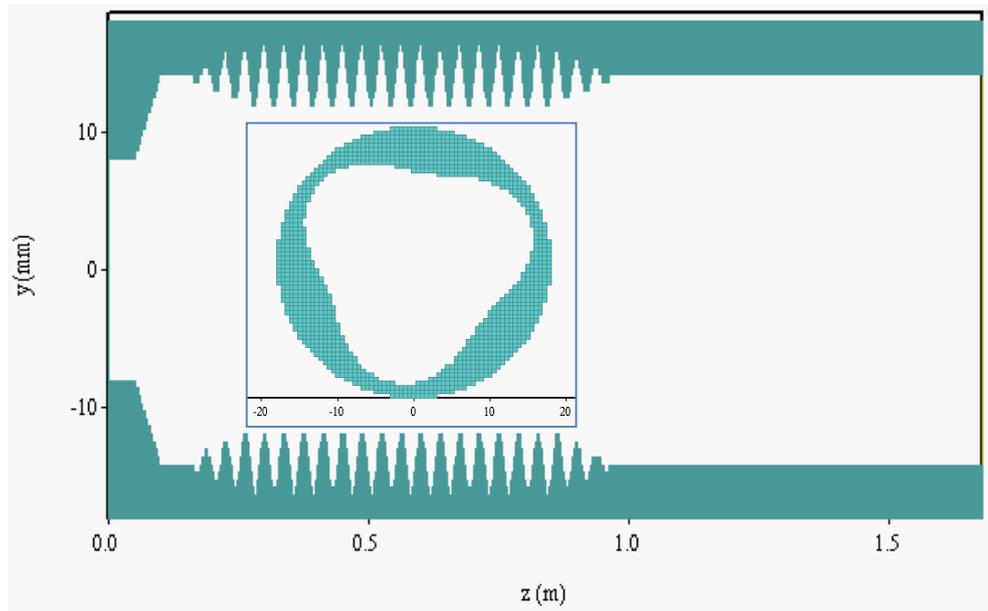
Figure 4.3.1.1: Simulation geometry taken from MAGIC-3D of the X-band 2nd harmonic gyro-TWA, programmed using the Cartesian co-ordinate system.

The geometry displayed in *figure 4.3.1.1,* and subsequently used in all simulation results presented in this chapter was generated by creating a confining shell, with individual components which comprised the gyro-TWA system voided out. From left to right these components (parametrically defined through the use of 'mathematically' described surfaces) included an electron 'emission' wall surface, a 5cm long beam

62

tunnel, a 5cm long cylindrical up-taper, a 4cm long section of cylindrical waveguide, a 12cm long cylindrical to helical converter, a 60cm long section of helical waveguide, a 12cm long helical to cylindrical converter, a 70cm long output cylindrical waveguide and a waveguide output port.

Originally simulations were prepared in cylindrical co-ordinates before transferring to the Cartesian co-ordinate system. It was evident from early simulations using cylindrical co-ordinates that the unfavourably structured cells running axially through the centre of the entire system generated numerical noise which severely degraded and skewed the predictions of the amplifier performance, in spite of the simulations not having electrons traversing these cells. The effect appeared after a certain number of time steps and manifested itself in the form of strong high frequency electromagnetic signals associated with electric fields that inverted direction on each grid cell. By converting to the Cartesian co-ordinate system the mesh cell difficulty was removed, and cleaner more reliable results were obtained such that non-physical, strong, high frequency oscillations localised near to the waveguide axis were eliminated. In addition, the conversion of simulations to Cartesian co-ordinates eased computational requirements in terms of clock cycles on the processor, by increasing the time step that could be used whilst satisfying the Courant condition, *equation 3.2.1*. The disadvantages of utilising such a system however, included a significant increase in the memory required to describe the problem with adequate resolution as well as the loss of the conformal relationship between the input and output waveguides and the mesh. Nonetheless the advantages of utilising this co-ordinate system greatly outweighed the disadvantages and thus all results presented are from simulations coded in Cartesian co-ordinates.

The simulations were not a direct replica of the laboratory experiment. As has been detailed (*section 4.2.1*) the experiment utilised a rectangular side wall input coupler to launch the electromagnetic wave. In the simulations however, a linearly polarised cylindrical TE$_{11}$ wave was injected through the waveguide output port located at the

right hand side (RHS) of *figure 4.3.1.1*. This injected linearly polarised cylindrical TE_{11} wave was attenuated as it propagated through a dielectric absorber positioned in the output cylindrical waveguide, providing the correct level of drive power. The dielectric absorber was designed to improve the wideband match of the output port to prevent convective feedback oscillation due to non-physical mismatching between the output port and the wave signal. The dielectric absorber minimised reflections on the port with this technique implemented in all simulations. Poynting flux diagnostics either side of the dielectric absorber calculated the power in the injected TE_{11} wave and the power in the wave immediately after it had propagated through the dielectric. This allowed the properties of the dielectric to be verified together with the actual power in the input wave perceived by the amplifier which would later be used to calculate the gain of the system. Since the launched wave was linearly polarised (comprising of a left- and a right-circularly polarised wave) it was assumed that only half the power in the wave was associated with the correct rotating polarisation of the TE_{11} mode, as the helical structure couples only counter rotating (with respect to the helix) dipole (TE_{11}) modes to co-rotating quadrupole (TE_{21}) modes (i.e. only these waves generate the desired hybrid eigenwave). Gain calculations for all simulation data was based on this assumption. In all simulations the geometry of the amplifier was designed to ensure that the cylindrical TE_{11} wave was unable to propagate into the beam tunnel and ultimately to the electron 'emission' surface, since electromagnetic oscillations allowed close to such emission structures have been observed to generate non-physical axial modulation of the electron beam's velocity and density. This is especially true for cylindrical co-ordinate models however is also not recommended in Cartesian co-ordinate systems. Thus a 5cm long cylindrical taper section was positioned directly after the beam tunnel which caused the injected electromagnetic wave, upon encountering the taper section, to reflect and propagate back through the helical structure as a result of the wave becoming cut-off.

The simulations also differed from the experiment in the manner in which the electron beam was formed. As detailed (*section 4.2.1)* in the laboratory experiment the 185kV, 20A electron beam was generated by a Pierce-type electron gun with a kicker to impart

transverse velocity to the electrons. In the simulations a 185kV, 20A synthesised electron beam was emitted from the wall surface on the left hand side (LHS) of *figure 4.3.1.1*. The beam was defined with a specific transverse velocity for the electrons and thus no additional kicker system was required. Moreover, the electron beam was time delayed to take into account the propagation delay for the TE_{11} wave from injection through the RHS port, *figure 4.3.1.1,* to the cylindrical reflection taper. This also served to reduce the computational load.

In the experiment the axial confining magnetic field of 0.21T was provided by a water cooled dc solenoid. The simulations however implemented a variable guide magnetic field, for the purpose of optimisation, which spanned the axial range from 0m to ~1.00m (sufficient to guide the electrons through the interaction space). After the end of the interaction space the electron beam was released, by progressively reducing the magnetic field, and dumped onto the side walls of the output cylindrical waveguide. The simulations predicted the RF radiation generated in the amplifier by a Poynting flux diagnostic at an axial position which corresponded to a point between the end of the confining magnetic field and the edge of the dielectric absorber. This prevented the power diagnostic being compromised by the static fields caused by the electron beam which impacted on the wall upstream of this point.

4.3.2: Gyro-TWA simulation mesh resolution

The geometry of the gyro-TWA was difficult to mesh, requiring large computational resources to be accurately resolved. Ideally mesh elements in each axis, *dx*, *dy* and *dz,* would have been on the order of 0.1mm or less to facilitate >20 mesh cells over the amplitude of the corrugation. This would be less problematic in *dx* and *dy* where the dimension to be resolved was at a maxima of ~36mm. Longitudinally, the system measured over 1.5m and the division of this into 0.1mm would require substantial resources. The actual mesh resolution used in the simulations represented a

compromise with *dx*, *dy* and *dz* values corresponding to 0.55mm, 0.55mm and 1.1mm respectively. Such a mesh allowed some 30 nodes axially per free space wavelength and a similar resolution per axial corrugation. There were some 66 nodes across the transverse structure giving 8 mesh nodes across the corrugation amplitude. The output power and gain measurements from simulations with this mesh resolution were found to be in good agreement with those experimentally obtained, providing a high level of confidence in the simulations. A 10% variation in the mesh resolution was observed to yield comparable results for the same initial conditions, further suggesting that the mesh resolution was adequate to resolve the system. Moreover, the mesh resolution maintained an aspect ratio of 1:2 in the cell dimensions which provided for reasonably efficient computations.

4.3.3: Gyro-TWA simulation optimisation process

A sensitivity analysis was undertaken to allow for any uncertainty in the parameters from the experimental configuration. For example in a laboratory experiment it can be difficult to accurately determine the α (pitch) of a gyrating electron beam. Simulations were therefore undertaken sweeping α through a representative range to determine a configuration which delivered high output power at 9.4GHz. With gyro-TWA interactions also sensitive to magnetic field strength it was elected to also incrementally sweep this parameter to determine the combination of these two key parameters for achieving an output power in the range demonstrated by the experiment. Alternatively the voltage applied to the electron emission assembly could have been used as an optimisation parameter however since both this and the magnetic field strength appear in the definition of ω_c, *equation 1.2.2*, a change in either parameter would produce similar effects. Once an output power in the desired range was achieved for the experimental centre frequency of 9.4GHz, the simulations were rerun for varying frequencies to establish the bandwidth performance of the amplifier, since this would also be impacted by both the magnetic field strength and the α of the electron beam. As previously detailed, this output power would initially be determined

from a Poynting flux diagnostic located in the output cylindrical waveguide of the amplifier, with an example of this shown in *figure 4.3.3.1*. Later (*section 4.3.6*) an additional diagnostic would be used alongside the Poynting flux diagnostic to give further insight into the performance of the gyro-TWA.
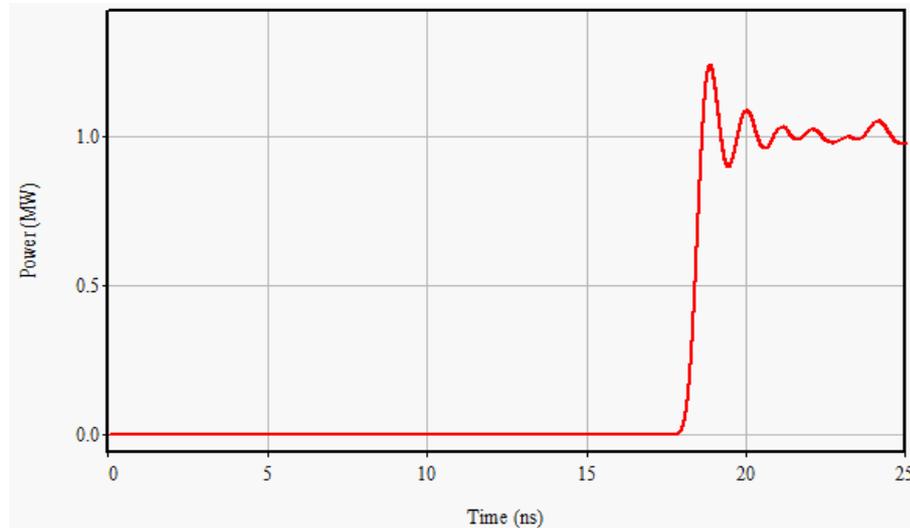
Figure 4.3.3.1: An example of the observed power of a simulated gyro-TWA predicted by a Poynting flux diagnostic for an input power of ~105W at 9.4GHz, taken from MAGIC-3D.

The plot of observed power as a function of time, *figure 4.3.3.1,* shows that the amplifier reached steady state operation for a sustained period of time, with the delay in the signal start associated with the transit times of the system. This observation gave an early indication that the simulation approach was a physically sound representation of the gyro-TWA system, however further validation of this would result from additional diagnostics designed to monitor all aspects of the beam-wave interaction. For example fast Fourier transforms (FFTs) were used to monitor the input and output frequencies to ensure they tracked each other, with *figure 4.3.3.2* an example of a FFT taken from MAGIC-3D.
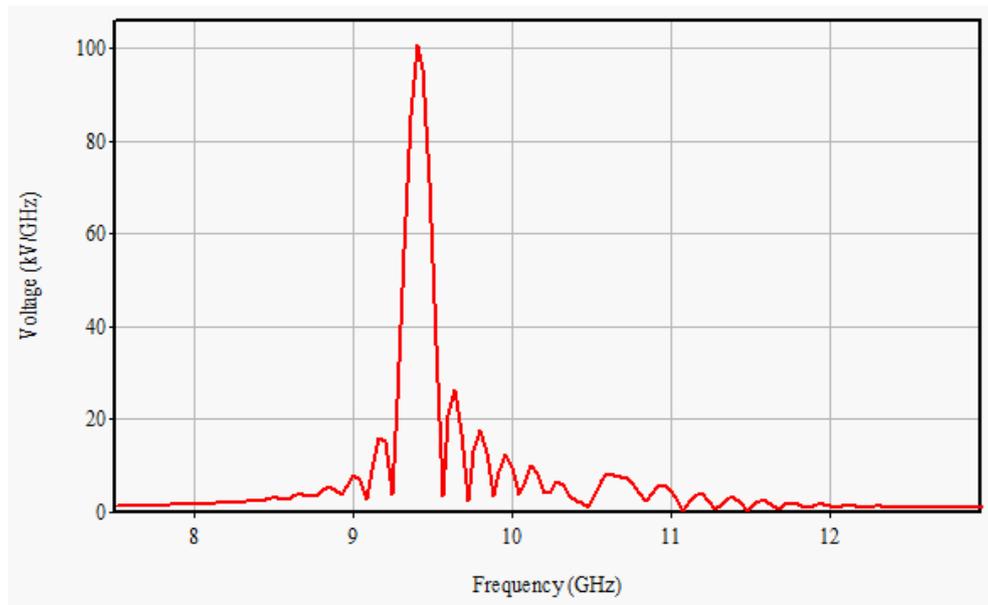
Figure 4.3.3.2: FFT showing the gyro-TWA operating at the desired frequency, in this instance 9.4GHz, taken from MAGIC-3D.

Moreover contour field diagnostics were positioned throughout the structure to verify that the injected wave was a cylindrical TE_{11} wave and that the output RF radiation was in the desired cylindrical TE_{11} mode. These field diagnostics were also positioned inside the helical interaction waveguide to determine the operating eigenwave, although this was harder to interpret appearing as a superposition of the electromagnetic modes and the complex fields sourced from the strongly modulated space charge of the electron beam. *Figure 4.3.3.3* is an example of a contour plot recorded in the output cylindrical waveguide of the gyro-TWA.
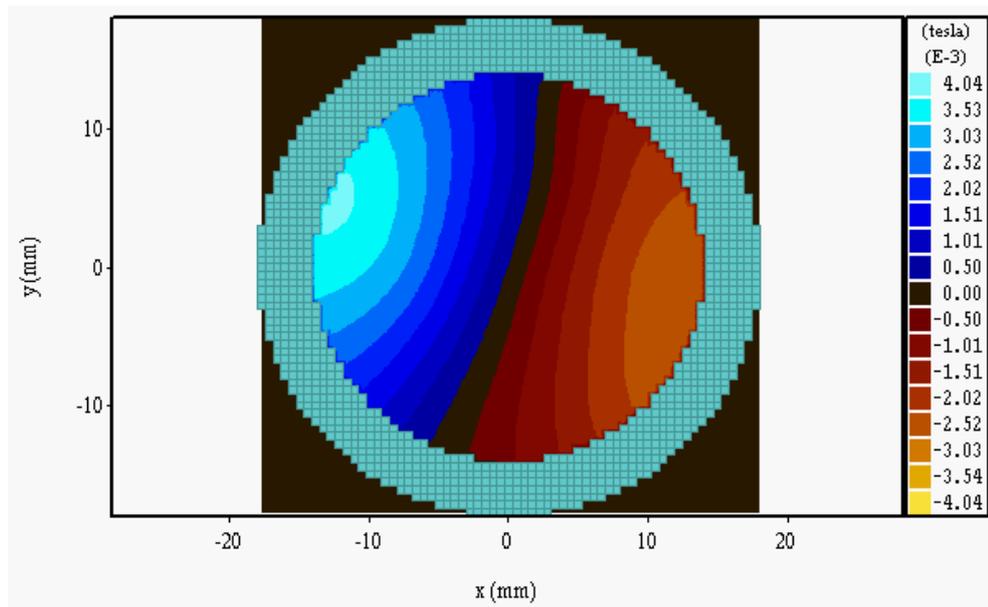
Figure 4.3.3.3: Contour plot in B_z showing the cylindrical TE_{11} mode at the output of the gyro-TWA, taken from MAGIC-3D.

Since the simulations were coded in the Cartesian co-ordinate system a co-ordinate transform would be required to reconstruct the E_x and E_y field components to most easily interpret the operating eigenmode. However the component of the electric field in B_z remains unchanged when converting between the cylindrical and Cartesian co-ordinate systems and in this instance can be easily recognised as the desired cylindrical TE_{11} mode, *figure 4.3.3.3.* Contour plots recorded over a narrow time frame showed that the cylindrical TE_{11} mode had a clockwise rotation, counter-rotating with respect to the helical waveguide. This observation was anticipated since only the component of the TE_{11} wave which counter-rotates with the helical structure couples to the operating eigenwave. These plots gave an insight into the behaviour of the electromagnetic wave, however to monitor the electron beam as it traversed the system required phase-space diagnostics. From the law of energy conservation the electron beam is required to lose energy in order for the kinetic energy of the electrons to be successfully transferred to the electromagnetic wave. This loss in energy can be readily interpreted from plots of average beam kinetic energy as a function of axial position, *figure 4.3.6.1*, but can also be inferred from phase-space plots showing the kinetic energy of all the electrons comprising the electron beam, *figure 4.3.3.4.*
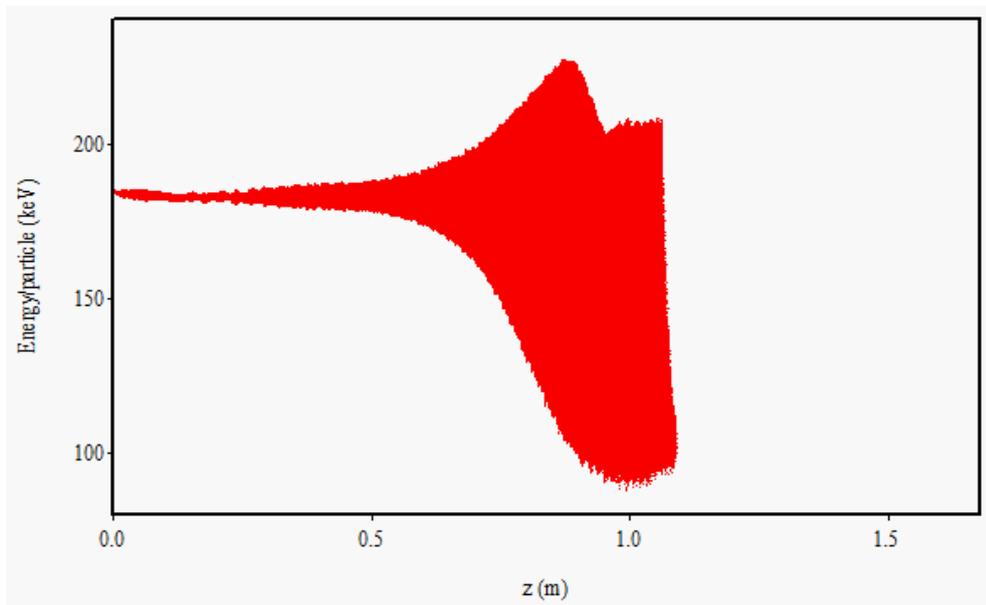
Figure 4.3.3.4: *An example of particle kinetic energy as a function of axial position, taken from MAGIC-3D.*

This phase-space plot shows the change in kinetic energy of individual electrons with axial position, from an initial value of 185keV. It was observed that as the electrons traversed the system some were accelerated whilst others were decelerated. Those subject to an acceleration increased in kinetic energy whilst those that were decelerated decreased in energy. For successful energy transfer a net deceleration in beam kinetic energy is required, as suggested in *figure 4.3.3.4*. The gyro-TWA operates at the 2nd cyclotron harmonic and thus it would be anticipated that two electron bunches would be visible as the beam interacts with, and becomes meaningfully perturbed by, the electromagnetic field. This observation was recorded in phase-space plots taken transversely at the end of the helical interaction waveguide, i.e. between 84cm and 84.375cm, *figure 4.3.3.5*. By recording these phase-space plots over a narrow time frame of 22ns to 22.06ns i.e. when the amplifier had reached steady state output, the evolution of the electron bunches were observed.

t = 22ns   t = 22.02ns

t = 22.04ns   t = 22.06ns
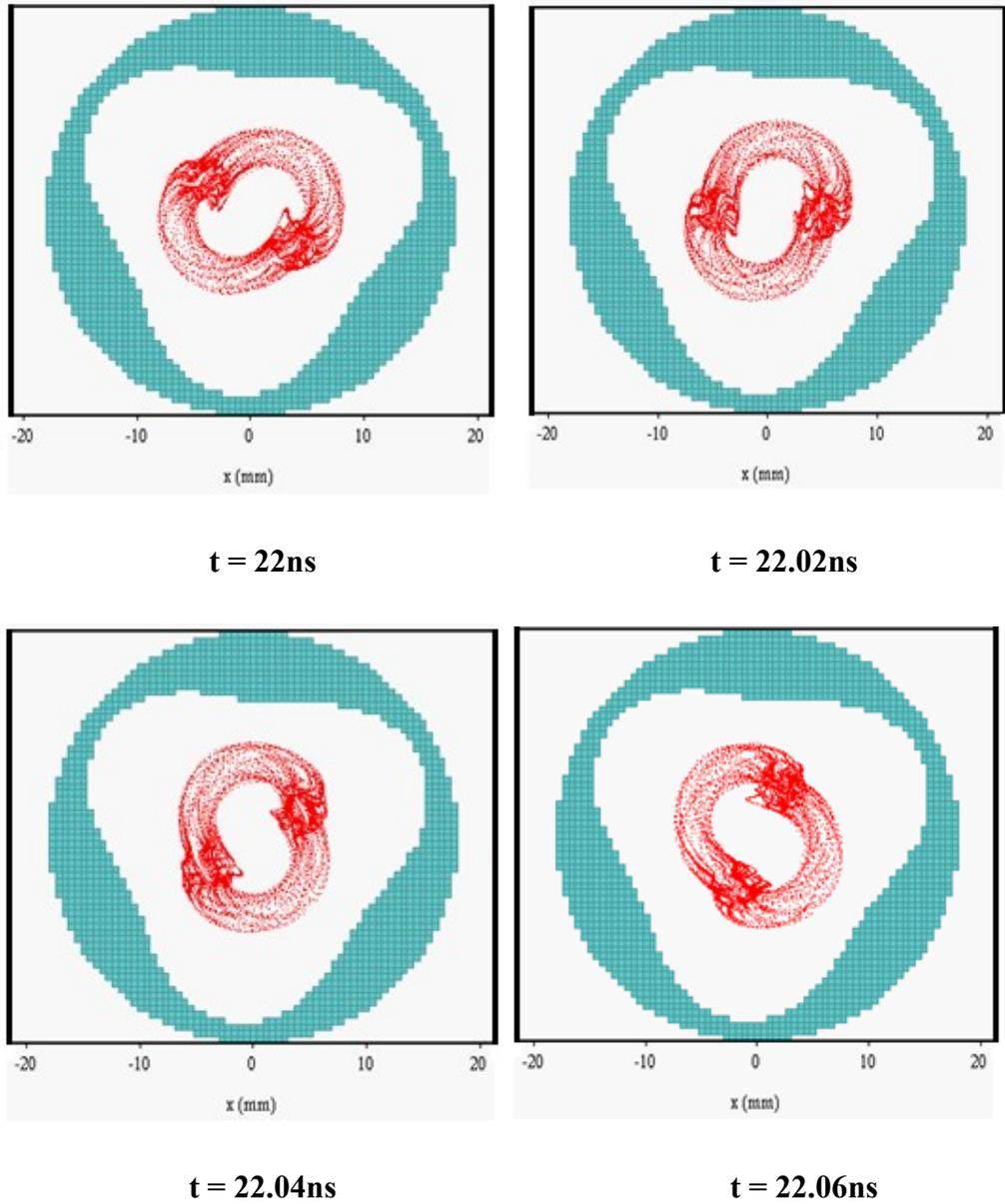
Figure 4.3.3.5: Transverse phase-space plots depicting the evolution of the electron beam as a function of time, taken from MAGIC-3D. The axial window these plots were recorded in corresponds to 1/10th of the axial periodicity of the helical waveguide i.e. 3.75mm with the start position of this window at 84cm i.e. close to the end of the uniform helical waveguide section.

It was observed that the electron beam rotated anti-clockwise, co-rotating with respect to the helical waveguide. This is defined by the orientation of the static magnetic field along the axis of the system. The electron beam is required to rotate in the same sense as both the helical waveguide and the TE_{21} mode, whilst the counter-rotating (with

respect to the helix) cylindrical TE_{11} mode couples to produce the operating eigenwave. This diagnostic suite was sufficient to determine whether the behaviour of each simulated amplifier was physical or non-physical and allowed the performance of each amplifier to be characterised.

4.3.4: The beam guiding centre

Simulations were initially undertaken with a coarser mesh than that used to obtain the primary results presented through the rest of the thesis, with mesh elements of 1mm in *dx*, *dy* and *dz* used. This mesh resolution was marginal in its ability to resolve the key dimensions however served to provide a rapid assessment of any limitation in the simulations that went beyond simple resolution effects, whilst allowing the diagnostic suite to be tested and enhanced rapidly. It was discovered initially that the simulations were delivering less than a tenth of the output power measured in the experiment for broadly similar control values, with extensive variation of these control parameters failing to resolve this issue. This problem was traced to the synthesised electron beam configuration. Initially the simulations utilised an electron beam with a 0mm guiding centre radius to deliver a 'perfect' axis encircling beam. By operating with a non-zero guiding centre radius (nominally a less ideally defined but much more realistic electron beam) and keeping all other parameters unchanged it was found that the output power dramatically increased, with this highlighted in *figure 4.3.4.1*. This change substantially increased the number of particles used in the simulation. It is possible that the 'perfect' electron beam may have presented an unfeasibly high plasma frequency resulting in non-physical effects in these first simulations.
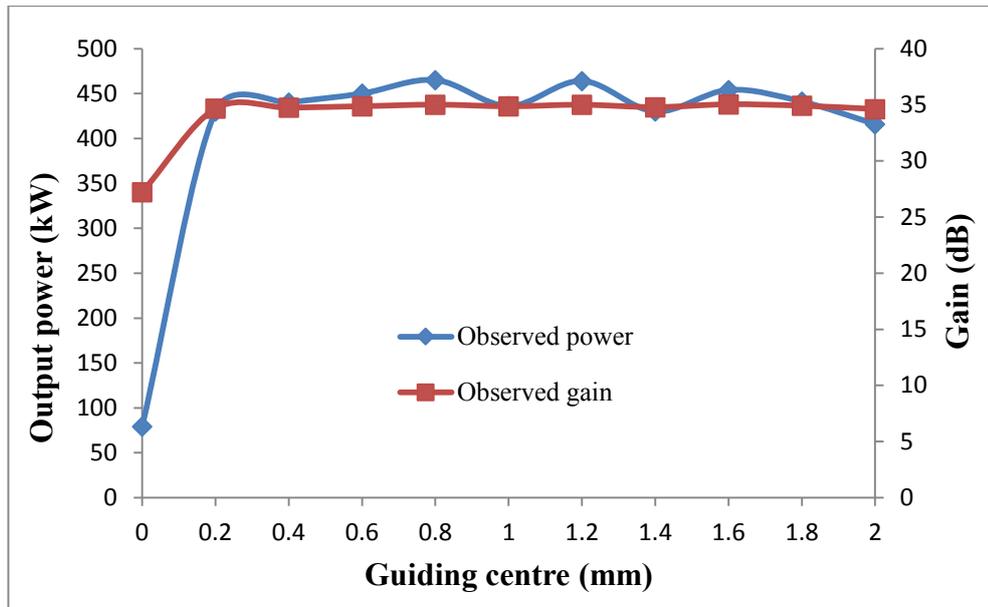
Figure 4.3.4.1: *Observed power and saturated gain as a function of beam guiding centre radii for the simulated X-band 2nd harmonic gyro-TWA, operating with a magnetic field strength of 0.21T and an α of 1.2 at 9.4GHz.*

The guiding centre radius was varied from 0mm to 2mm in 0.2mm increments with the confining magnetic field set at 0.21T. For direct comparison the drive power to the amplifier was kept constant at ~145W with the device operating at 9.4GHz, having a beam α of 1.2. It was clear that any value of guiding centre radius that was non-zero dramatically improved the observed power and gain performance of the amplifier when compared to the 0mm case, with all non-zero values delivering comparable performance. Although the output power was substantially increased by operating with non-zero guiding centre radii it was still down by over half on that demonstrated experimentally at the same frequency. The simulations suggested a high degree of insensitivity to the guiding centre radius providing it differed meaningfully from zero. Thus a guiding centre of 1.6mm was used which would yield a transverse beam thickness of 3.2mm, corresponding to ~10% of the waveguide diameter. This value appeared consistent with estimates from experimental imprints of the electron beam on phosphor scintillators.

4.3.5: Detailed iterative optimisation of the simulated gyro-TWA

The geometrical accuracy of the simulations for a parameter sweep of the key control variables was improved by increasing the mesh resolution from 1mm in *dx, dy,* and *dz* to 0.55mm, 0.55mm and 1.1mm respectively. This was undertaken to improve the simulation accuracy for the gyro-TWA and assisted to match the experimental measurements. Initially the previous simulation was replicated in all but resolution with a guiding centre radius of 1.6mm used together with a magnetic field strength of 0.21T and an α of 1.2. The output power achieved from this simulation was ~15.5kW for an input power of ~145W, substantially down on that observed from the equivalent simulation with the coarser mesh. It was found that the refined mesh generated a geometry which was a more accurate representation of the experimental set up but caused a slight shift in the beam-wave resonance. To overcome this, further parameter sweeps in α and the magnetic field strength were undertaken to achieve a suitable match of the electron beam and the electromagnetic wave dispersion. Simulations would be optimally tuned to match the experimental saturated output power at a spot frequency of 9.4GHz through an iterative 2D optimisation process of varying one parameter, either magnetic field strength or α, and subsequently the other. By initially keeping α constant at 1.2 and varying the magnetic field strength in small increments it was discovered that an output power of ~935kW, for an input power of ~120W, at ~0.2126T could be achieved, *figure 4.3.5.1.*
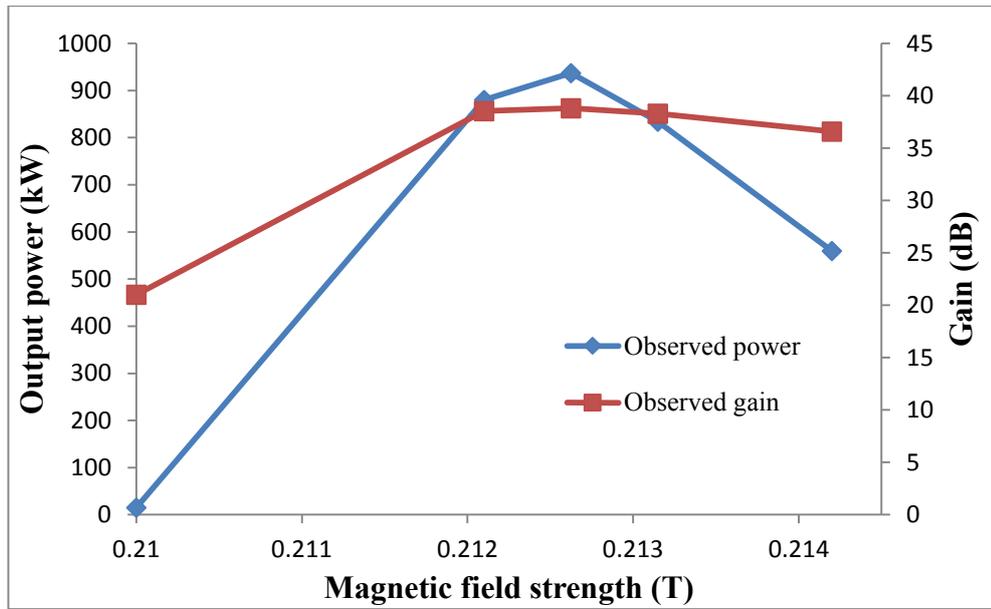
Figure 4.3.5.1: *Observed power and gain of the simulated gyro-TWA for varying magnetic field strengths, with an α of 1.2 at 9.4GHz.*

This observed power and corresponding saturated gain of ~38.8dB was a marked improvement on performance and more closely matched the results achieved experimentally. Although the maximum output power and gain were realised for a magnetic field strength of ~0.2126T, the saturated gain of the simulated amplifier remained fairly constant between ~0.212T and ~0.213T. Hence the laboratory experiment had a reasonably wide target range over which it could operate effectively. To optimise the simulations however, the magnetic field strength was kept constant at ~0.2126T with simulations rerun for varying values of α, *figure 4.3.5.2*.
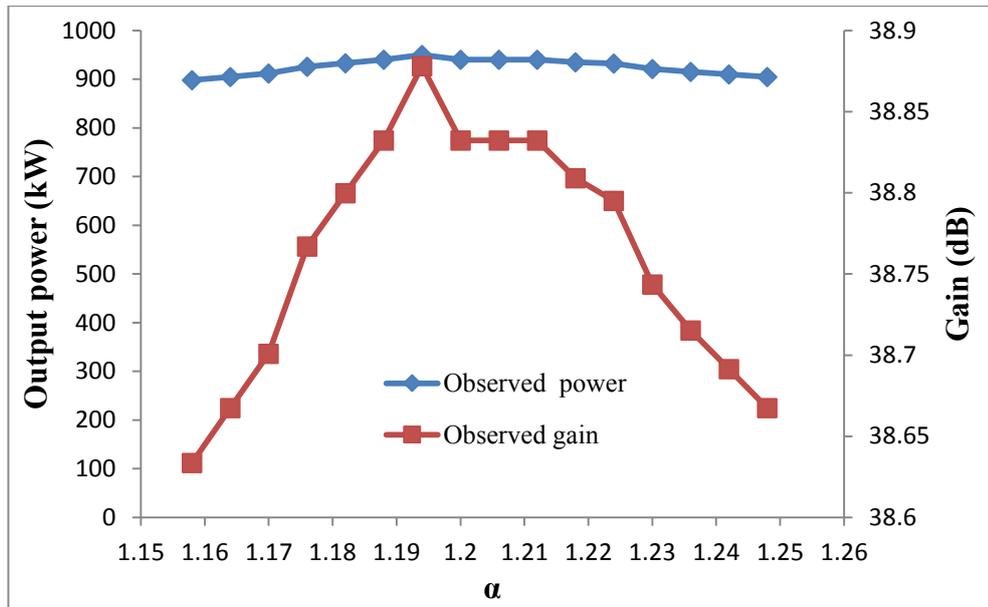
Figure 4.3.5.2: *Observed power and gain of the simulated gyro-TWA for varying α, with a magnetic field strength of ~0.2126T at 9.4GHz.*

The simulation data suggested that the output power and saturated gain of the amplifier did not significantly vary across the α range ~1.16 to ~1.25. However for an α of ~1.19 it was predicted that the amplifier could achieve an output power and gain of ~945kW ~38.9dB respectively, for an input power of ~120W. By operating with this *α* the simulations were again swept in magnetic field strength. At a magnetic field strength of ~0.2124T the same output power and gain were observed, leading to a further sweep in α at this new magnetic field strength, *figure 4.3.5.3.*
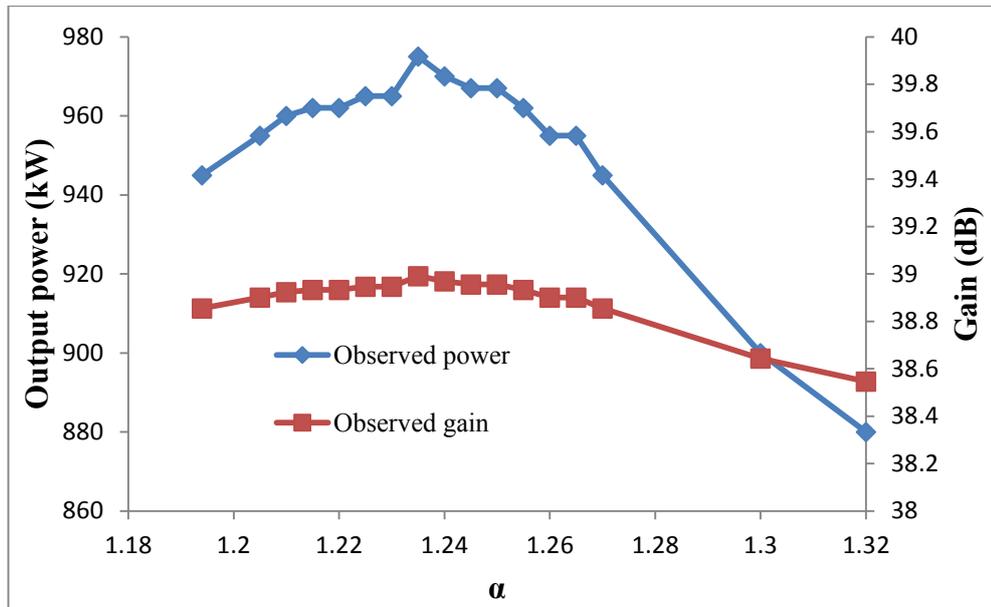
Figure 4.3.5.3: *Observed power and gain of the simulated gyro-TWA for varying α, with a magnetic field strength of ~0.2124T at 9.4GHz.*

These results suggested that an output power and gain of ~975kW and ~39dB respectively for an input power of ~120W could be achieved, operating with an α of ~1.24 and magnetic field strength of ~ 0.2124T. These results were in good agreement with the experimental data and suggested that provided the α range was between ~1.2 to ~1.27 inclusive the amplifier could expect to achieve an output power and gain closely matched to the optimal performance.   To verify whether the optimum performance configuration for the simulated gyro-TWA had been achieved, the magnetic field strength was once again incrementally varied for an α of ~1.24, *figure 4.3.5.4.*
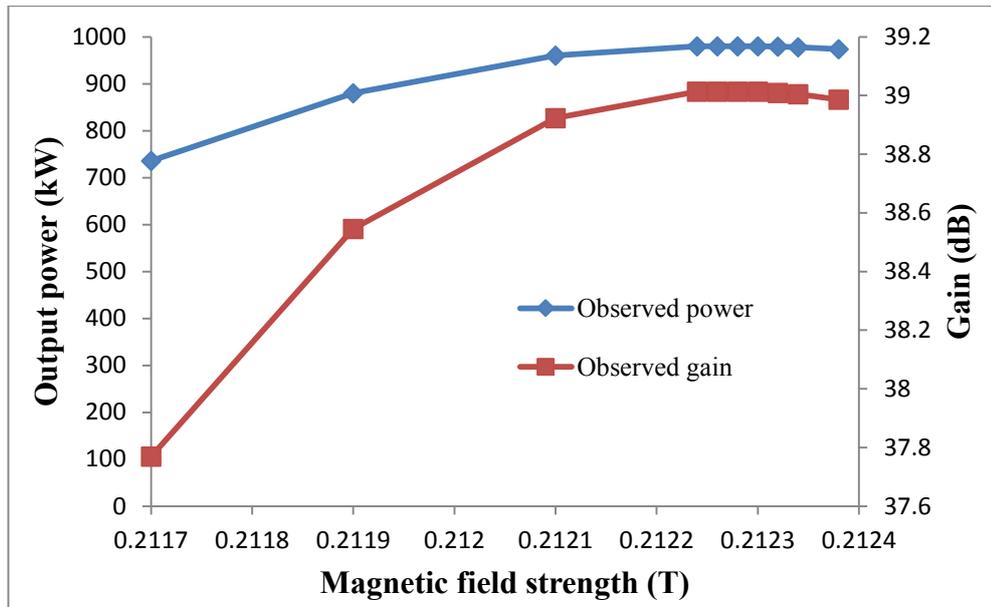
Figure 4.3.5.4: Observed power and gain of the simulated gyro-TWA for varying magnetic field strengths, with an α of ~1.24 at 9.4GHz.

For magnetic field strengths in the range ~0.2122T to ~0.2124T, an α of ~1.24 and an input power of ~120W, the output power and gain for the amplifier were consistently observed to be ~980kW and ~39dB respectively. By choosing a magnetic field strength of ~0.2123T and varying α it was found that for an α value of ~1.27 the output power of the amplifier could be increased to ~995kW (for an input power of ~120W) corresponding to a saturated gain of ~39.1dB, *figure 4.3.5.5*.
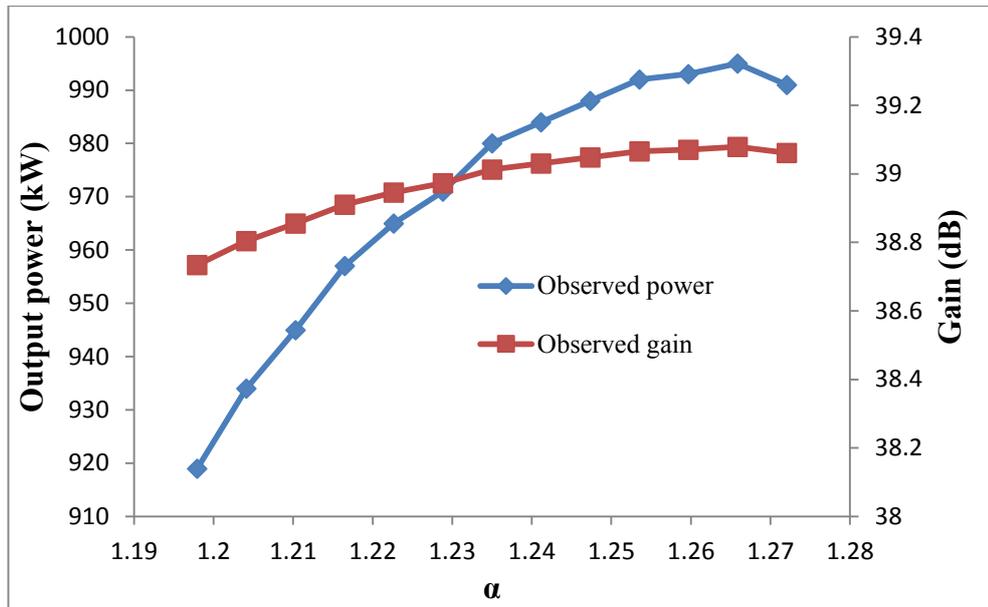
Figure 4.3.5.5: Observed power and gain of the simulated gyro-TWA for varying α, with a magnetic field strength of ~0.2123T at 9.4GHz.

This result agreed favourably with the experimental data and as a result the drive power to the amplifier was varied to establish the full performance of the device, *figure 4.3.5.6*.
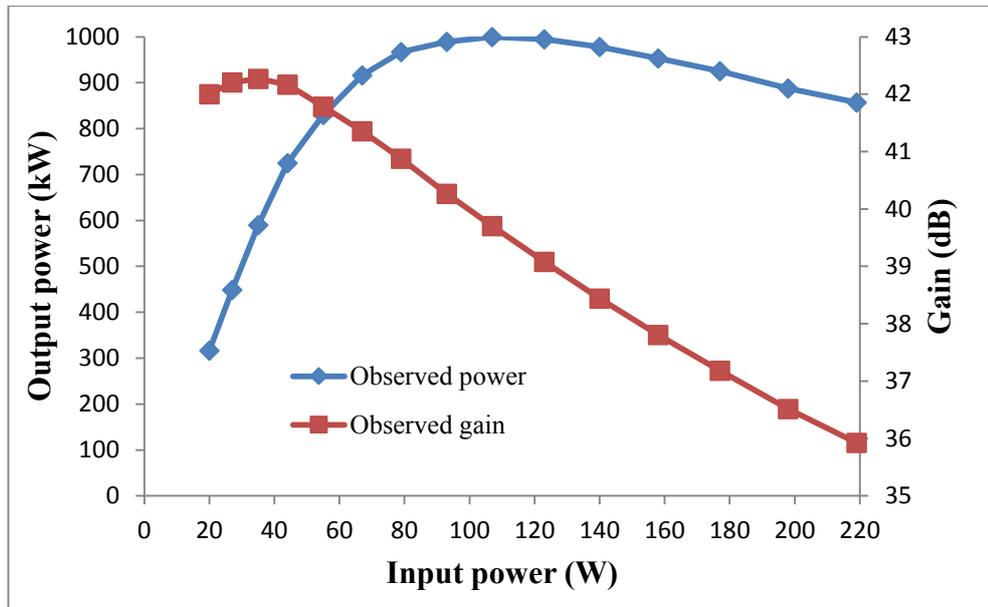
Figure 4.3.5.6: Transfer curve for the simulated gyro-TWA with a magnetic field strength ~0.2123T and an α of ~1.27 at 9.4GHz.

The transfer curve shows the rollover from the linear regime of operation of the gyro-TWA to the saturated regime. It was observed for an input power of ~105W that the amplifier could achieve an output power of ~1.0MW, corresponding to a saturated efficiency of ~27%. In the linear regime MAGIC-3D predicted a gain of up to ~42dB and in the saturated regime a gain of ~39.7dB. The simulations were able to predict saturated gain extremely well when compared to the experimental data however the predictions of linear gain were lower than that measured experimentally. However in the experiment the saturated gain was measured over the range 8.4GHz to 10.4GHz in 200MHz increments with the linear gain measured over the frequency range 8.4GHz to 10.2GHz in ~400MHz increments. This increase in sampling points for the saturated gain data, together with the greater confidence asserted by the experimental team in the measurements of the saturated gain over the linear gain, provides assurance that the saturated gain of the amplifier was a better benchmark for tuning the simulations. By keeping the input power approximately constant, between ~105W and ~110W, simulations to determine the performance of the amplifier, *figure 4.3.5.7* and *figure 4.3.5.8*, across the chosen bandwidth were undertaken.
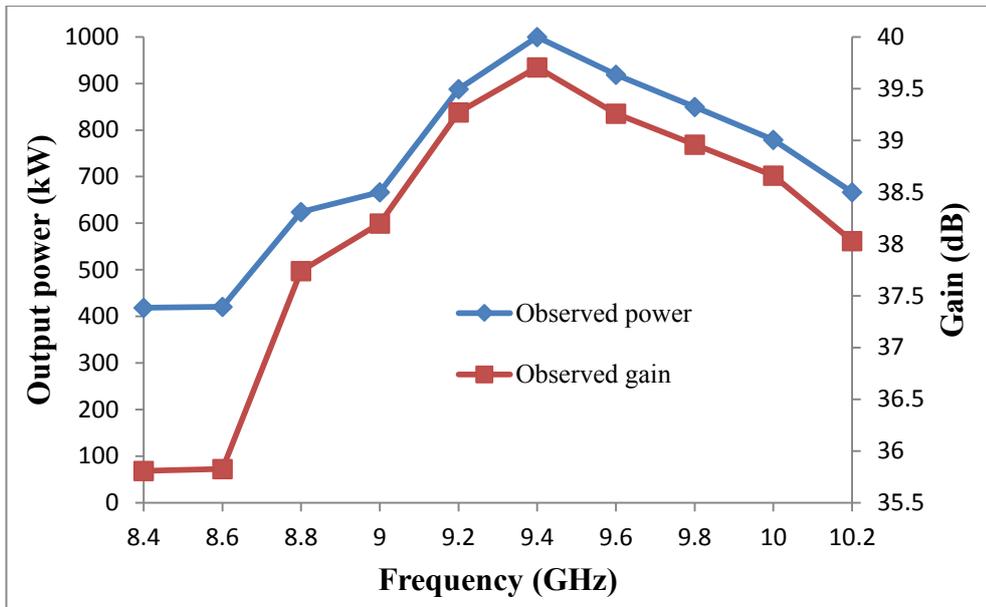
Figure 4.3.5.7: Observed power and gain of the gyro-TWA as a function of frequency for input powers of ~105W to ~110W with a magnetic field strength of ~0.2123T and an α ~1.27.
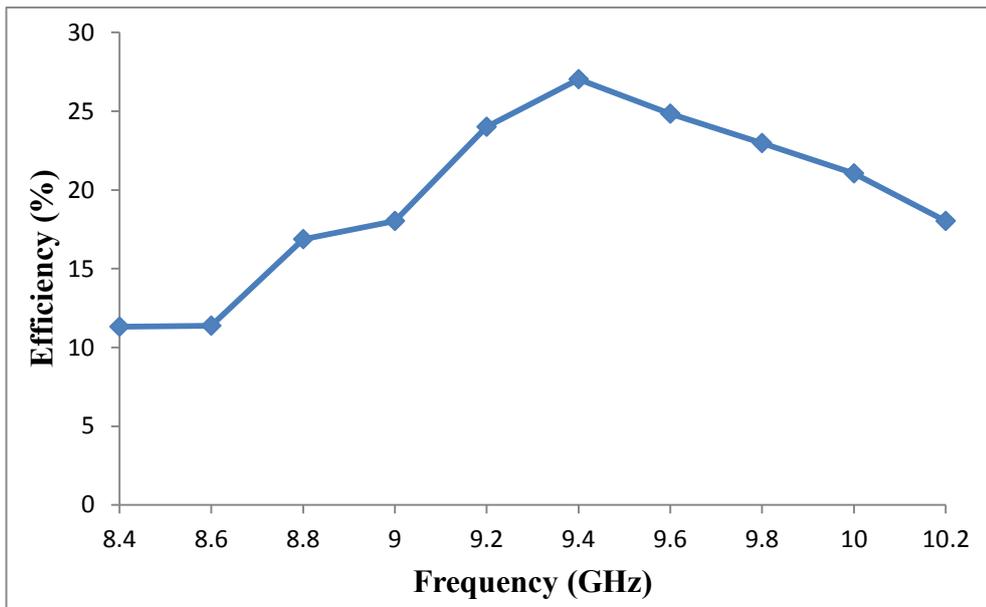
Figure 4.3.5.8: Predicted efficiency of the gyro-TWA as a function of frequency for input powers of ~105W to ~110W with a magnetic field strength and an α of ~0.2123T and ~1.27 respectively.

From the simulations investigating the spectral response of the amplifier, it was evident that the performance was better at the upper frequency range than at the lower frequency range. Between 9.2GHz and 10.0GHz inclusive the amplifier realised an

efficiency of >20%. The efficiency at 8.4GHz and 8.6GHz fell to ~11% but at 10.2GHz the drop off was less dramatic, measuring ~18%. Contour diagnostics at the upper frequency limit of 10.4GHz suggested that the amplifier was radiating in the TE_{21} mode instead of the desired TE_{11} mode. However the cut-off frequency for the TE_{21} mode in the output waveguide was calculated to be ~10.3GHz and so the amplifier would be susceptible to launching partly in this mode. For this reason the results at 10.4GHz have not been included in the previous graphs. These simulations would however suggest that the drop to -3dB in power performance observed in the experiment at 10.4GHz may have reflected a change in the output mode rather than a limit in the amplifier's gain bandwidth.

The performance of the gyro-TWA was also analysed as a function of input power across the simulation frequency bandwidth i.e. 8.4GHz to 10.2GHz, *figure 4.3.5.9* and *figure 4.3.5.10*. These figures show the maximum output power predicted by the simulations at any given frequency as the drive signal was adjusted to ensure the amplifier was just in saturation.
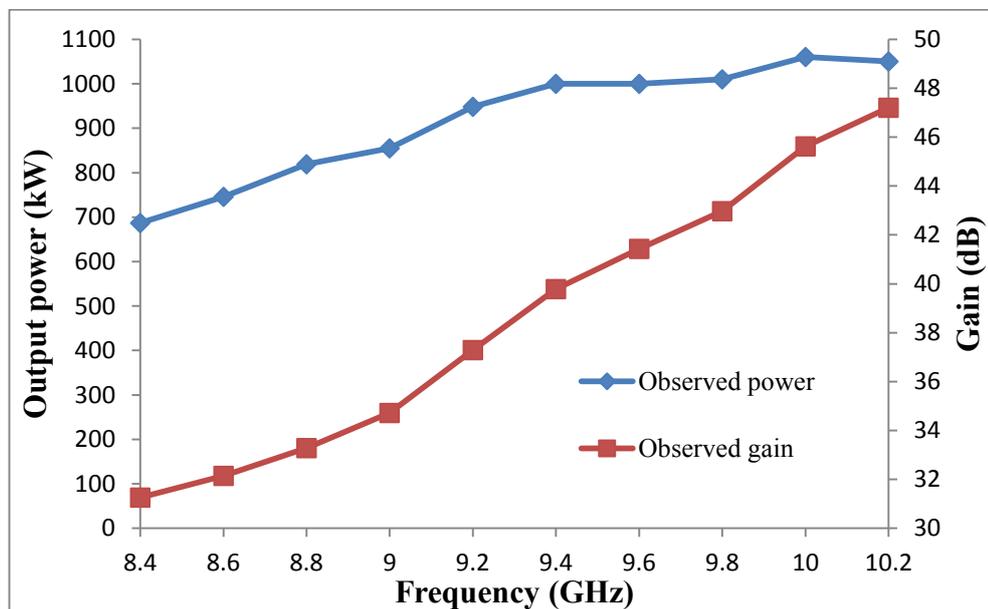
Figure 4.3.5.9: Maximum observed power and saturated gain of the simulated gyro-TWA as a function of frequency, with varying drive power at each frequency.
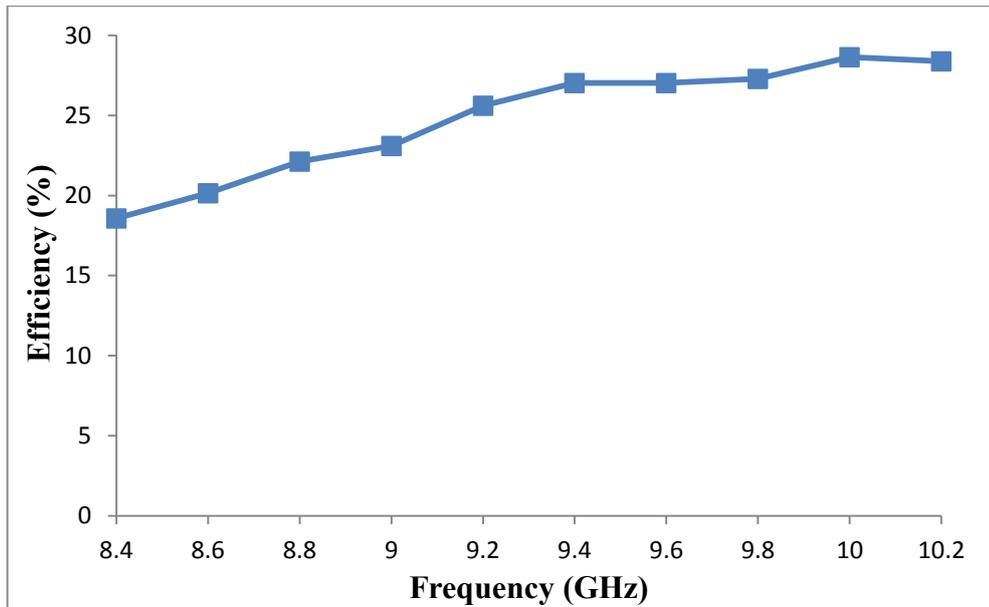
Figure 4.3.5.10: Predicted saturated efficiency of the simulated gyro-TWA as a function of frequency, with varying drive power at each frequency.

The results suggested that the amplifier had higher performance towards the upper end of the chosen (single mode TE_{11} output) frequency bandwidth, realising an observed output power and saturated gain of ~1.06MW and ~45.6dB for an input power of ~30W at 10.0GHz. This was an increase in observed output power of ~60kW and saturated gain of ~5.9dB when compared to the 9.4GHz simulation. The saturated gain performance of the amplifier increased with increasing frequency with the simulations predicting gains of ~31.3dB at 8.4GHz and ~47.2dB at 10.2GHz, as the drive power required to realise optimum observed output power at each frequency significantly decreased with increasing frequency. The predicted saturated efficiency of the amplifier at 9.4GHz was ~27%, with this increasing to ~28.6% at 10.0GHz. These results would imply that the amplifier was being severely under driven at the lower frequency edge of its bandwidth and severely overdriven at the upper edge in the previous simulated spectral response, *figure 4.3.5.7*. The results would also suggest that the experimental amplifier had in fact been overdriven at the upper end of its frequency spectrum and that greater output powers and bandwidth may in fact be possible from the instability than had hitherto been experimentally demonstrated. Furthermore from these results it would be expected that future parameter profiled

simulations of the gyro-TWA (for the purpose of performance enhancement, *chapter 5*) would have greater performance capabilities at frequencies exceeding the original bandwidth of the experiment.

4.3.6: Theoretical optimum performance of the simulated gyro-TWA instability

The average kinetic energy of the electrons which comprised the electron beam were monitored as a function of axial position to establish the maximum possible efficiency of the simulated gyro-TWA, *figure 4.3.6.1*, at a frequency of 9.4GHz (i.e. the efficiency which could have been achieved if the length of the amplifier had been optimised for a given operating condition). For this comparison the magnetic field strength and α were kept at ~0.2123T and ~1.27 respectively to correspond to the initial conditions that had predicted the output power and saturated efficiency which most closely matched the experimental measurements at 9.4GHz, *figure 4.3.5.6.*
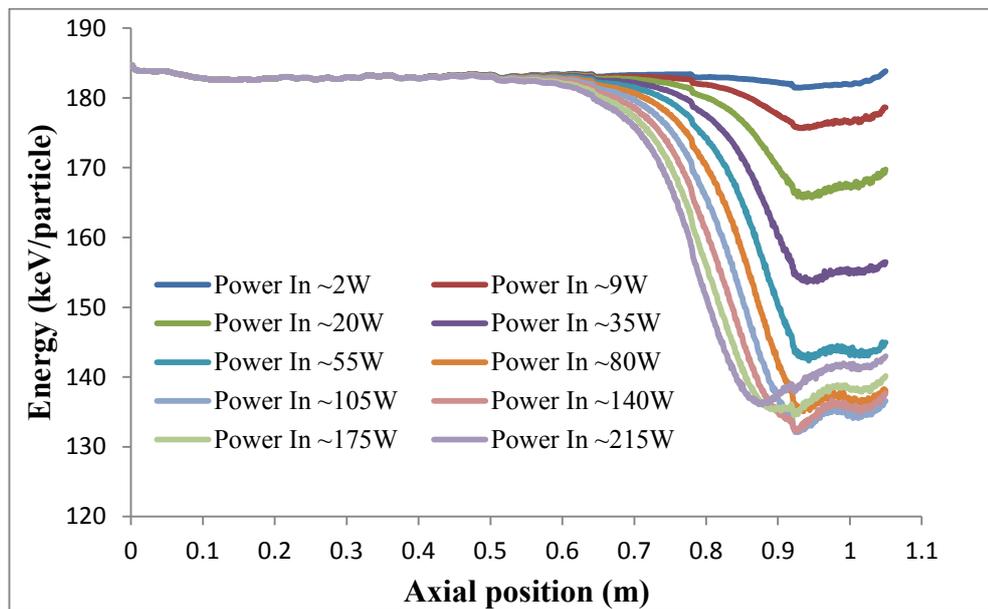
Figure 4.3.6.1: Predicted average kinetic energy of the beam electrons in the simulated gyro-TWA as a function of axial position and drive power, taken at 9.4GHz.

The plots of average kinetic energy as a function of axial position would suggest, for input powers of greater than ~105W, that this amplifier was being overdriven. However, if at the axial position where the average kinetic energy minima occurred for each input power, the magnetic field no longer constrained the electrons then the maximum output power and gain of the simulated gyro-TWA could be determined, *figure 4.3.6.2*. To distinguish between the performance values determined from the Poynting flux diagnostic in the output cylindrical waveguide of the amplifier (which have been used up to this point) to those calculated from the plots of average kinetic energy as a function of axial position, the terminology observed efficiency/power and gain and particle efficiency/equivalent power and equivalent gain respectively have been adopted.
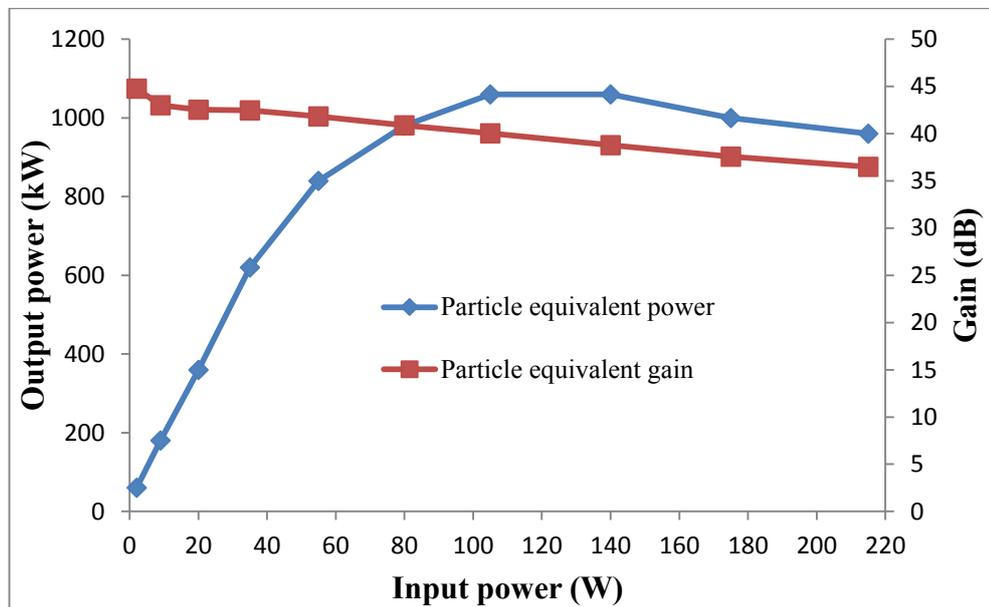
Figure 4.3.6.2: Particle equivalent power and gain of the simulated gyro-TWA as a function of input power at 9.4GHz.

These results show that in theory the gyro-TWA could hope to achieve a particle equivalent power of up to ~1.06MW for input powers between ~105W and ~140W at 9.4GHz. For a drive power of ~105W this would correspond to a saturated efficiency of ~28.6% which is comparable to the ~29% experimentally achieved, suggesting that the experiment had been optimally configured. Moreover using this analysis the linear

gain of the amplifier was predicted to be up to ~45dB which more closely matched the ~47dB estimated experimentally.

To demonstrate the increase in output power using the above analysis the optimised 9.4GHz simulation was modified to cause the electron beam to become unconstrained at an axial position close to the minimum average kinetic energy value, *figure 4.3.6.1*. This was realised by reducing the span of the axial magnetic field from ~1.00m to ~0.91m (this optimisation step was also performed in the experiment with the electrons deflected onto the side wall at an arbitrary axial location, chosen to maximise performance, by a large transverse magnetic field). The raw data extracted from MAGIC-3D, *figure 4.3.3.1* and *figure 4.3.6.3*, show the original observed power of ~1.0MW and a revised particle equivalent power showing a slight increase to ~1.03MW, for an input power of ~105W.
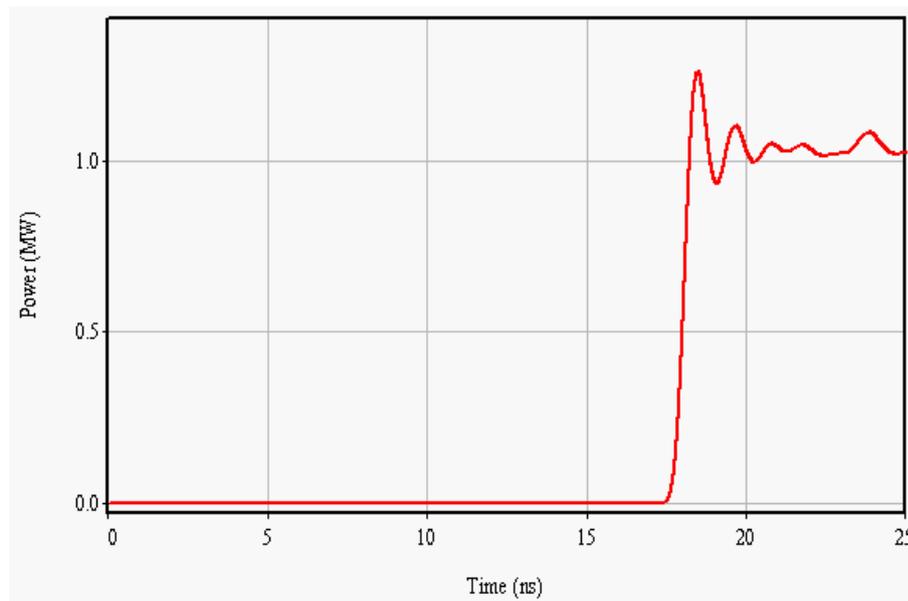
Figure 4.3.6.3: Revised output power (particle equivalent power) for an input power of ~105W at 9.4GHz, taken from MAGIC-3D with the magnetic field spanning the axial range 0m to ~0.91m.

4.3.7: Interaction length

The experimental X-band 2nd harmonic gyro-TWA had a helical waveguide of length 60cm and therefore the simulated gyro-TWA was optimised for this interaction length. However the performance of the simulated gyro-TWA in terms of both output power and gain were monitored for varying interaction lengths, *figure 4.3.7.1,* with both the drive power to the amplifier and frequency of operation kept constant at ~105W and 9.4GHz respectively. Here, *figure 4.3.7.1,* as with previous simulations, both observed power and gain were calculated from the output power predicted to be radiated from the given length of interaction space, with the particle equivalent power and gain computed from the minimum averaged kinetic energy of the electrons attained in the helix.
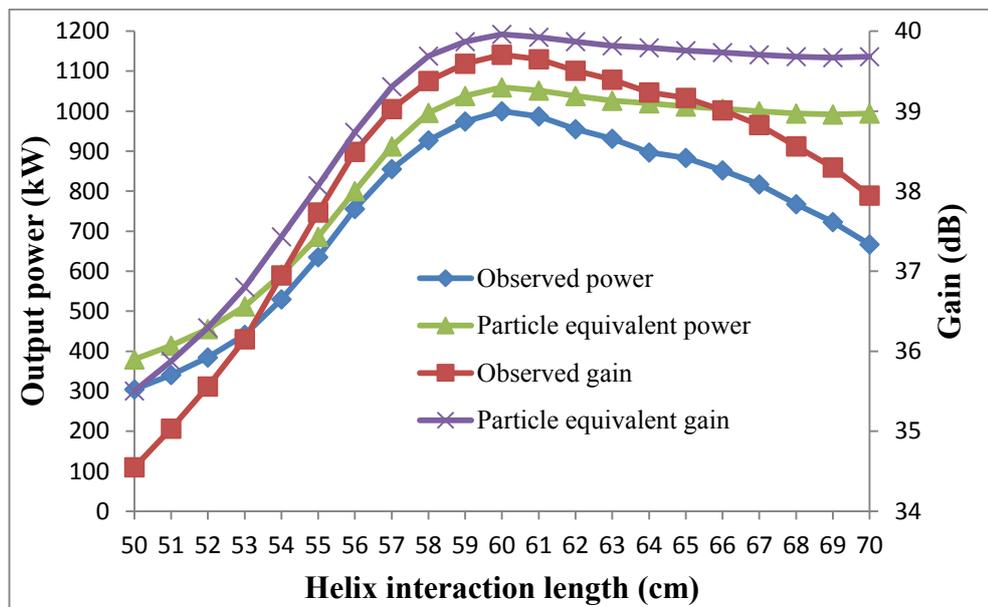
Figure 4.3.7.1:   Observed power/gain and particle equivalent power/gain of the simulated gyro-TWA as a function of interaction length, at 9.4GHz for an input drive power of ~105W.

The interaction length was increased in increments of 1cm from 50cm to 70cm. It was observed that the output power and gain dropped off rapidly with a reduction in the length of the interaction region since the amplifier was no longer in saturation for these

lengths at this drive power. Extending the length of the interaction waveguide beyond 60cm resulted in a more gradual decrease in the output power and gain, with phase trapping causing the electrons to re-absorb some of the emitted signal, since in this condition the amplifier was being overdriven, *figure 4.3.7.2*.
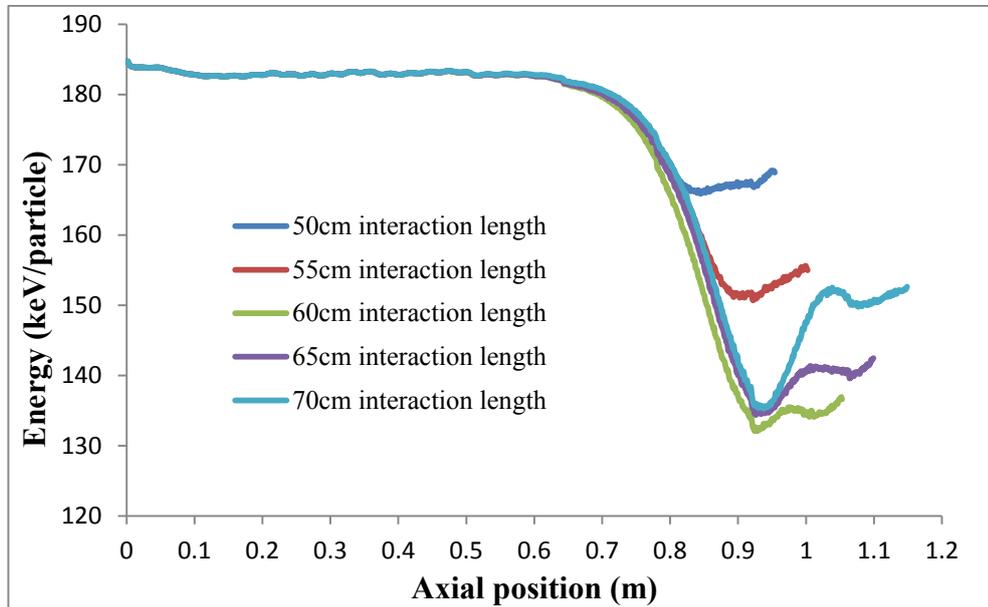
Figure 4.3.7.2: Predicted average kinetic energy of the beam electrons as a function of axial position taken at 9.4GHz, for varying lengths of helical interaction waveguide.

Owing to the simulation geometry (as detailed in *section 4.3.1*) the uniform helical interaction waveguide start position corresponded to an axial position of 0.26m. It is clear from the plots of average kinetic energy as a function of axial position, *figure 4.3.7.2*, that optimum performance for this given level of drive power was achieved when the helical interaction length was set to 60cm, consistent with the optimisation of the beam parameters for this length of interaction space. For interaction lengths shorter than 60cm the average kinetic energy minimum of the electrons was observed to be substantially higher than that predicted for the 60cm interaction length, corresponding to the sharp drop off in the output power and gain, *figure 4.3.7.1*. For interaction lengths greater than 60cm it was observed that the minimum kinetic energy of the beam electrons was slightly higher than that predicted for the 60cm case and thus the drop off in output power and gain above this length was less aggressive than

that of the shorter interaction lengths. However regardless of the interaction length of the amplifier the plots of average kinetic energy as a function of axial position show a progressive drop in average kinetic energy of the electrons starting consistently at an axial position of ~0.78m, as the average electron energy starts to be meaningfully perturbed by the RF interaction. In all instances the average kinetic energy of the electrons eventually reached a minimum before the beam electrons and the electromagnetic wave started to drift out of synchronism (evident by the increase in average kinetic energy of the electrons). By attempting to delay the onset of this condition one may maximise the efficiency of the amplifier.

4.3.8: Axial periodicity of the helical waveguide

The performance of the gyro-TWA was sensitive to variations in both magnetic field strength and α. This was evident in the MAGIC-3D simulations whereby incremental adjustments to both these parameters, from initial best estimates taken from [Bratman, 2000] to highly optimised simulations, resulted in an overall improvement in observed power from ~15.5kW to ~1.0MW. However the gyro-TWA was also sensitive to the geometry of its interaction waveguide. To demonstrate this, the axial periodicity of the helical corrugation was increased from 37.5mm to 39mm, with this value primarily chosen as it matched that of a previous X-band 2nd harmonic gyro-TWA experiment at the University of Strathclyde detailed in [Cross, 2007]. This gyro-TWA, with a 3-fold helically corrugated waveguide, had an otherwise similar interaction region to that of the experimental gyro-TWA detailed in [Bratman, 2000]. In this experiment a Pierce-type electron gun generated a 185kV, 6A rectilinear beam with a kicker imparting transverse velocity to generate an axis encircling beam with an α of ~1.2. This gyro-TWA, at a frequency of 9.6GHz, realised an output power of ~220kW corresponding to a saturated gain of ~24dB. The device had an efficiency of ~20% with measured saturated bandwidth of 2.0GHz from 8.4GHz to 10.4GHz.

Inevitably a change to the axial periodicity of the helical waveguide alters the dispersion characteristics of the amplifier with small adjustments in magnetic field strength and α necessary to offset the increased periodicity to attain desired coupling. The same optimisation technique was used for the 39mm axial periodicity simulations as that of the 37.5mm simulations with the simulations optimised at a frequency of 9.4GHz. This optimisation process was continued until it was established with reasonable confidence that the amplifier had achieved optimum observed output power and gain. To illustrate the impact of the axial periodicity of the helical corrugation and its impact on the electron beam cyclotron frequency and most importantly pitch angle, these simulations had a beam current of 20A as used in both the experiment detailed in [Bratman, 2000] and the previously detailed gyro-TWA simulations. It was found that for a helical corrugation with axial periodicity of 39mm that optimum performance occurred when the magnetic field strength was ~0.2112T with an α of ~1.09. This is consistent with the decrease in pitch angle one would expect in order to be able to match to the slightly steeper dispersion curve that would be produced by the smaller axial Bragg wavevector for this configuration. For this parameter set, input power was varied and observed output power and gain predicted, *figure 4.3.8.1*.
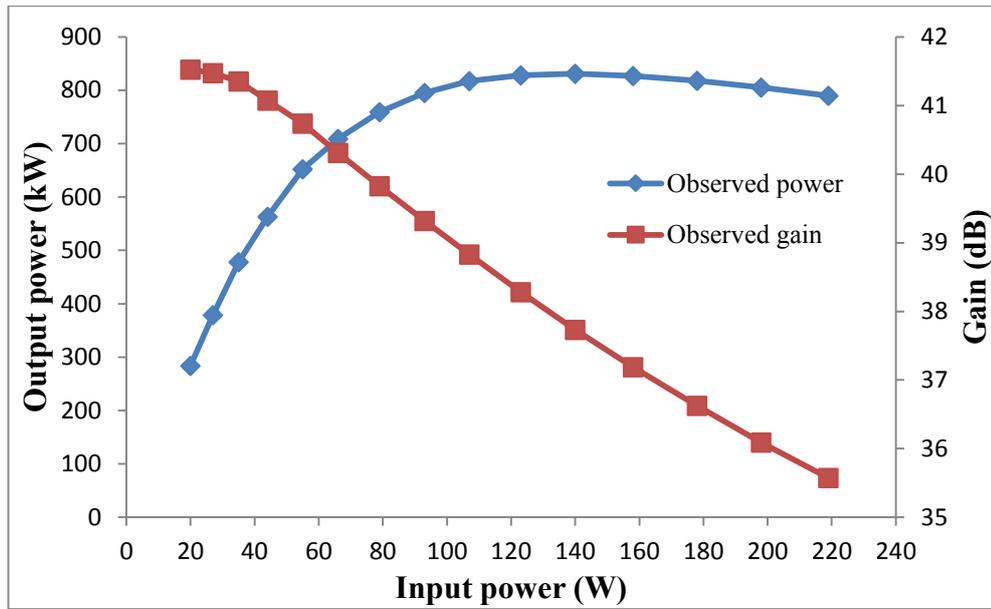
Figure 4.3.8.1: Observed power and gain as a function of input power for the simulated gyro-TWA with a helical interaction waveguide of axial period 39mm, with a magnetic field strength of ~0.2112T and an α ~1.09 at 9.4GHz.

The results suggested that for an input power of ~140W the amplifier could achieve an observed power of ~830kW and corresponding gain of ~37.7dB. This corresponded to a decrease in observed power, saturated gain and saturated efficiency of ~170kW, ~2dB and ~4.5% respectively when compared to the fully optimised 37.5mm axial periodicity gyro-TWA at the same frequency. This is consistent with the lower α and hence reduced rotational energy in the electron beam.

It has been demonstrated that an increase in the axial periodicity of the helical structure resulted in a decrease in the output power, gain and efficiency of the amplifier when compared to the optimised gyro-TWA simulations which had an axial periodicity of 37.5mm. In the following simulations the periodicity of the helix was set to 36mm with magnetic field strength and α adjusted to offset the decrease in periodicity to attain the desired coupling. Once again the simulations were optimised by alternating between sweeps in magnetic field strength and α. As with previous simulations the electron beam current would be set to 20A. The incremental sweeps in both magnetic

field strength and α suggested that the amplifier realised optimum performance with a magnetic field strength of ~0.2149T and an α ~1.27 (a very slight increase over that used in the 37.5mm period calculations) at a frequency of 9.4GHz. The transfer curve for this amplifier is plotted in *figure 4.3.8.2* and shows how the observed output power and gain of the device varied with input power for this parameter set.
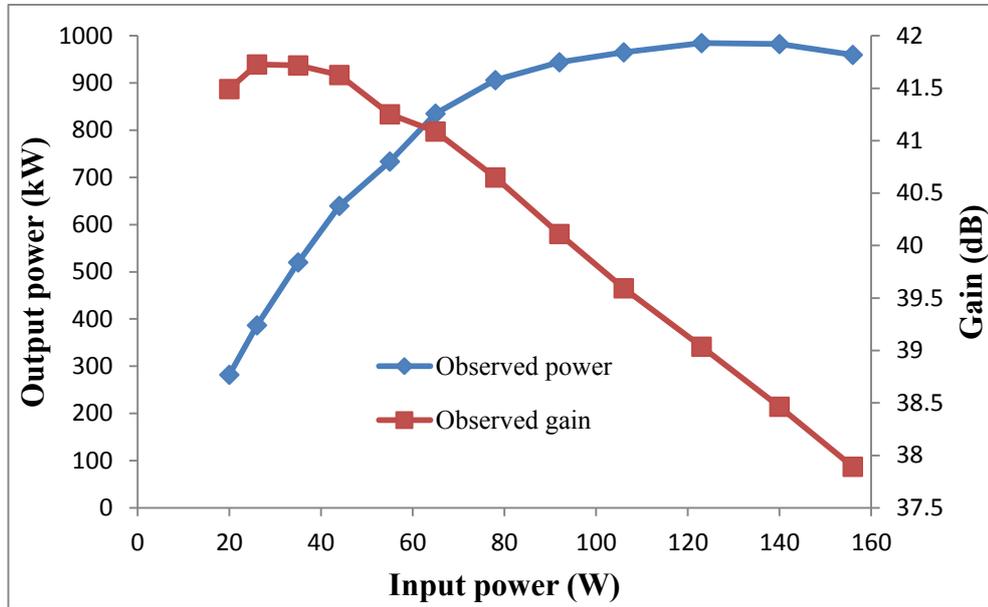
Figure 4.3.8.2: *Observed power and gain as a function of input power for the simulated gyro-TWA with a helical interaction waveguide of axial period 36mm, with a magnetic field strength of ~0.2149T and an α ~1.27 at 9.4GHz.*

The results suggested that for an input power of ~120W the amplifier could achieve an observed output power of ~985kW and corresponding gain of ~39.1dB. Overall it was observed that a decrease in the axial periodicity of the helical waveguide from 37.5mm to 36mm and subsequent increase of both magnetic field strength and α to accommodate this change resulted in a marginal reduction in the performance of the gyro-TWA in terms of both output power and gain. At 9.4GHz, this corresponded to a decrease in observed output power, saturated gain and saturated efficiency of ~15kW, ~0.7dB and ~0.5% respectively when compared to the optimised gyro-TWA with an axial periodicity of 37.5mm, operating at the same frequency. This sensitivity analysis further highlighted that investigations to evaluate the possible performance

enhancements of exploiting a tapered microwave circuit in the gyro-TWA should utilise a helical waveguide with an axial periodicity of 37.5mm.

4.4: Dispersion calculations of the gyro-TWA

As the complex corrugated waveguide is strongly non-conformal on any simple mesh, it was prudent to confirm that the dispersive characteristics of the gyro-TWA's helically corrugated interaction waveguide simulated in MAGIC-3D, were accurate. This was undertaken by determining the Faraday rotation angle (*chapter 3)* of a linearly polarised wave as it propagated through the device. To calculate the dispersive characteristics of the operating eigenwave two separate sections of helically corrugated waveguide were simulated in MAGIC-3D. The first section of helical waveguide was 7.5cm long, corresponding to two full periods of the helical structure. This section of helical waveguide was positioned between two 12cm long cylindrical to helical converters which also feature in the full gyro-TWA simulations. Two small sections of cylindrical waveguide at the input and output of the structure completed the geometry. Unlike the full gyro-TWA simulations which utilised only one waveguide port, the dispersion simulations had two waveguide ports. The first of these on the LHS of *figure 4.4.1* was the output port whilst the RHS port, *figure 4.4.1,* acted as the input port through which a linearly polarised cylindrical TE_{11} wave was launched. This wave was polarised in the *x* direction. As with the full gyro-TWA simulations, a dielectric absorber was positioned in the output cylindrical waveguide to minimise reflections on the output port. In all dispersion simulations the mesh resolution was retained from the full gyro-TWA simulations with *dx*, *dy* and *dz* mesh values of 0.55mm, 0.55mm and 1.1mm respectively used.
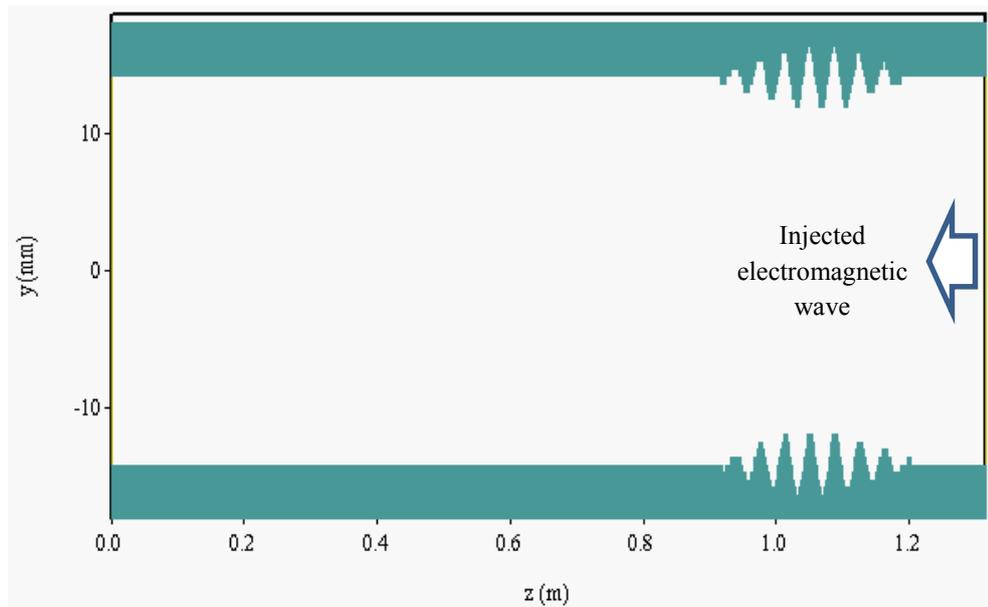
Figure 4.4.1: Simulation geometry including a 7.5cm long helically corrugated waveguide section used to calculate the dispersion of the helix.

At a position between the output of the helical to cylindrical converter and the edge of the dielectric absorber the magnitude of the electric field components E_x and E_y were determined, to ascertain the degree of rotation the wave had been subjected to as it propagated through the dispersive medium. These calculations were then repeated for a chosen frequency range of interest of 8.0GHz to 10.9GHz in 100MHz increments. From the equation of Faraday rotation, *equation 3.6.4*, the angle of rotation the wave was subjected to as it propagated through the helically corrugated waveguide was determined. For the dispersion calculations it was assumed that the two 12cm long helical to cylindrical converters equated to two 6cm long sections of actual helix and thus the total length of helix simulated was assumed to be 19.5cm. In essence this assumed that the discrepancy between the dispersion for the uncoupled and coupled modes was linearly proportional to the corrugation amplitude. To eliminate the uncertainty in the integer number of half turns the wave polarisation had rotated, the dispersion results from MAGIC-3D were plotted against the dispersion calculated from perturbation theory, *figure 4.4.2,* with a correction factor included for the MAGIC-3D dispersion allowing for the number of half rotations the wave would have made. This correction factor appears in the rotation angle as an integer multiple of π.
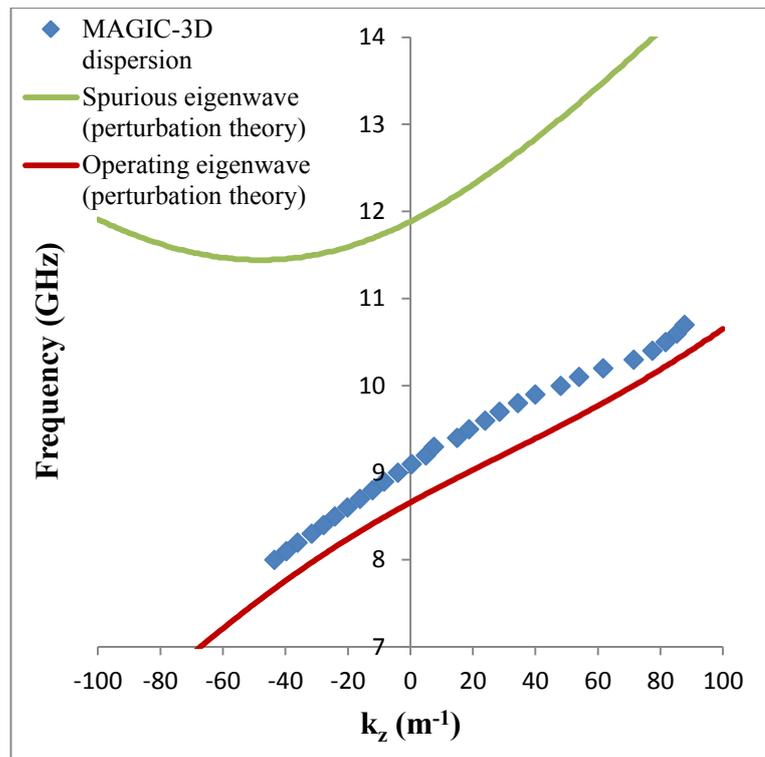
Figure 4.4.2: MAGIC-3D dispersion calculation for a 7.5cm section of helix plotted alongside the dispersion calculated from perturbation theory (cubic approximation).

In the helical to cylindrical converters k_z varies and thus to determine this value without ambiguity a second set of calculations were required which would repeat the previous dispersion calculations in all but helix length, allowing the dispersion of the helix minus contributions from the helical to cylindrical converters to be determined. Thus the simulation was slightly modified to include a section of helix 30cm in length, *figure 4.4.3,* increasing the original dispersion calculation from two full periods of the helix to eight.
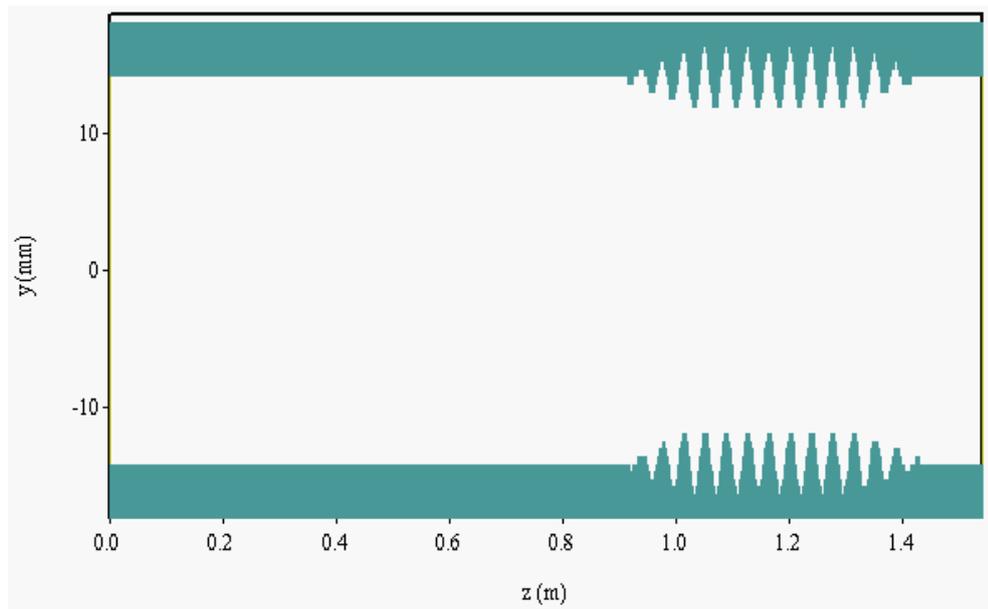
Figure 4.4.3: Simulation geometry including a 30cm long helically corrugated waveguide section used to calculate the dispersion of the helix.

Once again it was assumed that the two cylindrical to helical converters were each equivalent in length to 6cm of helical waveguide, with the total length of the simulated helix in this instance, including tapers, assumed to be 42cm. As with the previous dispersion calculation the results were plotted alongside those attained from perturbation theory, *figure 4.4.4.*
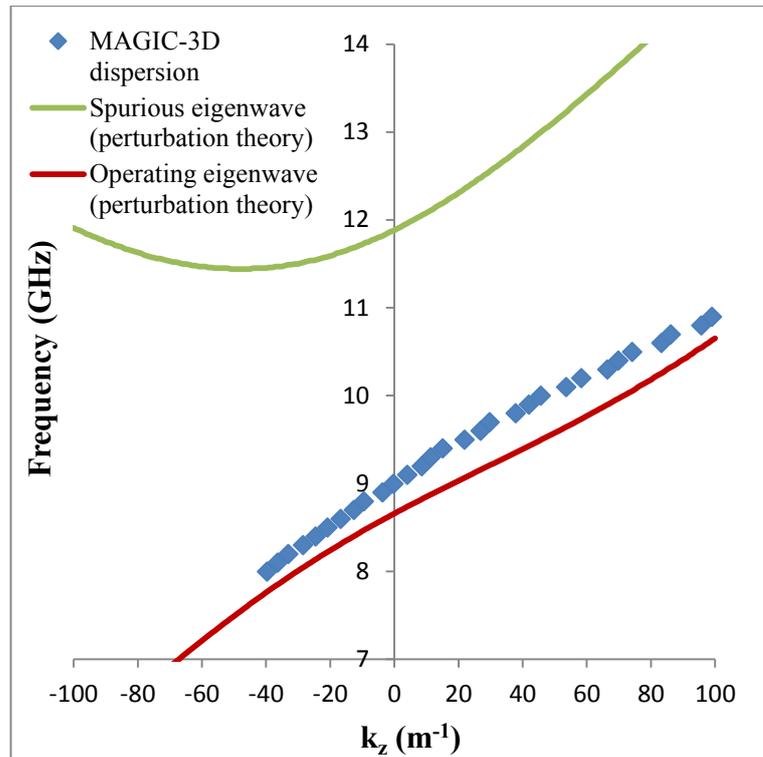
Figure 4.4.4: MAGIC-3D dispersion calculation for a 30cm long section of helix plotted alongside the dispersion calculated from perturbation theory (cubic approximation).

Both MAGIC-3D dispersion calculations, *figure 4.4.2* and *figure 4.4.4,* showed good agreement with each other and in each instance suggested that perturbation theory had slightly underestimated the frequency of the operating eigenwave. However to eliminate any contribution from the cylindrical to helical converters the phase shift in the first MAGIC-3D dispersion calculation, *figure 4.4.2,* was subtracted from the second, *figure 4.4.4.* By taking the length of the helical section to be 22.5cm i.e. 30cm-7.5cm and the difference between the degree of rotation for the simulation at 30cm and 7.5cm at each frequency of interest, the values of k_z were determined, *figure 4.4.5*.
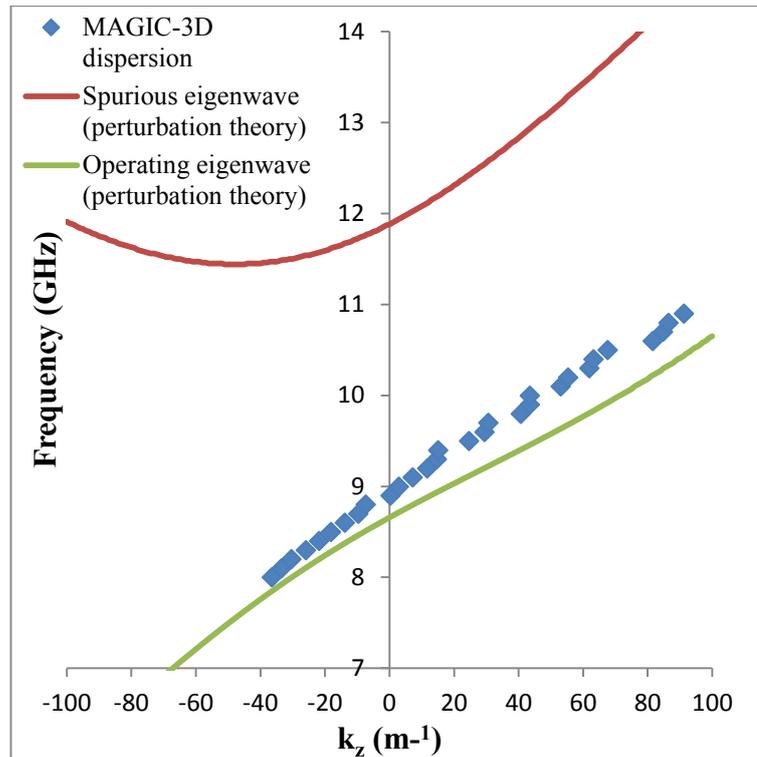
Figure 4.4.5: MAGIC-3D dispersion calculation of the helical waveguide minus contributions from the cylindrical to helical converters.

This dispersion calculation eliminates any systematic uncertainty arising from the helical to cylindrical converters by means of the subtraction and suggests that the original assumption of the converter length being comparable to half the length of a helical waveguide section was valid, since the three MAGIC-3D dispersion calculations, *figure 4.4.2, figure 4.4.4* and *figure 4.4.5* are highly consistent with each other. The subtracted dispersion calculation however, *figure 4.4.5,* is at the price of increased random uncertainty. Once again the subtracted MAGIC-3D dispersion calculation suggested that perturbation theory had slightly underestimated the frequency for the dispersion characteristics of the operating eigenwave in the 3-fold helically corrugated waveguide.

To substantiate the dispersion calculations from MAGIC-3D a separate modelling package, in this instance CST Microwave studio, was also used to calculate the

dispersive characteristics of the helically corrugated waveguide. In this simulation, a section of helix one period in length i.e. 37.5mm was simulated with periodic boundaries at the input, z_{min}, and output, z_{max}, of the structure, *figure 4.4.6*. The frequency bandwidth was set from 8.0GHz to 12.0GHz.
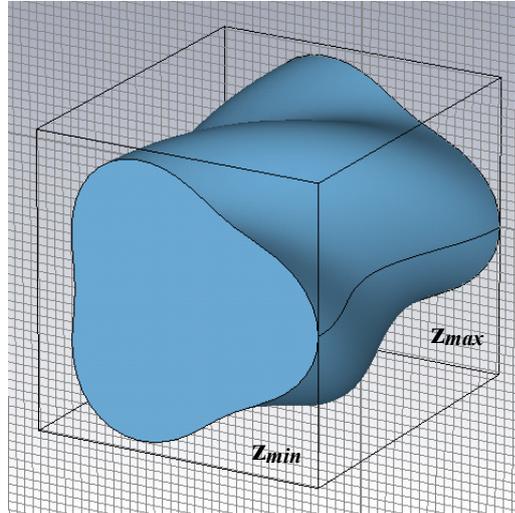
Figure 4.4.6: A one period section (37.5mm) of helical waveguide used in the gyro-TWA dispersion simulations, taken from CST Microwave Studio.

The phase shift of the electromagnetic fields between z_{min} and z_{max} were defined as a phase variable which was swept from -180^0 to 180^0 in 2^0 increments. The eigenmode solver was then used to compute the resonant frequencies, *figure 4.4.7,* of a specified number of modes (in this instance 10) and their corresponding electric and magnetic fields.
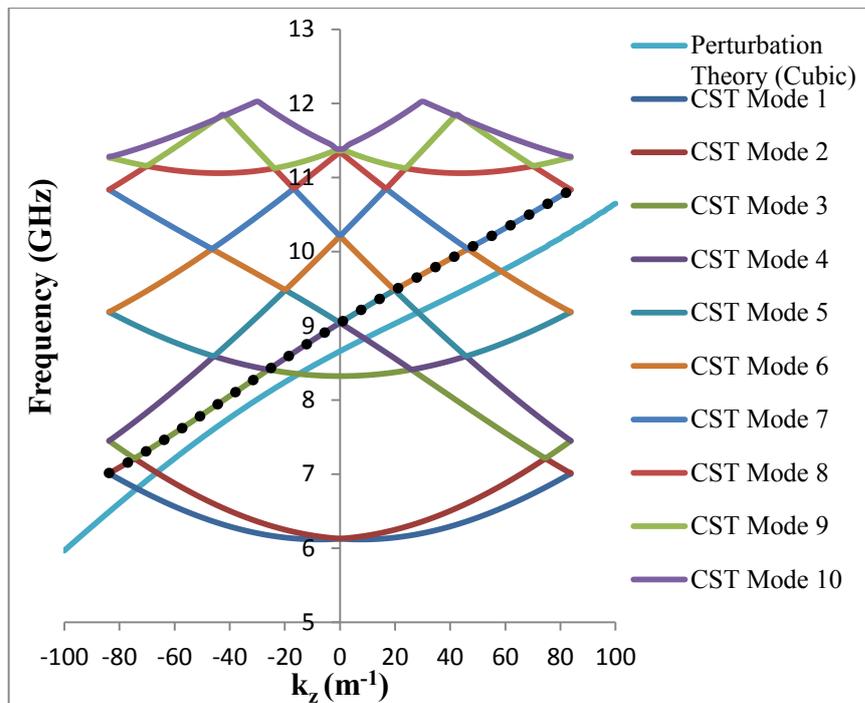
Figure 4.4.7: Dispersion calculation from CST Microwave Studio with the dotted line indicating the operating eigenwave.

From CST Microwave Studio's calculation of resonant frequencies as a function of phase shift the operating eigenwave was deduced (dotted line *figure 4.4.7*). It was found that the dispersion calculations from MAGIC-3D and CST Microwave Studio agreed very favourably with each other, *figure 4.4.8,* with both suggesting that perturbation theory had slightly underestimated the frequency for the dispersion of the helically corrugated waveguide.
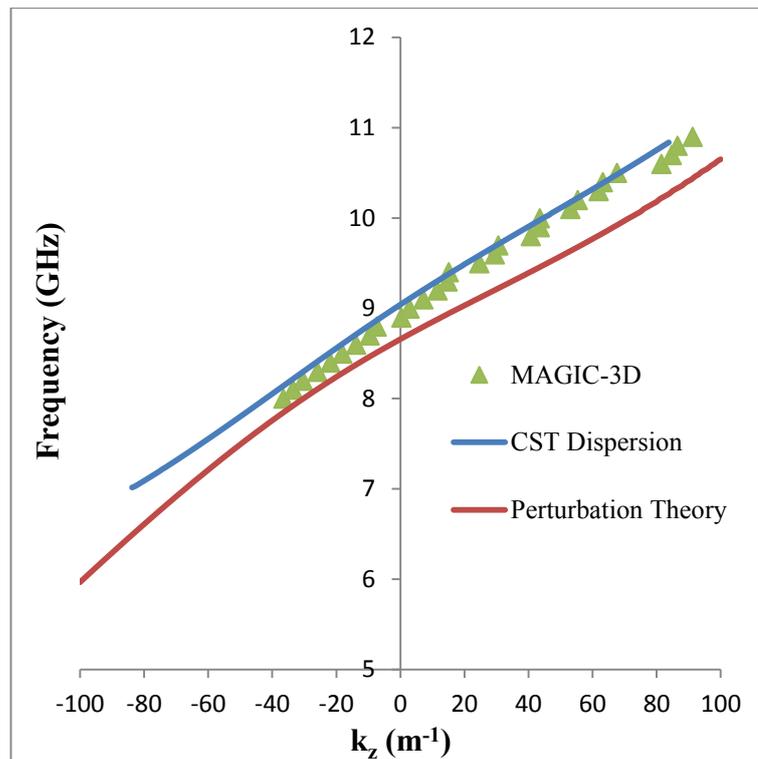
Figure 4.4.8: Dispersion calculation from CST Microwave Studio plotted alongside the dispersion predictions from perturbation theory and MAGIC-3D.

With two different methods of calculating the dispersion characteristics of the helical waveguide strongly agreeing with each other i.e. MAGIC-3D and CST Microwave Studio, the results of the X-band 2nd harmonic gyro-TWA calculated in MAGIC-3D can be further substantiated. These results clearly demonstrate that the MAGIC-3D simulations had adequate resolution to accurately simulate the dispersion of the corrugated waveguide (since the CST Microwave Studio software is highly optimised and widely used for solving this particular type of problem, and able to simulate dispersion with a very compact volume with high resolution). These dispersion calculations alongside the close comparison of the MAGIC-3D simulation results to the experimental results mean a high level of confidence can be placed on the numerical model of the gyro-TWA.

4.5: Summary

Extensive parameter sweeps of both the magnetic field strength and α were undertaken to optimise PiC MAGIC-3D simulations of an X-band 2nd harmonic gyro-TWA with a helically corrugated waveguide to achieve results comparable to those demonstrated experimentally [Bratman, 2000]. It can be concluded from these simulations that for a magnetic field strength of ~0.2123T and α of ~1.27 that the gyro-TWA would expect to achieve an observed output power in the range of ~1.0MW for an input power of ~105W at 9.4GHz. This corresponds to a saturated gain of ~39.7dB and saturated efficiency of ~27%. The theoretical particle equivalent power/gain and efficiency of the amplifier for these initial conditions were calculated to be up to ~1.06MW, ~40dB and ~28.6% respectively, with these results offering a close comparison to the experimental measurements. This good comparison and the close agreement between the different dispersion calculation methods used to determine the operating eigenwave demonstrate a high level of confidence in the prediction capability of the simulations. This naturally presents the modelling code as a suitable foundation to investigate potential performance enhancement of the gyro-TWA, with simulations indicating clear scope for improvement towards the upper band edge of the amplifier.

Chapter five: PiC simulations of a parameter profiled helically corrugated interaction waveguide gyro-TWA

5.1: Overview

An X-band 2nd harmonic gyro-TWA with uniform helically corrugated waveguide was simulated in the PiC code MAGIC-3D, having parameters similar to those of a gyro-TWA experiment detailed in [Bratman, 2000]. The optimised simulations *(chapter 4)* demonstrated good correlation to the experimental measurements providing both a benchmark for the numerical techniques and a starting point for evaluating whether the performance of the amplifier could be improved through parameter profiling of the interaction region of the device. Critically the strong agreement between the experimental and numerical data provides assurance that the simulation approach is a good and physically sound representation of the experimental behaviour. This chapter presents simulation results for the X-band 2nd harmonic gyro-TWA as detailed in *chapter 4*, modified to include a tapered interaction waveguide. These results analyse the impact on both efficiency and bandwidth as the length and rate of the down taper on the output end of the interaction waveguide are adjusted.

5.2: Optimisation of the down taper

5.2.1: Simulation results prior to the inclusion of the down taper

In the fully optimised gyro-TWA simulations as detailed in *chapter 4,* two diagnostics were used to characterise the performance of the amplifier. The first of these was a Poynting flux diagnostic positioned in the output cylindrical waveguide of the amplifier which calculated the output power directly observed in the simulation, whilst the second diagnostic used plots of average beam kinetic energy as a function of axial position to determine the maximum potential performance of the device. Once again, in the interest of brevity, the results associated with these two diagnostics will be referred to as the observed efficiency/power/gain and the particle efficiency/equivalent power and equivalent gain respectively. Using these definitions the fully optimised gyro-TWA simulation was shown to achieve an observed power of ~1.0MW and a particle equivalent power of up to ~1.06MW for an input power of ~105W at 9.4GHz. These values correspond to a saturated observed gain and particle equivalent gain of ~39.7dB and up to ~40.0dB respectively. Hence the observed efficiency and particle efficiency of the amplifier at 9.4GHz were calculated to be ~27% and up to ~28.6%. This latter value closely matched that demonstrated in the experiment [Bratman, 2000], where a saturated efficiency of ~29% was achieved at 9.4GHz, corresponding to an output power of ~1.1MW and saturated gain of ~37dB. These optimised simulation results would suggest that the experiment had been optimally configured.

These fully optimised simulations would be used as the foundation to introduce a down taper towards the output of the helical interaction waveguide to investigate the potential for efficiency and bandwidth enhancement. The original gyro-TWA laboratory experiment had a measured bandwidth of 2.0GHz, spanning the range 8.4GHz to 10.4GHz. The simulated gyro-TWA was unable to completely replicate this having a bandwidth of 1.8GHz, spanning the range 8.4GHz to 10.2GHz. Above

this frequency it was discovered that the TE_{21} mode radiated out along the cylindrical output waveguide, which for a radius of 14.1mm was feasible since the cut-off frequency for this mode in this waveguide was ~10.3GHz. The simulation results would imply that the observed drop in saturated power by -3dB in the laboratory experiment at 10.4GHz potentially reflected a change in the output mode rather than an intrinsic limitation of the bandwidth of the instability. Thus by reducing the output diameter of the interaction waveguide and subsequently increasing the cut-off frequency of the TE_{21} mode it was anticipated that single mode output (TE_{11}) would be possible at higher frequencies (i.e. 10.4GHz and above). Moreover, suitable design of the down taper was also anticipated to improve the efficiency of the amplifier through resonant trapping of the beam electrons. Implementation of this would require the taper to alter the characteristic dispersion of the amplifier's waveguide along its axis in the region where the beam was losing energy (resulting in a rising ω_c), to maintain the beam-wave synchronism for a given radiation frequency for the entire length of the device. Accordingly, simulations were undertaken to investigate the performance of the gyro-TWA with such a down taper positioned towards the output of the interaction region, with results comparing the observed performance and the particle equivalent performance of the amplifier for different tapering strategies.

5.2.2: Variable parameters of the down taper

The coupling coefficient, σ, of the two partial rotating waves in a helically corrugated waveguide can be approximated as the ratio of the corrugation amplitude, l, to the mean radius, r_0. By using this approximation helical down tapers were designed to maintain σ between the uniform helical interaction waveguide section and the helical down tapered section such that the ratio of l to r_0 for both sections was kept constant, *figure 5.2.2.1*. To achieve this, l was proportionally decreased with decreasing r_0 along the entire length of the helically down tapered section. This tapering strategy was intended to ensure the group velocity of the wave was not strongly affected whilst the phase velocity was progressively increased.
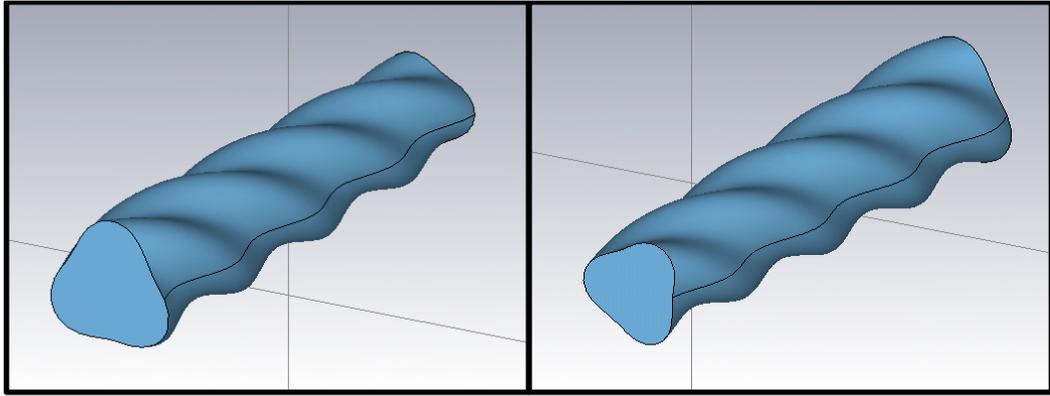
Figure 5.2.2.1: An example of a helical down taper and a helical up taper which maintain the ratio of l to r_0 along the transition length, taken from CST Microwave Studio. The down taper has an initial mean radius and corrugation amplitude of r_0 and l respectively with a final mean radius and corrugation amplitude of ~0.80*r_0 and ~0.80*l respectively. The up taper is the inverse of the down taper.

Initial simulations would focus on this type of taper. Later *(section 5.4)* it will be shown using the full definition for σ, that the coupling of the two modes in the operating eigenwave has a strong dependence on both r_0 and frequency and thus σ is not constant along the length of the helical taper at a given frequency.

It has been highlighted in recent research undertaken at the University of Strathclyde investigating gyro-TWAs with helically corrugated interaction waveguides [Robertson, 2012] that a slight reduction (~1% - ~2%) in the output mean radius of the helical to cylindrical converter along the transition length suppresses the TE_{21} mode radiating out at the highest frequency of interest (in this case 10.4GHz), *figure 5.2.2.2*. These converters represent a slight evolution of the helical to cylindrical converters which featured in the original gyro-TWA geometry *(chapter 4)* where a constant mean radius was maintained along the converter transition length.
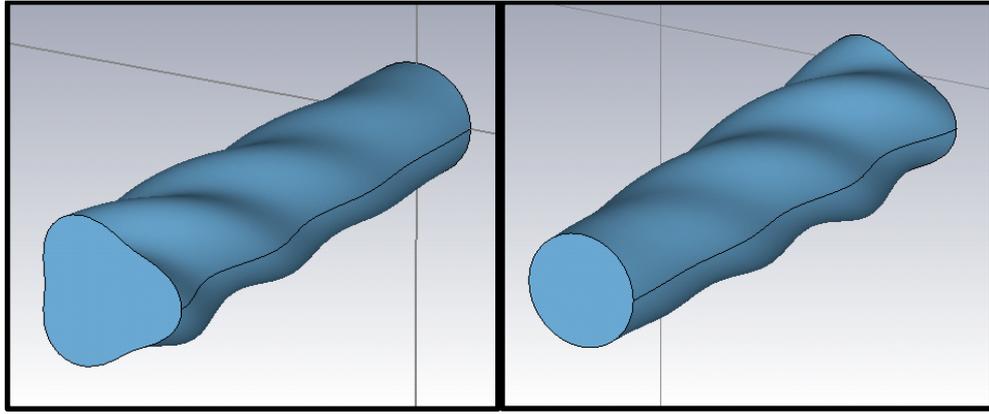
Figure 5.2.2.2: An example of a helical to cylindrical converter and a cylindrical to helical converter taken from CST Microwave Studio. The helical to cylindrical converter has an initial mean radius and corrugation amplitude of r_0 and l respectively with a final mean radius and corrugation amplitude of ~0.80*r_0 and 0 respectively. The cylindrical to helical converter is the inverse of the helical to cylindrical converter.

These tapered converters, *figure 5.2.2.2,* were designed to convert from a helical cross-section of mean radius $r_{0initial}$ and corrugation amplitude l to a cylindrical cross-section with a reduced mean radius r_{0final} and corrugation amplitude of 0. Hence the principle difference of these tapers to that shown in *figure 5.2.2.1* is that the tapering of the corrugation amplitude is substantially faster than that of the mean radius allowing the structure to become circular at one end. This tapering strategy does not attempt to maintain the shape of the wave dispersion and thus does not preserve the group velocity of the operating eigenwave.

Several taper parameters were varied to establish a suitable taper design which improved the performance of the gyro-TWA. One key parameter was the selection of the start position for the taper which would initially be calculated from the average kinetic energy plots of the beam electrons in the optimised gyro-TWA simulations, *figure 5.2.2.3.* Although originally optimised for 9.4GHz, the simulations suggested that a maximum output power and saturated efficiency could in fact be realised for a drive frequency of 10.0GHz, provided the input power was reduced to ~30W to avoid overdriving the amplifier (the bandwidth measurements in the laboratory experiments

were performed at nominally fixed drive signal levels). In principle, and with the support of simulations such as those presented here, this realistically represents the maximum attainable performance of the original amplifier, later to be used as a control to assess the impact on efficiency of a tapered output waveguide. Using this data, the particle equivalent power and gain of the original amplifier were calculated to be up to ~1.06MW and ~40.0dB at 9.4GHz and up to ~1.2MW and ~46.2dB at 10.0GHz for input powers of ~105W and ~30W respectively.
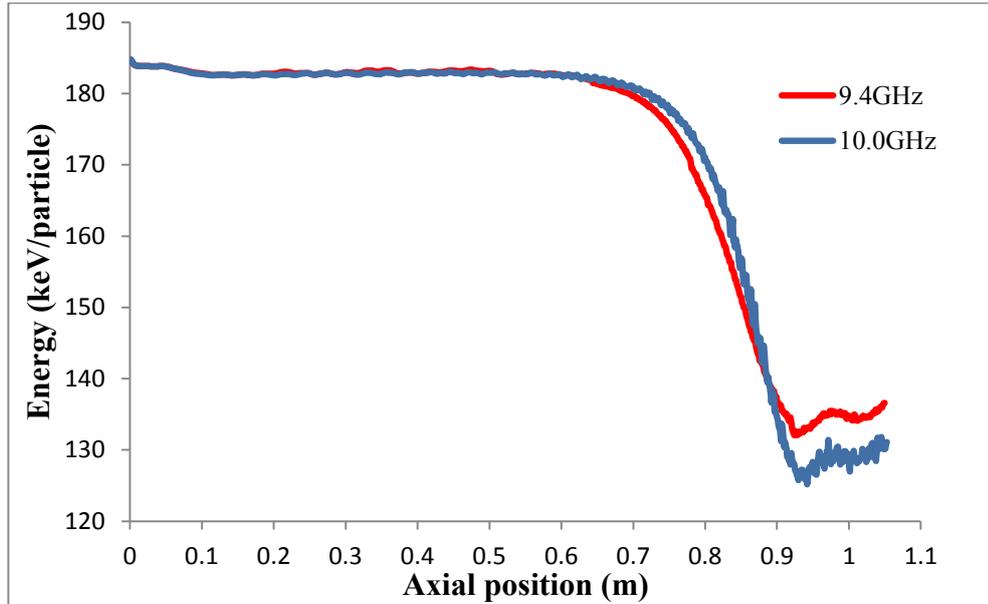
Figure 5.2.2.3: Predicted average kinetic energy of the beam electrons as a function of axial position for an input power of ~105W at 9.4GHz and for an input power of ~30W at 10.0GHz. These results are based on the original gyro-TWA geometry as detailed in chapter 4.

The initial start position of the proposed down taper was taken to be the axial position corresponding to a ~10% drop in the average beam electron kinetic energy from an initial value of ~185keV, *figure 5.2.2.3*. Such a drop in average kinetic energy is equivalent to a change in both γ and ω_c of between ~2% and ~3% and is similar to the typical detuning for such a system. At 9.4GHz this ~10% drop was taken to correspond to an axial position of 0.78m, increasing to 0.82m at 10.0GHz. However the position of this ~10% decrease is a function of the drive power to the amplifier and therefore initial simulations would investigate various down tapers starting at axial positions within this range. To facilitate this, the length of the uniform helical waveguide in the

original simulation was reduced by between 8cm and 4cm from an initial length of 60cm, to correspond to start positions of 0.78m and 0.82m respectively, *figure 5.2.2.4*.
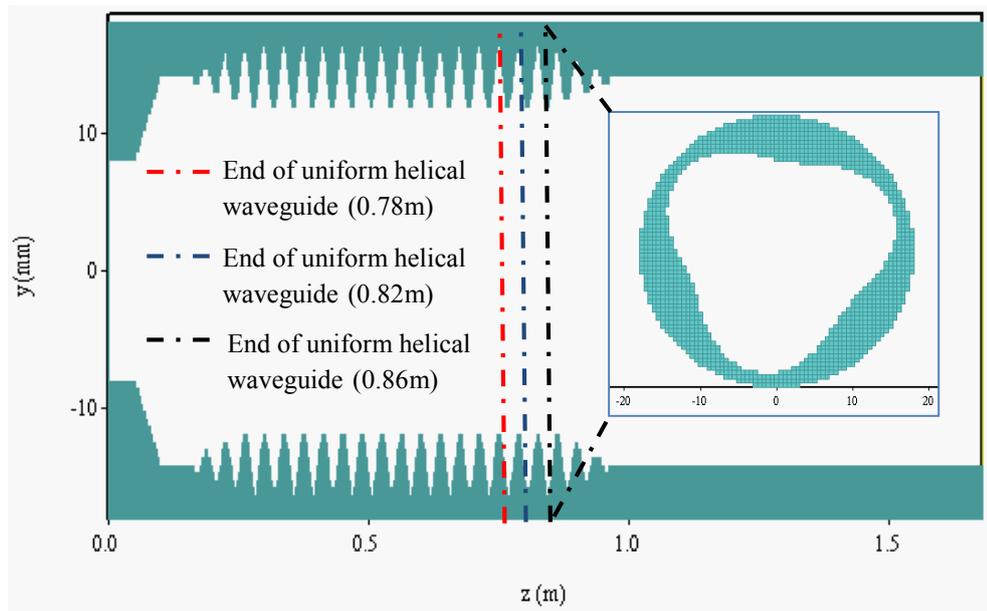
Figure 5.2.2.4: Original simulation geometry as detailed in chapter 4 showing the original end to the uniform helical waveguide section at 0.86m and the new proposed end range of 0.78m to 0.82m to facilitate the start of the down taper, taken from MAGIC-3D.

With the gain of the amplifier strongly affected by the length of the uniform helical waveguide section it was anticipated that decreasing the length of this section would result in a reduction in the linear (and possibly the saturated) gain of the amplifier (when compared to the original amplifier results for each frequency as detailed in *chapter 4*). However it was expected that the maximum output power over the original simulated bandwidth range of 8.4GHz to 10.2GHz would be largely unaffected, though possibly requiring higher drive powers to achieve comparable output powers to the control configuration.

The simulation geometries which included a down taper towards the output of the interaction region of the amplifier, *figure 5.2.2.5*, were generated using the same method as previous MAGIC-3D simulations *(chapter 4)* with a confining shell created

and individual components comprising the system voided out. These individual components were once again parametrically defined through the use of 'mathematically' described surfaces.
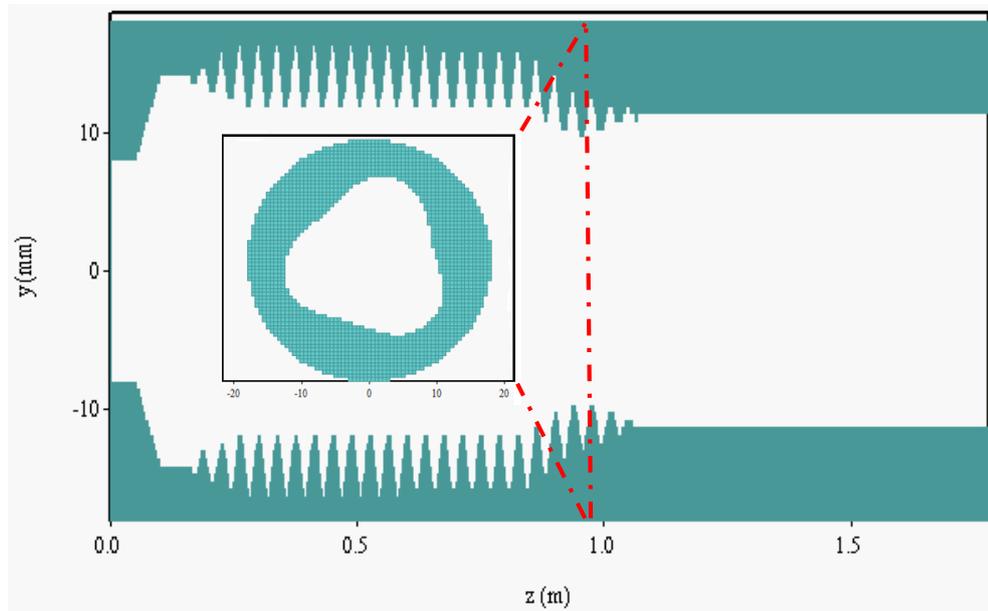
Figure 5.2.2.5: An example of a proposed simulation geometry taken from MAGIC-3D. Here the gyro-TWA geometry includes a 14cm long helical down taper starting at an axial position of 0.82m. The output mean radius and corrugation amplitude of the taper have been reduced by ~20% from initial values of 14.1mm and 2.2mm respectively. In this instance the uniform helical waveguide section measures 56cm in length.

The majority of the components from the original gyro-TWA simulations would remain unchanged with the electrons still emitted from the surface on the far LHS of *figure 5.2.2.5.* The electron beam would be injected into a magnetic field strength of ~0.2123T with an α of ~1.27, with these parameters having been shown to be optimal for the control amplifier as detailed in *chapter 4*. The 5cm long beam tunnel would remain from the original simulations alongside the 5cm long cylindrical up taper, the 4cm long section of cylindrical waveguide and the 12cm long cylindrical to helical converter. For simulations incorporating a helical down taper starting at an axial position of 0.78m the length of the uniform helical waveguide section would be set at 52cm, increasing to 56cm for those tapers starting at 0.82m, with this section positioned immediately before the down taper. For the majority of the simulations the

110

12cm long helical to cylindrical converter would remain from the original simulations although the mean radius and corrugation amplitude at the input of this converter would be subject to change to match the output mean radius and corrugation amplitude of the helical down taper. In simulations where the helical down taper was replaced by a tapered helical to cylindrical converter (see *figure 5.2.2.2*) the length, output mean radius and corrugation amplitude of the converter would be used as variables for the simulations. For all simulations the 70cm long output cylindrical waveguide, the waveguide port and the mesh resolution would be retained from the original optimised simulations although the radius of the output waveguide would be subject to change to correspond to the output radius of the adjoining converter.

With preliminary start positions for the down taper established, other taper parameters to be considered were taper length and taper radius. There were no real constraints on taper length. A rapid taper would increase the likelihood of unwanted reflections but would make the amplifier more compact, potentially benefiting a laboratory experiment or practical device where space may be restricted. Alternatively a gradual taper would decrease the likelihood of reflections but potentially result in the overall system becoming rather large since long amplifiers cost in both space and weight. For example a major contributor to the weight of the system is the magnet with this component also often a considerable power drain. Such costs together with alignment issues increase with increasing length of amplifier and thus in reality it can be desirable to keep systems compact. Physical constraints on the taper radius limited the extent to which r_0 could be reduced, with the minimum r_0 required to be sufficient to ensure the TE_{11} mode was not below cut-off and unable to propagate for the lowest frequency of interest (indeed it is important in practical systems to not approach the cut-off limit).

It had originally been anticipated [Savilov, 2010] that a long and gradual taper might enable efficiency enhancement of the gyro-TWA through resonant trapping of the beam electrons, in a manner analogous to that proposed by A. V. Savilov for CARM amplifiers [Savilov, 1998, Savilov, 2001 and Savilov, 2002]. Here the electrons

should remain in phase constrained orbits defined by the electromagnetic wave's potential well, providing the wave-particle resonance can be maintained for a given wave frequency as the electrons increase in ω_c. Therefore simulations would be undertaken to determine the effect such tapering to the output interaction region of the amplifier had on the efficiency potential of the device. In addition simulations would be undertaken to investigate the impact on device efficiency from tapers designed to track the reduction in average kinetic energy of the beam electrons, with this approach qualitatively comparable to the conventional tapering processes used in Cherenkov TWT devices [Gilmour, 1994]. Plots of average beam kinetic energy as a function of axial position, *figure 5.2.2.3*, would suggest that implementation of this method would require a taper that was relatively short and rapid.

5.3: Dispersion calculations for uniform helical waveguides of varying mean radii and corrugation amplitudes

The mechanism of resonant trapping *(chapter 2)*, in principle, would extend the synchronism between the electromagnetic wave and the beam electrons during the energy extraction process resulting in an increase in the efficiency of the instability. To realise this one must attempt to hold a population of electrons resonant with a given frequency of radiation in spite of the variation in the kinetic energy of the electrons and hence ω_c by changing the shape of the wave dispersion. It was anticipated that this could be achieved through suitable tapering of the interaction waveguide, and hence simulations were undertaken to determine the effect decreasing the mean radius and corrugation amplitude of the helical waveguide had on the operating eigenwave.

The dispersive characteristics of the operating eigenwave of the original gyro-TWA were calculated using both MAGIC-3D and CST Microwave Studio *(chapter 4)*. The strong agreement of these results provides assurance that the results from either method were a sound representation of the dispersion characteristics of the operating

eigenwave and that both methods were suitable for future dispersion calculations. Post processing was more automated in CST Microwave Studio than MAGIC-3D (minimising the potential for errors) and so this method was implemented to determine the dispersive characteristics of various sections of 3-fold helical waveguide. In these simulations both r_0 and l were subject to the same reduction from initial values of 14.1mm and 2.2mm respectively to maintain σ. In keeping with previous CST dispersion calculations a section of helical waveguide one period in length i.e. 37.5mm with periodic boundaries at the input and output of the structure was simulated. For each simulation the bandwidth was set from 8.0GHz to 12.0GHz with the phase shift of the electromagnetic fields between the periodic boundaries of the helix swept from -180^0 to 180^0 in 2^0 increments. From CST Microwave Studio's calculation of the resonant frequencies as a function of phase shift, the dispersion of the operating eigenwave was deduced for each section of helical waveguide, *figure 5.3.1.*
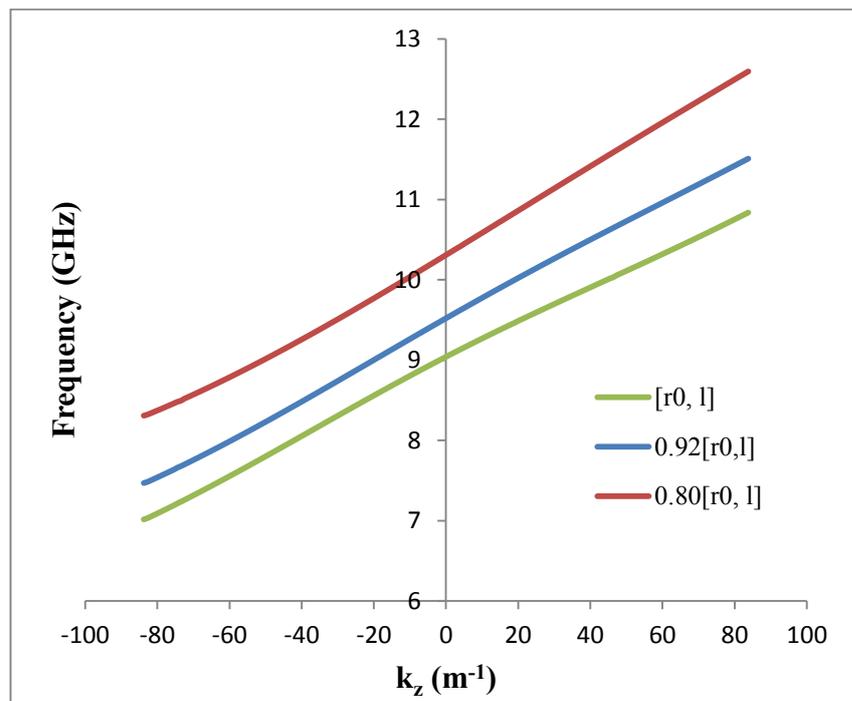
Figure 5.3.1: Dispersion calculations for one period sections of helical waveguide with varying output mean radii and corrugation amplitudes, simulated in CST Microwave Studio. This plot highlights the frequency shift of the operating eigenwave for sections of helical waveguide with r_0 and l decreasing from initial values of 14.1mm and 2.2mm respectively to ~80% (~0.80[r$_0$, l]) and ~92% (~0.92[r$_0$, l]) of these values.

As detailed *(chapter 2)* in the evolving interaction of an electron beam and electromagnetic wave the electron beam line shifts up in frequency (as a result of the increase in ω_c) but does not (significantly) change its axial drift velocity. Hence to maintain the interaction the operating eigenwave is required to also shift up in frequency. The dispersion calculations, *figure 5.3.1,* show that the operating eigenwave shifts up in frequency as the mean radius and corrugation amplitude of the helical waveguide are decreased, consistent with the increasing cut-off frequencies of the two waveguide modes coupled by the corrugation, whilst the group velocity, which is required to remain close to the electron beam axial drift velocity, is not significantly perturbed. Thus these dispersion calculations would suggest that it may be possible to improve both the efficiency and bandwidth of the gyro-TWA through suitable tapering of the interaction waveguide.

5.4: Content of the upper and lower modes in the operating eigenwave

An investigation into the composition of the operating eigenwave in the 3-fold helically corrugated waveguide for varying drive frequencies was undertaken in CST Microwave Studio. Here the transient solver of this modelling suite was used to model two separate geometries, both including a 15cm (i.e. four periods) section of uniform helical waveguide of mean radius r_0 (14.1mm) and corrugation amplitude l (2.2mm) positioned between two cylindrical to helical converters of length 11.25cm (i.e. three periods). In the first geometry the mean radius of both cylindrical to helical converters was kept constant at r_0 with the corrugation amplitude varying between l and 0 to generate the desired helical to cylindrical cross sectional transition*, figure 5.4.1.*
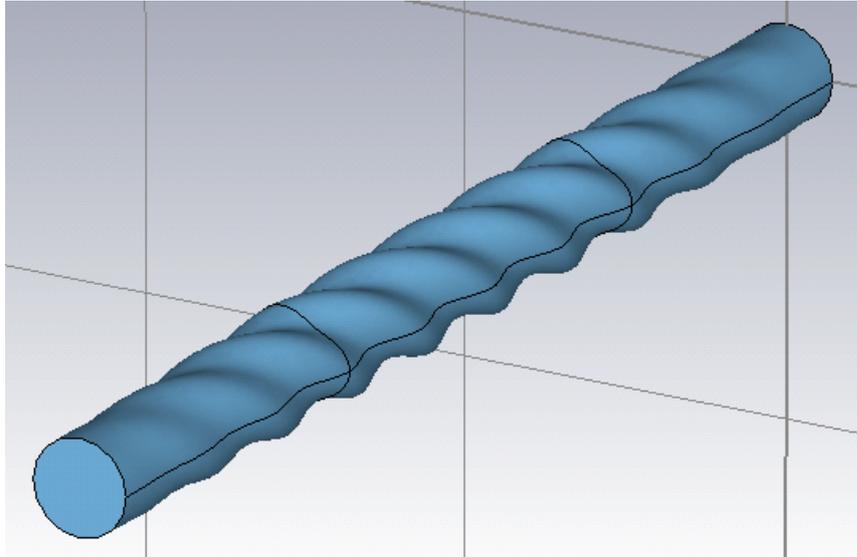
Figure 5.4.1: 3D representation of a section of helical waveguide with a mean radius and corrugation amplitude of r_0 and l respectively bracketed by two cylindrical to helical converters, taken from CST Microwave Studio. The cylindrical to helical converter has a constant mean radius of r_0 and a corrugation amplitude which varies from 0 to l along the transition length. The helical to cylindrical converter is the inverse of the cylindrical to helical converter.

The second geometry included an additional helical up taper and a helical down taper, both of length 14cm, positioned immediately before and after the 15cm long uniform helical waveguide section. The helical up taper had an initial mean radius and corrugation amplitude of ~0.80*r_0 and ~0.80*l and a final mean radius and corrugation amplitude of r_0 and l. The down taper was the inverse of the up taper and will later be shown *(section 5.5.2)*, when positioned towards the output of the interaction region of the benchmark gyro-TWA, to modestly improve the efficiency of the amplifier at 10.0GHz. To accommodate these helical tapers, the cylindrical to helical converters were required to have a constant mean radius of ~0.80*r_0, with the corrugation amplitude varying between ~0.80*l and 0 along the transition length, *figure 5.4.2.*
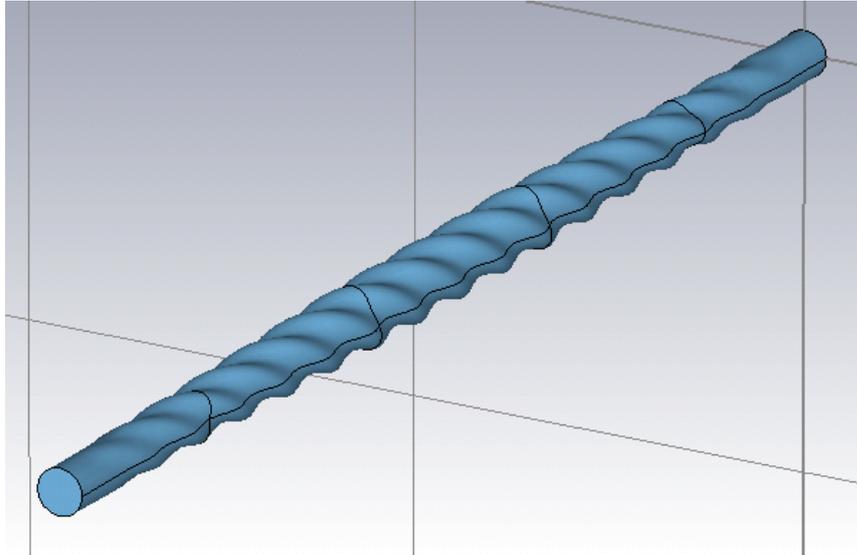
Figure 5.4.2: 3D representation of a section of uniform helical waveguide with a mean radius and corrugation amplitude of r_0 and l respectively bracketed by two helical tapers and two cylindrical to helical converters, taken from CST Microwave Studio. Here one end of each helical taper has a mean radius and corrugation amplitude of r_0 and l respectively with the other end having a reduced mean radius and corrugation amplitude of $\sim 0.80*r_0$ and $\sim 0.80*l$ respectively. The cylindrical to helical converter has a constant mean radius of $\sim 0.80*r_0$ and a corrugation amplitude which varies from 0 to $\sim 0.80*l$ along the transition length. The helical to cylindrical converter is the inverse of the cylindrical to helical converter.

Field diagnostics were positioned transversely throughout both structures to monitor the field structure of the operating eigenmode at each frequency of interest. Simulations of the first geometry, *figure 5.4.1,* were run for drive frequencies of 8.2GHz to 10.4GHz inclusive in 200MHz increments. In these simulations it was anticipated that the TE_{21} mode would radiate out of the cylindrical waveguide at 10.4GHz. Since the output of the second geometry, *figure 5.4.2,* had a reduced mean radius to that of the first, the frequency at which the TE_{21} mode would radiate out was increased and therefore these simulations were run from 8.2GHz to 11.0GHz inclusive. In both structures a circularly polarised TE_{11} wave was launched at the input port (defined as two orthogonal linearly polarised waves with a 90^0 phase shift). In CST Microwave Studio this 90^0 phase shift is defined as a temporal shift between the two orthogonal modes and therefore true only at a given frequency. Hence individual simulations were run for each frequency of interest to ensure that the launched TE_{11}

wave was always truly circularly polarised. In both structures, the input and output field diagnostics showed a well-defined circularly polarised TE_{11} mode over the frequency range of 8.2GHz to 10.2GHz inclusive. However the structure without helical tapers, *figure 5.4.1,* at a drive frequency of 10.4GHz, showed a well-defined circularly polarised TE_{11} mode at the input and a TE_{21} mode at the output. This result was highly consistent with MAGIC-3D simulations of the original gyro-TWA *(chapter 4)* which also indicated that the device radiated in the TE_{21} mode at 10.4GHz. However the structure which included the helical tapers, *figure 5.4.2,* showed a well-defined TE_{11} mode at both the input and output over the entire frequency range of 8.2GHz to 11.0GHz, since the decrease in the output circuit radius increased the cut-off frequency of the TE_{21} mode above the highest frequency of interest.

Transverse field diagnostics located in the middle of the uniform helically corrugated waveguide section monitored the operating mode at each frequency. Over the frequency range 8.2GHz to 11.0GHz this field diagnostic showed the operating eigenwave as a superposition of the cylindrical TE_{11} mode, *figure 5.4.3(LHS)* and the TE_{21} mode, *figure 5.4.3(RHS)* as expected.
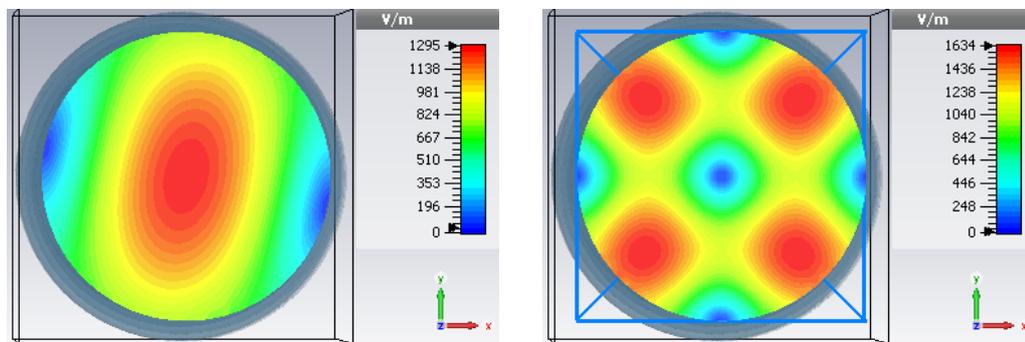
Figure 5.4.3: Example of a cylindrical TE_{11} mode and a TE_{21} mode, taken from CST Microwave Studio.

However the content of these modes in the operating eigenwave varied with drive frequency. At low frequency the simulations suggested that the operating eigenwave was dominated by the TE_{11} (dipole) mode whilst at higher frequency the simulations

suggested that the operating eigenwave became dominated by the TE_{21} (quadrupole) mode, *figure 5.4.4, figure 5.4.5* and *figure 5.4.6.*
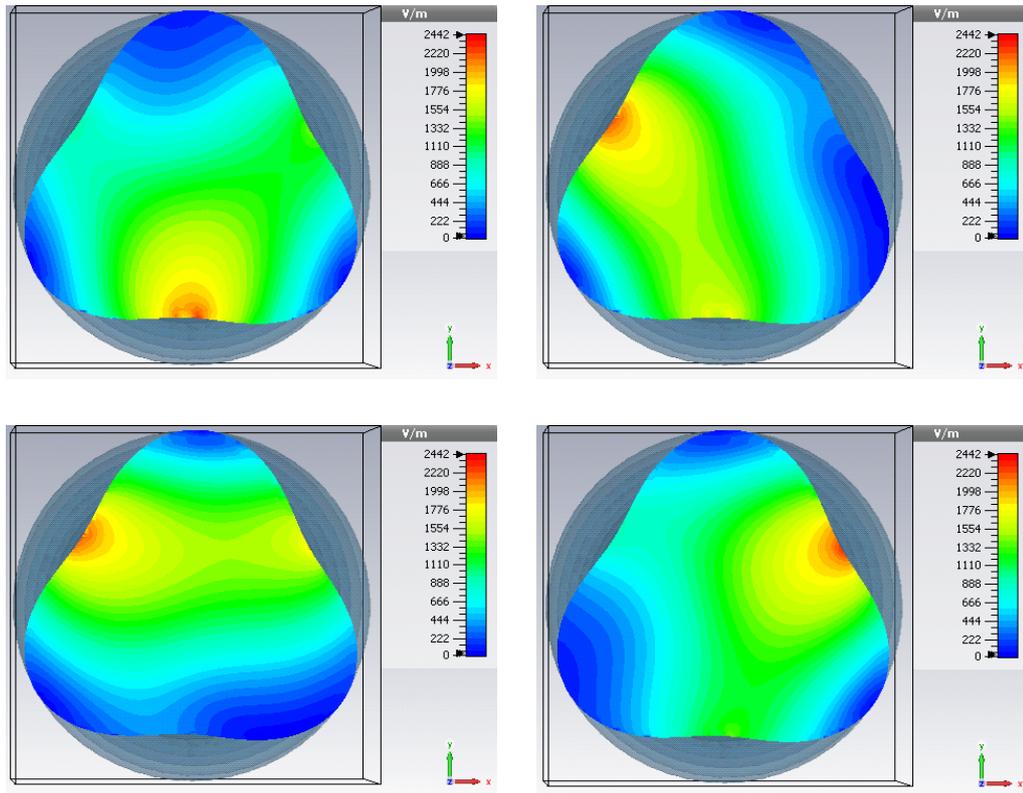
Figure 5.4.4: Evolution of the electric field (phase angle 0^0, 45^0, 90^0, 135^0) for a drive frequency of 8.2GHz, taken from CST Microwave Studio. Here the field diagnostic was positioned midway along the length of the uniform helical waveguide section (see figure 5.4.2) and indicates a predominantly dipole (TE_{11}) structure.
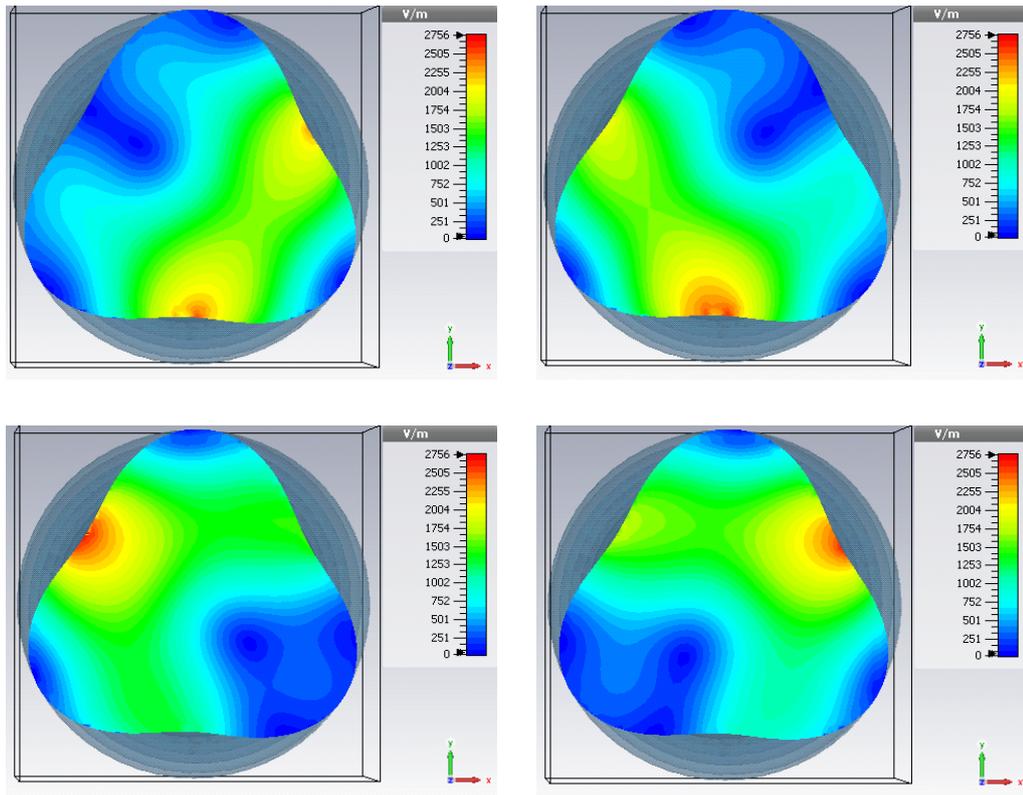
Figure 5.4.5: Evolution of the electric field (phase angle 0^0, 45^0, 90^0, 135^0) for a drive frequency of 9.4GHz, taken from CST Microwave Studio. Here the field diagnostic was positioned midway along the length of the uniform helical waveguide section (see figure 5.4.2) and indicates a predominantly dipole (TE_{11}) structure.

119
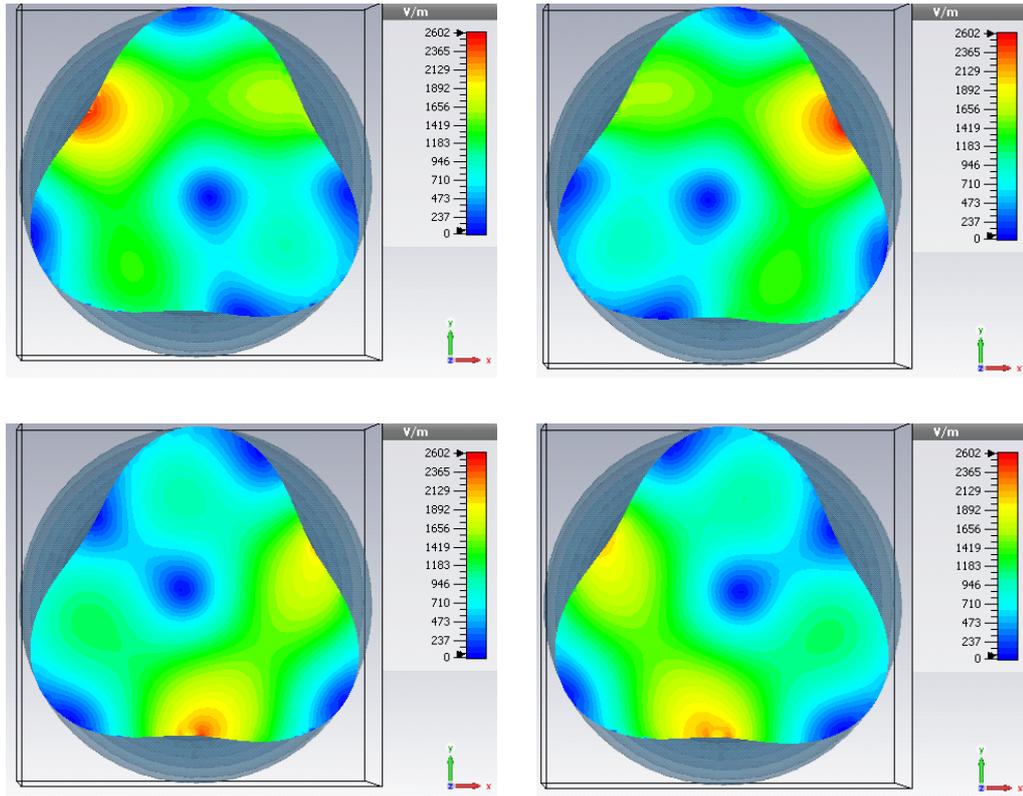
Figure 5.4.6: Evolution of the electric field (phase angle 0^0, 45^0, 90^0, 135^0) for a drive frequency of 10.8GHz, taken from CST Microwave Studio. Here the field diagnostic was positioned midway along the length of the uniform helical waveguide section (see figure 5.4.2) and indicates a predominantly quadrupole (TE$_{21}$) structure.

These results show the operating eigenwave at varying phase angles with this field evolution repeating every 180^0. TE$_{11}$ dipole modes tend to be associated with strong fields in the centre of the waveguide, whilst the quadrupole TE$_{21}$ modes tend to have their fields concentrated outside $\frac{r_o}{2}$. At 8.2GHz the electric field distribution contour, *figure 5.4.4,* shows a variation in strength between the centre and $\frac{r_o}{2}$ in the helical structure of ~700Vm^{-1} (~1100Vm^{-1} in the centre and ~1800Vm^{-1} around $\frac{r_o}{2}$), with the contour plots rather similar to a dipole like TE$_{11}$ mode. At 9.4GHz the variation in electric field distribution between the centre and outer edges of the helical structure, *figure 5.4.5,* increased to ~1000Vm^{-1} (~1000Vm^{-1} in the centre and ~2000Vm^{-1} around $\frac{r_o}{2}$). The structure of the mode still more closely mimicked that of a TE$_{11}$ mode than a TE$_{21}$ mode however a greater change in electric field strength between the centre and

the outer edges would suggest that the TE_{21} mode was becoming more significant at this frequency. At 10.8GHz the variation in electric field distribution between the centre and outer edges, *figure 5.4.6,* again increased to ~1200Vm^{-1} (~700Vm^{-1} in the centre and ~1900Vm^{-1} around $\frac{r_o}{2}$), with the mode pattern similar to the quadrupole structure of a TE_{21} mode. Thus these results would suggest that the TE_{21} mode in the operating eigenwave of the helical waveguide became more dominant at higher frequency.

A diagnostic line was positioned axially through the centre of the first geometry *(figure.5.4.1)* to monitor the strength of the absolute electric field as a function of axial position for varying drive frequencies, *figure 5.4.7.* CST Microwave Studio requires a section of non-varying waveguide at the input and output of a structure to accurately calculate the fields on the ports. For the simulations presented here, two sections of 40mm long cylindrical waveguide i.e. one at the input and one at the output were modelled alongside the helical structures although they do not appear in *figure 5.4.1* and *figure 5.4.2.* Thus the total length of the first geometry, *figure 5.4.1,* was 455mm. For each frequency of interest a cylindrically polarised TE_{11} mode was launched.
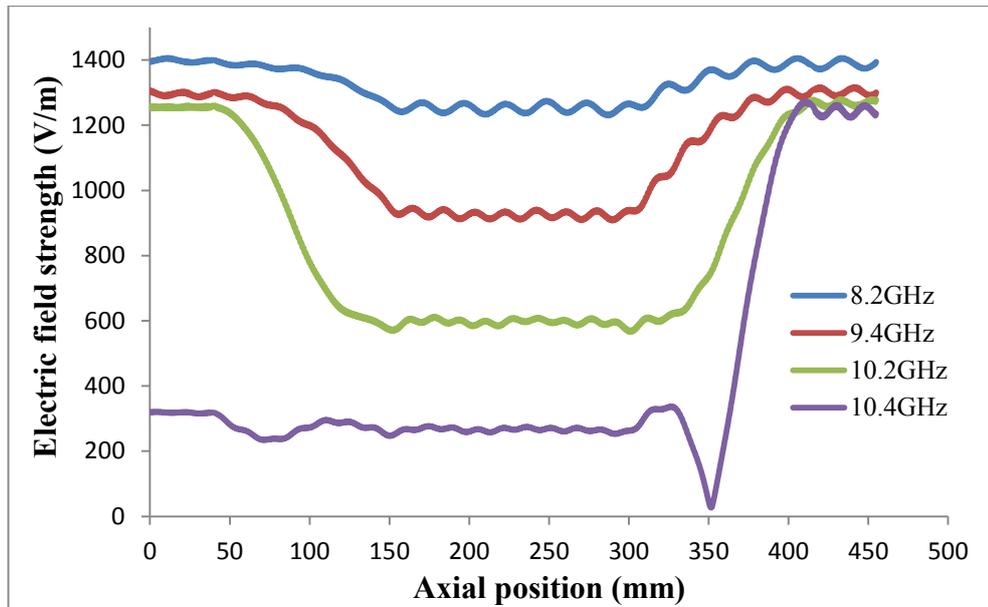
Figure 5.4.7: Absolute electric field strength monitored axially through the centre of the helical structure which did not include helical tapers (figure 5.4.1) for varying drive frequencies.

Were the operating eigenwave dominated by the TE_{11} mode it would be expected that the strength of the electric field at the centre of the structure would remain fairly constant with varying axial position. However as evidenced in *figure 5.4.7* this was not the case. The results highlight a variation between the electric field strength at the input and output (455mm and 0mm respectively) to that in the uniform helical waveguide section (227.5mm) as the frequency was increased. Between 8.2GHz and 10.2GHz inclusive the helical to cylindrical transition (415mm to 302.5mm) was observed to decrease the strength of the electric field with this effect more pronounced as frequency was increased. In each instance, along the length of the uniform helical waveguide section (302.5mm to 152.5mm), the electric field strength remained fairly uniform with the helical to cylindrical transition (152.5mm to 40mm) restoring the electric field strength back to that observed at the input. At 8.2GHz, *figure 5.4.4* and *figure 5.4.7,* it was clear that the wave amplitude along the centre line was only weakly reduced by the helical corrugation, inferring that the operating eigenwave in this instance was dominated by the TE_{11} mode. Where the difference between the electric field strength at the input and the uniform helical waveguide section was large, such as that observed at 10.2GHz, it can be inferred that the operating eigenwave was

122

dominated by the quadrupole fields reminiscent of the TE_{21} mode. At 10.4GHz however, in the structure which did not include helical tapers, the TE_{21} mode was no longer cut-off at the output transition with the plot of absolute electric field as a function of axial position showing a much weaker field strength towards the output of the structure to that at the input. This would again suggest that the output mode more closely mimicked that of the TE_{21} mode than the TE_{11} mode at this frequency, and that the TE_{21} mode radiated out of the structure as evidenced in the gyro-TWA simulations undertaken in MAGIC-3D *(chapter 4)*.

It was also possible to analytically ascertain the content of TE_{21} mode in the operating eigenwave at a given frequency. This could be calculated from [Denisov, 1998a]

Equation 5.4.1

$$\chi = \frac{2\left[k_{z1} + \Delta_g - \frac{\delta}{k_{z0}}\right]}{3k_{z1}^2 + 2k_{z1}\left(\Delta_g - \frac{\delta}{k_{z0}}\right) - 2\delta}$$

where k_{z1} is the solution of the 'cold' dispersion equation *(equation 2.3.6.10)* corresponding to the hybrid eigenwave. The coefficient χ appears in a modification of the Pierce parameter, C, *(equation 2.4.2.2)*, resulting from a simplification of the 'hot' dispersion equation *(equation 2.4.2.1)* from a fifth- to a third-order equation in k_z *(equation 5.4.2)*, through consideration of only the operating eigenwave solution.

Equation 5.4.2

$$[k_z - k_{z1}]\left[k_z - \frac{(\delta - \Delta_H)}{\beta_{\parallel 0}}\right]^2$$

$$= \hat{C}^3\left(1 + \frac{2s\beta_{\parallel 0}}{\beta_{\perp 0}^2}\left[k_z - \frac{(\delta - \Delta_H)}{\beta_{\parallel 0}}\right]\right)$$

where

$$\hat{C} = C\left(\frac{\chi}{2}\right)^{\frac{1}{3}}$$

The coupling coefficient, σ, of the two partial rotating waves in the helical waveguide is a function of frequency and can be calculated from *equation 2.3.7.1*. Substitution into this equation *(equation 2.3.7.1)* for the helical waveguide parameters detailed in [Bratman, 2000] allowed σ (describing energy transfer between the two modes) to be

calculated over a chosen frequency range, in this instance from 8.2GHz to 11.0GHz in 100MHz increments, *figure 5.4.8.*

GHz	σ	GHz	σ	GHz	σ
8.2	0.171	9.2	0.142	10.2	0.120
8.3	0.167	9.3	0.139	10.3	0.118
8.4	0.164	9.4	0.137	10.4	0.116
8.5	0.161	9.5	0.134	10.5	0.114
8.6	0.158	9.6	0.132	10.6	0.112
8.7	0.155	9.7	0.130	10.7	0.111
8.8	0.152	9.8	0.128	10.8	0.109
8.9	0.149	9.9	0.126	10.9	0.107
9.0	0.147	10	0.123	11.0	0.106
9.1	0.144	10.1	0.121		

Figure 5.4.8: Table showing the coupling coefficient, σ, of the two modes in the operating eigenwave of a helically corrugated waveguide with structural parameters of r_0 (14.1mm) and l (2.2mm), for a given frequency.

It was clear that σ decreased with increasing frequency for a given helically corrugated waveguide, dropping from a value of 0.171 at 8.2GHz to 0.106 at 11.0GHz. Using the value of σ for a given frequency, and substituting it into the 'cold' dispersion equation *(equation 2.3.6.10)* allowed the three roots for the axial wavevectors of the allowed eigenmodes of the helically corrugated waveguide to be calculated. In the frequency range of interest i.e. 8.2GHz to 11.0GHz the roots of this dispersion equation appear as one real root and two complex conjugate roots, with only the real root substituted into *equation 5.4.1* to determine χ for a given frequency, *figure 5.4.9.*
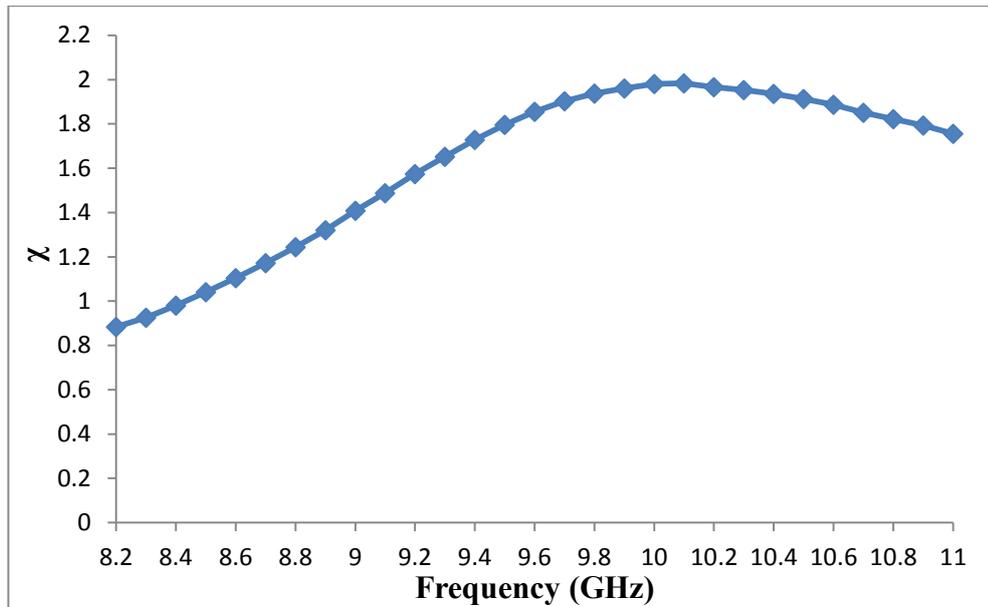
Figure 5.4.9: The content of the TE$_{21}$ mode, χ, in the operating eigenwave as a function of frequency for a section of uniform helical waveguide with a mean radius and corrugation amplitude of r$_0$ (14.1mm) and l (2.2mm).

The plot of χ as a function of frequency suggested that the content of the TE$_{21}$ mode in the operating eigenwave was greater towards the middle and upper range of the chosen frequency bandwidth peaking at a frequency of ~10.0GHz. This data agreed favourably with CST Microwave Studio which also suggested that the content of the TE$_{21}$ mode was greater at higher frequency. Typically, large orbit gyrotron devices, operating in the nth harmonic couple strongly to modes with an azimuthal index corresponding to n and thus the X-band gyro-TWA operating in the 2nd cyclotron harmonic presented here, should couple strongly to modes with an azimuthal index of 2. Since the content of the TE$_{21}$ mode was greatest at ~10.0GHz it would be anticipated that the gyro-TWA would perform best at this frequency. Indeed this result will be shown to agree strongly with all PiC simulations of the gyro-TWA undertaken in MAGIC-3D which suggested that optimum performance of the amplifier (with and without a down taper in the interaction region) occurred when operating with a drive frequency of 10.0GHz. The content of the TE$_{21}$ mode was predicted to show a gradual drop off after 10.0GHz (though this may be a limit of the analytical method) but it would be anticipated that the amplifier would still perform favourably over these

125

frequencies provided the geometry of the output was such to prohibit the TE_{21} mode radiating out, whilst still allowing the TE_{11} mode to propagate at the lowest frequency of interest. This result would suggest that a bandwidth enhancement of the amplifier may be possible assuming the output circuit of the gyro-TWA was suitably tapered.

The content of the TE_{21} mode in the operating eigenwave was calculated for various sections of helical waveguide. Here the output mean radius and corrugation amplitude of the waveguide were subject to the same reduction with σ in each instance recalculated for a given frequency, *figure 5.4.10*.
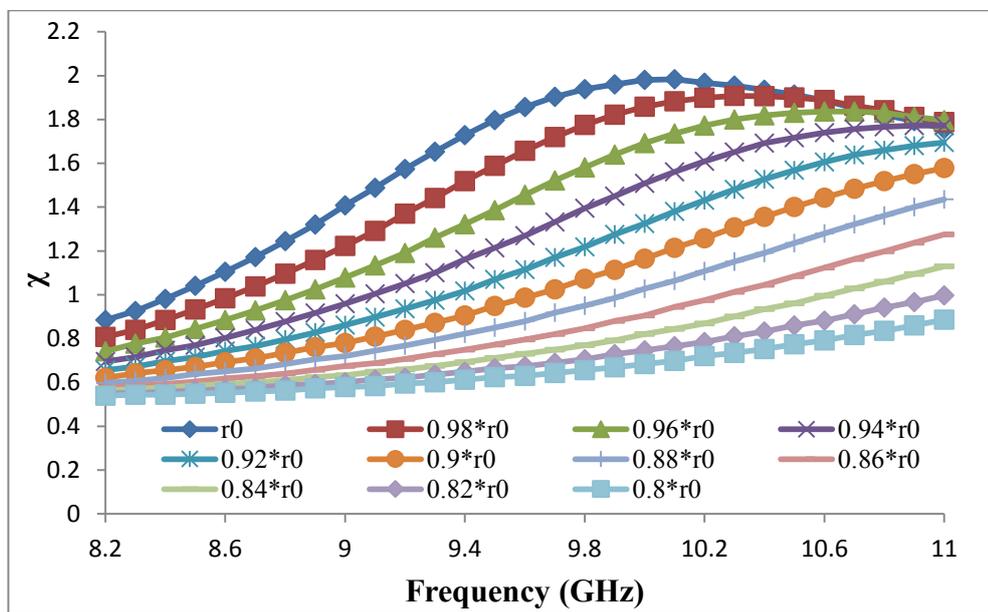
Figure 5.4.10: The content of the TE_{21} mode, χ, in the operating eigenwave as a function of frequency for helical waveguides with varying mean radii and corrugation amplitudes.

These calculations suggest that the coupling of the helically corrugated waveguide's eigenmode to the electron beam would vary depending upon the value of the mean radius and corrugation amplitude of the helical waveguide. When the mean radius and corrugation amplitude of the helically corrugated waveguide were incrementally decreased from initial values of 14.1mm and 2.2mm respectively, it was observed that the value of χ, for a given frequency, reduced. As noted, the parameter χ determines

the fraction of the quadruple (TE_{21}) mode in the hybrid operating eigenwave [Denisov, 1998a], and as it drops at any given frequency (with reducing mean radius and corrugation amplitude) a shrinking of the separatrix width may be expected, leading to detrapping of the electrons. Thus these results would suggest that it may not be possible to establish a resonant trapping regime in the gyro-TWA and consequently increase the efficiency of the amplifier through tapering the output circuit of the device.

5.5: Investigation of taper impact on efficiency

5.5.1: Evolution of trapping regime for efficiency enhancement

Preliminary simulations of the gyro-TWA with a helically corrugated down taper positioned towards the output of the interaction region suggested that optimal performance of the amplifier was at a drive frequency of 10.0GHz. This was consistent with expectations from the benchmark simulations of the original gyro-TWA *(chapter 4)* which also suggested that the device would realise optimum output power and efficiency at 10.0GHz provided the drive power was suitably adjusted. Since it had originally been anticipated that gradual tapering of the interaction waveguide could potentially improve the efficiency of the gyro-TWA through resonant trapping of the beam electrons, initial simulations would focus on this type of tapering at 10.0GHz. For this investigation the start position of the taper would be set to 0.78m to give a uniform helical waveguide section of length 52cm.

To analyse the impact on the efficiency of gyro-TWAs including a relatively long and gradual helical down taper positioned towards the output of the interaction region of the device, fixed reductions in both the output mean radius, r_0, and the corrugation amplitude, l, of the tapers were chosen, such that these tapers had an input and output

helical cross-section with the input matched to that of the uniform helical waveguide section of the amplifier, *figure 5.2.2.1*. The reduction in both r_0 and l would correspond to a ~10% decrease from initial values of 14.1mm and 2.2mm respectively and in principle would represent a decrease in resonant γ from an initial value of ~1.36 to ~1.23 and subsequent decrease in the kinetic energy of the electrons from ~185keV to ~115keV. Thus with this configuration the instability, in theory, could hope to realise an efficiency of close to 40%, should the effect of resonant trapping and deceleration of electrons be realised. To realise this regime, it was anticipated that a relatively long taper should be required, keeping the electrons trapped in their closed phase trajectories whilst lowering their average kinetic energy. Initially a taper length of 40cm was chosen as this represented a significant increase in the length of the original gyro-TWA interaction region (the original amplifier had a uniform helical waveguide of length 60cm). The input power of the 10.0GHz drive signal was varied, and the average kinetic energy of the electrons as a function of axial position was monitored, *figure 5.5.1.1*. From this data the particle equivalent power and gain of the instability could be determined (assuming the electrons became unconstrained at the point of minimum kinetic energy in the interaction waveguide).
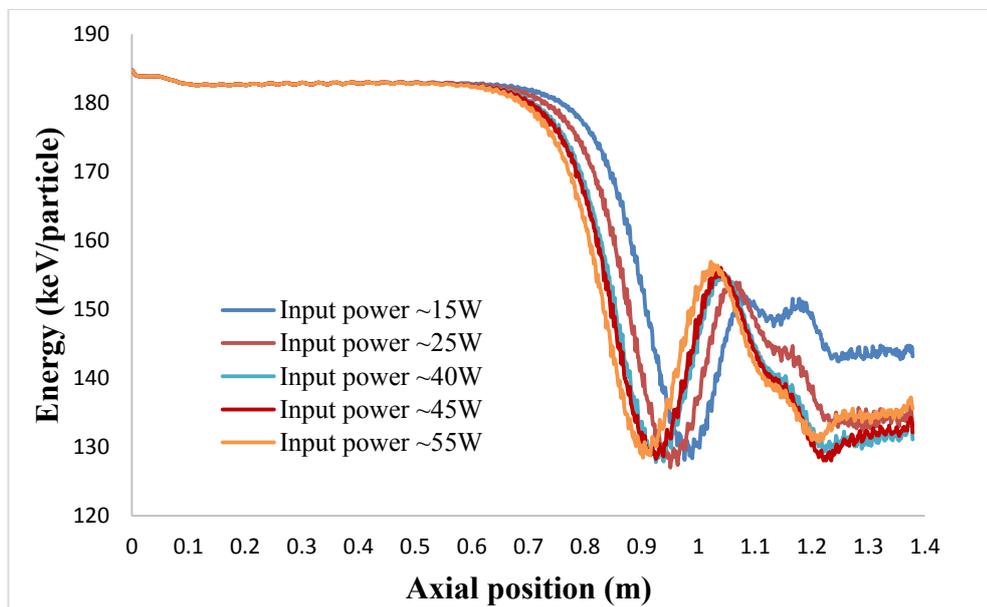
Figure 5.5.1.1: Predicted average kinetic energy of the beam electrons as a function of axial position and input power at 10.0GHz, for a gyro-TWA including a helical down taper of length 40cm to an output mean radius and corrugation amplitude of ~0.90[r₀, l]. Here the uniform helical waveguide section measured 52cm in length.

The results highlight that the position of the initial drop in the average kinetic energy of the beam electrons had the expected dependence on the input power to the amplifier with this drop occurring at a slightly shorter axial position as drive power was increased. However in each instance the rate at which the electrons lost their kinetic energy was comparable such that the initial minimum in average kinetic energy also occurred at a slightly reduced axial position the harder the amplifier was being driven (consistent with less gain being required to reach saturation). In all instances however the initial minimum in average kinetic energy of the electrons was comparable. Since the helical down taper measured 40cm in length and started at an axial position of 0.78m, the results highlight that the electrons had only transitioned along ~15cm of the helical down taper before they had relinquished as much energy to the wave as possible. It was observed that the electrons always transitioned into accelerating phase, corresponding to an increase in the average kinetic energy of the electrons, with the amount of energy reabsorbed by the beam appearing to be largely insensitive to the input power of the amplifier, typically recovering about half the energy they had lost to the wave. After this accelerating phase the electrons returned to decelerating phase where they would reinforce the electric field, however only when the amplifier was driven at ~40W to ~45W was the minimum average energy in this second cycle of the bunch orbits comparable to the initial minimum observed at ~0.93m. Using this data it was possible to calculate the particle equivalent power of the gyro-TWA which was determined to be up to ~1.14MW for a drive power of ~45W, yielding a particle equivalent gain of up to ~44.2dB. Comparison to the control gyro-TWA at 10.0GHz, *figure 5.2.2.3*, shows that the addition of the taper had decreased the performance of the amplifier from ~1.2MW and ~46.2dB respectively. However the results presented in *figure 5.5.1.1* would suggest that a further decrease in the average kinetic energy of the electrons may be possible by increasing the length of the taper, providing the reduced rate at which the resonant energy of the system was tuned allowed the electrons to remain in trapped orbits. This was tested by extending the length of the helical taper in stages from 40cm to 200cm. In each instance the output mean radius and corrugation amplitude of the taper were held at ~$0.90*r_0$ (~12.7mm) and ~$0.90*l$ (~2mm) respectively, *figure 5.5.1.2,* such that the gradient of the taper (taper rate) decreased with increasing length. For all simulations the length of the uniform helical

waveguide section remained at 52cm with the drive power to the amplifier held at ~45W.
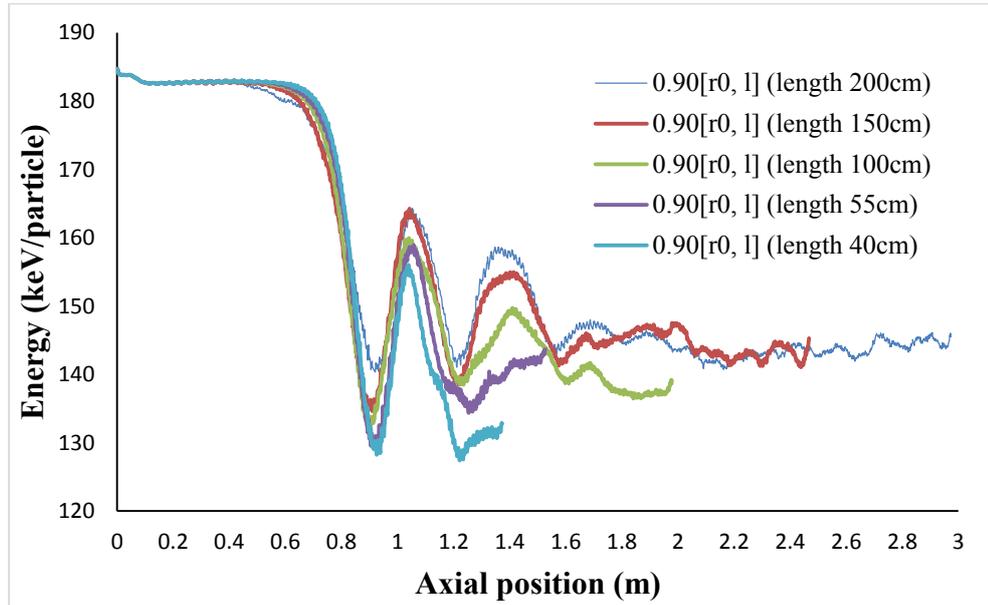
Figure 5.5.1.2: Predicted average kinetic energy of the beam electrons as a function of axial position for gyro-TWA geometries including helical tapers of lengths between 40cm and 200cm, with output mean radii and corrugation amplitudes of ~0.90[r_0, l], at 10.0GHz. In all instances the length of the uniform helical waveguide section measured 52cm.

Increasing the helical down taper from 40cm to 55cm appeared to have little impact on the average kinetic energy of the beam electrons over the first ~1.00m of the gyro-TWA structure, with the average kinetic energy of the electrons for each taper configuration tracking almost identical paths over this range. In each instance the beam kinetic energy reached a minimum at an axial position corresponding to ~0.93m, prior to the electrons transitioning into accelerating phase. It is at the maxima of the first accelerating phase transition that the kinetic energy plots for the two tapers i.e. the 40cm and 55cm tapers, show any significant variation with the amount of energy reabsorbed from the wave appearing to have a dependence on the gradient of the taper. The results show that less energy was reabsorbed when the taper was shorter and consequently the resonant energy was being tuned more rapidly, reaching ~155keV for the gyro-TWA including the 40cm long taper and ~159keV for the 55cm long taper geometry. In both instances however the beam electrons eventually returned to

decelerating phase. In contrast to the 40cm long helical taper configuration, where the second kinetic energy minima coincided with the end of the helical taper section (~1.2m), the second kinetic energy minima of the 55cm long taper configuration occurred at an axial position before the end of the taper (i.e. before ~1.35m). Thereafter the electron energy appeared to vary in a non-synchronous manner with this result suggesting that at a position before the end of the taper the average kinetic energy of the electrons no longer had a dependence on the electromagnetic wave, suggestive of the majority of the particles in the bunch having crossed the separatrix. To test if de-trapping was caused by an excessively rapid change in the helix dispersion, the length of the helical down taper was increased to 100cm. As with the shorter taper configurations the average kinetic energy of the electrons in the 100cm long helical taper reached a minima at close to ~0.93m, at a value higher than that observed for the shorter tapers. After this position the electrons transitioned into accelerating phase with the amount of energy reabsorbed by the electrons greater than that observed for the shorter taper geometries. This shows that the oscillation of the particles in the separatrix, and length over which these oscillations occur corresponds to the region where the particles are trapped in phase. As the rate of change in the helical corrugation is reduced (longer taper) this region extends in length. However there is no evidence that the particles meaningfully follow the downward shift of the resonant energy as would be consistent with the trapping regime behaviour, but rather the particles appear to slowly exit from the closed phase orbits, typically at an average energy somewhat exceeding the minimum achievable average kinetic energy. By increasing the taper length further to 150cm and 200cm and by keeping all other parameters unchanged, it was again observed that such long and gradual tapers were ineffective at reducing the kinetic energy of the beam electrons. For both of these extended tapers the initial minima in average kinetic energy observed at ~0.93m was higher than that observed for all other taper configurations. Indeed the result for the geometry incorporating the 200cm long helical taper showed that over much of the length of the taper, the average electron kinetic energy appeared to no longer have any dependence on the electromagnetic wave (i.e. fluctuating randomly). This trend was also observed before the end of the 150cm long taper and confirms that a large proportion of the electrons had escaped the separatrix before the end of each taper,

transitioning from constrained phase orbits to unconstrained phase orbits. These results would imply that the theoretically predicted trapping regime was not being effectively established in this amplifier.

Up to this point all the amplifiers including a helical down taper, regardless of taper length, suggested that the inclusion of such tapers to the output of the interaction region of the device were detrimental to the overall performance of the amplifier. The results did however highlight a possible dependence on the reabsorbed energy of the electrons to the rate of the down taper prompting an investigation into helical tapers with reduced output r_0 and l. Thus helical tapers of length 35cm and 50cm, *figure 5.5.1.3,* with a reduction in output mean radius and corrugation amplitude to ~0.85*r_0 (~12mm) and ~0.85*l (~1.9mm) respectively were simulated. In these simulations the input power was set to ~40W with the amplifier operating at 10.0GHz. As with the previously detailed simulations the start position of the taper was set to 0.78m with the uniform helical waveguide section of the amplifier measuring 52cm in length.
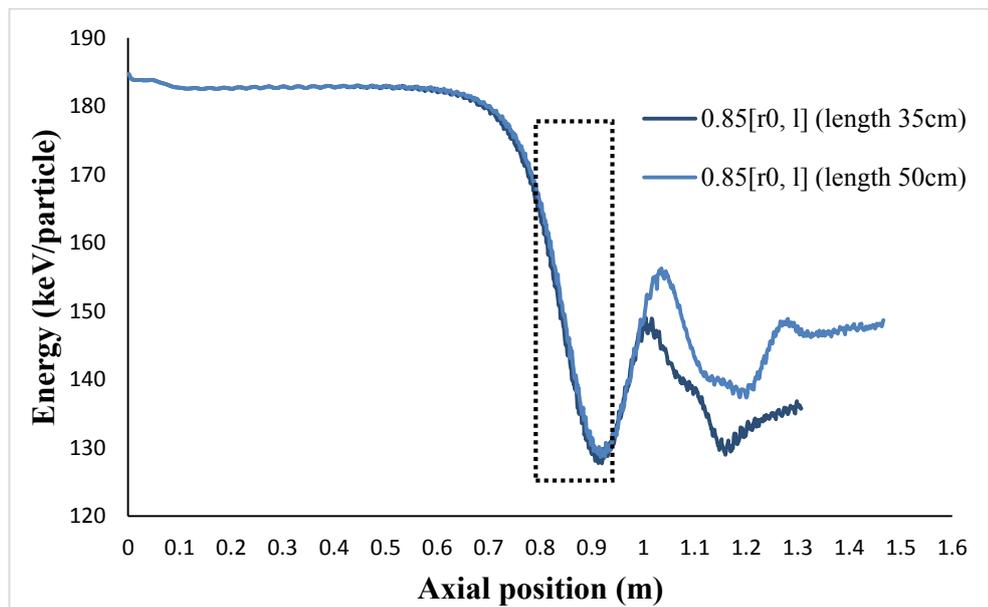
Figure 5.5.1.3: Predicted average kinetic energy of the beam electrons as a function of axial position for gyro-TWAs including helical tapers of lengths 35cm and 50cm with output mean radii and corrugation amplitudes of ~0.85[r₀, l], at 10.0GHz. In both instances the length of the uniform helical waveguide section measured 52cm.

Once again it was observed that the initial minimum average kinetic energy for both the gyro-TWA with the 35cm long helical taper and that including the 50cm long helical taper occurred at ~0.93m. Of all the helical tapers investigated, the 35cm long taper represented the most rapid taper and as anticipated best suppressed the amount of energy reabsorbed by the wave. These results further highlight an apparent dependence of the amount of energy reabsorbed by the particles from the wave to the rate of the down taper, corresponding to a breaking of the resonance condition as the particles enter phase trap saturation conditions.

In summary, the results for all the gyro-TWAs including a helical down taper suggest that the regime of resonant trapping was not successfully realised with the predicted efficiency of the benchmark amplifier at 10.0GHz greater than that achieved when any extended helical down taper was introduced into the interaction region of the device. The original gyro-TWA *(chapter 4)* had a uniform helical interaction waveguide of length 60cm with the longest system simulated here having a significantly increased interaction region of length 252cm, comprising of a 52cm long section of uniform helical waveguide and a 200cm long helical down taper. Thus while it cannot be completely ruled out that a parameter set may exist to realise resonant trapping of the beam electrons in the gyro-TWA, the results presented here would suggest that such a parameter set may not be a practically viable option.

5.5.2: An investigation into conventional tapering akin to that used in Cherenkov TWTs for efficiency enhancement

The relatively long and gradual tapers appeared ineffective at improving the efficiency of the gyro-TWA through achieving the trapping regime of operation and so an investigation into tapers designed to simply track the decrease in average kinetic energy of the beam electrons was undertaken. It was observed in the previous simulations *(section 5.5.1)* that the minimum in average kinetic energy of the electrons

occurred at approximately the same axial position (i.e. ~0.93m), regardless of the taper gradient. This characteristic was also observed in the original amplifier, *figure 5.2.2.3*. In all instances the decrease in average kinetic energy over the axial range of ~0.78m to ~0.93m was substantial (highlighted in *figure 5.5.1.3*). At 10.0GHz, the control amplifier simulation predicted a decrease in average kinetic energy of ~60keV from an initial ~185keV (γ ~1.361) to ~125keV (γ ~1.244) to yield a particle efficiency of up to ~32.3%. This change in energy would imply that the cyclotron frequency had increased by ~9% and that the mean radius of the helical waveguide should be reduced by the same amount to shift the dispersion upwards to compensate for this, to maintain the detuning of the beam-wave synchronism at the original frequency of operation. It was therefore anticipated that this reduction in mean radius should be implemented over the range in which the electrons appeared to be meaningfully perturbed by the wave i.e. over a taper length of between 10cm and 15cm, to extend the beam-wave interaction. Hence this analysis would form a starting point to design a taper which ideally delayed the electrons from transitioning into accelerating phase for as long as possible.

A sensitivity analysis was undertaken to determine the impact on efficiency of the amplifier to changes in the gradient of the taper, in the range previously estimated to be appropriate for the variation in average kinetic energy being observed in the electron beam, *figure 5.2.2.3*. Therefore helical tapers of length 10cm to output mean radii and corrugation amplitudes between ~0.91[r_0, l] and ~0.75[r_0, l] inclusive were simulated. To clarify, as with the previously discussed tapers in *section 5.5.1*, these tapers would have a helical cross-section at each end with the input matched to the output of the uniform helical waveguide section. Once again the start position of the taper would be set to 0.78m such that the length of the uniform helical waveguide section measured 52cm, with the amplifier operating at a drive frequency of 10.0GHz. In each taper configuration the drive power to the amplifier was varied to ascertain the optimal performance of the device, *figure 5.5.2.1*.

134
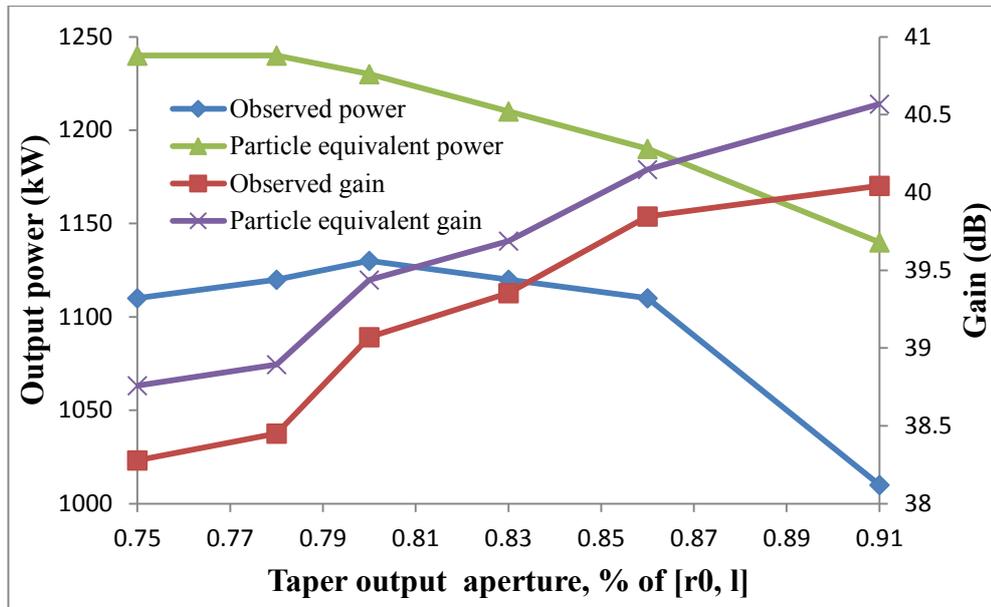
Figure 5.5.2.1: Observed output power/gain and particle equivalent power/gain as a function of output circuit aperture and input power at 10.0GHz. In each instance the gyro-TWA included a 10cm long helical taper and had a uniform helical waveguide measuring 52cm.

It became evident that the drive power required to achieve the maximum observed power increased with decreasing output circuit mean radii and corrugation amplitude, varying between ~165W for the amplifier with the ~0.75$[r_0, l]$ output circuit to ~100W for the ~0.91$[r_0, l]$ output circuit. This corresponded to a decrease in the gain of the amplifier with decreasing output circuit dimensions. The gain in each instance was always significantly less than that of the benchmark amplifier but could of course be recovered by increasing the length of the uniform section of the corrugated waveguide. The results show that the predicted output power of the amplifier was largely insensitivity to changes in the gradient of the taper provided the output aperture of the taper was reduced below ~0.91$[r_0, l]$, consistently achieving an observed power of ~1.12MW. These results represent a slight increase in observed power of ~60kW when compared to the control amplifier operating at the same frequency, and correspond to an increase in observed efficiency of ~1.7%, from ~28.6% to ~30.3%, at 10.0GHz. Only when the amplifier had an output circuit aperture of ~0.91$[r_0, l]$ was the performance of the amplifier observed to be less than that of the control amplifier. However in all other instances it has been shown that these tapers were significantly

135

more effective than the long and more gradual helical tapers *(section 5.5.1)* at increasing the efficiency of the gyro-TWA, whilst at the same time being a much more practical proposition. The average kinetic energy in the electron beam was predicted as a function of axial position for all the gyro-TWAs including a 10cm long helical down taper in their interaction region, *figure 5.5.2.2*. In terms of maximum particle efficiency the inclusion of such helical down tapers into the interaction region of the amplifier (providing the output aperture was reduced below ~0.91[r_0, l]) was shown to increase the efficiency of the device by ~1.3%, from ~32.3% to ~33.6%, at 10.0GHz.
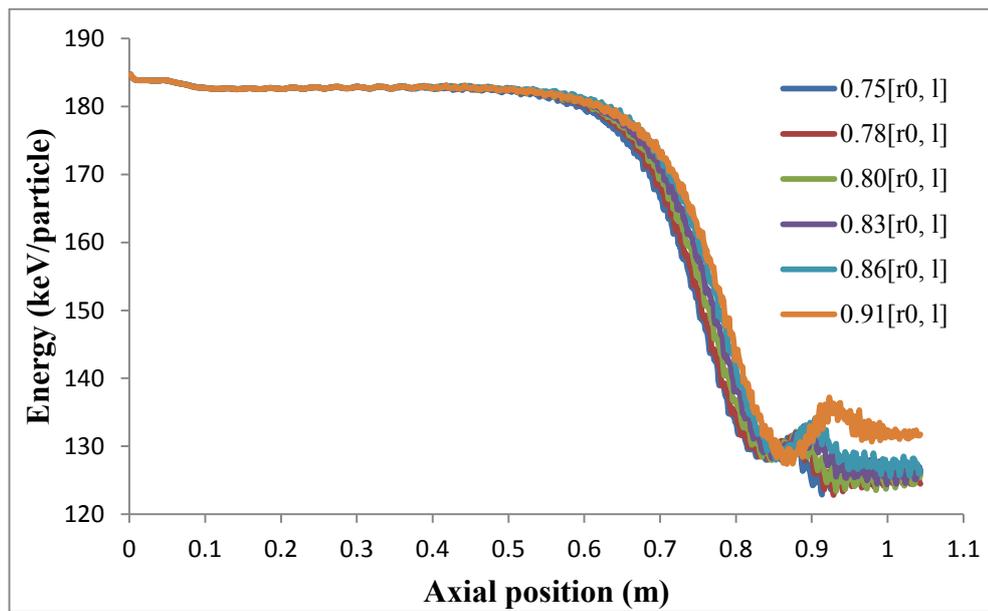
Figure 5.5.2.2: Predicted average kinetic energy of the beam electrons as a function of axial position for gyro-TWAs including 10cm long helical tapers with output mean radii and corrugation amplitudes of ~75% to ~91% of the original values (i.e. from an initial r_0 of 14.1mm and l of 2.2mm). In all instances the uniform helical waveguide measured 52cm with the amplifier operating at 10.0GHz.

There is little to distinguish between the average kinetic energy plots of the beam electrons for those gyro-TWAs with an output circuit measuring between ~0.75[r_0, l] and ~0.86[r_0, l] inclusive. In each instance it was observed that the decelerating electrons reached an initial minima in average kinetic energy at an axial position of ~0.84m prior to transitioning into accelerating phase. In this phase it was observed that the average kinetic energy of the electrons increased by ~3keV, down by between ~15keV and ~30keV when compared to the same data for the gyro-TWAs including

comparatively long and gradual tapers, *figure 5.5.1.2* and *figure 5.5.1.3*. This further suggested that the shorter and more rapid taper dramatically limited the extent to which the electrons could reabsorb energy back from the wave. After this accelerating phase the electrons transitioned back into decelerating phase where they relinquished even more energy to the wave, a characteristic displayed in neither plots for the gyro-TWAs including relatively long and gradual tapers nor the plot for the gyro-TWA including the 10cm long helical taper to an output circuit of ~0.91[r_0, l]. These results combine to suggest that provided the helical down taper was suitably rapid, a gyro-TWA including such a taper could expect to experience a marginal increase in efficiency at 10.0GHz, with the gain of the system as trade-off. This effect can be understood, since in the presence of such a taper, even in the conditions where the electrons phase trap and start to re-accelerate, before they gain significant energy, the rapidly rising dispersion curve soon reverses the detuning to allow further deceleration to take place.

Simulations were also undertaken to determine the amplifier's sensitivity to changes in the length and start position of these more rapid helical tapers i.e. those tapers with an output aperture between ~0.75[r_0, l] and ~0.86[r_0, l] inclusive. Since the performance of the amplifier was predicted to not significantly vary for the 10cm long taper configurations with output apertures between ~0.75[r_0, l] to ~0.80[r_0, l] inclusive, a value within this range was chosen to conduct this analysis. The drive power to the amplifier was kept constant and corresponded to the input power in which maximum particle efficiency was realised for the equivalent 10cm long taper case, with the amplifier operating at 10.0GHz. Thus a taper output aperture of ~0.78[r_0, l] was chosen with the drive power set to ~160W. In the first instance the length of the taper was varied corresponding to a change in the gradient of the taper, *figure 5.5.2.3*.
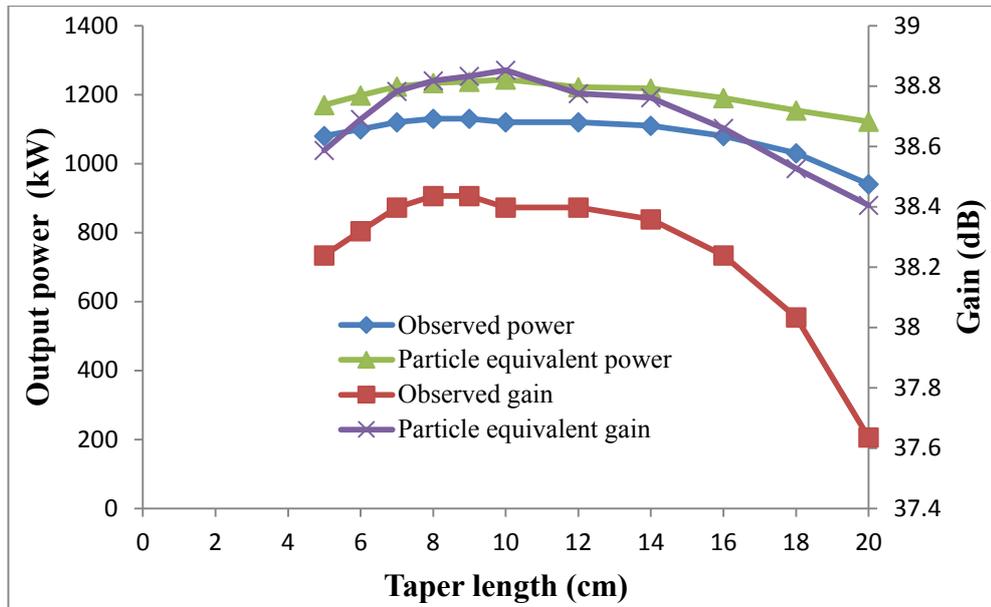
Figure 5.5.2.3: Observed power/gain and particle equivalent power/gain as a function of taper length for a gyro-TWA including a helical down taper with an output mean radius and corrugation amplitude of ~0.78[r_0,l], taken at 10.0GHz for a drive power of ~160W.

The observed power and gain and particle equivalent power and gain were fairly consistent for each taper length with the results suggesting that the amplifier would perform favourably with a helical down taper of lengths between ~7cm and ~14cm, with the performance gradually dropping off outside this range. These results would suggest that the efficiency of the gyro-TWA was largely insensitive to the length of the helical down taper provided the taper was sufficiently short and rapid. The length of the taper was then set to 10cm and the start position of the taper varied, *figure 5.5.2.4*. The original start position of the taper was 0.78m and thus values below and above this would correspond to a decrease and increase respectively in the length of the uniform helical waveguide section of the amplifier. As with the previous simulation the drive power to the amplifier and frequency of operation were set to ~160W and 10.0GHz respectively.
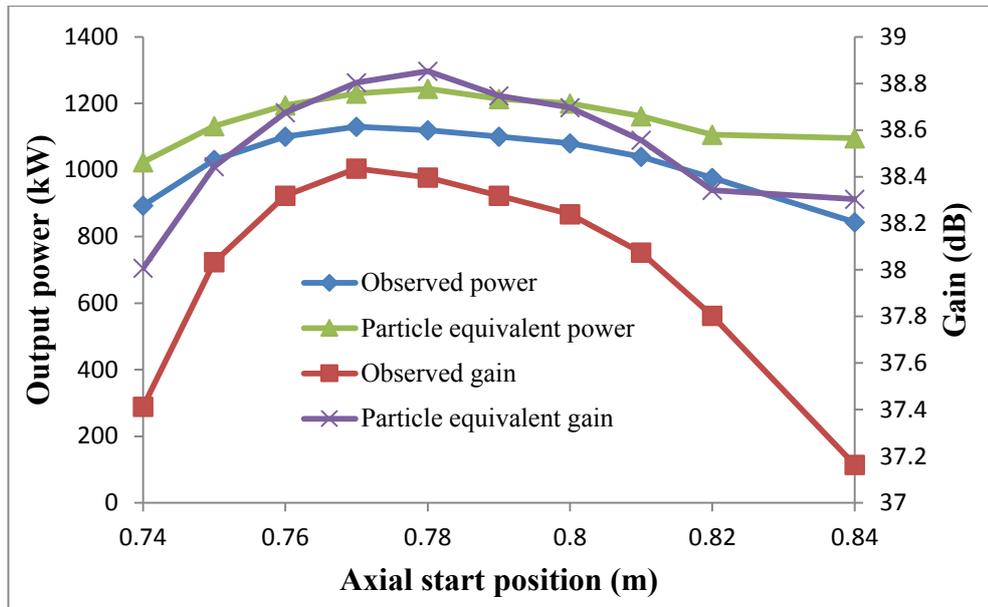
Figure 5.5.2.4: Observed power/gain and particle equivalent power/gain as a function of taper start position for a gyro-TWA including a helical down taper of length 10cm to an output mean radius and corrugation amplitude of ~0.78[r_0, l], taken at 10.0GHz for a drive power of ~160W.

The results show a marginal improvement to particle equivalent power and gain when the 10cm long helical down taper started at an axial position of 0.78m. However the results suggest that the amplifier would perform favourably with a taper start position between ~0.75m to ~0.82m, with the performance having being observed to gradually drop off outside this range. By increasing the start position of the helical down taper to 0.82m it would be anticipated that the gain of the amplifier would increase provided the drive power to the amplifier was suitably configured, since this start position would correspond to a 4cm increase in the length of the uniform helical waveguide section of the amplifier from 52cm to 56cm.

Previous simulation results for the gyro-TWAs including relatively short helical down tapers suggested that the output aperture of the taper had little impact on the performance of the amplifier provided the aperture was sufficiently reduced i.e. by between ~15% and ~25% of the original value. The simulations also suggested that the length and start position of the helical down taper could be increased, without

compromise to output power (providing the input power was suitably adjusted). This would potentially improve the gain of the amplifier. Therefore a gyro-TWA including a 14cm long helical down taper to an output mean radius and corrugation amplitude of ~0.80[r_0, l] starting at an axial position of 0.82m was simulated, to observe the effects this particular taper in the interaction region of the device had on both the output power and gain of the system, *figure 5.5.2.5*. As with previous simulations the amplifier would operate at 10.0GHz but in these simulations, owing to the increased start position of the taper, the uniform helical waveguide section of the amplifier would measure 56cm.
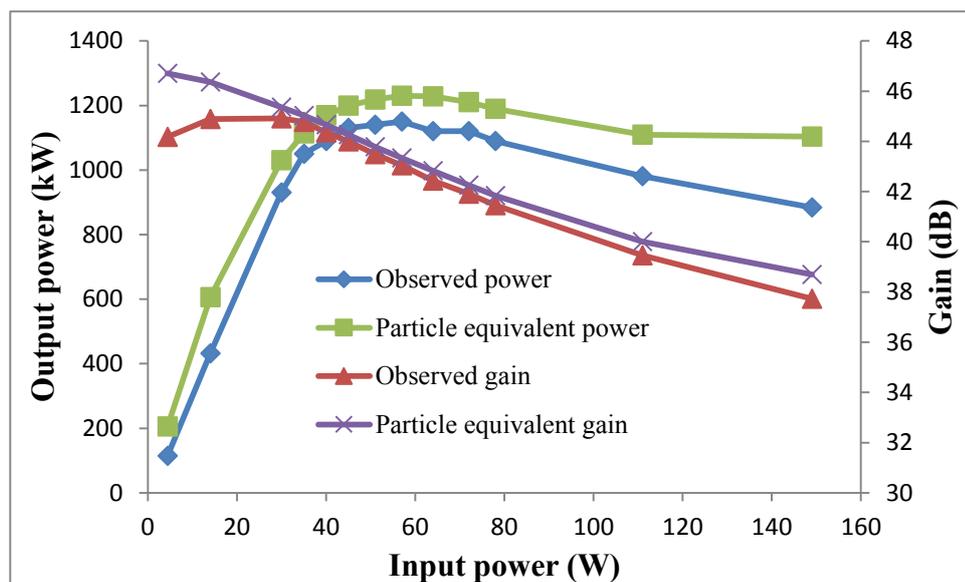
Figure 5.5.2.5: Observed power/gain and particle equivalent power/gain as a function of input power for a gyro-TWA including a 14cm long helical down taper to an output mean radius and corrugation amplitude of ~0.80[r_0, l], at 10.0GHz. The uniform helical waveguide section measured 56cm.

For an input power of ~55W the amplifier achieved an observed power of ~1.15MW and gain of ~43dB, corresponding to an observed saturated efficiency of ~31.1%. Hence this particular taper was observed to increase the saturated efficiency of the amplifier by ~2.5%, from ~28.6% to ~31.1%, a slight improvement in efficiency over the 10cm long helical taper configurations. For this same drive power the particle equivalent power and gain were predicted to be up to ~1.23MW and ~43.3dB respectively corresponding to a particle equivalent efficiency of ~33.2%. Moreover

the observed gain of the amplifier increased from an on average ~39dB for the 10cm long taper configurations to ~43dB, primarily due to the slightly extended region of the uniform helically corrugated waveguide. This result represented a better design compromise, more closely matching the gain of the control amplifier at 10.0GHz i.e. ~45.6dB.

In summary, modification of the original gyro-TWA geometry to include a relatively short and rapid helical down taper towards the output of the interaction region of the device was observed to marginally increase the efficiency of the amplifier at 10.0GHz. With the gyro-TWA modified to include a 14cm long helical down taper to an output mean radius and corrugation amplitude of ~0.80[r_0, l] positioned immediately after a 56cm long section of uniform helical waveguide, an observed power of ~1.15MW and gain of ~43dB at 10.0GHz were predicted. This result corresponds to an observed saturated efficiency of ~31.1% and represents a ~2.5% increase in the efficiency predicted for the reference amplifier i.e. from ~28.6% to ~31.1%. The original optimised gyro-TWA simulation and experiment were already reasonably efficient however this potential increase in efficiency could help reduce the requirements on the ancillary components comprising the full system. However for all the results presented the addition of a helical down taper towards the output of the interaction region of the amplifier served to decrease the gain of the device. This could be readily recovered by extending the uniform section of the amplifier, though it should be noted that arbitrarily extending the length of an amplifier brings additional practical issues.

5.6: Impact of the tapers on the device bandwidth

A limited but nonetheless welcome improvement to the efficiency of the gyro-TWA was observed when the output circuit of the amplifier included a 14cm long helical down taper to an output mean radius and corrugation amplitude of ~0.80[r_0, l], increasing the observed saturated efficiency of the amplifier by a modest ~2.5% at

10.0GHz i.e. from ~28.6% to ~31.1%. However, as detailed in *section 5.4,* there is also evidence to suggest that such a tapering strategy could significantly improve the bandwidth of the amplifier and this, together with the efficiency improvement, would make the helical taper a very worthwhile and beneficial inclusion into the gyro-TWA interaction region. Therefore the simulations of the gyro-TWA with this helical down taper were revisited to investigate the potential for bandwidth enhancement. A modification of the amplifier geometry was required for this investigation and appeared towards the input of the amplifier (LHS of uniform helical waveguide in *figure 5.2.2.5*). Up to this point all the amplifier geometries included a short section of cylindrical waveguide towards the input i.e. before the cylindrical to helical converter, which had a radius of 14.1mm. In this section of waveguide the TE_{21} mode is cut-off up to a frequency of ~10.3GHz and was therefore unable to propagate to the reflection taper and back through the helical interaction region for all frequencies of interest in previous simulations (at 10.4GHz it was observed that the TE_{21} mode radiated out of the system in the benchmark simulations). However extending the frequency of operation above 10.3GHz in the gyro-TWA with the helical down taper, without modifying the input cylindrical waveguide, would allow both the TE_{11} mode and TE_{21} mode to propagate to, and reflect off, the reflection taper and back through the helical interaction region. It was anticipated that the energy propagating in the TE_{21} mode in this upstream waveguide could interact either constructively or destructively with the uncoupled and coupled waves of the TE_{11} mode in this section of cylindrical waveguide (since the two modes have different propagation constants) and potentially skew the gain predictions of the amplifier. Therefore to eliminate this possibility as the frequency of operation was extended above 10.3GHz, the radius of the input cylindrical waveguide was reduced, *figure 5.6.1.*
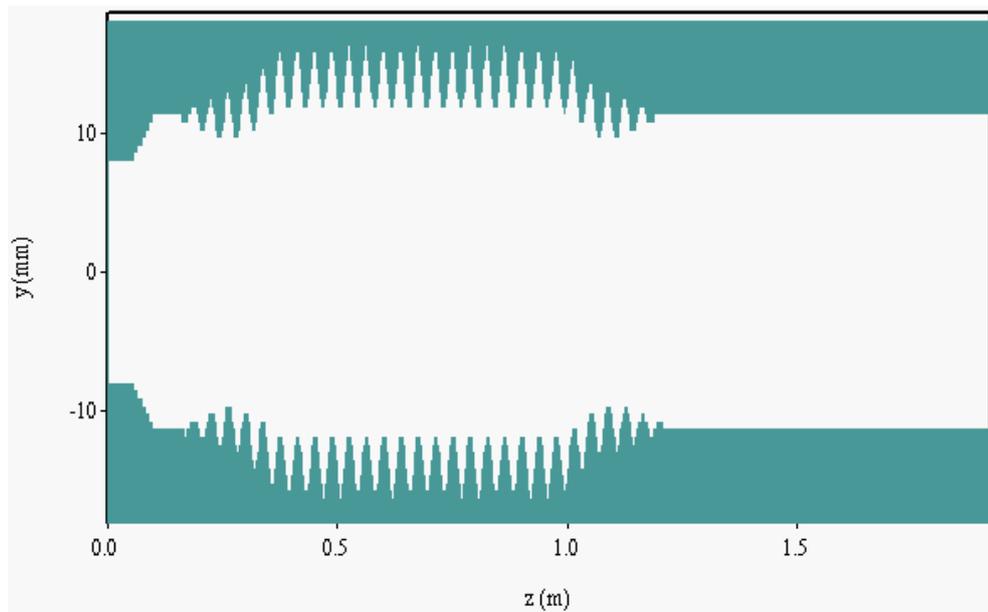
Figure 5.6.1: A gyro-TWA geometry with a 14cm long helical up taper with an initial mean radius and corrugation amplitude of 0.80[r₀, l] to final values of [r₀, l], taken from MAGIC-3D. The up taper is the inverse of the helical down taper which features towards the output of the interaction region of the amplifier. This geometry is primarily that of figure 5.2.2.5, but with the addition of a helical up taper positioned immediately before the uniform helical waveguide section.

The radius of the input cylindrical waveguide was reduced by 20% to a value of ~11.3mm. This reduction in waveguide radius was chosen as it would easily ensure that the TE_{21} mode was cut-off for all frequencies of interest (indeed the cut-off frequency for this mode in this section of waveguide is ~12.9GHz) whilst ensuring that the TE_{11} mode was allowed to propagate at the lowest frequency of interest i.e. 8.2GHz (the cut-off frequency for the TE_{11} mode in this waveguide is ~7.8GHz). Thus this reduction in radius should be more than adequate to both determine the bandwidth of the amplifier and accurately calculate the gain of the system for all frequencies of interest. The inclusion of this helical up taper and subsequent reduction to the mean radius of both the cylindrical to helical converter and the input cylindrical waveguide should have no bearing on the performance of the amplifier at frequencies below 10.3GHz. To verify this a selection of simulations at frequencies between 8.2GHz and 10.2GHz were run using both geometries (see *figure 5.2.2.5* and *figure 5.6.1*) with equivalent simulations yielding comparable results.

The optimisation process of the control amplifier, as detailed in *chapter 4,* highlighted that the drive power required to achieve optimum output power at 9.4GHz was substantially greater than that required at 10.0GHz i.e. ~105W at 9.4GHz and ~30W at 10.0GHz. This is consistent with predictions of the content of the upper mode i.e. the TE_{21} mode in the operating eigenwave as frequency is increased (*section 5.4*). Therefore to determine the bandwidth of the gyro-TWA with the optimised tapered microwave circuit it was elected, for each frequency of interest, to sweep the drive power to the device, *figure 5.6.2.* From this data the optimum drive conditions, output power and efficiency of the amplifier could be ascertained. Therefore simulations were run between 8.2GHz to 11.1GHz inclusive. At 11.1GHz it was observed that the gain of the amplifier had substantially reduced and therefore 11.0GHz was taken to be the upper bandwidth limit of the beam-wave interaction underpinning the amplifier, in spite of the amplifier achieving an observed power within the conventionally accepted -3dB power performance limit at 11.1GHz.
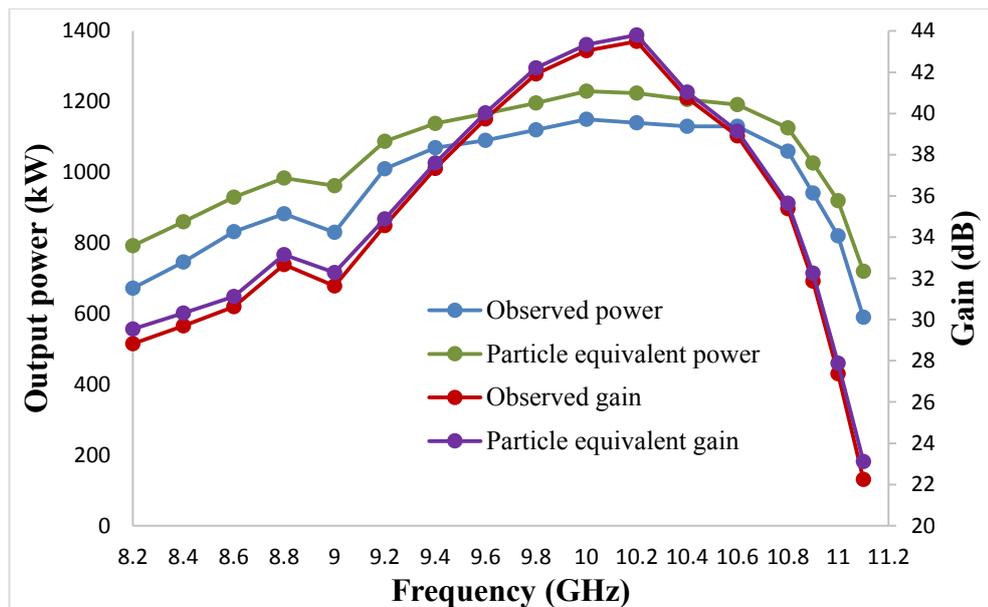
Figure 5.6.2: Observed power/gain and particle equivalent power/gain as a function of frequency (with optimised input power) for the gyro-TWA which included a 14cm long helical down taper to an output mean radius and corrugation amplitude of ~0.80[r_0, l] positioned towards the output of the interaction region of the device. In all simulations the uniform helical waveguide section measured 56cm.

Between 9.2GHz and 10.8GHz inclusive the amplifier achieved an observed output power of greater than 1.0MW, peaking at ~1.15MW at 10.0GHz. At the lower and upper limits of the spectral range i.e. 8.2GHz and 11.0GHz the observed output power was predicted to be ~670kW and ~820kW respectively with this lower power falling just within the -3dB power performance limits to define the bandwidth of the amplifier. This gives the amplifier a relative bandwidth of ~29.2%, an increase of close to 8% when compared to the control amplifier which had a relative bandwidth of ~21.5% (assuming the benchmark amplifier performed as anticipated at 8.2GHz). This represents a significant improvement to the bandwidth of the amplifier. It is also relevant to note that over the range 9.6GHz to 10.6GHz the enhanced amplifier demonstrated a flat gain response with a total variation of only ~4dB, this bodes well for its ability to amplify relatively wideband signals faithfully.

To ensure the TE_{21} mode was cut-off and unable to radiate out at the upper bandwidth limit i.e. 11.0GHz, the output circuit mean radius of the interaction region need only reduce to ≤ ~13.25mm. This would represent a decrease from the output circuit mean radius of the original amplifier of ~6%. However simulation results presented here *(section 5.5.2)* suggested that operating with a relatively short helical taper with an output circuit mean radius reduced by less than ~9% of the original value would compromise the maximum output power of the instability when compared to helical tapers of the same length with a reduced circuit mean radius of between ~15% and ~25%. Thus to experience the greatest performance benefits in terms of both efficiency and bandwidth from the inclusion of a helical down taper the results would suggest that the output circuit mean radius of the amplifier should be significantly reduced below this ~6% minimum limit.

In summary, a 14cm long helical down taper to an output mean radius and corrugation amplitude of ~0.80[r_0, l] positioned towards the output of the interaction region of the gyro-TWA was observed to increase both the efficiency and bandwidth of the amplifier by ~2.5%, from 28.6% to 31.1%, at 10.0GHz and by 800MHz respectively.

5.7: Direct tapering to circular aperture

All tapers presented thus far were designed to approximately maintain the coupling coefficient, σ, (or more exactly the dispersion group velocity) of the two partial rotating waves along the profiled interaction region of the gyro-TWA, *figure 5.2.2.1*. To realise this, both the input and output of the down taper had a 3-fold helical cross-section with the same profile, with the output at a reduced mean radius and corrugation amplitude to the input. Here an alternative tapering strategy would be investigated with the taper designed to convert from a 3-fold helical waveguide cross-section of mean radius r_0 i.e. 14.1mm and corrugation amplitude l i.e. 2.2mm to a cylindrical cross-section with a reduced mean radius of $\sim 0.80*r_0$ and corrugation amplitude of 0, *figure 5.2.2.2*. In this tapering strategy no attempt is made to maintain the group velocity of the operating eigenwave along the transition. Implementation of this type of down taper removes the need for a separate helical down taper and helical to cylindrical converter as featured in previous simulations *(section 5.5* and *section 5.6)*. As such the tapered helical to cylindrical converter would combine both the length (14cm) and output mean radius of the helical down taper which showed the greatest efficiency enhancement of the gyro-TWA at 10.0GHz, with the length of the original 12cm long helical to cylindrical converter to give a tapered helical to cylindrical converter of length 26cm to an output mean radius $\sim 0.80*r_0$, *figure 5.7.1*. The start position of this direct down taper to cylindrical waveguide would correspond to an axial position of 0.82m to match the simulations in *figure 5.5.2.5* which showed the greatest efficiency potential. This start position would correspond to a uniform helical waveguide section of length 56cm.

146
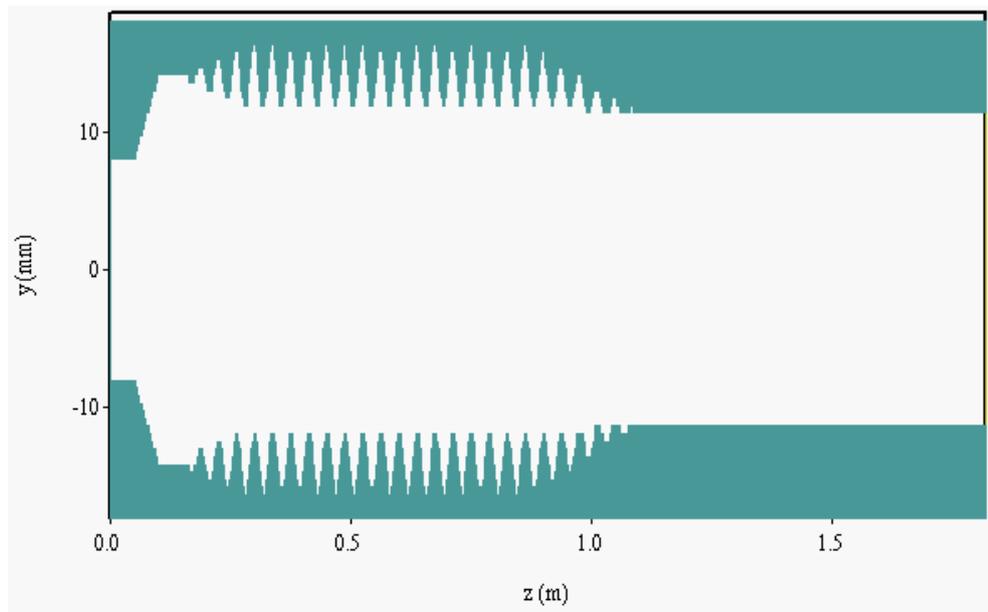
Figure 5.7.1: Simulation geometry taken from MAGIC-3D showing a 26cm long tapered helical to cylindrical converter towards the output of the interaction region of the gyro-TWA with an output radius of ~0.80*r$_0$. In this geometry the uniform helical waveguide section measured 56cm in length.

As with previous efficiency simulations the drive power to the amplifier was varied with the drive signal set at 10.0GHz, *figure 5.7.2.*
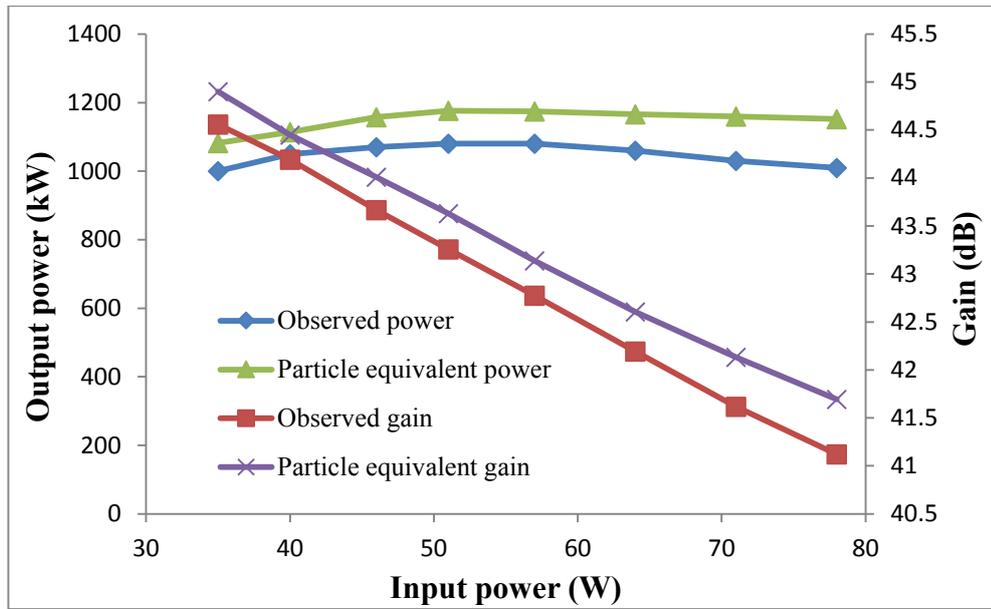
Figure 5.7.2: Observed power/gain and particle equivalent power/gain as a function of input power for a gyro-TWA including a 26cm long tapered helical to cylindrical converter with an output radius of ~0.80*r₀, at 10.0GHz. Here the uniform helical waveguide section of the amplifier measured 56cm.

For an input power of ~50W the amplifier achieved an observed power of ~1.08MW and corresponding gain of ~43.3dB. If it is assumed that the electrons became unconstrained at the position of minimum average kinetic energy, *figure 5.7.3,* then this amplifier could hope to achieve a particle equivalent power and gain of up to ~1.18MW and ~43.6dB respectively. However the amplifier which included a separate 14cm long helical down taper and adjoining helical to cylindrical converter with the same output radius of ~0.80*r_0 achieved an observed power of ~1.15MW and gain of ~43dB. When particle equivalent power and gain were considered these values increased to up to ~1.23MW and ~43.3dB, *figure 5.7.3.* The gain of each amplifier was comparable however the observed power and particle equivalent power of the amplifier with the direct 26cm long helical to cylindrical converter was down by ~70kW and ~50kW respectively on that of the amplifier with the compound taper i.e. the 14cm long helical down taper and separate 12cm long helical to cylindrical converter.
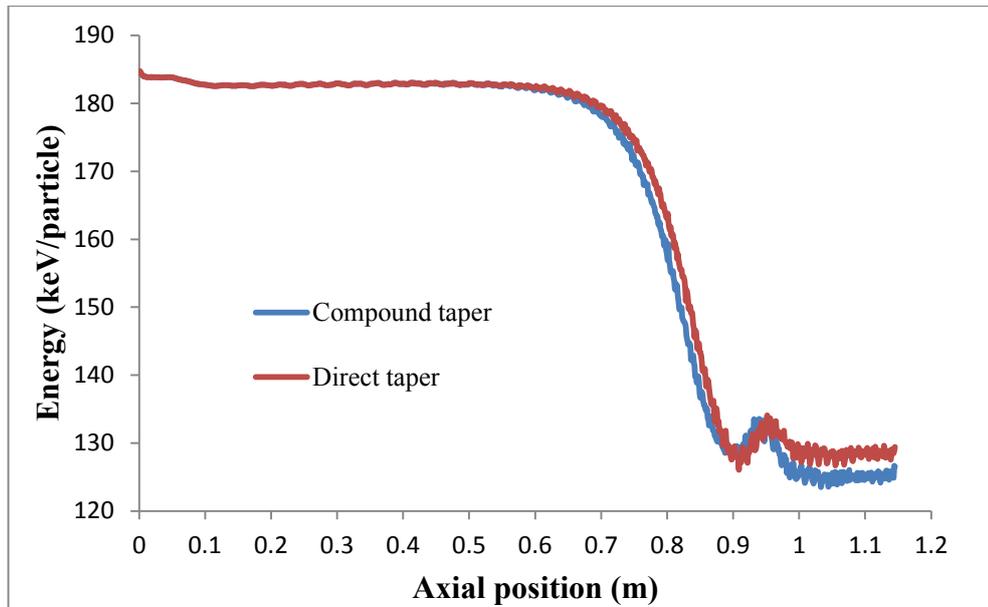
Figure 5.7.3: Predicted average kinetic energy of the beam electrons as a function of axial position for a gyro-TWA including a 14cm long helical down taper with an adjoining 12cm long helical to cylindrical converter to an output radius of ~0.80*r₀ i.e. the compound taper, and for a gyro-TWA including a 26cm long direct helical to cylindrical converter to an output radius of ~0.80*r₀, at 10.0GHz i.e. the direct taper. In each instance the uniform helical waveguide section measured 56cm in length.

The plots of average electron kinetic energy as a function of axial position for these two configurations were similar up to an axial position of ~0.95m. In both instances the initial minima in average kinetic energy was observed around ~0.90m. After this position the electrons, in each instance, transitioned into accelerating phase with the average kinetic energy of the electrons increasing by ~3keV. After this accelerating phase the electrons transitioned back into decelerating phase. It is at this transition that the two average kinetic energy plots show significant variation with the average kinetic energy of the electrons in the gyro-TWA with the compound taper less than that of the device with the direct taper. Indeed the average kinetic energy of the electrons in the direct taper configuration in decelerating phase was at best comparable to the initial minimum observed at ~0.90m. However in the compound taper configuration the average kinetic energy of the electrons in this decelerating phase was less than the initial minimum. The implementation of a direct taper to cylindrical waveguide yielded an observed saturated efficiency of ~29.2% at 10.0GHz, a drop of

~1.9% from ~31.1% when compared to the compound taper configuration at the same frequency. These results suggest that a compound taper which seeks to extend the length of the interaction region is superior to a similar taper which directly transitions to a smaller cylindrical waveguide (and hence does not particularly extend the interaction length).

In summary, the replacement of the 14cm long helical down taper and adjoining 12cm long helical to cylindrical converter to an output radius of ~$0.80*r_0$ with a 26cm long tapered helical to cylindrical converter to an output radius of ~$0.80*r_0$, was observed to decrease the saturated efficiency of the amplifier by ~2% i.e. from ~31.1% to ~29.2%. Indeed the inclusion of this latter direct tapering strategy in the output of the interaction region of the gyro-TWA represented an increase in saturated efficiency of only ~0.6% when compared to the original gyro-TWA *(chapter 4)* operating at the same frequency. It would however be expected that this amplifier would still benefit from the increased bandwidth capabilities over the original gyro-TWA as a result of the decreased diameter of the output circuit of the device. Nonetheless the greater performance predicted by the inclusion of the compound taper makes this tapering strategy a more attractive alternative.

Chapter six: Marie-type converter

6.1: Overview

It was originally anticipated that this research project might investigate the potential performance improvements to cyclotron autoresonance maser amplifiers (CARMs) through system parameter profiling [Bandurkin, 2004 and Savilov, 2002] in addition to an X-band 2nd harmonic gyro-TWA with a helically corrugated interaction waveguide. In each amplifier different parameters would be profiled. For the gyro-TWA simulations, the interaction region of the device was tapered towards the output *(chapter 5)* whilst the CARM simulations would implement a tapered confining magnetic field to potentially enhance the performance of the device.

Gyro-TWAs with helically corrugated interaction waveguides have a range of practical applications and are relevant to industry. These devices already realise reasonably high efficiencies but the potential for further performance improvements makes these devices even more applicable and desirable to industrial applications. In contrast, whilst CARMs have scope to be efficient sources of coherent and broadband radiation, in practice they typically realise relatively low efficiencies as a consequence of the interaction's sensitivity to beam velocity spread. Due to this it is difficult to create an efficient CARM amplifier in a laboratory experiment.

Initially the research on the CARM amplifier would have considered cylindrical TE_{01} mode systems since this mode has low transmission loss and is of significant practical importance for applications where lengthy waveguide runs or high frequency operation are required [Wolfert, 1963]. The TE_{01} mode is not the fundamental mode in cylindrical waveguide and as such a device operating in this mode would require a complex input coupler, with the testing of any components e.g. cavities and Bragg reflectors demanding a wideband transformer with high mode purity.

To excite the cylindrical TE_{01} mode from the fundamental mode in standard single mode rectangular waveguide typically requires a converter with intricate internal geometry (unlike the simple sidewall converters used for excitation of the cylindrical TE_{11} mode). Typically inline coupled converters are used which make use of deformed waveguide structures. These converters can have extensive transition lengths with examples for rectangular TE_{10} to cylindrical TE_{01} mode conversion including the Sector-type [Xue, 2005], Twin-Sector-type [Southworth, 1950] and the Marie-type [Cairns, 1997] mode converter. Here a slightly modified X-band Marie-type converter geometry was considered, with this design chosen predominantly for ease of fabrication as the inner geometric structure of the device is simply a series of straight lines which could be fabricated using the technique of wire erosion. The converter was simulated in the modelling suite CST Microwave Studio (*chapter 3)* and fabricated in aluminium with the simulation results experimentally verified using a vector and scalar network analyser (VNA/SNA). Although the CARM project was not pursued, it was appreciated that the mode converter had alternate applications and therefore this component was completed and tested. The mode converter was used to test a radiation transparent cathode for a Penning trap required for a simulation of auroral radio wave production which was intended to radiate in the TE_{01} mode in cylindrical waveguide.

6.2: Simulation results of the Marie-type converter

The Marie-type converter designed and used in this project [Saad, 1977] had an operational frequency of 9.0GHz, optimised for 2.0GHz bandwidth, and comprised of three equal length main sections together with an additional small taper section (appearing between the output of section 1 and the input of section 2), *figure 6.2.1*. The structure was chosen such that the number of sections comprising the converter were at a minimum to reduce reflections and spurious mode excitation. With each section manufactured by cutting straight lines through metal with a wire erosion system the length of each section was limited by the capacity of the largest wire erosion machine available at the time of fabrication. As such the three main sections of the converter were each just over 30cm in length with the additional small taper section 3cm in length making the total length of the converter ~94cm. At the input of the converter the rectangular waveguide had major and minor axis dimensions of ~26.2mm and ~10.6mm respectively with the output cylindrical aperture of the converter measuring ~6cm in diameter. The closest standard waveguide dimensions to these input dimensions were WG16 which has major and minor axis dimensions of 22.86mm and 10.16mm respectively. Thus to connect the input rectangular waveguide of the fabricated Marie-type converter to the WG16 test kit a small rectangular transition section of 3cm was fabricated. This section was in addition to the small taper used to smoothly transition between the output of section 1 and the input of section 2 of the converter and does not appear in the simulations.
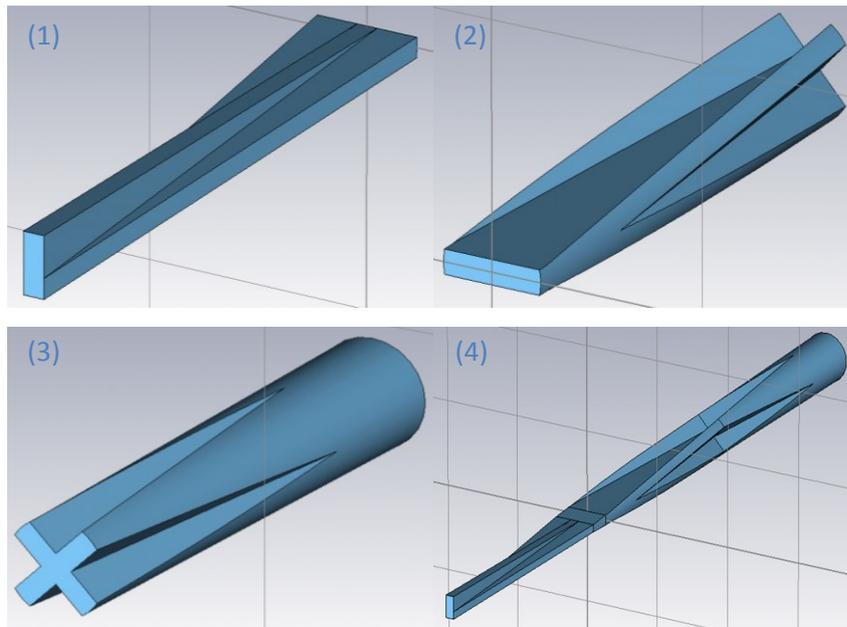
Figure 6.2.1: *The three main sections ((1), (2) and (3)) and the full 3D representation (4) of the Marie-type converter which includes a 3cm taper between the output of section 1 and the input of section 2, taken from CST Microwave Studio.*

The Marie-type converter design was frequency scalable with this demonstrated in the design and simulation of a second converter operational at centre frequency 5.2GHz and optimised for 1.0GHz bandwidth (approximately comparable to the 2.0GHz bandwidth of the 9.0GHz converter). This 5.2GHz converter had three main sections each just over 52cm in length with the major and minor axis dimensions of the input rectangular waveguide measuring ~45.4mm and ~18.3mm respectively. The output cylindrical aperture of the converter had a diameter of ~10.4cm. To date this Marie-type converter has not been fabricated.

As previously mentioned a small taper transition *(figure 6.2.1(4))* was required between the output of section 1 *(figure 6.2.1(1))* and the input of section 2 *(figure 6.2.1(2))* with this transition appearing in both the 5.2GHz and 9.0GHz converter structures. Here the objective was to establish a suitable length of taper which

154

sufficiently minimised reflections without considerably increasing the overall length of the Marie-type converter. As such two taper lengths were initially considered, the first of length 0.5cm and the second of length 3cm. The S-parameter results for the Marie-type converters incorporating these two tapers are presented in *figure 6.2.2* and *figure 6.2.3* with these results suggesting that the 3cm taper significantly outperformed the 0.5cm taper for both converters, by reducing reflections across their respective frequency bandwidths. This correlates well with the expectation that reflections are minimised if the tapering transition is smooth and gradual.
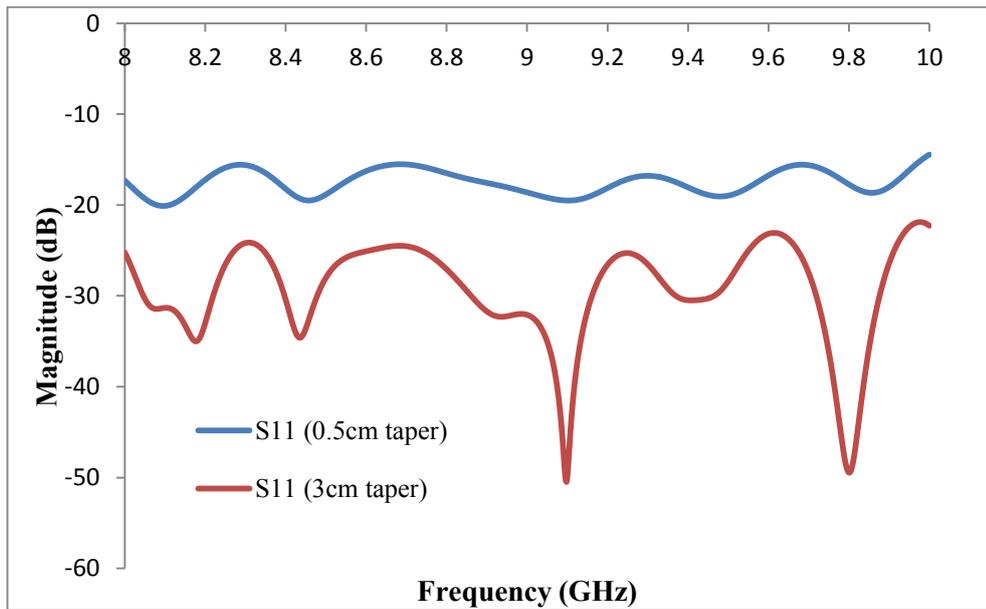
Figure 6.2.2: S-parameter plots for the 9.0GHz Marie-type converter with a 0.5cm taper and a 3cm taper transition between the output of section 1 and the input of section 2.

The S-parameter plot for the 9.0GHz Marie-type converter suggested that by using a transition taper of length 0.5cm it would be expected that the forward reflection (S_{11}) for the converter across the frequency bandwidth would be less than -15dB. However an increase in transition taper length to 3cm was expected to reduce the forward reflection to less than -20dB across the frequency bandwidth.

Similarly the S-parameter plot, *figure 6.2.3,* for the 5.2GHz Marie-type converter suggested that the 3cm transition taper outperformed the 0.5cm taper.
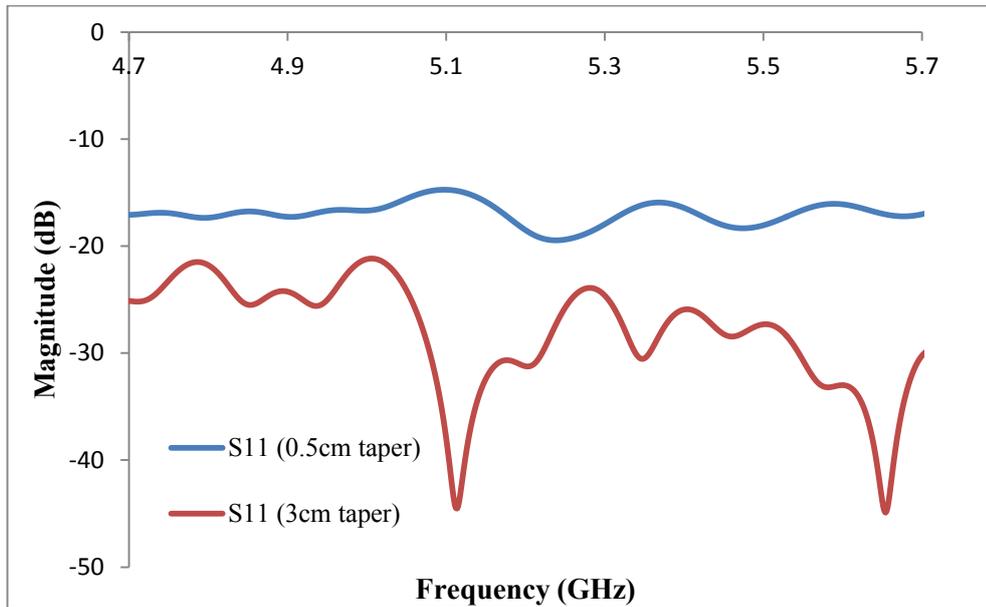
Figure 6.2.3: *S-parameter plots for the 5.2GHz Marie-type converter with a 0.5cm taper and a 3cm taper transition between the output of section 1 and the input of section 2.*

The observed forward reflection for the 0.5cm transition taper for the 5.2GHz converter was approximately -15dB between 4.7GHz and 5.7GHz with this reducing to approximately -20dB or less when the taper length was increased to 3cm. To scale with the 9.0GHz converter, the 3cm transition taper of the 5.2GHz converter should have been approximately doubled, however the performance of the 3cm taper over the entire frequency range was more than adequate. Since the 3cm taper performed well for both the 5.2GHz and 9.0GHz converters and did not contribute greatly to the overall length of each converter, no other taper lengths were considered and all further results presented include this 3cm taper transition between the output of section 1 and the input of section 2, *figure 6.2.1(4)*.

For each simulated converter, field monitors, *figure 6.2.4* and *figure 6.2.5*, located at the input and output sections of the device suggested effective conversion from the rectangular TE_{10} to cylindrical TE_{01} mode as desired.
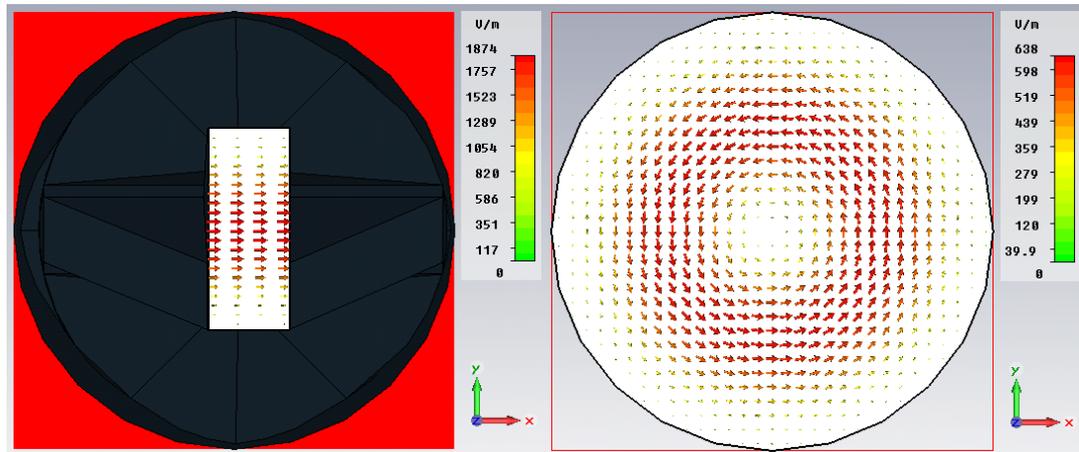
Figure 6.2.4: *Vector electric field distribution patterns (modes) at the input and output of the 9.0GHz Marie-type converter respectively, taken from CST Microwave Studio.*
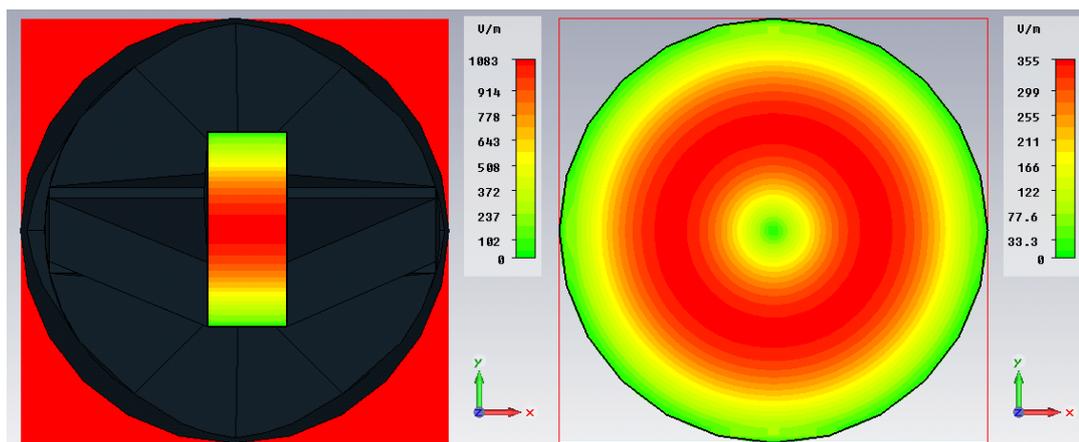
Figure 6.2.5: *Contour electric field distribution patterns (modes) at the input and output of the 5.2GHz Marie-type converter respectively, taken from CST Microwave Studio.*

Electric field monitors were also distributed along the length of the Marie-type converter at the input and output to each of the three main sections of the device, *figure 6.2.6*. These monitors clearly show the evolution of the electric field and the field intensity at various locations in the structure. Also shown is the progression of the mode conversion from the rectangular TE_{10} to the cylindrical TE_{01} mode and how the

inner geometrical structure of the device progressively manipulates the fields to realise this conversion.
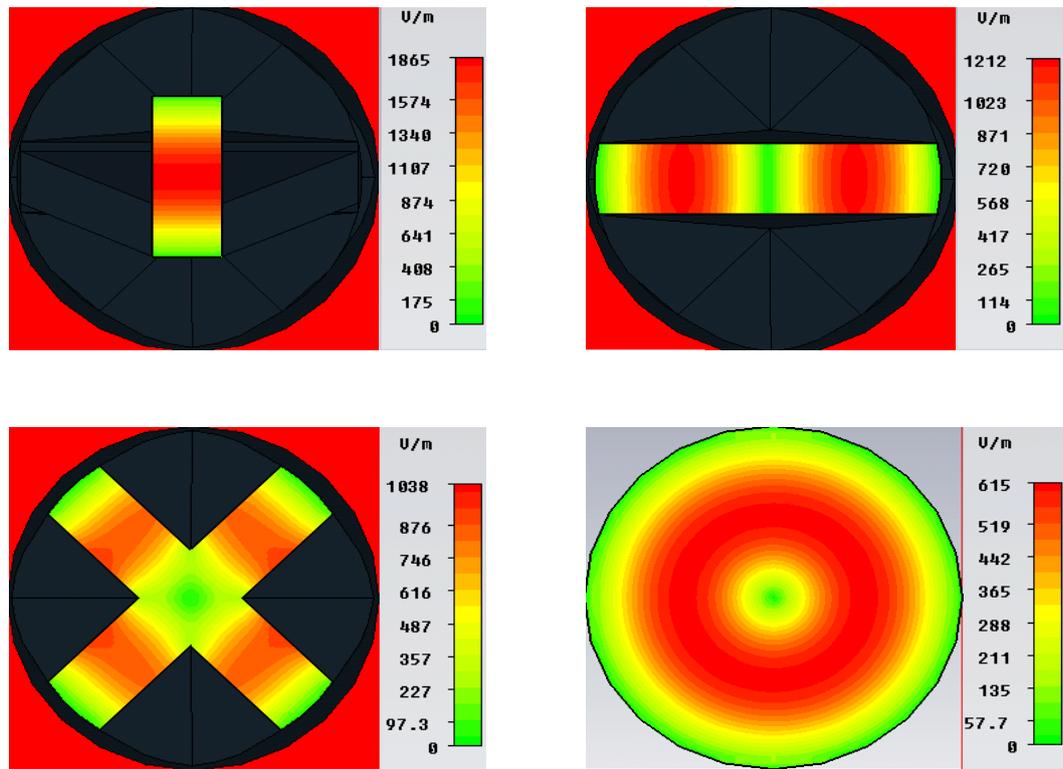
Figure 6.2.6: *Mode patterns at the input and output for each main section of the Marie-type converter with operating centre frequency of 9.0GHz.*

S-parameter plots, *figure 6.2.7*, reaffirm this observation with coupling efficiency into the cylindrical TE_{01} mode of better than 98% with a reflection coefficient of less than 1% over the frequency bandwidth for the 9.0GHz converter. Coupling into all undesired modes supported by the device was less than 1%.
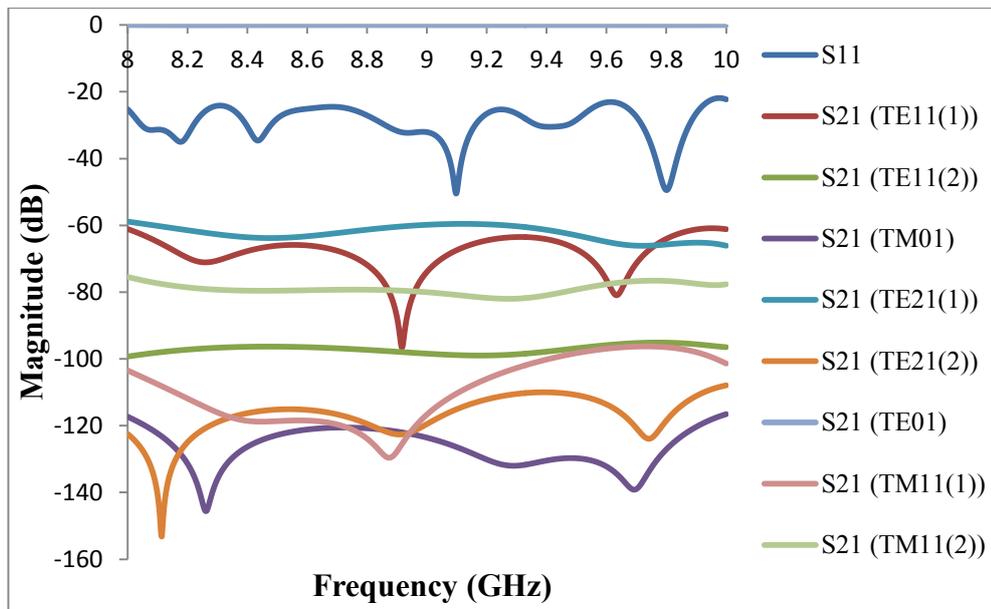
Figure 6.2.7: *S-parameter plot for the 9.0GHz Marie-type converter.*

The S-parameter plot shows the more dominant modes in the structure and suggests that coupling into these modes (TE_{11}, TE_{21}, TM_{01} and TM_{11}) was negligible. Here modes with both azimuthal and radial variations, i.e. the TE_{11}, TE_{21} and TM_{11} are represented in two polarisations with both S_{21} predictions plotted. Predicted results for the 5.2GHz converter are shown in *figure 6.2.8*.
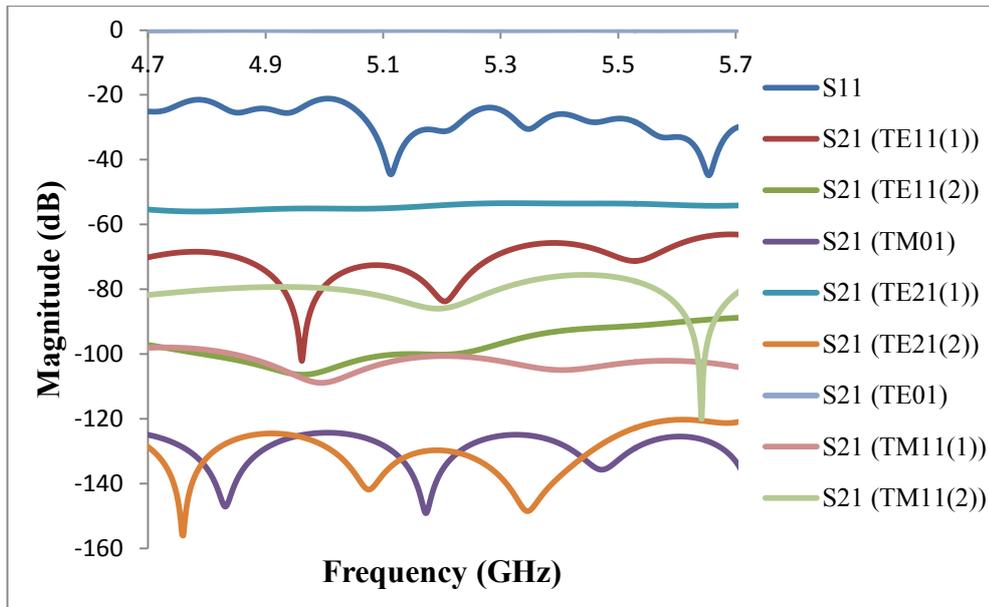
Figure 6.2.8: *S-parameter plot for the 5.2GHz Marie-type converter.*

The S-parameters for the 5.2GHz Marie-type converter, *figure 6.2.8,* suggested coupling efficiency into the cylindrical TE_{01} mode of better than 98% with a reflection coefficient of approximately -20dB or less across all of the optimised frequency bandwidth. Over the 1.0GHz optimised bandwidth the performance of the 5.2GHz converter was similar to that of the 9.0GHz converter. As has been demonstrated by the 9.0GHz design, coupling into other modes supported in the 5.2GHz structure such as the $TE_{11,}$ $TE_{21,}$ TM_{01} and the TM_{11} mode were negligible, with the most significant impact of the shorter normalised taper transition length (L/λ) the increase in transmission of the TE_{21} mode.

6.3: Experimental measurements of the 9.0GHz Marie-type converter

The promising predicted performance of the simulated 9.0GHz Marie-type converter *(section 6.2)* merited the fabrication of the device. Due to limitations in the wire erosion process used to fabricate the converter a slight modification of the converter design was required. This modification appears in the complex middle section *(figure 6.2.1(2))* but was a marginal deviation from the actual simulated design such that overall device performance was not affected.

A vector network analyser (VNA) was calibrated using an offset-short-load calibration and the Marie-type converter connected to one port. An anechoic environment was created from radiation absorbent material and positioned a short distance away from the output aperture of the converter to minimise potential reflections from the surroundings. The S_{11} measurement from the VNA showed that the level of reflection in the converter was less than -20dB across the whole frequency bandwidth, *figure 6.3.1*, with this in good agreement with that predicted by CST Microwave Studio.
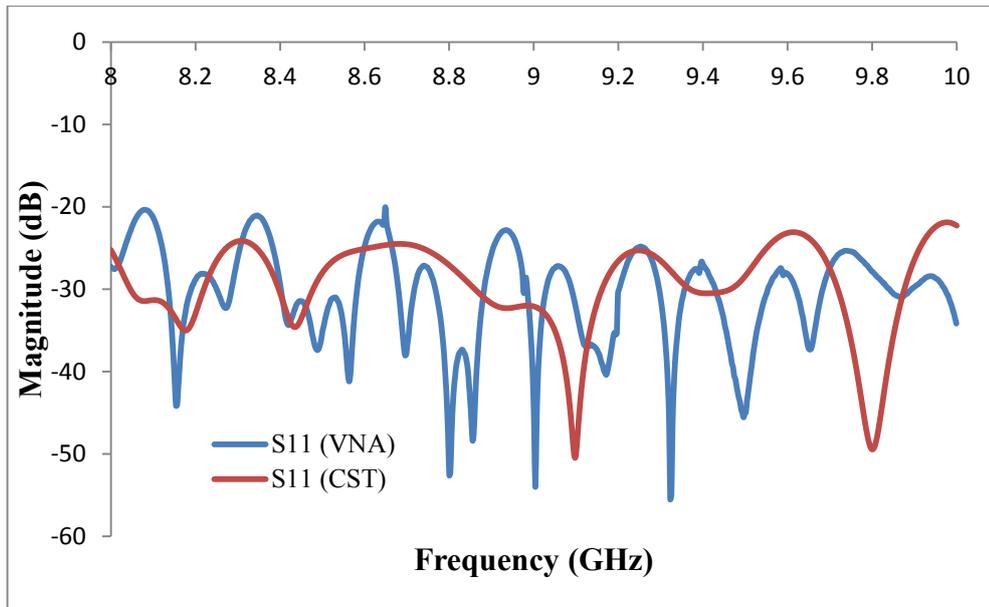
Figure 6.3.1: Plot showing the forward reflection coefficient (S_{11}) measured with the VNA alongside that predicted by CST Microwave Studio for the 9.0GHz Marie-type converter.

The forward transmission coefficient of the converter could not be directly determined as only one converter was fabricated. This made it impossible to directly measure the transmission through to the second port of the VNA since the cylindrical output aperture of the converter could not be down converted back to the rectangular waveguide required to connect the DUT (Device Under Test - the Marie-type converter) to the VNA. However far field measurements with varying orientation of the Marie-type converter combined with orientation of the receiving antenna were undertaken, with the receiving antenna positioned a set distance of ~83cm from the output aperture of the converter on a 180^0 rotating arm (*chapter 3*).

The measurements obtained using the SNA at each orientation (0^0, 45^0 and 90^0) of the Marie-type converter (*chapter 3*) confirmed that the output radiation was that of a well-defined cylindrical TE_{01} mode. The results show the azimuthal, *figure 6.3.2,* and radial, *figure 6.3.3,* polarisation components of the output radiation for the case of 0^0 orientation of the converter across the entire frequency bandwidth, scanned from -55^0 to 55^0 in 1^0 increments. Here it was observed that there was very little deviation in

field profile over the frequency range and that the mode was always well-defined and TE_{01}. This is evidenced by the weak signal observed in the radial polarisation compared to the strong, single lobed structure observed in the azimuthal polarisation.
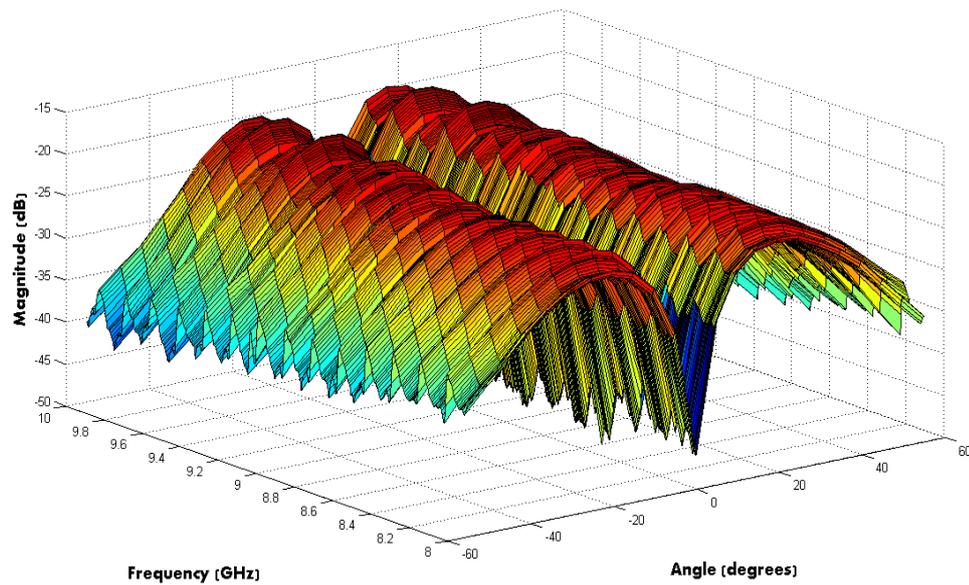
Figure 6.3.2: *3D plot of the far field azimuthal polarisation component across the entire frequency bandwidth, measured with the SNA.*
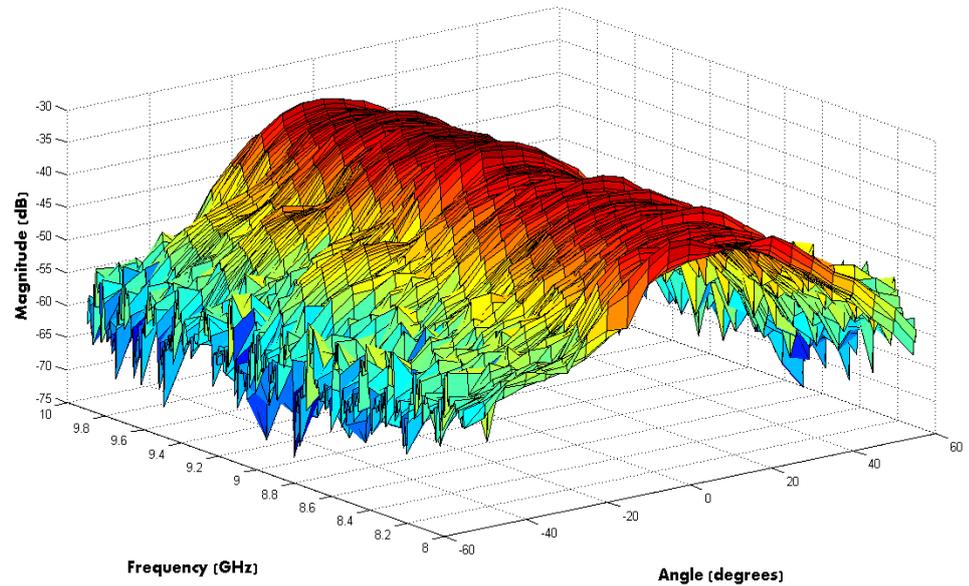
Figure 6.3.3: *3D plot of the far field radial polarisation component across the entire frequency bandwidth, measured with the SNA.*

Plots taken at the centre frequency of 9.0GHz with varying orientation of the Marie-type converter confirmed that the output mode was that of a well-defined cylindrical TE_{01} mode, *figure 6.3.4* and *figure 6.3.5*. Here the receiving antenna was scanned from -55^0 to 55^0 in 5^0 increments.
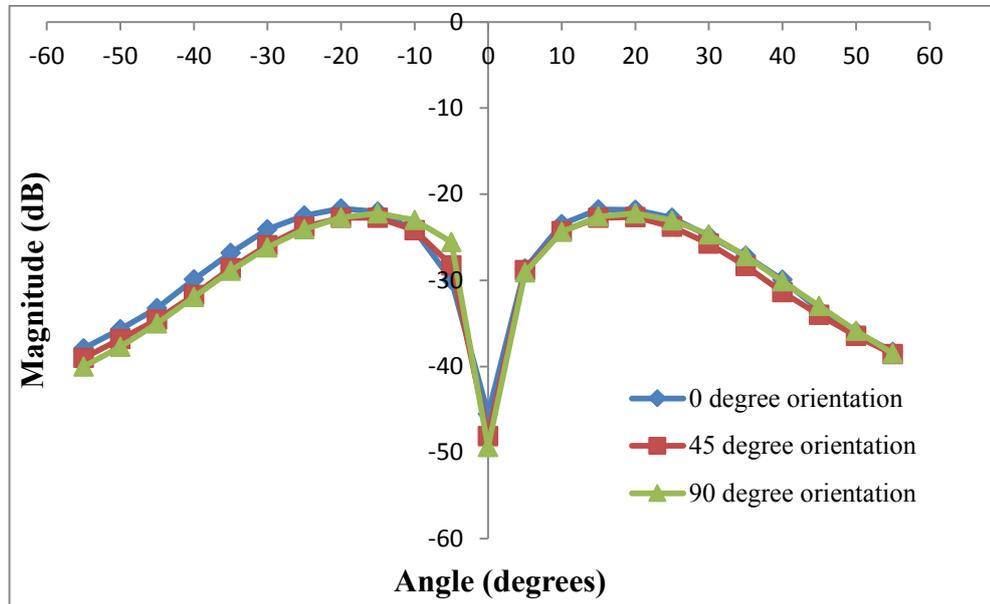
Figure 6.3.4: *Azimuthal polarisation component of the electric field distribution at the centre frequency of 9.0GHz, with the Marie-type converter at 0^0, 45^0 and 90^0 orientations.*
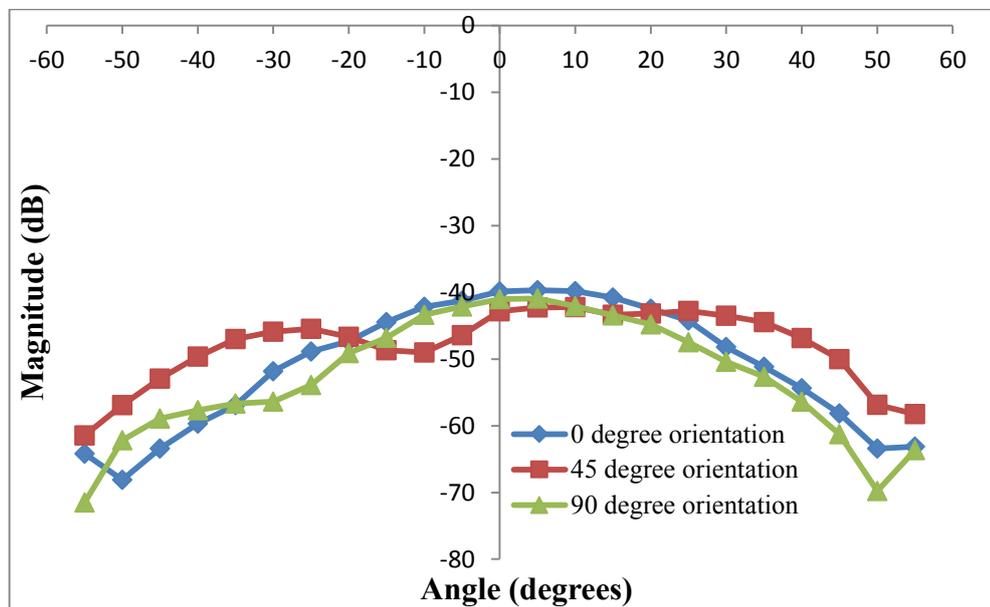
Figure 6.3.5: *Radial polarisation component of the electric field distribution at the centre frequency of 9.0GHz, with the Marie-type converter at 0^0, 45^0 and 90^0 orientations.*

6.4: Application of the 9.0GHz Marie-type converter

The Marie-type converter was used as a test device for a radiation transparent electrostatic plasma confinement component [McConville, 2011] contained within the Auroral Kilometric Radiation (AKR) laboratory experiment at the University of Strathclyde, Glasgow [Cairns, 2005 and Speirs, 2005]. This experiment can operate up to the frequency over which the 9.0GHz Marie-type converter was optimised, in a range of $TE_{0,m}$ modes.

AKR emission occurs in the polar regions of the Earth's magnetosphere [Gurnett, 1974 and Benson, 1985] and is driven by a variation of the CRM instability *(chapter 2)*. In this magnetospheric region particles accelerate downwards and are subjected to an increasing magnetic field, forming a horseshoe distribution in velocity space [Bingham, 2000]. The AKR laboratory experiment was designed to recreate this naturally occurring effect but scaled to a higher frequency [Ronald, 2008a, Cairns, 2011 and Vorgul, 2011]. In the magnetosphere AKR emission is polarised in the X-mode [Pritchett, 1985], propagating perpendicular with respect to the magnetic field close to the cyclotron frequency. For the laboratory experiment this can be best replicated by operating with near to cut-off cylindrical $TE_{0,m}$ modes [Speirs, 2010]. In more recent times a Penning trap was integrated into the scaled laboratory experiment to fully replicate those conditions in the magnetosphere through generation and confinement of a background plasma in the interaction region of the experiment [Gillespie, 2008, McConville, 2008, Ronald, 2008b, Speirs, 2008 and Ronald, 2011]. This Penning trap required an electrostatic cathode transparent to the $TE_{0,m}$ modes to help define the discharge volume. In experiments [McConville, 2009] the radiation pattern observed was rather unexpected and posed the question of whether the cathode structure was behaving as expected, or if the wave generation was into an unexpected mode. Therefore it was desirable to measure the transmission response of the Penning cathode. This was possible using the Marie-type converter since the output mode from

the converter and the anticipated operating mode of the scaled AKR experiment were equivalent.

The cathode piece comprised of an eight spoke copper mesh, *figure 6.4.1*, which was tapered to minimise reflections by creating a smooth transition to the output waveguide.

Figure 6.4.1: *Cathode mesh with eight spoke copper wire structure.*

This copper mesh had two functions. The first of which was to allow unperturbed passage of radiation through the mesh, specifically radiation in $TE_{0,m}$ modes. The mesh's second function was to act as an electrostatic reflector to confine plasma electrons. This was achieved through radial orientation of all mesh wires such that $TE_{0,m}$ modes drive no current in the wires. Since these modes have no radial electric field then in theory the radiation passes through unperturbed. Thus the inclusion of the wire mesh to the output of the Marie-type converter should reproduce the far field patterns obtained when the mesh was not present. The results displayed in *figure 6.4.2* and *figure 6.4.3* show only minimal variation between the azimuthal polarised radiation pattern with no mesh present to that with the mesh present at the centre frequency 9.0GHz. This statement also holds for the radial polarisation component with these trends observed across the whole frequency bandwidth, *figure 6.4.4* and

figure 6.4.5. All these measurements were taken with the Marie-type converter at 0^0 orientation.
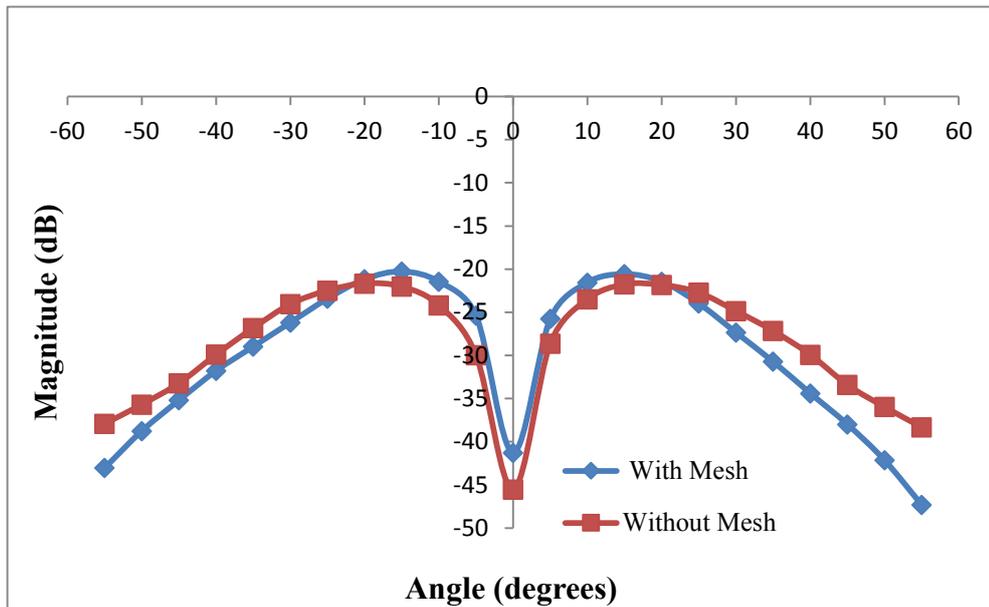
Figure 6.4.2: *Comparison of the azimuthal polarisation component of the electric field distribution at 9.0GHz centre frequency, with and without the plasma confinement mesh.*
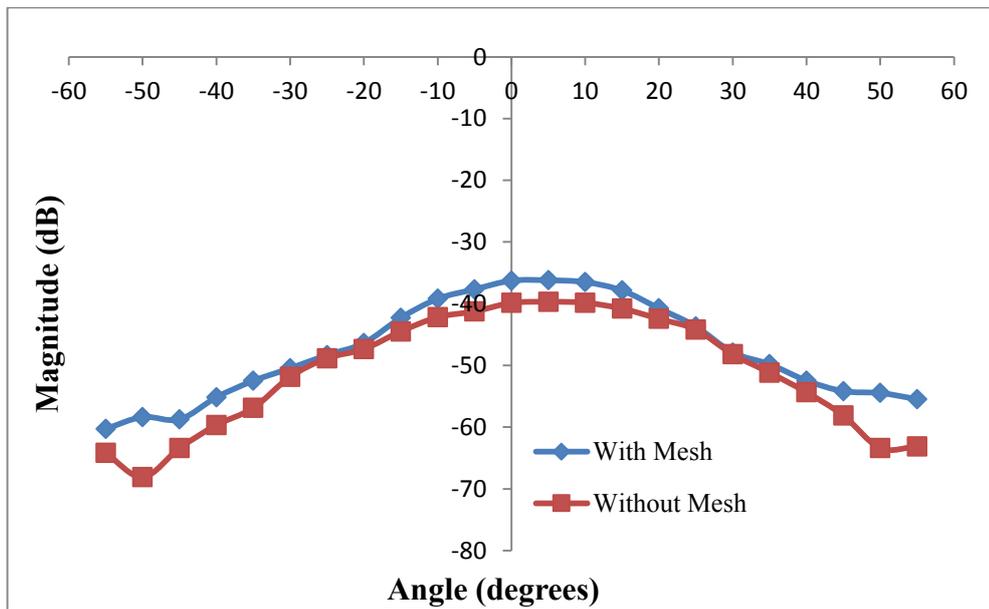
Figure 6.4.3: *Comparison of the radial polarisation component of the electric field distribution at 9.0GHz centre frequency, with and without the plasma confinement mesh.*
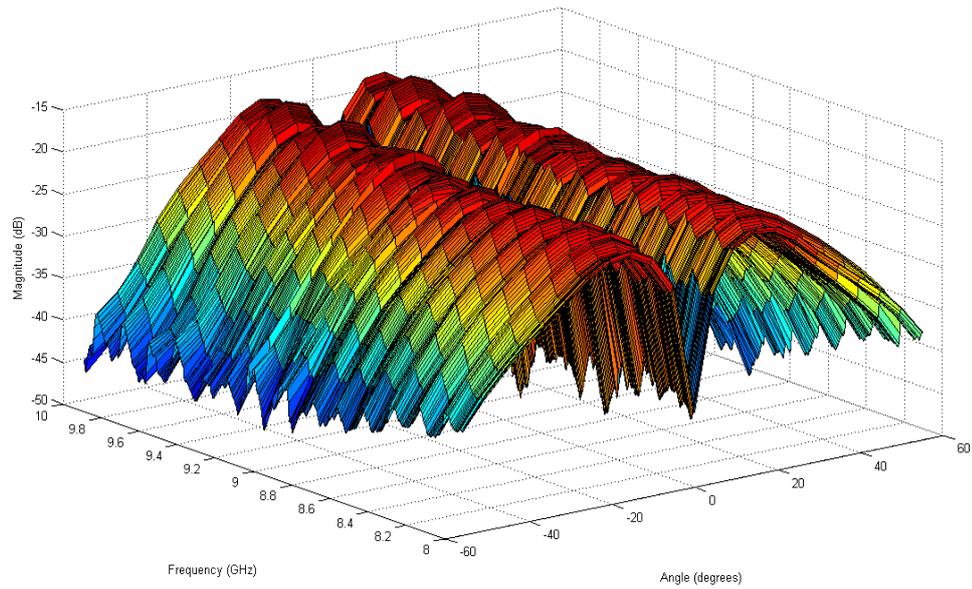
Figure 6.4.4: *3D plot of the azimuthal polarisation component with the mesh present, measured with an SNA over the entire optimised 2.0GHz frequency bandwidth of the converter.*
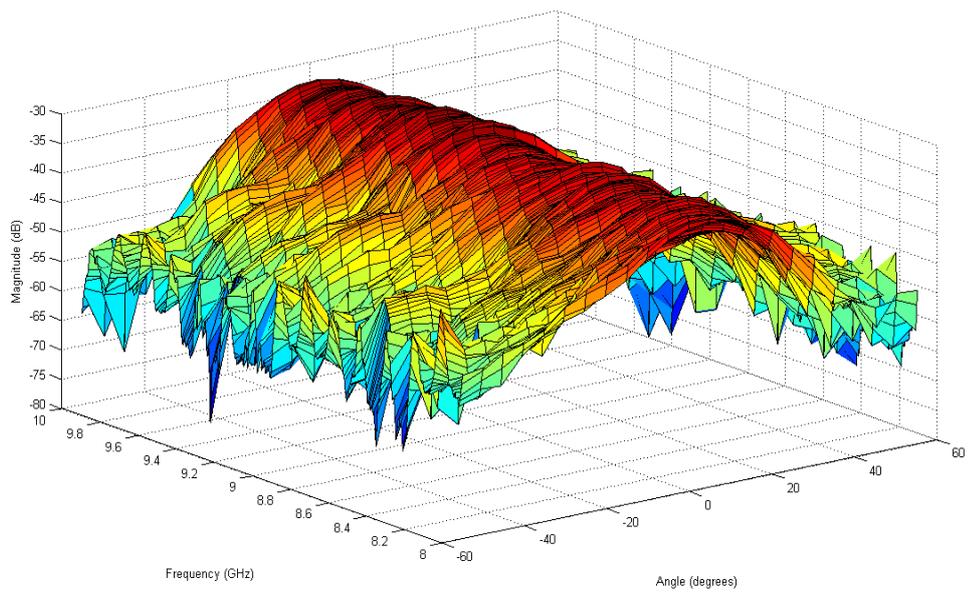
Figure 6.4.5: *3D plot of the radial polarisation component with the mesh present, measured with an SNA over the entire optimised 2.0GHz frequency bandwidth of the converter.*

The 3D plots, *figure 6.4.4* and *figure 6.4.5,* of the far field measurements for both the azimuthal and radial polarisation components of the electric field across the entire frequency bandwidth with the mesh present, were consistent with that of a cylindrical

168

TE$_{01}$ mode. The marginal offset in maximum field amplitude (magnitude and position) evidenced in the azimuthal component when the mesh was present compared to when the mesh was absent, *figure 6.4.2,* arose from the slight increase in radius between the output aperture of the converter and the radius of the output taper in the 8-spoke mesh. Analytical theory for TE modes, [Silver, 1949] *equation 3.5.2* and *equation 3.5.3,* verify that a change in radius would have this effect on the field distribution patterns.

The forward reflection coefficient of the Marie-type converter with the 8-spoke mesh attached at the output was measured using the VNA from an offset-short-load calibration (the same calibration used when the mesh was not present). Again the measured S$_{11}$ suggested that across almost the entire frequency bandwidth the Marie-type converter had a forward reflection of better than –20dB, *figure 6.4.6*. This measurement provides further validation that the inclusion of the cathode mesh had no significant effect on the performance of the Marie-type converter and that the cathode mesh performs as required for the AKR laboratory experiment.
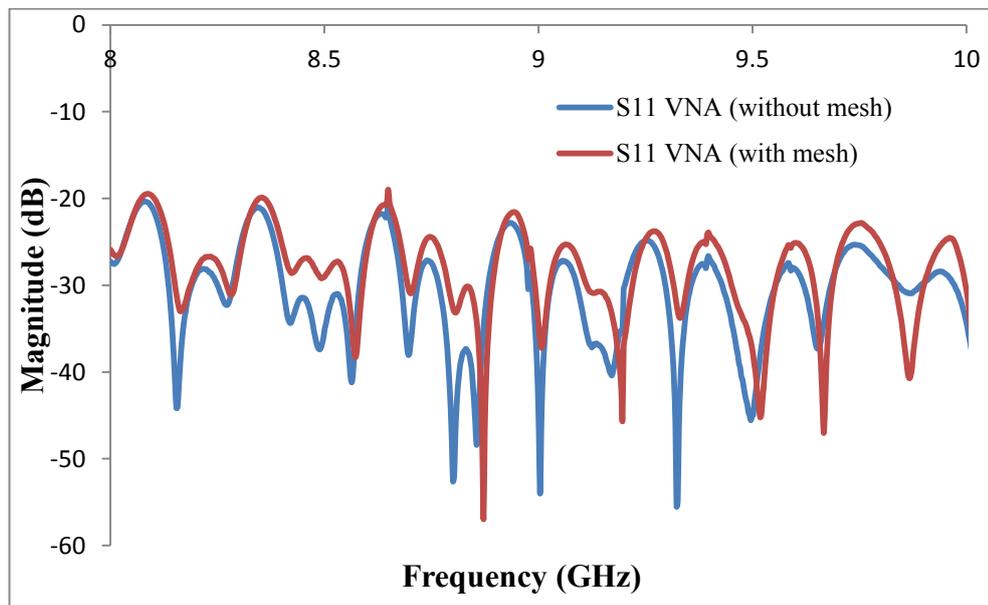
Figure 6.4.6: *Forward reflection coefficient (S$_{11}$) with the presence of the 8 spoke cathode mesh compared to the same measurement taken when the mesh was not present, measured using a VNA.*

6.5: Summary

The purity of the output cylindrical TE_{01} mode from the Marie-type converter made the device suitable to test the radiation transparent Penning cathode mesh designed for the AKR experiment.   Both far field measurements and forward reflection measurements taken without the mesh, and repeated with the mesh present, show that inclusion of the cathode mesh had no significant effect on the performance of the Marie-type converter and that the mesh did indeed allow egress of radiation in the cylindrical TE_{01} mode.

Chapter seven: Conclusions and future work

7.1: Overview

This chapter will highlight and review the principle findings of the research contained within this thesis and discuss the future scope of this work.

7.2: Gyro-TWA simulations

In this thesis (*chapter 4*), multidimensional simulations of an X-band 2nd harmonic gyro-TWA with helically corrugated interaction waveguide modelled in Cartesian co-ordinates were presented. These simulations offered enhanced numerical stability over cylindrical co-ordinate systems and were observed to consistently reproduce experimental measurements for similar parameters. In the laboratory experiment an output power of ~1.1MW, saturated gain of ~37dB and saturated efficiency of ~29% were achieved at 9.4GHz with the amplifier having a measured bandwidth of 2.0GHz from 8.4GHz to 10.4GHz. In the experiment a confining magnetic field of 0.21T was used together with a Pierce-type electron gun and kicker to deliver a 185kV, 20A axis encircling electron beam with an α estimated to be ~1.2. The fully optimised gyro-TWA simulation realised an observed power of ~1.0MW, saturated gain of ~39.7dB and saturated efficiency of ~27% at 9.4GHz, having a bandwidth of 1.8GHz from 8.4GHz to 10.2GHz. To realise this a confining magnetic field of ~0.2123T was used

together with a synthesised axis encircling electron beam of 185kV and 20A with a defined α of ~1.27. In the optimised simulations it was possible to monitor the average kinetic energy of the beam electrons as a function of axial position, with this data providing the particle equivalent power and particle equivalent gain of the instability for given frequencies. Thus in theory, the simulated amplifier could hope to achieve a particle equivalent power of up to ~1.06MW for an input power of ~105W at 9.4GHz, corresponding to a saturated particle efficiency of ~28.6%. These results provided assurance that the numerical model was a sound representation of the experiment and would suggest that the laboratory experiment had been optimally configured.

The simulation results highlighted some interesting details about the gyro-TWA system which may have been overlooked when the original experiment was undertaken. For example the experimental amplifier had a measured saturated bandwidth range 200MHz larger than that of the simulated amplifier with this discrepancy appearing at the upper frequency limit of the band i.e. at 10.4GHz. However simulations of the amplifier and its output structure at this frequency, both in the modelling code MAGIC-3D and CST Microwave Studio, suggested that the TE_{21} mode partially radiated out of the cylindrical waveguide, rather than the desired TE_{11} mode. These results were also consistent with waveguide theory. These observations raise doubts over the measured 10.4GHz experimental result and suggest that the output mode of the experiment at this frequency had changed. Revisiting the experiment and running at this frequency would enable this result to be truly verified. Moreover the simulation results suggested that the experimental amplifier was being overdriven towards the upper frequency of its band and that optimum performance of the amplifier was at 10.0GHz, rather than the 9.4GHz measured experimentally. In the simulations an observed power and gain of ~1.06MW and ~45.6dB for an input power of ~30W were achieved at 10.0GHz. These values increase to up to ~1.2MW and ~46.2dB respectively when particle equivalent power and gain were considered. The results correspond to an increase in observed power of ~60kW and observed gain of ~5.9dB respectively when compared to the optimal simulation performance recorded at 9.4GHz. As such the observed saturated efficiency of the amplifier also

increased by ~1.6% from ~27% at 9.4GHz to ~28.6% at 10.0GHz. When particle equivalent power and gain were considered the saturated particle efficiency of the amplifier was predicted to increase from ~28.6% at 9.4GHz to ~32.3% at 10.0GHz. These values would, if realised in practice, represent a significant improvement to the performance demonstrated experimentally at this frequency.

Ideally in the future the laboratory experiment of the gyro-TWA would be revisited to investigate the interesting behaviour of the device highlighted in the 3D simulations. Initially the experiment should be rerun at 10.4GHz to establish whether the device was radiating partially in the quadrupole TE$_{21}$ mode as has been suggested from both waveguide theory and the modelling codes MAGIC-3D and CST Microwave Studio. The saturated bandwidth measurements should also be rerun with lower drive powers towards the upper limit of the bandwidth to determine whether the saturated performance of the amplifier over these frequencies could be improved as is predicted in the simulations. Moreover, the reliability displayed by the numerical model also suggests that in the future the parameters of the model could be readily modified to investigate gyro-TWAs with helical interaction waveguides at different frequencies. It is also anticipated that with simple modification to the current model the dynamics of gyro-BWOs with helically corrugated waveguides could also be accurately modelled.

Once it had been established with reasonable confidence that the PiC simulations of the gyro-TWA behaved sensibly, achieving output powers and saturated efficiencies in good agreement with that demonstrated experimentally at 9.4GHz, a helical down taper was introduced into the interaction region of the device for the purpose of performance enhancement. Initially it had been anticipated that a relatively long and gradual taper positioned towards the output of the interaction region of the gyro-TWA could increase the efficiency of the device by maintaining beam-wave synchronism for the duration of the interaction space (by holding the electron bunch in trapped orbits whilst decreasing the resonant energy). Such long and gradual tapers proved to be

detrimental to the performance of the amplifier with plots of average kinetic energy of the beam electrons as a function of axial position suggesting that the electrons became phase trapped (saturation of the CRM instability), transitioning between decelerating and accelerating phase along the length of the taper. The average kinetic energy plots also suggested that the taper was ineffective in reducing the average kinetic energy of the electrons below that displayed without the taper present with the minima in each instance corresponding to the same axial position i.e. ~0.93m, associated with the first minimum of the electron bunch's oscillation in the closed orbits within the separatrix. This led to an investigation of relatively short and rapid tapers for the purpose of efficiency enhancement.

At 10.0GHz it was established that a 14cm long helical down taper to an output mean radius, r_0, of ~11.3mm and corrugation amplitude, l, of ~1.76mm (corresponding to a ~20% reduction in both parameters from that of the original amplifier) positioned towards the output of the interaction region of the amplifier (at an axial position 0.82m) improved the performance of the device, achieving an observed power of ~1.15MW for an input power of ~55W. This corresponded to an observed saturated gain of ~43dB and observed saturated efficiency of ~31.1%. Thus the inclusion of this taper into the interaction region of the gyro-TWA was observed to increase the saturated efficiency of the amplifier by ~2.5%, from ~28.6% to ~31.1%, at 10.0GHz. Particle efficiency was also predicted to increase by ~1% at 10.0GHz, from ~32.3% to ~33.2%. However achieving this modest increase in saturated efficiency came at the expense of the observed gain of the amplifier which decreased by ~2.6dB at 10.0GHz when compared the optimised original gyro-TWA with no taper present in the interaction region. This decrease in gain had been anticipated since the gain section of the original gyro-TWA was required to be reduced by 4cm from 60cm to 56cm to accommodate the start of the helical down taper.

Tapering to the output of the interaction waveguide of the gyro-TWA was also studied as a technique to increase the bandwidth performance of the amplifier. By utilising

the helical down taper which successfully increased the efficiency of the device at 10.0GHz, the bandwidth of the device was predicted. It was observed that the taper increased the saturated bandwidth performance of the simulated amplifier by 800MHz, from 8.2GHz to 11.0GHz. This represents a significant improvement in bandwidth performance of the amplifier whilst also maintaining reasonable efficiency.

The original gyro-TWA was already reasonably efficient with an experimentally obtained saturated efficiency of ~29% at 9.4GHz with simulation observed efficiencies of ~27% and ~28.6% at 9.4GHz and 10.0GHz respectively. However increasing the efficiency of the amplifier by tapering the microwave circuit, even by the modest ~2.5% at 10.0GHz (i.e. from ~28.6% to ~31.1%) as predicted here, would reduce the requirements of additional components comprising the full system. For example fewer X-rays would be produced such that lighter shielding to house the system would be required. Moreover less energy in the spent electron beam would reduce the requirements and complexity of the collector since less heat would be dissipated in the system. However the increase in efficiency coupled with the significantly increased bandwidth performance of the amplifier through the inclusion of a 14cm long helical down taper to an output mean radius of ~11.3mm ($0.80*r_0$) and corrugation amplitude of ~1.76mm (~$0.80*l$) in the interaction region of the device, makes this an attractive avenue to explore experimentally. Thus the future scope of this work includes an experimental investigation into tapering the interaction region of the gyro-TWA with successful observation of both efficiency and bandwidth enhancement meriting the investigation of such performance enhancements for amplifiers operating at higher frequencies for potential communication and sensing applications. Furthermore, an investigation into tapering of the confining magnetic field of the gyro-TWA could be undertaken however it is anticipated that such parameter profiling would be less effective than tapering the interaction waveguide.

7.3: Marie-type converter

An X-band Marie-type mode converter, designed to convert from the rectangular TE_{10} mode to the cylindrical TE_{01} with minimal reflections, was simulated in CST Microwave Studio. The converter had an operating centre frequency of 9.0GHz with optimised bandwidth of 2.0GHz and was fabricated in aluminium from the technique of wire erosion. Limitations in the fabrication technique resulted in a marginal deviation between the simulated and fabricated converter designs however this did not affect the overall performance of the converter as confirmed through 'cold' test measurements of the fabricated component. The S-parameters of the simulated Marie-type converter suggested a coupling efficiency into the cylindrical TE_{01} mode of better than 98% across the frequency bandwidth with a reflection coefficient of less than 1%. Coupling into all other modes supported by the structure was also found to be less than 1%. The reflection performance of the fabricated Marie-type converter was measured to be less than -20dB across the optimised 2.0GHz bandwidth, in good agreement with simulation results from CST Microwave Studio. Moreover far field measurements would show that the output radiation was in the desired cylindrical TE_{01} mode. The good agreement between the simulated and fabricated converter results provided assurance in the performance of the fabricated converter and thus the component was used to test a radiation transparent Penning cathode mesh, designed to allow unperturbed passage of radiation in $TE_{0,m}$ modes. Thus its inclusion to the output of the Marie-type converter was expected to reproduce the far field patterns obtained when the mesh was not present. This would be confirmed where only a minimal offset between the azimuthal far field plots with the mesh present to that without the mesh present was observed, accounted for by the slightly increased radius of the mesh to that of the output of the Marie-type converter. Therefore it can be concluded that the Penning cathode mesh performed as required for the AKR experiment it was originally designed for. With this confirmed the future scope of this work is limited. However the Marie-type converter could be used for numerous applications were launching a well-defined cylindrical TE_{01} mode is required as the design is frequency scalable as demonstrated in the simulation of a 5.2GHz converter optimised for 1.0GHz

bandwidth. The relatively simple fabrication of the converter (as modified in the design presented here) makes it an attractive alternative to other converter geometries designed for the same mode conversion. Moreover future simulations of the converter could investigate whether the main sections comprising the converter could be shortened without compromise to the performance since the fabricated converter measured ~1.00m in length.

7.4: Summary

To summarise, an X-band 2nd harmonic gyro-travelling wave amplifier (gyro-TWA) with a helically corrugated waveguide was simulated in MAGIC-3D and benchmarked to a laboratory experiment with a similar parameter set. The numerical model was simulated using the Cartesian co-ordinate system which offered enhanced numerical stability over previous models. The simulations were observed to accurately and consistently reproduce results comparable to the experimental measurements, creating a powerful multidimensional design tool for analysing such devices. The numerical model was used to investigate potential performance enhancement of the gyro-TWA achieved through profiling the microwave circuit. By incorporating a 14cm long helical down taper to an output mean radius of ~11.3mm (~0.80*r_0) and corrugation amplitude of ~1.76mm (~0.80*l) towards the output of the interaction region of the amplifier, it was observed that the saturated efficiency and bandwidth of the amplifier increased by up to ~2.5% i.e. from ~28.6% to ~31.1% and by ~800MHz respectively. The promising improvement in the performance of the gyro-TWA through parameter profiling of the interaction region warrants an experimental demonstration of this prediction.

References

Balanis, C. A., (1982), 'Antenna Theory: Analysis and Design (Second Edition)', John Wiley and Sons, Inc.

Bandurkin, I. V., Phelps, A. D. R. and Savilov, A. V., (2004), 'Regime of nonresonant trapping in a CARM oscillator', IEEE Transactions on Plasma Science, **32**(3), pp929-933.

Benson, R. F., (1985), 'Auroral kilometric radiation: Wave modes, harmonics and source region electron density structures', Journal of Geophysical Research: Space Physics, **90**, pp2753-2784.

Bingham, R. and Cairns, R. A., (2000), 'Generation of auroral kilometric radiation by electron horseshoe distributions', Physics of Plasmas, **7**, pp3089-3092.

Blank, M., Felch, K., James, B. G., Borchard, P., Cahalan, P., Chu, T. S., Jory, H., Danly, B. G., Levush, B., Calame, J. P., Nguyen, K. T. and Pershing, D. E., (2002), 'Development and Demonstration of High-Average Power W-Band Gyro-Amplifiers for Radar Applications', IEEE Transactions on Plasma Science, **30**(3), pp865-875.

Bott, I. B., (1965), 'A powerful source of millimetre wavelength electromagnetic radiation', Physics Letters, **14**(4), pp293-294.

Bratman, V. L., Denisov, G. G., Kol'chugin, B. D., Samsonov, S. V. and Volkov, A. B., (1995), 'Experimental demonstration of high-efficiency cyclotron-autoresonance-maser operation', Physical Review Letters, **75**(17), pp3102-3105.

Bratman, V. L., Cross, A. W., Denisov, G. G., He, W., Phelps, A. D. R., Ronald, K., Samsonov, S. V., Whyte, C. G. and Young, A. R., (2000), 'High-gain wide-band gyrotron traveling wave amplifier with a helically corrugated waveguide', Physical Review Letters, **84**(12), pp2746-2749.

Bratman, V. L., Fedotov, A. E., Kolganov, N. G., Samsonov, S. V. and Savilov, A. V., (2001), 'Experimental study of CRM with simultaneous excitation of traveling and near-cutoff waves (CARM-Gyrotron)', IEEE Transactions on Plasma Science, **29**(4), pp609-612.

Bratman, V. L., Denisov, G. G., Kolganov, N. G., Mishakin, S. V., Samsonov, S. V., Cross, A. W., He, W., Zhang, L., McStravick, M., Whyte, C. G., Young, A. R., Ronald, K., Robertson, C. W. and Phelps, A. D. R., (2010), 'Generation of 3GW microwave pulses in X-band from a combination of a relativistic backward-wave oscillator and a helical-waveguide compressor', Physics of Plasmas, **17**, 110703.

Burt, G., Samsonov, S. V., Ronald, K., Denisov, G. G., Young, A. R., Bratman, V. L., Phelps, A. D. R., Cross, A. W., Konoplev, I. V., He, W., Thomson, J. and Whyte, C. G., (2004), 'Dispersion of helically corrugated waveguides: Analytical, numerical, and experimental study', Physical Review E, **70**, 046402.

Burt, G., Samsonov, S. V., Phelps, A. D. R., Bratman, V. L., Ronald, K., Denisov, G. G., He, W., Young, A. R., Cross, A. W. and Konoplev, I. V., (2005), 'Microwave pulse compression using a helically corrugated waveguide', IEEE Transactions on Plasma Science, **33**(2), pp661-667.

Bykov, Yu., Eremeev, A., Glyavin, M., Kholoptsev, V., Luchinin, A., Plotnikov, I., Denisov, G., Bogdashev, A., Kalynova, G., Semenov, V. and Zharova, N., (2004), '24-84-GHz Gyrotron Systems for Technological Microwave Applications', IEEE Transactions on Plasma Science, **32**(1), pp67-72.

Cairns, R. A. and Phelps, A. D. R. (Editors), (1997), 'Generation and application of high power microwaves', IoP.

Cairns, R. A., Speirs, D. C., Ronald, K., Vorgul, I., Kellett, B. J., Phelps, A. D. R. and Bingham, R., (2005), 'A cyclotron maser instability with application to space and laboratory plasmas', Physica Scripta, **T116**, pp23-26.

Cairns, R. A., Vorgul, I., Bingham, R., Ronald, K., Speirs, D. C., McConville, S. L., Gillespie, K. M., Bryson, R., Phelps, A. D. R., Kellett, B. J., Cross, A. W., Robertson, C. W., Whyte, C. G. and He, W., (2011), 'Cyclotron maser radiation from inhomogeneous plasmas', Physics of Plasmas, **18**, 022902.

Casey, J. A., (1990), 'CIT Gyrotron ECRH System Design', Journal of Fusion Energy, **9**(1), pp7-18.

Chen, S. H., Chu, K. R. and Chang, T. H., (2000), 'Saturated Behavior of the Gyrotron Backward-Wave Oscillator', Physical Review Letters, **85**(12), pp2633-2636.

Choi, D. H. and Hoefer, W. J. R., (1986), 'The Finite-Difference-Time-Domain Method and its Application to Eigenvalue Problems', IEEE Transactions on Microwave Theory and Techniques, **MTT-34**(12), pp1464-1470.

Chu, K. R. and Hirshfield, J. L., (1978), 'Comparative study of the axial and azimuthal bunching mechanisms in electromagnetic cyclotron instabilities', Physics of Fluids **21**(3), pp461-466.

Chu, K. R., Granatstein, V. L., Latham, P. E., Lawson, W. and Striffler, C. D., (1985), 'A 30-MW Gyroklystron-Amplifier Design for High-Energy Linear Accelerators', IEEE Transactions on Plasma Science, **PS-13**(6), pp424-434.

Chu, K. R. and Lin, A. T., (1988), 'Gain and bandwidth of the gyro-TWT and CARM amplifiers', IEEE Transactions on Plasma Science, **16**(2), pp90-104.

Chu, K. R., (2004), 'The electron cyclotron maser', Reviews of Modern Physics, **76**(2), pp489-540.

Clemens, M. and Weiland, T., (2001), 'Discrete electromagnetism with the finite integration technique', Progress in Electromagnetics Research, **PIER 32**, pp65-87.

Collin, R. E., (1992), 'Foundations for microwave engineering, second edition (IEEE Press Series on Electromagnetic Wave Theory)', Wiley-Blackwell.

Cooke, S. J., Cross, A. W., He, W. and Phelps, A. D. R., (1996), 'Experimental operation of a cyclotron autoresonance maser oscillator at the second harmonic', Physical Review Letters, **77**(23), pp4836-4839.

Cooke, S. J., (1998), 'Linear theory of a wide-band gyro-TWT amplifier using spiral waveguide', IEEE Transactions on Plasma Science, **26**(3), pp519-530.

Cross, A. W., He, W., Phelps, A. D. R., Ronald, K., Whyte, C. G., Young, A. R., Robertson, C. W., Rafferty, E. G. and Thomson, J., (2007), 'Helically corrugated waveguide gyrotron traveling wave amplifier using a thermionic cathode electron gun', Applied Physics Letters **90**, 253501.

Daimon, M. and Jiang, W., (2007), 'Modified configuration of relativistic magnetron with diffraction output for efficiency improvement', Applied Physics Letters, **91**, 191503.

Danilov, Yu. Yu., Kuzikov, S. V. and Petelin, M. I., (2000), 'Theory of a microwave-pulse compressor based on a barrel-shaped cavity with helical-corrugated surface', Technical Physics, **45**(1), pp63-65, Translated from Zhurnal Tekhnicheskoĭ Fiziki, **70**(1), 2000, pp65-67.

Denisov, G. G. and Reznikov, M. G., (1982), 'Corrugated cylindrical resonators for short-wavelength relativistic microwave oscillators', Institute of Applied Physics. Translated from Izv. Vyssh. Uchebn. Zaved., Radiofizika, **25**(5), pp562-569.

Denisov, G. G., Bratman, V. L., Phelps, A. D. R. and Samsonov, S. V., (1998a), 'Gyro-TWT with a helical operating waveguide: new possibilities to enhance efficiency and frequency bandwidth', IEEE Transactions on Plasma Science, **26**(3), pp508-518.

Denisov, G. G., Bratman, V. L., Cross, A. W., He, W., Phelps, A. D. R., Ronald, K., Samsonov, S. V. and Whyte, C. G., (1998b), 'Gyrotron traveling wave amplifier with a helical interaction waveguide', Physical Review Letters, **81**(25), pp5680-5683.

Donaldson, C. R., He, W., Cross, A. W., Li, F., Phelps, A. D. R., Zhang, L., Ronald, K., Robertson, C. W., Whyte, C. G. and Young, A. R., (2010), 'A cusp electron gun for millimetre wave gyrodevices', Applied Physics Letters, **96**, 141501.

Donaldson, C. R., He, W., Zhang, L. and Cross, A. W., (2013), 'A W-band multi-layer microwave window for pulsed operation of gyro-devices', IEEE Microwave and Wireless Components Letters, **23**(5), pp237-239.

Dumbrajs, O., (1997), 'A multifrequency gyrotron for plasma heating and diagnostics', International Journal of Infrared and Millimeter Waves, **18**(11), pp2111-2115.

Edelvik, F., Schuhmann, R. and Weiland, T., (2004), 'A general stability analysis of FIT/FDTD applied to lossy dielectrics and lumped elements', International Journal of Numerical Modelling: Electronic Networks, Devices and Fields, **17**(4), pp407-419.

Flyagin, V. A., Gaponov, A. V., Petelin, M. I. and Yulpatov, V. K., (1977), 'The Gyrotron', IEEE Transactions on Microwave Theory and Techniques, **MTT-25**(6), pp514-521.

Flyagin, V. A. and Nusinovich, G. S., (1988), 'Gyrotron oscillators', Proceedings of the IEEE, **76**(6), pp644-656.

Gaponov, A. V., (1959a), 'Interaction between electron fluxes and electromagnetic waves in waveguides', Izv. Vyssh. Uchebn. Zahved. Radiofizika, **2**, pp450-462.

Gaponov, A. V., (1959b), 'Addendum', Izv. Vyssh. Uchebn. Zahved. Radiofizika, **2**, pp836-837.

Gillespie, K. M., Speirs, D. C., Ronald, K., McConville, S. L., Phelps, A. D. R., Bingham, R., Cross, A. W., Robertson, C. W., Whyte, C. G., He, W., Vorgul, I., Cairns, R. A. and Kellett, B. J., (2008), '3D PiC code simulations for a laboratory experimental investigation of Auroral Kilometric Radiation mechanisms', Plasma Physics and Controlled Fusion, **50**, 124038.

Gilmour, A. S., (1994), 'Principles of Traveling Wave Tubes', Artech House, Incorporated, Boston.

Goldenberg, A. L., Denisov, G. G., Zapevalov, V. E., Litvak, A. G. and Flyagin, V. A., (1996), 'Cyclotron resonance masers: state of the art', Radiophysics and Quantum Electronics, **39**(6), pp423-446.

Granatstein, V. L. and Alexeff, I. (Editors), (1987), 'High-power microwave sources', Artech House.

Gurnett, D. A., (1974), 'The Earth as a radio source: terrestrial kilometric radiation', Journal of Geophysical Research: Space Physics, **79**, pp4227-4238.

He, W., Ronald, K., Young, A. R., Cross, A. W., Phelps, A. D. R., Whyte, C. G., Rafferty, E. G., Thomson, J., Robertson, C. W., Speirs, D. C., Samsonov, S. V., Bratman, V. L. and Denisov, G. G., (2005), 'Gyro-BWO experiments using a helical interaction waveguide', IEEE Transactions on Electron Devices, **52**(5), pp839-844.

He, W., Cross, A. W., Phelps, A. D. R., Ronald, K., Whyte, C. G., Samsonov, S. V., Bratman, V. L. and Denisov, G. G., (2006), 'Theory and simulations of a gyrotron backward wave oscillator using a helical interaction waveguide', Applied Physics Letters, **89**(091504).

He, W., Donaldson, C. R., Zhang, L., Ronald, K., McElhinney, P. and Cross, A. W., (2013), 'High power wideband gyrotron backward wave oscillator operating towards the terahertz region', Physical Review Letters, **110**, 165101.

Hirshfield, J. L. and Granatstein, V. L., (1977), 'The electron cyclotron maser – an historical survey', IEEE Transactions on Microwave Theory and Techniques, **MTT-25**(6), pp522-527.

Ishihara, T., Tadano, H., Shimawaki, H., Sagae, K., Sato, N. and Yokoo, K., (1996), 'Space harmonic peniotron in a magnetron waveguide resonator', IEEE Transactions on Electron Devices, **43**(5), pp827-833.

Jain, R. and Kartikeyan, M. V., (2010), 'Design of a 60GHz, 100kW CW gyrotron for plasma diagnostics: GDS-V.01 simulations', Progress in Electromagnetics Research B, **22**, pp379-399.

Kartikeyan, M. V., Borie, E. and Thumm, M. K. A., (2004), 'Gyrotrons: High-power microwave and millimetre wave technology', Springer-Verlag Berlin Heidelberg, Germany.

Katsenelenbaum, B. Z., Mercader Del Rio, L., Pereyaslavets, M., Sorolla Ayza, M. and Thumm, M., (1998), 'Theory of nonuniform waveguides: The cross-section method', The Institution of Electrical Engineers, London.

Kolomensky, A. A. (1973), 'Particle Acceleration by Electron Beams', Particle Accelerators, **5**, pp73-79.

Korolyov, A. N., Gelvich, E. A., Zhary, Y. V., Zakurdayev, A. D. and Poognin, V. I., (2004), 'Multiple-Beam Klystron Amplifiers: Performance Parameters and Development Trends', IEEE Transactions on Plasma Science, **32**(3), pp1109-1118.

Kroll, N. M., Morton, P. L. and Rosenbluth, M. N., (1980), 'Enhanced energy extraction in free-electron lasers by means of adiabatic decrease of resonant energy', Physics of Quantum Electronics, **7**, pp113-145.

Kumar, N., Singh, U., Singh, T. P. and Sinha, A. K., (2011), 'Design of 95GHz, 2MW Gyrotron for Communication and Security Applications', Journal of Infrared, Millimeter and Terahertz Waves, **32**, pp186-195.

Lin, A. T. and Lin, Chih-Chien. (1985), 'Doppler-shift dominated cyclotron maser amplifiers', International Journal of Infrared and Millimeter Waves, **6**(1), pp41-51.

Link, G., Feher, L., Thumm, M., Ritzhaupt-Kleissl, H.-J., Böhme, R. and Weisenburger, A., (1999), 'Sintering of Advanced Ceramics Using a 30-GHz, 10-kW, CW Industrial Gyrotron', IEEE Transactions on Plasma Science, **27**(2), pp547-554.

Manheimer, W. M., (1992), 'On the possibility of high-power gyrotrons for super range resolution radar and atmospheric sensing', International Journal of Electronics, **72**(5-6), pp1165-1189.

McConville, S. L., Speirs, D. C., Ronald, K., Phelps, A. D. R., Cross, A. W., Bingham, R., Robertson, C. W., Whyte, C. G., He, W., Gillespie, K. M., Vorgul, I., Cairns, R. A. and Kellett, B. J., (2008), 'Demonstration of auroral radio emission mechanisms by laboratory experiment', Plasma Physics and Controlled Fusion, **50**.

McConville, S. L., (2009), Ph.D. Thesis, University of Strathclyde.

McConville, S. L., Koepke, M. E., Gillespie, K. M., Matheson, K., Whyte, C. G., Robertson, C. W. and Speirs, D. C., (2011), 'Characterization of a Penning discharge for investigation of auroral radio wave generation mechanisms', Plasma Physics and Controlled Fusion, **53**, 124020.

McElhinney, P., Donaldson, C. R., Zhang, L. and He, W., (2013), 'A High Directivity Broadband Corrugated Horn for W-band Gyro-Devices', IEEE Transactions on Antennas and Propagation, **61**(3), pp1453-1456.

McStravick, M., Samsonov, S. V., Ronald, K., Mishakin, S. V., He, W., Denisov, G. G., Whyte, C. G., Bratman, V. L., Cross, A. W., Young, A. R., MacInnes, P., Robertson, C. W. and Phelps, A. D. R., (2010), 'Experimental results on microwave pulse compression using helically corrugated waveguide', Journal of Applied Physics, **108**(054908).

Mishakin, S. V. and Samsonov, S. V., (2011), 'Analysis of dispersion and losses in helically corrugated metallic waveguides by 2-D vector finite-element method', IEEE Transactions on Microwave Theory and Techniques, **59**(9), pp2189-2196.

Munteanu, I. and Weiland, T., (2007), 'RF & microwave simulation with the finite integration technique – from component to system design', Scientific Computing in Electrical Engineering Mathematics in Industry, **11**, pp247-260.

Nguyen, K. T., Calame, J. P., Pershing, D. E., Danly, B. G., Garven, M., Levush, B. and Antonsen, T. M., (2001), 'Design of a Ka-Band Gyro-TWT for Radar Applications', IEEE Transactions on Electron Devices, **48**(1), pp108-115.

Nusinovich, G. S. and Dumbrajs, O., (1996), 'Theory of Gyro-Backward Wave Oscillators with Tapered Magnetic Field and Waveguide Cross Section', IEEE Transactions on Plasma Science, **24**(3), pp620-629.

Nusinovich, G. S., (2004), 'Introduction to the Physics of Gyrotrons', The John Hopkins University Press, Baltimore, Maryland.

Palevsky, A. and Bekefi, G., (1979), 'Microwave emission from pulsed, relativistic e-beam diodes II - The multiresonator magnetron', Physics of Fluids, **22**(5), pp986-996.

Pantell, R. H., (1959), 'Backward-wave oscillations in an unloaded waveguide', Proc. IRE **47**, pp1146.

Park, G. S., Park, S. Y., Kyser, R. H., Armstrong, C. M., Ganguly, A. K. and Parker R. K, (1994), 'Broadband Operation of a Ka-Band Tapered Gyro-Traveling Wave Amplifier', IEEE Transactions on Plasma Science, **22**(5), pp536-543.

Poděbrad, O., Clemens, M. and Weiland, T., (2003), 'New flexible subgridding scheme for the finite integration technique', IEEE Transactions on Magnetics, **39**(3), pp1662-1665.

Pozar, D. M., (2004), 'Microwave engineering, third edition', John Wiley & Sons.

Pritchett, P. L. and Strangeway, R. J., (1985), 'A simulation study of kilometric radiation generation along an auroral field line', Journal of Geophysical Research: Space Physics, **90**, pp9650-9662.

Roberson, C. W. and Sprangle, P., (1989), 'A review of free-electron lasers', Physics of Fluids B, **1**(1), pp3-42.

Robertson, C. W. and Whyte, C. G., (2012), Private communication.

Ronald, K., Speirs, D. C., McConville, S. L., Phelps, A. D. R., Robertson, C. W., Whyte, C. G., He, W., Gillespie, K. M., Cross, A. W. and Bingham, R., (2008a), 'Radio frequency resonator structure and diagnostic measurements for a laboratory simulation of auroral kilometric radiation', Physics of Plasmas, **15**, 056503.

Ronald, K., McConville, S. L., Speirs, D. C., Phelps, A. D. R., Robertson, C. W., Whyte, C. G., He, W., Gillespie, K. M., Cross, A. W. and Bingham, R., (2008b), 'Electron beam measurements for a laboratory simulation of auroral kilometric radiation', Plasma Sources Science and Technology, **17**, pp1-8.

Ronald, K., Speirs, D. C., McConville, S. L., Gillespie, K. M., Phelps, A. D. R., Bingham, R., Vorgul, I., Cairns, R. A., Cross, A. W., Robertson, C. W., Whyte, C. G., He, W. and Kellett, B. J., (2011), 'Auroral magnetospheric cyclotron emission processes: numerical and experimental simulations', Plasma Physics and Controlled Fusion, **53**.

Saad, S. S., Davies, J. B. and Davies, O. J., (1977), 'Analysis and design of a circular TE$_{01}$ mode transducer', Microwave, Optics and Acoustics, **1**(2), pp58-62.

Samsonov, S. V., Phelps, A. D. R., Bratman, V. L., Burt, G., Denisov, G. G., Cross, A. W., Ronald, K., He, W. and Yin, H., (2004), 'Compression of frequency-modulated pulses using helically corrugated waveguides and its potential for generating multigigawatt rf radiation', Physical Review Letters, **92**(11), 118301.

Savilov, A. V., (1998) 'Regime of trapping and adiabatic deceleration of electrons in a sectioned electron RF generator', IEEE Transactions on Plasma Science, **26**(1), pp36-40.

Savilov, A. V., (2001), 'Cyclotron resonance maser with a tapered magnetic field in the regime of "nonresonant" trapping of the electron beam', Physical Review E, **64**(066501).

Savilov, A. V., (2002), 'CARM-amplifier in the regime of 'nonresonant' trapping of the electron beam', IEEE Transactions on Plasma Science, **30**(3), pp927-930.

Savilov, A. V., (2010), Private communication.

Schneider, J., (1959), 'Stimulated emission of radiation by relativistic electrons in a magnetic field', Physical Review Letters, **2**(12), pp504-505.

Schuhmann, R. and Weiland, T., (2001), 'Conservation of discrete energy and related laws in the finite integration technique', Progress in Electromagnetics Research, **PIER 32**, pp301-316.

Siegel, P. H., (2004), 'Terahertz Technology in Biology and Medicine', IEEE Transactions on Microwave Theory and Techniques, **52**(10), pp2438-2447.

Silver, S., (1949), 'Microwave antenna theory and design', Mc-Graw-Hill Book Company, Inc.

Southworth, G. C., (1950), 'Principles and applications of waveguide transmission', D. Van Nostrand Company.

Speirs, D. C., Vorgul, I., Ronald, K., Bingham, R., Cairns, R. A., Phelps, A. D. R., Kellett, B. J., Cross, A. W., Whyte, C. G. and Robertson, C., (2005), 'A laboratory experiment to investigate auroral kilometric radiation emission mechanisms', Journal of Plasma Physics, **71**, pp665-674.

Speirs, D. C., McConville, S. L., Gillespie, K. M., Ronald, K., Phelps, A. D. R., Cross, A. W., Bingham, R., Robertson, C. W., Whyte, C. G., Vorgul, I., Cairns, R. A. and Kellett, B. J., (2008), 'Numerical simulation of auroral cyclotron maser processes', Plasma Physics and Controlled Fusion, **50**, pp1-15.

Speirs, D. C., Ronald, K., McConville, S. L., Gillespie, K. M., Phelps, A. D. R., Cross, A. W., Bingham, R., Robertson, C. W., Whyte, C. G., He, W., Vorgul, I., Cairns, R. A. and Kellett, B. J., (2010), 'Numerical investigation of auroral cyclotron maser processes', Physics of Plasmas, **17**, 056501.

Sprangle, P. and Drobot, A. T., (1977), 'The linear and self-consistent nonlinear theory of the electron cyclotron maser instability', IEEE Transactions on Microwave Theory and Techniques, **MTT-25**(6), pp528-544.

Sprangle, P., Tang, C. - M. and Manheimer, W. M., (1979), 'Nonlinear formulation and efficiency enhancement of free-electron lasers', Physical Review Letters, **43**(26), pp1932-1936.

Sprangle, P., Tang, C. – M. and Manheimer, W. M., (1980), 'Nonlinear theory of free-electron lasers and efficiency enhancement', Physical Review A, **21**(1), pp302-318.

Speirs, D. C., Phelps, A. D. R., Konoplev, I. V., Cross, A. W. and He, W., (2004), 'Simulation of high power broadband cyclotron autoresonance maser amplifier and electron beam experiments', Review of Scientific Instruments, **75**(4), pp826-831.

Sullivan, D. M., (2000), 'Electromagnetic simulation using the FDTD method', IEEE Press Series on RF and Microwave Technology, IEEE Press.

Taflove, A. and Brodwin, M. E., (1975), 'Numerical solution of steady-state electromagnetic scattering problems using the time-dependent Maxwell's equations', IEEE Transactions on Microwave Theory and Techniques, **MTT-23**(8), pp623-630.

Taflove, A., (1988), 'Review of the formulation and applications of the finite-difference time-domain method for numerical modelling of electromagnetic wave interactions with arbitrary structures', Wave Motion, **10**(6), pp547-582.

Taflove, A., (1995), 'Computational electrodynamics: The finite-difference time-domain method', Artech house.

Taflove, A., (1998), 'Advances in Computational Electrodynamics: The Finite-Difference Time-Domain Method', Artech House Inc.

Tatsukawa, T., Doi, A., Teranaka, M., Takashima, H., Goda, F., Idehara, T., Ogawa, I., Kanemaki, T. and Nishizawa, S., (2002), 'Submillimeter Wave Irradiation of Living

Bodies Using a Gyrotron and a Catheter', Japanese Journal of Applied Physics, **41**, pp5486-5489.

Thumm, M., (2005), 'High power gyro-devices for plasma heating and other applications', International Journal of Infrared and Millimeter Waves, **26**(4), pp483-503.

Twiss, R. Q., (1958), 'Radiation transfer and the possibility of negative absorption in radio astronomy', Australian Journal of Physics. **11**(4)**,** pp564-579.

Vorgul, I., Kellett, B. J., Cairns, R. A., Bingham, R., Ronald, K., Speirs, D. C., McConville, S. L., Gillespie, K. M. and Phelps, A. D. R. (2011), 'Cyclotron maser emission: Stars, planets, and laboratory', Physics of Plasmas, **18**, 056501.

Wang, Q. S., Huey, H. E., McDermott, D. B., Hirata, Y. and Luhmann Jr., N. C., (2000), 'Design of a W-Band Second-Harmonic TE_{02} Gyro-TWT Amplifier', IEEE Transactions on Plasma Science, **28**(6), pp2232-2237.

Weiland, T., (1996), 'Time domain electromagnetic field computation with finite difference methods,' International Journal of Numerical Modelling: Electronic Networks, Devices and Fields', **9**(4), pp295-319.

Weiland T., Timm, M. and Munteanu, I., (2008), 'A practical guide to 3-D simulation', IEEE Microwave Magazine, **9**(6), pp62-75.

Whyte, C. G., Ronald, K., Young, A. R., He, W., Robertson, C. W., Rowlands, D. H. and Cross, A. W., (2012), 'Wideband Gyro-Amplifiers', IEEE Transactions on Plasma Science, **40**(5), pp1303-1310.

Wolfert, P. H., (1963), 'A wide-band rectangular-to-circular mode transducer for millimetre waves', IEEE Transactions on Microwave Theory and Techniques, **11**, pp430-431.

Xue, Q. Z., Zhang, S. C. and Liu, P. K., (2005), 'Design of the H10 to H01 sector-type mode converter at Ka-band', International Journal of Infrared and Millimeter Waves, **26**, pp1407-1415.

Yee, K. S., (1966), 'Numerical Solution of Initial Boundary Value Problems Involving Maxwell's Equations in Isotropic Media', IEEE Transactions on Antennas and Propagation, **14**(3), pp302-307.

Zhang, L., He, W., Ronald, K., Phelps, A. D. R., Whyte, C. G., Robertson, C. W., Young, A. R., Donaldson, C. R. and Cross, A. W., (2012) 'Multi-mode coupling wave theory for helically corrugated waveguide', IEEE Transactions on Microwave Theory and Techniques, **60**(1), pp1-7.

Zhu, S., Wang, E., Li, H., Li, H. and Feng, J., (2012), 'Self-consistent nonlinear theory and simulation of gyro-TWT with helically corrugated waveguide', IEEE Transactions on Plasma Science, **40**(2), pp443-450.